# 4D Monte Carlo investigation of organ motion in radiotherapy for lung cancer

Emily Heath

Department of Physics
McGill University, Montreal
February 2008

*A thesis submitted to the Faculty of Graduate Studies and Research in partial fulfillment of the requirements of the degree of Doctor of Philosophy in Physics*

# Abstract

A limitation of current dose calculation algorithms employed in radiotherapy treatment planning is the assumption that the patient's anatomy is static throughout the imaging, planning and delivery. 4D dose calculation methods employ non-linear image registration to determine the cumulative dose received in a deforming anatomy. In this work, we developed a 4D Monte Carlo dose calculation code, designated defDOSXYZ, which determines the dose received in a deforming voxel grid. Voxel deformations were determined from deformation vectors resulting from non-linear image registration between images of the reference and target states. The ANIMAL non-linear image registration algorithm was implemented for registration of thoracic 4D CT images. Modifications were performed to ANIMAL to minimize deformation vector discontinuities. A method for correcting artifacts in 4D CT images was developed which uses non-linear image registration to interpolate voxel intensities from temporally adjacent artifact-free images. Dose calculations in deforming phantoms and 4D CT patient data using defDOSXYZ were compared to conventional center-of-mass (COM) and trilinear (TL) dose remapping methods.

defDOSXYZ calculations were determined to be accurate to within 1% by comparison with DOSXYZ calculations and internal consistency checks. Conventional dose remapping methods were found to underestimate the dose by 29% and 8%, on average, when remapping dose from Exhale to Inhale within simple deforming phantoms with voxel sizes of 1 cm and 0.5 cm, respectively. These discrepancies were reduced to 0.2% for voxel sizes of 0.25 cm and smaller, however dose errors of 20-30% still existed in regions of steep dose gradients.

The accuracy of non-linear image registration between inhale and exhale images for 5 lung patients was found to be within 2 mm which was deemed acceptable for clinical dose calculations. Temporal interpolation using ANIMAL was demonstrated to improve image quality in 4D data sets containing motion artifacts.

Comparison of dose remapping from Inhale to Exhale in an anatomical breathing phantom revealed that interpolation methods underestimate the dose in the penumbra and near the surface. defDOSXYZ calculations were also compared with two dose remapping methods in 4D CT patient data. Systematic offsets between the dose calculation methods

were noted which were attributed to inconsistent handling of voxel mass conservation in the image registration and dose calculations. A mass-consistent comparison of defDOSXYZ calculations and remapping calculations for clinically relevant planning scenarios and dose grid sizes revealed discrepancies in regions of steep gradients which was consistent with the phantom studies. No clinically significant differences in planning volume doses were noted between all three dose calculation methods, although conventional dose remapping failed to predict certain details of the cumulative dose distribution which may be important for 4D conformal treatment planning.

# Résumé

L'hypothèse que l'anatomie du patient est statique tout au long de l'imagerie, de la planification et du traitement est une limite des algorithmes actuels de calcul de dose en planification de traitement radiothérapeutique. Des méthodes de calcul de dose en 4D utilisent le recalage d'image non linéaire pour déterminer la dose cumulée reçue par une anatomie déformable. Dans cette thèse, nous avons développé un code Monte-Carlo de calcul de dose en 4D, appelé defDOSXYZ, qui détermine la dose reçue dans une grille de voxels déformables. La déformation des voxels a été établie à partir de la variation des vecteurs résultant du recalage d'image non linéaire entre les états de référence et les états cibles. L'algorithme de recalage d'image non linéaire ANIMAL a été appliqué au recalage d'images thoraciques obtenues en tomodensitométrie 4D. Des modifications ont été apportées à ANIMAL afin de minimiser les discontinuités dans la variation des vecteurs. Une méthode a été développée pour corriger les images de tomodensitométrie 4D ; cette méthode utilise le recalage d'image non linéaire pour interpoler l'intensité dans les voxels à partir d'images sans artéfacts consécutives dans le temps. Les calculs de dose avec defDOSXYZ dans les fantômes déformables et sur des images tomodensitométriques 4D de patients ont été comparés aux méthodes conventionnelles de redistribution de dose, l'une dite « du centre de mass » (COM), l'autre trilinéaire (TL).

Les calculs avec defDOSXYZ ont été mesurés et sont exacts à mieux que 1 % en comparaison des calculs de DOSXYZ et de tests d'autocohérence. Nous avons trouvé que les méthodes conventionelles de redistribution de dose sous-estiment la dose, en moyen, par 29% et 8% dans de simples fantômes déformables avec des tailles de voxel de 1.0 cm et 0.5 cm, respectivement. Les divergences étaient réduites jusqu'à 0.2% pour des tailles de voxel de 2.5 mm et plus petits, malgre des regions de divergences de 20-30% existaient encore dans des régions de hautes gradients de dose. La précision du recalage non linéaire entre les images à l'inspiration et les images à l'expiration de cinq cas de poumon a été mesurée et est inférieure à 2 mm, ce qui a été jugé acceptable pour des calculs de dose cliniques. Nous avons démontré que l'interpolation temporelle à l'aide d'ANIMAL améliore la qualité d'image pour des images 4D contenant des artéfacts de mouvement.

La comparaison de la redistribution de dose entre l'inspiration et l'expiration dans un fantôme respiratoire anatomique a révélé que les méthodes d'interpolation sous-estiment la dose dans la pénombre et près de la surface. Les calculs avec defDOSXYZ ont aussi été compares avec deux méthodes de redistribution de dose sur des images de patient obtenues en tomodensitométrie 4D. Nous avons noté des différences systématiques entre les méthodes de calcul de dose, que nous avons attribuées a un traitement incohérent de la conservation de masse des voxels pendant le recalage d'image et le calcul de dose. Une comparaison, cohérent par rapport a la masse, des calculs de defDOSXYZ et des calculs de redistribution pour des scénarios pertinents de planification clinique et de taille de grille de doses ont révélé de grandes différences dans les régions a forts gradients cohérentes avec les études dans des fantômes. Bien qu'aucune différence cliniquement significative n'ait été notée entre les trois méthodes de calcul de dose, la redistribution conventionnelle de dose ne parvient pas a prédire certains détails de la distribution de dose cumulée qui pourrait être importante pour la planification de traitement conformationnelle 4D.

# Acknowledgements

I would first and foremost like to thank my supervisor, Dr. Jan Seuntjens, for his tireless support and guidance.

I would also like to acknowledge the financial support of the National Cancer Institute of Canada/Terry Fox Foundation which provided funding for this project through a Research Studentship.

I would like to thank Dr. Ervin Podgorsak and the staff and students of the McGill Medical Physics Unit for the fruitful 4 years that they have shared with me. I would particularly like to acknowledge the contributions of Dr. Francois DeBlois and Andrew Alexander who provided their software for patient DVH analysis. Dr. DeBlois was also involved in the development of the artifact correction method. Monica Margeanu assisted with the study of reproducibility of patient landmark identification. Laurent Tantot translated the abstract. Many thanks to Dr. Wamied Abdel-Rahman for maintaining our computer cluster and answering many of my Monte-Carlo related questions. I would also like to thank Dr. Frank Verhaegen and Dr. Gabriela Stroian for many useful discussions and advice. Thank you to the dosimetrists who patiently answered all my questions about treatment planning and Dr. Segio Fario M.D. for advice on contouring structures in the lung.

At the Montreal Neurological Institute I would like to acknowledge the significant contribution of Dr. Louis Collins and his students Mallar Chakravarty and Dr. Irina Kezele first of all providing us with the ANIMAL code, answering questions about image registration and general feedback. Dr. Andrew Janke provided the code for calculating the Jacobian maps. Without the involvement of the MNI group in all aspects of the code modification and development of the registration procedure much of this work would not have been possible.

I would like to thank the third member of my thesis committee, Dr. Paul Keall, for providing his valuable insight and knowledge of 4D radiotherapy. It was with Dr. Keall's assistance that we were able to obtain the 4D CT images necessary for this project. I would also like to acknowledge the contribution of his colleague Dr. Elisabeth Weiss M.D. at the

Virginia Commonwealth University who performed contouring on these data sets. Many thanks to Dr. Lei Dong and Dr. Zhongxing Liao M.D. at the MD Anderson Cancer Center who provided the 4D CT patient data used in the registration study.

I would like to thank Dr. Paul Segars from the University of North Carolina (Chapel Hill) for providing us with his NCAT phantom as well as answering our questions and performing any necessary modifications to the phantom.

Dr. Conrado Pla (Nucletron Inc.) provided us with the surface triangulation method.

Thank you to the physics group at the Massachusetts General Hospital in Boston who provided some of the data for the dose warping comparison study. Dr. Joao Seco and Dr. Harald Paganetti provided the 4D CT data, treatment plans and data for Monte Carlo calculations. Dr. Greg Sharp and Dr. Ziji Wu provided the deformation fields.

There are many people who contributed to this project though interesting discussions and useful advice. Among them I would like to particularly acknowledge Dr. Kristy Brock, for her advice on quantification of image registration accuracy, and Dr. Uwe Oelfke who raised the question of mass conservation in non-linear image registration, an issue which proved to be a very important avenue of research. Blake Walters and Dr. Iwan Kawrakow answered questions and provided coding advice for the modification of DOSXYZ.

# Table of Contents

# Chapter 1:

# Introduction

## 1.1 INTRODUCTION

In 2007, an estimated 159,900 new cases of cancer will be diagnosed in Canada[1]. Currently, lung cancer is ranked as the leading cause of death due to cancer, accounting for 29% and 26% of cancer deaths in men and women, respectively. The current 5-year survival rate ratios, compared to general survival for the public, was determined to be around 16%. Lung cancers are classified into non-small cell lung cancers (NSCLC) and small cell lung cancers (SCLC)[2]. The former group comprises adenocarcinomas, squamous cell cancers and large-cell cancers.

Approximately 61% of all lung cancer patients require treatment with radiotherapy[3]. Radiotherapy can be applied alone or in combination with surgery and chemotherapy. Ionizing radiation may be used to destroy cancer cells as it induces DNA strand breaks by interactions which result in cell death and mutation. The goal of any treatment regimen is to maximize the therapeutic ratio, that is to maximize tumor cell kill while minimizing the incidence of side effects related to the treatment. In radiation therapy this translates to a goal of delivering a maximal dose of radiation to the tumor while keeping dose to normal tissues to a minimum.

Radiotherapy may be delivered by external beam therapy or brachytherapy, where radioactive sources are placed inside the patient. External beam radiotherapy may use indirectly ionizing particles, such as photons, or directly ionizing particles such as electrons and protons. Photons are indirectly ionizing because they do not deposit dose directly, rather they transfer energy to electrons in tissues through their interactions. An important concept for radiotherapy is the absorbed dose to the medium. The absorbed dose is defined as the energy deposited in a small mass of medium by charged particles divided by the mass of that medium. The SI unit of absorbed dose is the Gray [1 Gy = 1 Joule/kg].

## 1.2 RADIOTHERAPY PROCESS

The steps of a typical radiotherapy treatment are summarized in Figure 1.

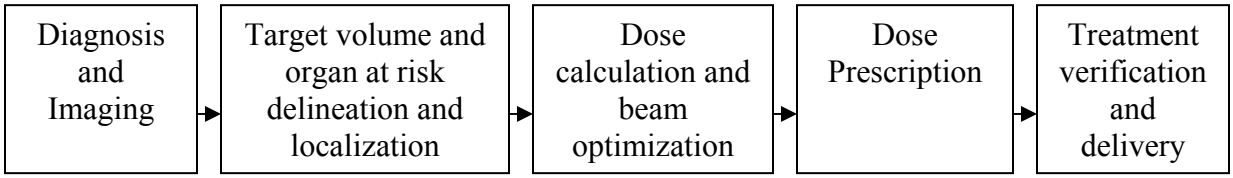


Figure 1. Radiotherapy process [adapted from reference 4]

Current 3D radiotherapy planning techniques require an accurate three-dimensional (3D) representation of the patient geometry and composition which is obtained from images acquired by computed tomography (CT), magnetic resonance imaging (MRI) or positron emission tomography (PET). In CT imaging, a kilovoltage x-ray tube produces a fan beam which rotates around the patient. Attenuated photons which pass through the patient are measured by a 360° ring of detectors. The raw CT data consists of line integrals of linear attenuation coefficients as a function of tube angle and detector distance. These projections, or image slices, are acquired in either an axial or helical fashion. In the former case the CT couch stays fixed as each image slice is acquired while in the latter case the CT couch translates the patient through the gantry simultaneously as the projection data is acquired. The CT *pitch* is defined as the couch movement divided by the slice width. The raw data may be viewed as a *sinogram* (see Figure 2).

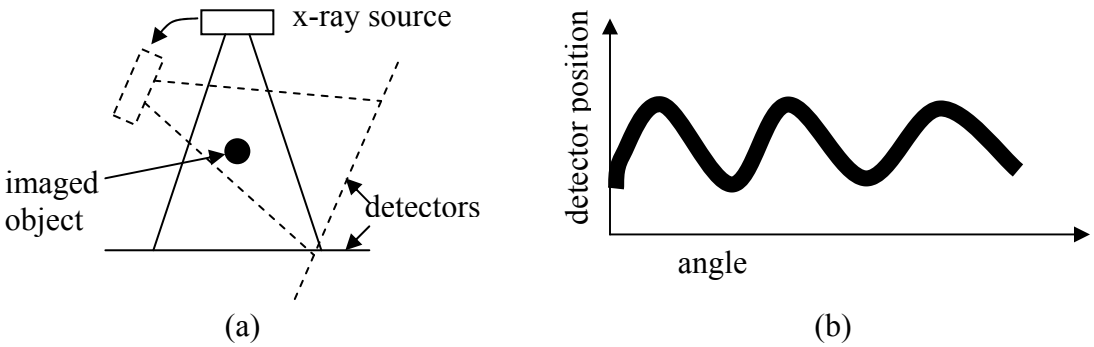


Figure 2. Illustration of (a) CT acquisition and (b) resulting sinogram.

Using back-projection methods[5] the 3D patient anatomy can be reconstructed. The image voxel intensities are reported in Hounsfield Unit (HU) which is the linear attenuation coefficient $\mu$ scaled to the attenuation coefficient of water $\mu_w$

$$HU = 1000 \times \frac{\mu - \mu_w}{\mu_w} \quad . \tag{1}$$

In a PET image acquisition the patient is injected with a radioactive tracer such as fluorodeoxyglucose-18 (FDG-18) labeled with the positron emitter fluorine-18. The FDG is preferentially taken up by regions of high metabolic activity, such as tumour cells, and once it is metabolized it cannot be cleared thus the radioactive tracer is retained in such regions. The patient is then placed inside a ring detector where pairs of annihilation photons created by electron-positron annihilation are detected by a coincidence timing circuit. 3D images may be reconstructed from the detected photon counts using techniques similar to those employed in CT. PET represents a functional imaging modality as it does not provide images of the patient anatomy but of the metabolic processes (ie., glucose uptake) taking place. For this reason it must usually be combined with an anatomical imaging modality such as CT for radiotherapy planning (see Figure 3).

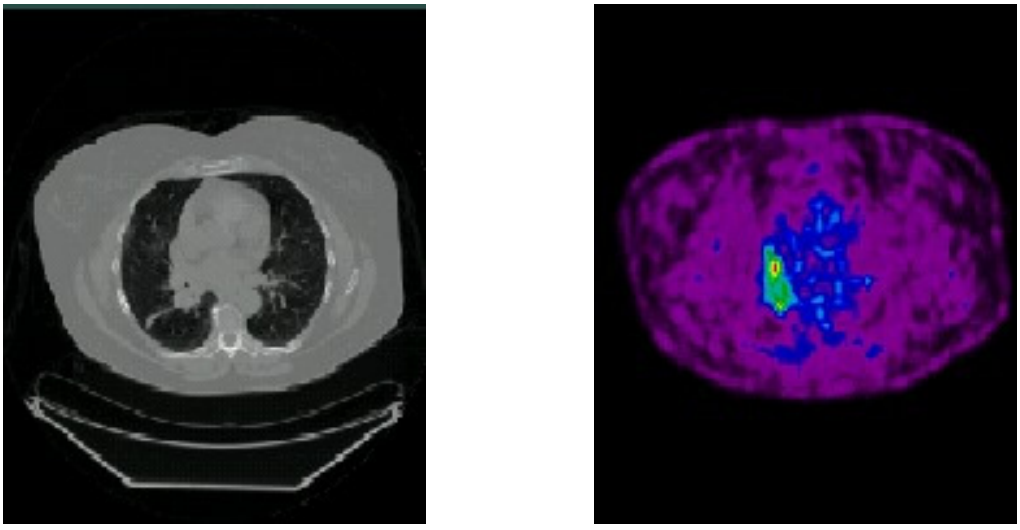

(a) (b)

Figure 3. Comparison of (a) anatomical (CT) and (b) functional (PET) images.

The second step of the radiotherapy planning process is to identify the target volume(s) and any nearby dose-limiting organs. The International Commission on Radiation Units and Measurements (ICRU) defines concepts of target volumes for radiotherapy planning[6] including the gross target volume (GTV), clinical target volume (CTV) and planning target volume (PTV). The GTV is defined as the detectable tumor volume while the CTV encompasses the GTV plus a margin for undetectable microscopic disease. Additional margins for uncertainties in the planning and dose delivery process are added to ensure coverage of the CTV. The goal of the treatment plan is to ensure that this PTV receives within 95% to 107% of the prescription dose. In an update[7] to ICRU Report 50 the PTV margin was redefined to consist of a patient setup error margin (SM) and an internal margin (IM) which accounts for motion occurring during the treatment delivery.

The third step is to determine a geometrical arrangement of treatment beams and their energies which best meet the treatment plan objectives. The conventional approach is to define the beam arrangement based on previous experience or a planning protocol, calculate the dose distribution, evaluate the plan and then make any necessary adjustments and repeat the above procedure. Automated inverse treatment planning methods may also be used where first the treatment plan objectives are defined in terms of doses to target volume and organs at risk and then a mathematical optimization process is used to determine the beam arrangements which minimize an objective function determined from plan objectives. The latter approach is mainly used for intensity-modulated radiotherapy treatment (IMRT) where each beam is subdivided into 2D beamlets whose intensity is optimized. The advantage of this approach is that the dose distribution can be made to conform to the PTV very tightly which allows a higher dose to be delivered without exceeding dose limits of normal tissues[8]. Delivery of IMRT treatment plans requires a device for beam intensity modulation. Most commonly the intensity map is decomposed into a sequence of weighted subfields which can be delivered using a multi-leaf collimator (MLC).

The core of a treatment planning software is the dose calculation engine. The properties of a radiation beam may be characterized by a number of dosimetric quantities,

including the percentage depth dose distribution (PDD) and off-axis ratio (OAR) shown in Equations 2(a) and (b)):

$$PDD(d) = 100 \times \frac{D(d)}{D(d_{\max})} \qquad 2(a)$$

$$OAR(d,x) = \frac{D(d,x)}{D(d,0)} \qquad 2(b)$$

where $d$ is the depth along the beam axis, $x$ is the lateral distance measured from the beam axis and $D(d,x)$ is the dose at the location $(d,x)$. A typical depth dose curve and off-axis profile for a 6 MV photon beam are shown in Figure 4.

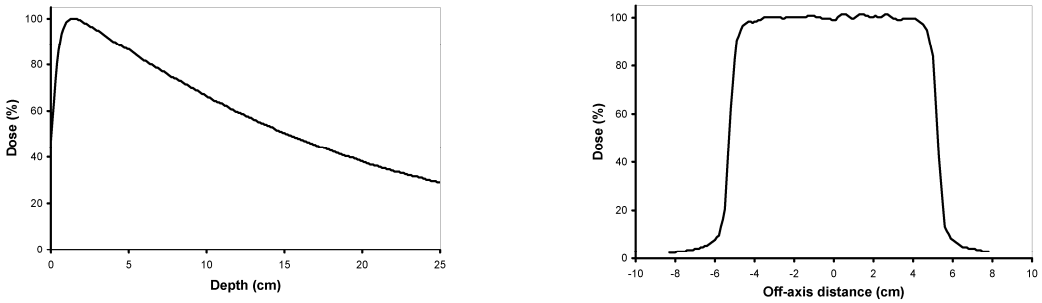


(a) (b)

Figure 4: (a) percentage depth dose and (b) off-axis dose profile.

Such quantities are easily measured and from them the dose at any point can be determined. However, they are usually measured in simple, homogeneous geometries with a flat surface and perpendicular beam incidence. In complex patient geometries the determination of these quantities becomes more difficult. Instead 3D dose calculation algorithms are used. These can be subdivided into correction-based algorithms or model-based algorithms such as convolution-superposition and pencil beam models[9]. Correction-based algorithms make use of dose distributions obtained from an extensive set of dose measurements, such as PDDs and OARs, to which corrections are applied to account for the irregular field apertures, beam modifiers, patient contours and inhomogeneities that may be present for the patient dose calculation. In contrast, model-

based algorithms attempt to model the physical process of dose deposition from first principles in order to calculate the dose distribution directly on the patient data.

Various metrics exist by which the calculated dose distribution can be evaluated to determine if the treatment plan objectives have been met. The most commonly used metric is the dose volume histogram (DVH) which can be used to evaluate what volumetric fraction of a given structure is covered by a given dose level. An example of ideal and typical cumulative DVHs for a target volume and organ at risk are shown in Figure 5. Ideally 100% of the target volume receives the prescription dose $D_{pres}$ and the organ at risk receives no dose. Practically, the organs at risk will receive some dose and the planner must verify that the volume receiving a given dose level does not exceed known organ tolerance doses[10].

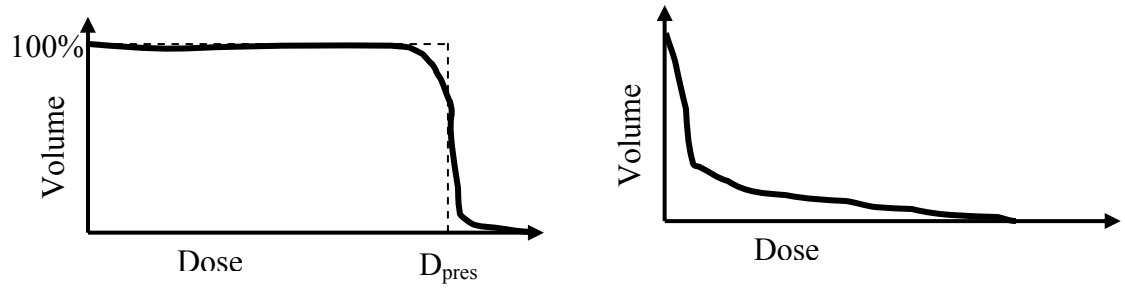


(a) target volume (b) organ at risk

Figure 5. Ideal and typical cumulative dose-volume for (a) target volume and (b) organ at risk. Ideal DVHs are shown by dashed lines, typical DVHs by solid lines.

For organs at risk many studies have been carried out to link dose-volume parameters to biological endpoints such as the amount of surviving cells after irradiation. These efforts have led to the development of biological models[11] which can be used to predict the treatment outcome. The most basic quantities are the tumor control probability (TCP), normal tissue complication probability (NTCP) and equivalent uniform dose[12] (EUD). The EUD is defined as the dose which, if uniformly delivered to an organ, results in the same biological outcome as the current dose distribution.

The final step before treatment delivery is to verify the plan delivery and dose calculation. The patient setup must also be checked to ensure that tumor is in the same position as in the planning image. It is known that patient geometry changes can occur on an inter-fraction (between treatments) or intra-fraction (during treatment) time scale. Examples of inter-fraction geometry changes include weight loss or gain and tumour regression. Intra-fraction changes can occur due to physiological processes such as respiration, digestion and cardiac motion. It is therefore important to have an imaging device available at the treatment unit. Electronic portal imaging devices (EPID) mounted on the linear accelerator are capable of either conventional 2D image acquisition or 3D cone-beam imaging when 2D projections are acquired at multiple gantry angles.

## 1.3 MONTE CARLO METHODS FOR RADIATION TRANSPORT

Monte Carlo methods can be used to solve problems that are described by random processes[13]. Radiation transport, for example, is a random process where the probabilities of particle interactions are determined by their cross-sections[14]. In contrast to analytical dose calculation algorithms, Monte Carlo-based dose calculation algorithms directly simulate the physical interactions of particles which lead to energy deposition in a medium and therefore provide a potentially very accurate means of dose calculation.

The basic process for a Monte Carlo simulation of radiation transport is outlined in Figure 6. Using a random number generator the different interaction cross-sections are sampled to determine the distance to the next interaction point and which type of interaction a particle will undergo. Additional geometry checking routines are often required to track the particle's current location in the simulation geometry. User specified cutoff energies are defined below which particle transport is terminated. The simulation of the trajectory a single particle, including all secondary particles which are generated, is termed a history.

A number of Monte Carlo dose calculation algorithms have been developed for treatment planning of photon and electron beams[15-17]. Monte Carlo techniques have also been employed to simulate the generation of treatment beam particles in the treatment machine[18,19].

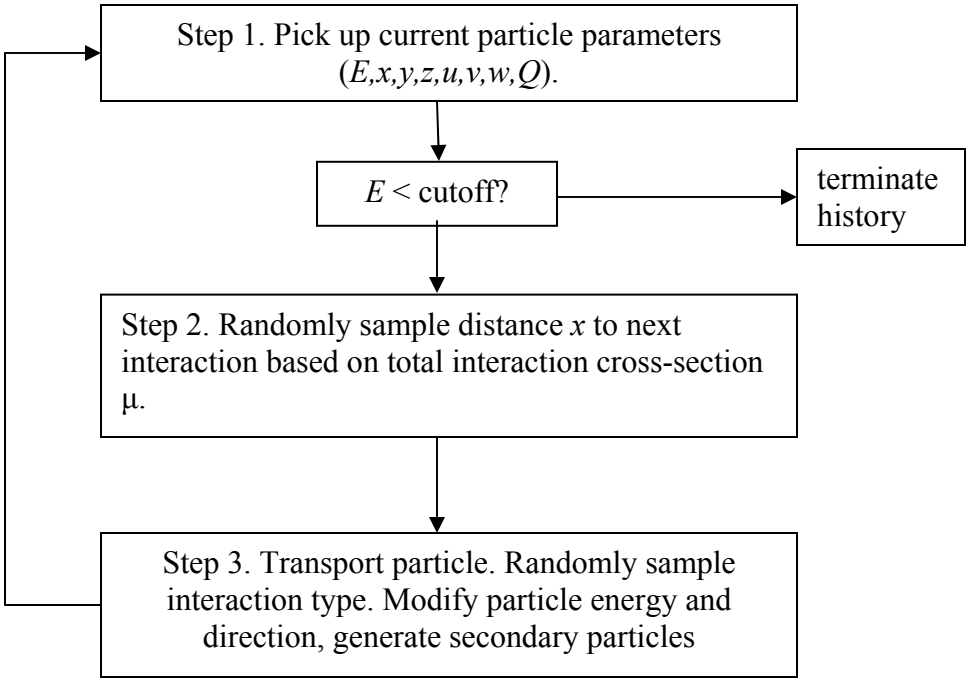


Figure 6. Outline of Monte Carlo simulation of photon transport

## 1.4. ISSUES AFFECTING THE ACCURACY OF LUNG RADIOTHERAPY

Despite significant improvements in radiotherapy delivery techniques, 5-year survival rates for unresectable non-small cell lung cancer remain quite low at less than 20%[20,21]. Currently, most treatment protocols use prescription doses of approximately 60 Gy, delivered in 2 Gy fractions[22]. Many studies have indicated improved survival with increased dose[23,24], however, this is limited by the incidence of radiation pneumonitis and fibrosis[25] arising from irradiation of healthy lung. Both conditions lead to loss of lung function and potentially death. The incidence of radiation pneumonitis appears to correlate with mean dose and volume of lung irradiated[25-27].

A number of physical issues have been identified which need to be addressed in order to improve radiotherapy of lung[28-30]. The first is the improvement of dose calculation accuracy in order to better predict treatment outcome. Many studies have clearly demonstrated that conventional dose calculation algorithms fail to accurately predict the dose in lung[31-33]. Monte Carlo-based dose calculation algorithms are now widely regarded as the gold standard for dose calculation accuracy in such situations. A

second issue to be addressed is the delineation of tumors in the lung. CT images alone do not always provide sufficient information to distinguish cancerous tissues from collapsed lung or necrotic tissue. Large variations in physician delineations of lung tumours have been reported[34]. Combined PET-CT imaging has been demonstrated to reduce this variation as well as improve identification of involved lymph nodes or distant metasteses[35]. Finally, it is known that lung tumors are not stationary and that due to respiration may move up to 3 cm[36] during treatment delivery. The most basic effect of such motion is a decreased conformality of the treatment beam to the target and increased irradiation of the surrounding lung tissue. Such motion also leads to errors in the image acquisition, dose calculation and delivery. 4D radiotherapy planning methods[37] including 4D imaging, dose calculation and delivery methods are being developed to address this issue. 4D dose calculations methods have been developed which used non-linear registration to track how tissue elements move and deform with respiration. However, these methods involve a number of assumptions and it is not clear how this affects the accuracy of the dose calculation.

## 1.5 THESIS OBJECTIVES AND ORGANIZATION

In this thesis we report the development of a novel 4D Monte Carlo dose calculation algorithm for the determination of cumulative dose received by a breathing patient during radiotherapy delivery. The dose calculations are performed using the deformation vectors obtained from non-linear image registration of 4D CT lung images. We also report on the implementation of a registration algorithm, ANIMAL, for non-linear registration of 4D CT thoracic images.

The two main hypotheses to be addressed in this thesis are then:

1. Inaccuracies due to interpolation in current 4D dose calculation methods result in clinically significant differences in the cumulative dose received over a breathing cycle.

2. The accuracy of non-linear registration of 4D CT images of the thorax using the ANIMAL non-linear image registration algorithm is clinically acceptable for application in 4D dose calculations in lung.

The thesis is organized as follows. The second chapter reviews the impact of organ motion and current motion compensation methods in radiotherapy. In the third chapter we review current methods for incorporating the effects of patient motion into dose calculations. Chapter 4 introduces concepts related to non-linear image registration and summarizes currently available algorithms and their applications in radiotherapy. In Chapter 5 we discuss the development and validation of the defDOSXYZ 4D Monte Carlo dose calculation algorithm. The ANIMAL non-linear registration algorithm is introduced in Chapter 6 including a procedure for thoracic 4D CT registration and validation. In Chapter 7 we discuss a method of 4D CT artifact correction based on non-linear image registration. In Chapter 8 we present a comparison of dose calculations performed with defDOSXYZ and conventional deformable dose calculation methods in lung patients. Finally, the thesis findings are discussed in Chapter 9 and some conclusions are presented.

## 1.6 REFERENCES

[1] Canadian Cancer Society/National Cancer Institute of Canada "Canadian Cancer Statistics 2007" Toronto, Canada (2007).

[2] Murshed H. "Clinical fundamentals for radiation oncology residents" Medical Physics Publishing, Madison WI (2006).

[3] Tyldesley S., Boyd C. Schulze K., Walker H. and W. J. Mackillop "Estimating the need for radiotherapy for lung cancer: an evidence-based, epidemiological approach" Int. J. Radiat. Oncol. Biol. Phys. **49** 973-985.

[4] Van Dyk J. "The modern technology of radiation oncology" Medical Physics Publishing, Madison WI (1999).

[5] Curry T.S., Dowdey J.E. and Murry R.C. "Christensen's Physics of Diagnostic Radiology 4th Ed." pp. 303-307 Lippincott Williams & Wilkins, PA (1990).

[6] International Commission on Radiation Units and Measurements (ICRU), ICRU Report 50 "Prescribing, Recording, and Reporting Photon Beam Therapy" ICRU, Bethesda MD (1993).

[7] International Commission on Radiation Units and Measurements (ICRU), ICRU Report 60 "Prescribing, Recording, and Reporting Photon Beam Therapy (Supplement to ICRU Report 50)" ICRU, Bethesda MD (1999).

[8] Liu H.H., Wang X., Dong L., Wu Q., Liao Z., Stevens C.W., Guerrero T.M., Komaki R., Cox J.D. and R. Mohan "Feasibility of sparing lung and other thoracic structures with intensity-modulated radiotherapy for non-small-cell lung cancer" Int. J. Radiat. Oncol. Biol. Phys. **58** 1268-1279 (2004).

[9] Mackie T.R., Reckwedt P., McNutt T., Gehring M., Saunders C. "Photon beam dose computations. Teletherapy: present and future" pp.104-135 (1996).

[10] Emami B., Lyman J., Brown A., Coia L., Goitein M., Munzenrider J.E., Shank B., Solin J.L. and M. Wesson "Tolerance of normal tissue to therapeutic irradiation" Int. J. Radiat. Oncol. Biol. Phys. **21** 109-122 (1991).

[11] Yorke E. "Biological indices for evaluation and optimization of IMRT" Intensity Modulated Radiation Therapy, AAPM pp. 77-114 (2003).

[12] Niemierko A. "Reporting and analyzing dose distributions: a concept of equivalent uniform dose" Med. Phys. **24** 103-110.

[13] Raeside D.E. "Monte Carlo principles and applications" Phys. Med. Biol. **21** 181-197 (1976).

[14] Rogers D.W.O. and A.F. Bielajew "Monte Carlo techniques of electron and photon transport for radiation dosimetry" The Dosimetry of Ionizing Radiation Chapt. 5 Vol III (1990).

[15] DeMarco J.J., Solberg T.D. and J.B. Smathers "A CT-based Monte Carlo simulation tool for dosimetry planning and analysis" Med. Phys. **25** 1-11 (1998).

[16] Ma C-M., Li J.S., Pawlicki T., Jiang S.B., Deng J., Lee M.C., Koumrian T., Luxton M. and Brain S. "A Monte Carlo dose calculation tool for radiotherapy treatment planning" Phys. Med. Biol. **47** 1671-1689 (2002).

[17] Fippel M. "Fast Monte Carlo dose calculation for photon beams based on the VMC electron algorithm" Med. Phys. **26** 1466-1475 (1999).

[18] Verhaegen F. and J. Seuntjens "Monte Carlo modeling of external radiotherapy photon beams" Phys. Med. Biol. **48** R107-164 (2003).

[19] Rogers D.W.O., Faddegon B.A., Ding G.X., Ma C-M. and J. We "BEAM: a Monte Carlo code to simulate radiotherapy treatment units" Med. Phys **22** 503-524 (1995).

[20] Jassem J. "The role of radiotherapy in lung cancer: where is the evidence?" Radiotherapy and Oncology **83** 203-213 (2007).

[21] Lagerwaard F.J., Senan S., van Meerbeeck J.P. and Graveland W.J. "Has 3-D conformal radiotherapy (3D CRT) improved the local tumour control for stage I non-small cell lung cancer?" Radiotherapy and Oncology **63** 151-157 (2002).

[22] Tai P., Yu E., Battista J. and J. Van Dyk "Radiation treatment of lung cancer – patterns of practice in Canada" Radiotherapy and Oncology **71** 167-174 (2004).

[23] Belderbos J.S.A., Heemsbergen W.D., De Jaeger K., Baas P. and J.V. Lebesque "Final results of a Phase I/II dose escalation trial in non-small-cell lung cancer using three-dimensional conformal radiotherapy" Int. J. Radiat. Oncol. Biol. Phys. **66** 126-134 (2006).

[24] Kong F-M., Ten Haken R.K., Schipper M.J., Sullivan M.A., Chen M., Lopez C., Kalemkerian G.P. and J.A. Hayman "High-dose radiation improved local tumor control and overall survival in patients with inoperable/unresectable non-small-cell lung cancer: long-term results of a radiation dose escalation study" Int. J. Radiat. Oncol. Biol. Phys. **63** 324-333 (2005).

[25] Vujaskovic Z., Marks L.B. and M.S. Anscher "The physical parameters and molecular events associated with radiation-induced lung toxicity" Seminars in Radiation Oncology **10** 296-307 (2000).

[26] Yorke E.D., Jackson A., Rosenzweig K.E., Braban L., Leibel S.A. and C.C. Ling "Correlation of dosimetric factors and radiation pneumonitis incidence for non-small-cell lung cancer (NSCLC) patients in a recently completed dose escalation study" Int. J. Radiat. Oncol. Biol. Phys. **60** S240 (2004).

[27] Seppenwoolde Y, Lebesque J.V., de Jaeger K., Belderbos J.S.A., Boersma L.J., Schilstra C., Henning G.T., Hayman J.A., Martel M.K. and R.K. Ten Haken "Comparing different NTCP models that predict the incidence of radiation pneumonitis" Int. J. Radiat. Oncol. Biol. Phys. **55** 724-735 (2003).

[28] Ling C.C., Yorke E., Amols H., Mchalakos J., Erdi Y., Leibel S., Rosenzweig K. and A. Jackson "High-tech will improve radiotherapy of NSCLC: a hypothesis waiting to be validated" Int. J. Radiat. Oncol. Biol. Phys. **60** 3-7 (2004).

[29] Armstrong J. and C. McGibney "The impact of three-dimensional radiation on the treatment of non-small cell lung cancer" Radiotherapy and Oncology **56** 157-167 (2000).

[30] Beckmann G.K., Kolbl O., Krieger T., Wulf J. and M.P. Flentje "How can we further improve radiotherapy for stage-III non-small-cell lung cancer?" Lung Cancer **45** S125-132 (2004).

[31] De Neve W. and C. De Wagter "Lethal pneumonitis in a phase I study of chemotherapy and IMRT for NSCLC: the need to investigate the accuracy of dose calculation" Radiotherapy and Oncology **75** 246-247 (2005).

[32] Knoos T., Ahnesjo A., Nilsson P. and L. Weber "Limitations of a pencil beam approach to photon dose calculations in lung tissue" Phys. Med. Biol. **40** 1411-1420 (1995).

[33] Arnfeld M., Siantar C.H., Siebers J., Garmon P., Cox L. And R. Mohan "The impact of electron transport on the accuracy of computed dose" Med Phys. **27** 1266-1274 (2000).

[34] Giraud P., Elles S., Helfre S., De Rycke Y., Servois V., Carette M-F., Alsieu C., Bondiau P-Y., Dubray B., Touboul E., Housset M., Rosenwald J-C. and J-M. Cosset "Conformal radiotherapy for lung cancer: different delineation of the gross tumor volume (GTV) by radiologists and radiation oncologists" Radiotherapy and Oncology **62** 27-36 (2002).

[35] Bradley J., Thorstad W.L., Mutic S., Miller T.R., Dehdashti F., Siegel B.A., Bosch W. and R.J. Bertrand "Impact of FDG-PET on radiation therapy volume delineation in non-small cell lung cancer" Int. J. Radiat. Oncol. Biol. Phys. **59** 78-86 (2004).

[36] Keall P.J., Mageras G.S., Balter J.M., Emery J.S., Forster K.M., Jiang S.B., Kapatoes J.M., Low D.A., Murphy M.J., Murray B.R., Ramsey C.R., Van Herk M.B., Vedam S.S., Wong J.W. and E. Yorke "The management of respiratory motion in radiation oncology report of AAPM Task Group 76" AAPM Report 91, Med. Phys. **33** 3874-3900 (2006).

[37] Keall P.J., Chen G.T.Y and S. Joshi "Time – the fourth dimension in radiotherapy (ASTRO panel discussion)" Int. J. Radiat. Oncol. Biol. Phys. **57** S8-9 (2003).

# Chapter 2:

# Organ Motion in Radiation Therapy

## 2.1 INTRODUCTION

The effect of organ motion on the accuracy of radiotherapy has recently become a topic of research interest. The main focus of these research efforts have been respiratory-motion affected sites such as lung, liver and breast where the magnitude of the motion is largest. The AAPM Task Group 76[1] investigated the magnitude and impact of respiratory motion and provided recommendations for minimization of the resulting errors in radiotherapy. This task group identified three main areas of concern: (1) motion artifacts in image acquisition which lead to inaccurate organ delineation; (2) design of appropriate treatment plans ensuring adequate tumor coverage; and (3) dose delivery errors.

In this chapter we will discuss the magnitude of respiratory motion in the lung and its impact on radiotherapy of the lung. An overview of current respiration management techniques will also be given.

## 2.2 SOURCES OF ORGAN MOTION AND THEIR MAGNITUDES

The magnitude of lung tumor motion due to respiration has been measured to be up to 50 mm[1], depending on the mode of breathing (shallow or deep) though on average it is around 1.0 cm[2]. Motion is predominantly in the superior/inferior direction and is greater for tumors located in the lower lobes of the lung. The path of motion is not necessarily linear. Due to differences in lung pressure in the inhalation and exhalation phases the motion trajectory can exhibit a hysteresis. Motion of lung tumors is often modeled as sinusoidal, the average breathing period is 4 seconds[3], though in many patients the breathing traces can be highly irregular.

## 2.3 EFFECTS OF MOTION ON IMAGE ACQUISITION

Patient motion during conventional image acquisition (CT, PET, MR) is known to cause image artifacts. This results in an inaccurate representation of the patient geometry and physical characteristics of tissues such as density or retention of a radioactive tracer. This leads in turn to errors in treatment planning as organ delineation and dose calculation rely on accurate depiction of the patient anatomy.

The mechanism by which motion induced CT artifacts are created was described by Balter *et al.*[4]. Motion of an object along the superior/inferior direction during acquisition of axial projections leads to consecutive slices being acquired at different respiratory states, hence a discontinuous appearance. Motion within a single slice acquisition also leads to averaging of the object density states and blurring of the image.

The severity of motion artifacts has been found to depend on the scan time and the velocity of the object being imaged. Ritchie *et al.*[5] studied the minimum scan speed required for suppression of motion artifacts in thoracic CT imaging. They determined that to avoid barely perceptible artifacts in the pulmonary vessels, scan times of 25 msec or less were required. They concluded that even for ultrafast scanners with gantry rotation times of 50 msec motion artifacts would be present. Similarly, McCollough *et al.*[6] studied the effect of temporal resolution on motion artifacts in CT using contrast and spatial resolution phantoms. Motion artifacts were noticeable for a conventional CT scanner with a scan time of 0.5 revolutions/sec for object speeds of 10 mm/sec. A better image quality was obtained with an ultra-fast electron beam CT which had a scan time of 0.1 sec. Both studies indicated that for conventional CT scanners image artifacts will occur unless image acquisition methods can be modified to avoid them[5].

Gagne *et al.*[7] studied the impact of motion artifacts on intensity-based tumor delineation using mathematical simulations and a 3D motion phantom. They found that the spatial extent of the moving object was distorted in terms of shape and location and that the volume occupied over the object's full range of motion was not accurately represented. The mean reconstructed moving object density was on average less than the static case, up to 38% at some points. They also noted that significant distortion can occur when the amplitude of motion exceeds the objective dimensions. Chen *et al.*[8] analyzed distortions of spherical objects undergoing motion during CT acquisition for

realistic motion amplitudes and phases. The moving sphere images appeared to be lengthened or shortened by up to 2 cm along the axis of motion, depending on the motion phase at which the scan was initiated.

Respiration-induced motion causes the patient geometry to change as a function of time and necessitates adding another dimension to the image. A 3D image represents a single snapshot of the anatomy at a given point and time and may not accurately represent all the anatomical states which occur during the respiratory cycle. Shimizu *et al.*[9] investigated whether a free-breathing scan accurately represented the average tumor position for 13 lung patients. The tumor position and cross-sectional area on the free-breathing scan was compared with 20 sequential CT scans acquired at the position of maximum tumor cross-sectional area. In eight patients the tumor was not visible on the measured slice for some phases, this was found to occur mainly for tumors in the lower lobes. The tumor position was found to vary between 1.4 mm to 24.4 mm from the free-breathing scan and the maximum tumor area varied by 120% on average (range 95% to 183%). Evans *et al.*[10] also cautioned that the use of a single patient scan can contribute to systematic errors in radiotherapy planning since only a single sample of the probability distribution function of patient motion is obtained.

To summarize, breathing motion artifacts occur in most images acquired on conventional CT scanners. These artifacts lead to incorrect representation of the imaged objects' position and volume. For imaging of anatomy undergoing respiratory motion, a single scan may not provide adequate information about the average tumor position.

## 2.4 EFFECTS OF MOTION IN TREATMENT PLANNING

The potential consequence of not accounting for motion during treatment planning is a failure to adequately cover the tumor over the full range of motion. A secondary consequence is to not accurately predict the dose distribution and hence the treatment outcome. The effects of organ motion on the dose distribution will be discussed in the next section but the predominant effect is a blurring of the dose distribution over the path of motion[11].

Henkelman *et al.*[12] were the first to study the variations in the delivered dose caused by organ motion. They re-calculated the dose distribution on repeat CT scans acquired at

different respiratory phases. For an anterior-posterior beam arrangement with clinically realistic margins a 3% rms difference in the dose to 8 landmarks was noted between the time-averaged dose and the dose delivered at exhale. For a tangential beam used in a breast plan a 10% rms difference was found. A small blurring of the beam penumbra was noted for the time-averaged dose distribution but was judged clinically insignificant in comparison to the large penumbra of the $^{60}$Co beams used for treatment planning. The authors cautioned, however, that the penumbral blurring effects could be significant for linear accelerator beams. Ross *et al.*[13] examined the incidence of geographic misses in 20 patients with intrathoracic tumors treated with a parallel-opposed beam arrangement. Sequential images acquired with an ultra-fast scanner were examined to determine if the tumor moved outside of the 50% isodose line at any point in the respiratory cycle. The incidence of geographic misses, which were detected in 6 patients, correlated with the magnitude of tumor motion. In one case the minimum tumor dose was only 16% of the prescribed dose. Engelsman *et al.*[14] calculated DVHs for a similar beam arranged based on film measurements in a cork phantom with a Styrofoam insert to simulate a tumor. For a 5 mm breathing motion the TCP decrease to 41.7% from 50% and the tumor EUD dropped from 70 Gy to 66.7 Gy over 5 fractions.

For 3D-CRT and IMRT treatment plans where dose distributions are tightly conformed to the target, the potential for blurring of the steeper dose gradients[15] and inadequate tumor coverage due to motion are expected to be greater, however, the literature indicate that this depends on how the PTV margins were designed. Chetty *et al.*[16] estimated hot and cold spots of up to 15% in the PTV for the motion-convolved dose distribution compared to static calculations for 3 conformal lung patients when using standard margins. Mechalakos *et al.*[17] estimated the effect of motion on GTV coverage in 12 NSCLC patients treated with 3D-CRT and IMRT plans with conventional margins of 1 to 2 cm. On average the effects were small, the mean dose and TCP were reduced by 0.6% (SD 1.2%) and 1.4% (SD 3.8%), respectively. Larger discrepancies were noted in cases where the margin expansion was smaller than the tumor motion. The minimum target dose was reduced by 5.8% on average with larger discrepancies for patients with large, irregularly shaped tumors. Nioutsikou *et al.*[18] compared static and moving 3D-CRT and IMRT plan deliveries in a deformable phantom. They used a 1 cm PTV margin,

which was smaller than the motion amplitudes that were studied. Consequently an underdosage of the tumor, larger for 3D-CRT, was noted as well as blurring of the dose distribution in the tumor. Flampouri *et al.*[19] compared the effect of motion on IMRT lung plans using different planning margin strategies. The standard 1 cm PTV margin expansion was found to underdose 3 out of the 6 patients who had motion greater than 12 mm. No significant difference between the static and cumulative EUD to the lungs was noted due to volume averaging. Rosu *et al.*[20,21] argued that with proper PTV design breathing motion does not significantly affect organ motion. They used margins which encompassed the tumor at the inhale and exhale phases. Only a slight decrease in tumor coverage was noted and the lung DVHs were not significantly affected due to volume averaging of motion-related discrepancies which are confined to penumbral regions. However, to maintain a constant NTCP up to a 6 Gy change in the prescription dose was required for some patients.

To summarize, when organ motion was not considered during treatment planning a decrease in the tumor dose was noted. The magnitude of this underdosage depends on the design of the plan margins, and is most significant when the dose distribution is tightly conformed to the tumor.

## 2.5 EFFECTS OF MOTION ON RADIATION DELIVERY

Bortfeld[11] summarized three main effects of motion on the delivered dose distribution: blurring along the path of motion, spatial deformations and interplay effects. The first effect is considered to be dominant and results in a broadening of the beam penumbra and reduced conformality of the dose distribution. The amount of dose blurring depends on the amplitude of the motion and has a greater effect in regions with steep dose gradients. Localized dose deformations occur because the dose distribution can vary spatially due to displacements and deformations of internal anatomy and interfaces between different tissues. Interplay effects occur in the case of dynamic beam deliveries such as IMRT, enhanced dynamic wedge (EDW) and tomotherapy. In the case of IMRT, organ and MLC leaf relative motions may lead to large point variations in the dose (see Figure 1).

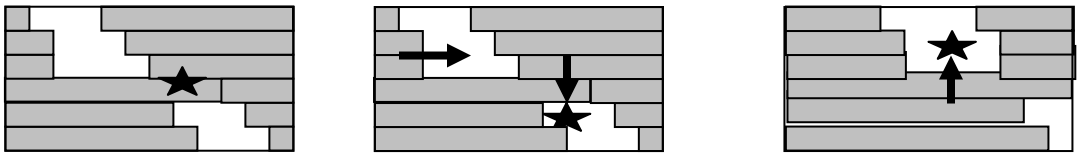

(a) (b) (c)

Figure 1. Illustration of the interplay between target and MLC leaf motion. An organ at risk, denoted by the black star, was blocked by a leaf during planning. However, due to a combination of leaf motion, from left to right, and target motion, from top to bottom, the organ is not shielded by the leaves at (b) and (c).

Many investigations into organ motion effects on dose delivery have concentrated on interplay effects. A theoretical investigation of interplay effects in dynamic MLC delivery was performed by Yu *et al.*[22] using an analytical model to calculate primary photon fluence variations in the target for different motion models. Point dose variations of up to 100% of the planned dose were found, the magnitude depended on the relative speed of leaf motion and target motion as well as the width of the beam defined by leaf pairs relative to the amplitude of target motion. For clinically realistic delivery parameters fluence variations ranged from 30% to 50%. The maximum deviations were noted when the scan speed was similar to the breathing velocity. A periodic dependence of dose variation on the breathing amplitude was noted for small leaf openings, with minima occurring when the beam width was a multiple of the breathing amplitude. Delivery of multiple fractions was found to smooth out these dose variations as the initial breathing phases varies and hence the effects of interplay vary randomly. Bortfeld *et al.*[23] further investigated the influence of fractionation on dose discrepancies due to interplay effects with DMLC, compensators and scanned beams. The expectation value of the dose was found to be independent of the delivery technique and was essentially a weighted average of the static dose over the path of motion. In a statistical interpretation of the interplay effect they demonstrated that the probability distribution function describing the dose variations approaches a Gaussian distribution for delivery of 30 fractions. The

standard deviation of this distribution was largest for the scanned beam and smallest for a physical compensator. A reduced dose rate or higher breathing frequency (less than 4 sec breathing period) reduced these deviations. The authors concluded that the dominant effect of organ motion on IMRT delivery is blurring of the dose distribution and the interplay effects due to dynamic delivery are small. However, they also cautioned that target underdosage can occur due to the tighter conformality of IMRT fields. It should be noted that spatial invariance of the dose distribution was assumed and the validity of this assumption requires further scrutiny.

The conclusions of these two studies have been tested by experimental investigations[24-26]. Generally these experiments confirmed that dose variations due to motion effects were independent of delivery technique and were around 1% to 2%, for a typical number of fractions, though some authors showed contradictory results[24]. One concern is that the radiobiological implications of dose variations due to interplay effects may be larger than the physical dose variations, as the dose delivered per fraction may vary significantly. However, Duan *et al.*[27] found that, although the physical target dose may vary by up to 20% for an IMRT field delivered to a moving phantom, the variation in the tumor control probability was less than 4.3% for a single fraction and was reduced to less than 2.4% for 2 or more fractions. Interplay effects may be non-insignificant in IMRT when leaf sequences contain segments with small MUs such that the time for delivery of a segment approaches the duration of the breathing period. Seco *et al.*[28] reported that deviations from the static dose distribution of up to 20% occurred even for 30 fractions when a single low-MU segment was delivered. For two clinical cases they found a 7% likelihood that dose discrepancies of greater than 1% could occur. The authors cautioned that low-MU segments should be avoided when treating moving targets with IMRT.

To summarize, the primary effect of breathing motion is to blur the delivered dose distribution. Anatomical deformations and motion of tissue interfaces also lead to localized dose deformations. For dynamic delivery techniques, interplay between the tumor and radiation beam motion can lead to very large point dose differences. However, for a clinically realistic delivery with multiple fractions dose differences are generally less than 2%.

## 2.6 MANAGEMENT OF RESPIRATORY MOTION IN RADIOTHERAPY

The deleterious effects of respiratory motion in radiotherapy have been demonstrated and recently much effort has been put into investigation of methods to minimize their impact. The AAPM Task Group 76 report[1] lists, in order of increasing complexity, 5 approaches to managing respiratory motion in treatment planning: (1) motion-encompassing methods; (2) forced shallow breathing; (3) breath hold; (4) gating; and (5) respiratory-synchronized radiotherapy.

### 2.6.1 Motion-encompassing methods

In the absence of any sophisticated equipment and 4D treatment techniques the physicist should ensure that the treatment plan provides adequate coverage of the tumor in the presence of respiratory motion. Basically, this entails increasing the safety margins which are added to the clinical target volume (CTV). An intra-fraction organ motion error must be measured to determine the internal target volume (ITV) defined by ICRU Report 60[29]. Generally, these errors are reported as standard deviations (SD) and added in quadrature[30,31], although there exist many so-called "margin recipes" for combining errors. Antolak *et al.*[32] used a margin of 1.65SD while Stroom[33] and van Herk[34] separated errors into random ($\sigma$) and systematic ($\Sigma$) components and added these as $2.5\Sigma+0.7\sigma$. This recipe was found to guarantee a minimum dose of 95% of the prescription dose to the CTV in 90% of patients but did not account for rotations or shape changes of the target volume.

Individualized patient margins can be derived from motion information measured from fluoroscopy or CT images. In the latter case there are three approaches: (1) slow CT; (2) union of contours drawn on inhale and exhale breath hold CT images; and (3) 4D CT. In a slow CT scan the scan time is approximately 4 sec per rotation or more so that the tumor is blurred over its path of motion. This allows the PTV to be determined directly from the image intensities. Target volumes generated by the slow CT scan method have been found to be more reproducible and cover a larger volume[35,36] than those delineated on free-breathing scans. Shih *et al.*[37] compared ITV margins determined from slow, free-breathing and breath hold CT scans for 13 lung patients. They found that the free-breathing scan had the largest margin (mean 3.5 mm, SD 4.2 mm), while the

margins determined from the breath hold images was smallest (mean 1.1 mm SD 1.9 mm).

#### *2.6.1.1 4D CT*

Four dimensional CT images (4D CT) provide a means of obtaining 3D information about patient anatomical motion and deformation. An over-sampled set of projections is obtained simultaneously with a respiratory monitoring signal. The respiratory phase determined by binning of this signal which is used to prospectively or retrospectively sort the projections by breathing phase in order to reconstruct a 3D image set for each of these phases. Originally 4D CT protocols were proposed for single-slice CT scanners but the image extent that could be scanned was limited by the low pitch required to minimize gaps between the reconstructed slices at each respiratory phase which led to rapid x-ray tube overheating[38,39]. The advent of multi-slice CT scans made it possible to overcome this limitation as scan times were greatly reduced. There are two approaches to acquiring a 4D data set on a multi-slice CT. The first method uses an axial acquisition protocol in which projections are continuously acquired at each couch position for a duration longer than the breathing period. Axial 4D-CT protocols have been reported using digital spirometry[40] and infra-red tracking of an external marker[41,42] to determine the breathing phase. A second 4D CT acquisition method employing a helical scan protocol was proposed by Keall *et al.*[43]. At the point of end-inspiration the respiratory monitoring system sends a pulse to the CT scanner which is used as a tag in the sinogram. The other time points are linearly interpolated throughout the sinogram and the corresponding image sets are reconstructed from the raw data at these points. A potential advantage of the helical acquisition protocol is that the patient dose received during the scan is not affected by the number of respiratory phases to be reconstructed. However, Pan[44] found that the cine acquisition protocol resulted in a lower patient dose because the scan time needed to be extended by 1 breathing period for the helical scan in order to properly determine the starting location of the breathing cycle. Furthermore, if breathing irregularities occur during a helical acquisition an entire re-scan is required and the slice thickness is broadened due to the lower pitch. A 4D cone-beam CT acquisition technique

has also been developed by Sonke *et al.*[45] which allows for daily 4D images to be acquired of the patient prior and during treatment.

There are a number of issues which need to be addressed in 4D CT imaging. These include: increased patient dose and artifacts resulting from inaccurate phase assignment. The prolonged scan acquisition times for 4D CT lead to increased dose to the patient. Li *et al.*[46] proposed that the x-ray tube current, and hence patient dose, can be reduced without significantly compromising image quality. Another significant concern is that breathing phases may be incorrectly assigned to acquired projections[47] or that due to variations in patient breathing patterns images acquired at different breathing amplitudes may be assigned the same phase. The latter issue may be addressed by employing an amplitude-based sorting instead of phase-based sorting. The differences between these two methods are illustrated in Figure 2. Fewer reconstruction artifacts have been noted when using amplitude binning[48-50] , however, with this approach there can be missing slices as images are not acquired at exactly the same amplitude[49]. The quality of phase-

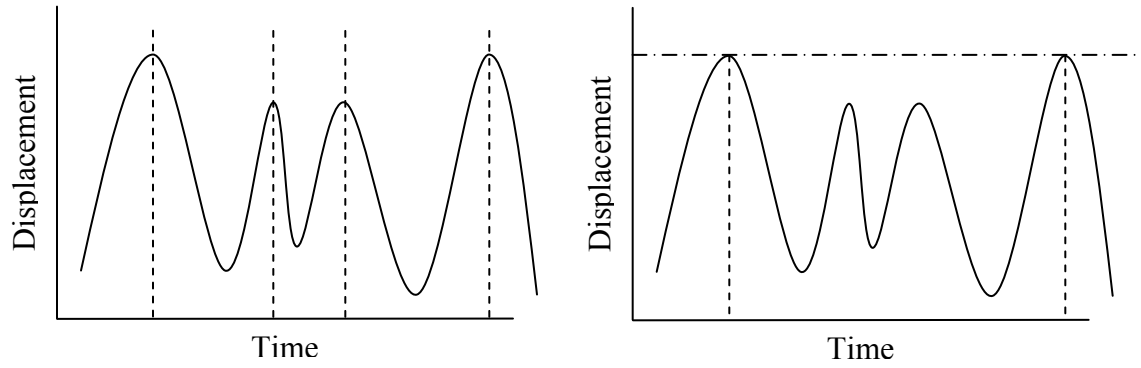


(a) phase-based binning (b) amplitude-based binning

Figure 2. Illustration of phase-based and amplitude-based binning methods for 4D CT image acquisition. Dashed lines indicate time-points which are assigned as end-inhalation. Note that in phase-based binning images with different motion amplitudes will be assigned to the same phase bin. Conversely, with amplitude-based binning the motion amplitudes are the same at each phase bin but slice data may be missing if the patient does not breathe consistently.

binned 4D CT images can also be improved by coaching patients to breathe more reproducibly[51]. The accuracy of the sorting is also dependent on the method used to determine the respiratory phase. As it is not possible to directly measure the respiratory phase during image acquisition internal motion, surrogates are required. Examples of internal motion surrogates include measuring the displacement of external markers placed on the abdomen[52,41,42], strain gauges to measure expansion of the thorax or abdomen[53] to and spirometry to measure air intake[40]. It is important to evaluate whether the surrogate motion correlates with the internal motion[54]. Finally, a 4D CT dataset is only accurate if the patient breathes reproducibly from the treatment planning through to delivery stages. For patients with poor pulmonary function it is possible that a drift exists in the motion amplitude and mean tumor position over the course of treatment[55].

#### *2.6.1.2 Patient specific margin determination*

Patient-specific internal margins can be derived from 4D CT images by a number of methods. First, internal margins can be derived by generation of a composite target volume from contours drawn on individual phases[56]. The effort required for manual delineation on all images can be greatly reduced if a non-linear registration algorithm is used to map contours from a reference phase to all subsequent images[57]. The process can also be automated by generating a maximum (MIP)[58] or average (AIP)[59] intensity projection image before contouring. The MIP technique consists of creating a single CT image from the 4D dataset in which the CT number assigned to each voxel is the maximum CT number which occurs in that voxel throughout the breathing cycle. The AIP method assigns to each voxel the average of the CT numbers which occur at that location over the whole breathing cycle. Effectively this reproduces the image acquired with a slow CT scan. Another strategy has been proposed by Wolthaus *et al.*[60] where a single *mid-ventilation* CT scan is chosen which represents as closely as possible the time-average position of the tumor over the respiratory cycle. Additional margins are then applied to encompass the tumor range of motion. Bosmans *et al.*[61] compared four contouring methods: slow CT, a composite ITV drawn on a 4D CT dataset, a mid-ventilation CT with an additional margin of A/4 (where A is the tumor motion amplitude) and free-breathing CT with an 8 mm margin for motion. An extra 5 mm margin was

added to the target volumes determined by these methods and they were assessed in terms of tumor coverage when the cumulative dose was calculated over the whole breathing cycle. They concluded that use of a slow CT resulted in underdosage of the target volume and that geographical misses occurred when using a free-breathing CT image. The mid-ventilation and 4D CT images produced equally good target volume coverage, however, the former method was preferred as it was less labor intensive[61].

#### *2.6.1.3 Inverse planning incorporating organ motion*

Methods for incorporating tumor have also been proposed for inverse treatment planning methods such as IMRT[62-66]. The advantage of these techniques is that an optimized plan may result in a more conformal dose distribution than conventional forward planning techniques. The general approach utilized by most authors is to use a 4D dose calculation method to determine a motion kernel describing the cumulative dose received over the respiratory cycle for each pencil beam. The dose distribution can then be optimized on each breathing phase individually (for gating or tracking) or simultaneously for all breathing phases (if no respiratory management device was available).

Coolens *et al.*[67] investigated whether smoothing could be applied to a combination of intensity maps optimized on the inhale and exhale states in order to reduce the effect of motion on the delivered dose distribution. They found that even the use of a large 5x5 median window filter did not significantly reduce motion effects for these plans.

### 2.6.2 Forced shallow breathing

Another strategy to deal with respiratory motion is to reduce the motion amplitude by forcing the patient to breath in a shallow manner. This approach is widely used for stereotactic body radiotherapy (SBRT) where the stereotactic localization frame[68,69] may incorporate an abdominal compression plate to limit breathing motion. Reductions of tumor motion amplitude to less than 1 cm have been reported with this device[70-72]. Others have used a body cast[73] or a vacuum-based immobilization system with an abdominal pressure pillow[74]. It is possible to significantly reduce respiratory motion by high

frequency jet ventilation but this has been reported only in animals[75], as it is an invasive procedure requiring anesthesia.

### 2.6.3 Breath hold techniques

If the patient is capable of holding his or her breath for 10 seconds or more then it is feasible to deliver the treatment at the end-inhalation or end-exhalation phases. Hanley *et al.*[76] proposed that a deep inspiration breath hold (DIBH) is better because the lung density is reduced, therefore reducing the irradiated lung volume, and irradiation of the heart may also be reduced. The DIBH maneuver usually requires some patient training and coaching and may be monitored by spirometry[76-78], external markers[79], an implanted fiducial[80] or a laser tracking method[81] to ensure that the patient has achieved the planned lung inflation level before starting irradiation. The beam on/off control may be handled by the therapist[77], patient[82-84] or a gating software[85,86]. Some authors have used visual feedback of respiration traces to improve patient breathing reproducibility[79,85].

The disadvantage of using a breath hold technique is that treatment times are prolonged by a factor of two or more[78] and may not be tolerated by patients with compromised pulmonary function. Generally, a residual motion amplitude of less than 3 mm has been reported using the DIBH procedure[77,80,82-84]. To improve the reproducibility of DIBH a device can be used which temporarily immobilizes patient breathing. This Active Breath Controller (ABC)[87] consists of two pairs of flow monitors and scissor valves to control inhalation and exhalation. The valves are activated at a preselected breathing phase and the duration of the breath holds is 15 to 20 seconds. A highly reproducible lung volume and reduced tumor residual motion has been reported[88-90] using this device.

### 2.6.4 Gating

It is also possible to deliver radiation only during a specific portion of the respiratory cycle. Gated radiotherapy was initially developed by Ohara *et al.*[91] for proton radiotherapy. An advantage of gating over breath hold techniques is that patient cooperation is not necessarily required. Gating is also better tolerated by patients with poor lung function. However, the treatment efficiency is greatly reduced because the

beam is on only during a short period of the breathing cycle. For this reason a combined gated breath hold may be preferable if it can be tolerated by the patient[92]. Gated radiotherapy has been shown to significantly reduce treatment margins, especially for highly mobile tumors[58,93,94].

Accurate gating requires a reliable respiration monitor which has a fast response time, low signal-to-noise ratio and minimal baseline drift[95]. For the latter reason spirometry may not be appropriate for amplitude-based gating[95,96]. Authors have reported the use of implanted gold markers[97,98], strain gauges placed around the abdomen[95,99], infrared tracking of reflective markers[100,101], stereocamera[102] laser systems[103] to measure abdominal displacements, fluoroscopy[104,105] and ultrasound[106,107]. A potential concern for the use of an implanted marker in the lung is that the implantation procedure is risky and markers may migrate to another part of the body which has prompted investigation of fluoroscopic tracking without an implanted marker[104,107]. External surface motion may not always be well correlated and in phase with the tumor motion. The highest correlations have been found between abdominal motion and superior/inferior tumor motion[108-110].

Some new concepts are introduced by gating (see Figure 3) including the gating window, duty cycle and residual motion. The gating window is defined by the thresholds which determine when the beam is turned on and off. The duty cycle is defined as the fraction of the breathing cycle for which the beam is on and is a measure of treatment efficiency. As the gating window increases the duty cycle, and and hence the treatment efficiency, is increased. A drawback of increasing the gating window, however, is that the residual motion will be increased. Therefore, when using gating an optimal balance between minimizing residual motion and treatment times must be found[100].

Similar to 4D CT, gating can be phase or amplitude based, although, for reasons similar to those for its preference in 4D CT, amplitude gating has been found to be more effective in reducing residual motion, however, this is negated if there is a baseline drift respiration signal[111]. The use of breath coaching and patient breathing mode, abdominal or chest breathing, also influence the residual motion[112,113]. Many gating systems also use motion prediction to reduce the time delay, or system latency, between crossing the threshold and sending an ON/OFF signal to the treatment device[114].

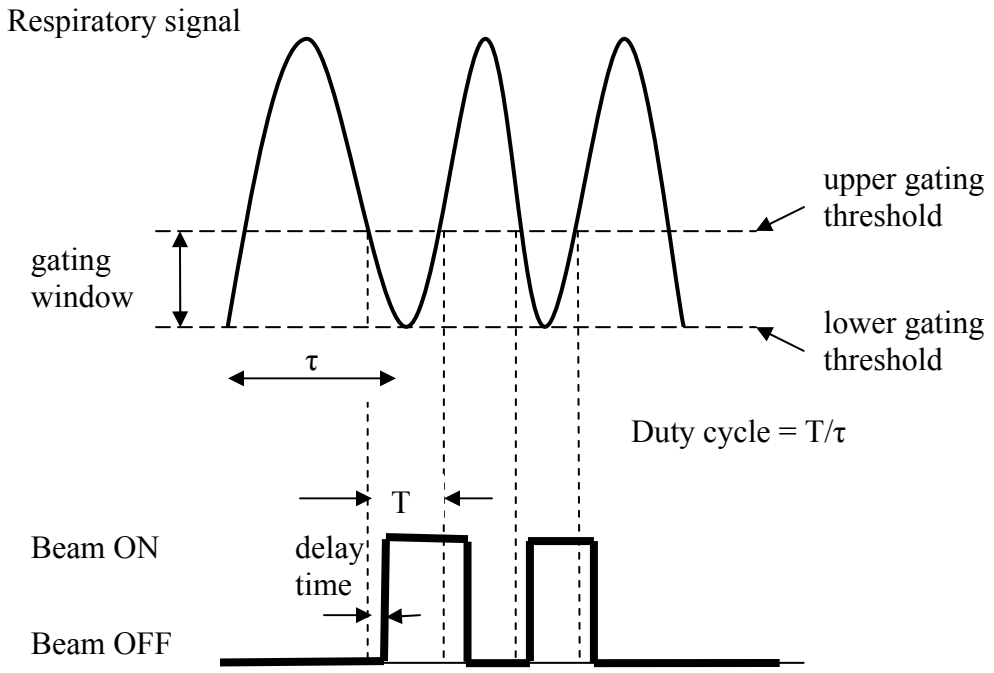


Figure 3. Illustration of the concepts of gating window and duty cycle for amplitude-based gating. Note that for amplitude gating the residual motion and the gating window are the same. The duty cycle is calculated as the ratio of the beam on time *T* to the breathing period τ.

The use of gated radiotherapy implies that either 4D CT or gated CT images must be acquired so that the treatment plan can be designed on the phase of interest. Gating has been used for axial and spiral scan CT protocols[115], including gating in sinogram space[116], and for cone beam CT acquisition[117]. Gating has also been used for delivery of dynamic treatments such as IMRT and EDW[118,119].

### 2.6.5 Respiration-synchronized radiotherapy

The most sophisticated approach for managing respiratory motion is to have the treatment beam follow and adapt to the tumor motion and deformation. Theoretically this respiration-synchronized delivery would eliminate the need for internal margins. However, in practice a safety margin is needed to protect against errors in the tumor tracking and dose delivery. As the beam is delivered during the full breathing cycle the

delivery efficiency could potentially reach 100%, in contrast to gating. Currently respiration-synchronized delivery remains a research tool with the exception of one commercial device, the Cyberknife (Accuray, Sunnyvale CA). Despite differences in hardware implementation, all respiration synchronized treatment delivery devices share common characteristics[120]: (1) a method for determining target position; (2) a motion prediction filter to anticipate target motion for a faster response time; and (3) a method to re-align the beam and adapt the delivered dose distribution. The technical challenge of real-time tracking is that detection and response to target motion must occur in less than 1 second. However, it is often difficult to image tumors that are located in soft-tissues. Therefore, implanted markers or an external surrogate are required. Continuous x-ray imaging of implanted markers is also limited by imaging dose received by the patient.

#### *2.6.5.1 Cyberknife*

The Cyberknife[121] consists of a compact X band linear accelerator, mounted on a robotic arm, capable of motion with 6 degrees of freedom (rotation and translation in 3 dimensions). It was originally developed for radiosurgery applications. Similar to conventional linac-based radiosurgery, the Cyberknife delivers multiple narrow beams from multiple directions to the target in order to obtain a highly conformal dose distribution. The target tracking system has two components: a stereo x-ray imaging system for tracking an implanted gold marker and infra-red tracking of external infra-red emittors placed on the patient's surface. The x-ray system samples the target position at a frequency of 0.1 Hz while the infra-red tracking system is capable of a sampling rate of 60 Hz. For this reason the tracking is based on the external motion using a correlation model which relates it to the internal motion. This correlation model is updated as the implanted marker motion is measured during treatment. The model can be linear or polynomial, although the latter model has been shown to be better at predicting internal motion when there is hysteresis[122].

#### *2.6.5.2 Dynamic MLC tracking*

An alternative approach to respiration-synchronized delivery was proposed using dynamic MLC delivery techniques[123-126] or robotic couch motion[127]. The DMLC-based

motion-adaptive x-ray therapy technique consists of maintaining a static beam's-eye view of the target by superimposing the target motion onto the planned static beams. Synchronization of the MLC leaf motion with the target motion would be performed using an external marker tracking system. This method allows only compensation of rigid motion, however, target deformations could be compensated for by use of a "4D radiotherapy" methodology[128]. In this method, beam apertures are defined on each respiratory phase to account for any shape changes in the tumor. During delivery the MLC then tracks both target position and shape changes. A potential concern for such DMLC tracking techniques is that the patient's breathing pattern may change over the course of delivery. It is therefore necessary to introduce a safety margin to the beam apertures. Alasti *et al.*[129,130] proposed a novel method of determining these safety margins by using a weighted combination of static and dynamic (changing as a function of phase) apertures. The weighting factor depends on the degree of irregularity in the patient's breathing pattern. The accuracy of DMLC tracking depends on geometric accuracy of the MLC leaf position, the time lag between target and leaf motion and the reproducibility of the patient breathing. Keall *et al.*[131] reported a geometric accuracy of less than 1.1 mm and a time lag of 160 ns for DMLC tracking of respiratory motion. Safety mechanisms must exist for shutting off the beam if large differences between the planned and measured tumor trajectory occur[124]. Furthermore, patient breath coaching in the form of audio and visual prompting is important to ensure consistent breathing patterns[132].

The DMLC tracking accuracy is also highly dependent on the accuracy with which the tumor position is inferred. Both internal and external tracking methods have been investigated, the former includes an implanted electromagnetic transponder which has demonstrated an average tracking error within 0.32 mm for lung tumors[133]. The inference of internal motion from an external measurement may be improved by the use of a composite signal derived from tracking of multiple markers placed on the patient's surface[134]. Motion prediction would allow reduction of time delay in the motion feedback loop controlling for leaf position changes in response to target motion. Prediction of irregular breathing is particularly challenging[135] but can potentially reduce beam-off time. Authors have investigated fitting periodic functions to breathing patterns[136] but it has been generally concluded that adaptive neural networks are best suited for breathing

motion prediction as they are able to adapt to changes in the breathing pattern[137-141]. The importance of accurate prediction was underlined by Vedam *et al.*[142] who found that the dosimetric effect of prediction errors could approach those resulting from uncompensated respiratory motion.

## 2.7 SUMMARY

The magnitude of respiration-induced motion of lung tumors is on average 1 cm or more and is mainly in the superior-inferior direction. This motion potentially leads to image artifacts, tumor underdosage and increased volume of irradiated lung. The dose delivered in the presence of breathing motion is predominantly blurred along the path of motion although localized dose deformations occur where organs deform and large dose variations can occur due to interplay effects between target motion and dynamic beam delivery. Thus far, evaluation of motion effects on the dose distribution has relied on simplistic measurements and dose calculation methods. Accurate 4D dose calculation methods are required to properly determine the magnitude and importance of breathing motion on radiotherapy treatment planning and delivery.

The most basic approach to compensate for respiratory motion is to increase the planning margins so that the tumor is covered throughout the breathing cycle. 4D CT imaging is a useful tool to gain patient-specific tumor motion information. More sophisticated motion management techniques include abdominal compression, breath hold techniques and gating. The newest development which holds the most promise, but is also the most complex, for conformal beam delivery in the presence of organ motion is respiration-synchronized radiation therapy using either a robotic linac or dynamic MLC tracking. Evaluation of the efficacy of all these motion compensation techniques requires a 4D dose calculation method to evaluate the dose delivered to the breathing patient.

## 2.8 REFERENCES

[1] Keall P.J., Mageras G.S., Balter J.M., Emery J.S., Forster K.M., Jiang S.B., Kapatoes J.M., Low D.A., Murphy M.J., Murray B.R., Ramsey C.R., Van Herk M.B., Vedam S.S., Wong J.W. and E. Yorke "The management of respiratory

motion in radiation oncology report of AAPM Task Group 76" AAPM Report 91, Med. Phys. **33** 3874-3900 (2006).

[2] Seppenwoolde Y., Shirato H., Kitamura K., Shimizu S., van Herk M., Lebesque J.V. and K. Miyasaka "Precise and real-time measurement of 3D tumor motion in lung due to breathing and heartbeat, measured during radiotherapy" Int. J. Radiat. Oncol. Biol. Phys. **53** 822-834 (2002).

[3] Shirato H., Seppenwoolde Y., Kitamura K., Onimura R. and S. Shimizu "Intrafractional tumor motion:lung and liver" Seminars in Radiation Oncology **14** 10-18 (2004).

[4] Balter J.M., Ten Haken R.K., Lawrence T.S., Lam K.L. and J.M. Robertson "Uncertainties in CT-based radiation therapy treatment planning associated with patient breathing" Int. J. Radiat. Oncol. Biol. Phys. **36** 167-174 (1996).

[5] Ritchie C.J., Godwin J.D., Crawford C.R., Stanford W., Anno H. and Y. Kim "Minimum scan speeds for suppression of motion artifacts in CT" Radiology **185** 37-42 (1992).

[6] McCollough C.H., Bruesewitz M.R., Daly T.R. and F.E. Zink "Motion artifacts in subsequent conventional CT and electron-beam CT: pictorial demonstration of temporal resolution" Radiographics **20** 1675-1681 (2000).

[7] Gagne I.M. and D.M. Robinson "The impact of tumor motion upon CT image integrity and target delineation" Med. Phys. **31** 3378-3392 (2004).

[8] Chen G.T.Y., Kung J.H. and K.P. Beaudette "Artifacts in computed tomography scanning of moving objects" Seminars in Radiation Oncology **14** 19-26 (2004).

[9] Shimizu S., Shirato H., Kagei K., Nishioka T., Bo X., Dosaka-Akita H., Hashimoto S., Aoyama H., Tsuchiya K. and K. Miyasaka "Impact of respiratory movement on the computed tomographic images of small lung tumors in three-dimensional (3D) radiotherapy" Int. J. Radiat. Oncol. Biol. Phys. **46** 1127-1133 (2000).

[10] Evans P.M., Coolens C. and E. Nioutsikou "Effects of averaging over motion and the resulting systematic errors in radiotherapy" Phys. Med. Biol. **51** N1-7 (2006).

[11] Bortfeld T., Jiang S.B. and E. Rietzel "Effects of motion on the total dose distribution" Seminars in Radiation Oncology **14** 41-51 (2004).

[12] Henkelman R.M. and K. Mah "How important is breathing in radiation therapy of the thorax?" Int. J. Radiat. Oncol. Biol. Phys. **8** 2005-2010 (1982).

[13]. Ross C.S., Hussey D.H., Pennington E.C., Stanford W. and J.F. Doornbos "Analysis of movement of intrathoracic neoplasms using ultrafast computerized tomography" Int. J. Radiat. Oncol. Biol. Phys. **18** 671-677 (1990).

[14] Engelsman M., Damen E.M.F., De Jaeger K., van Ingen K.M. and B.J. Mijnheer "The effect of breathing and set-up errors on the cumulative dose to a lung tumor" Radiotherapy and Oncology **60** 95-105 (2001).

[15] Kung J.H., Zygmanski P., Choi N. and G.T.Y. Chen "A method of calculating a lung clinical target volume DVH for IMRT with intrafractional motion" Med. Phys. **30** 1103-1109 (2006).

[16] Chetty I.J., Rosu M., McShan D.L., Fraass B.A., Balter J.M. and R.K. Ten Haken "Accounting for center-of-mass target motion using convolution methods in Monte Carlo-based dose calculations of the lung" Med. Phys. **31** 925-932 (2004).

[17] Mechalakos J., Yorke E., Mageras G.S., Hertanto A., Jackson A., Obcemea C., Rosenzweig K. and C.C. Ling "Dosimetric effect of respiratory motion in external beam radiotherapy of the lung" Radiotherapy and Oncology **71** 191-200 (2004).

[18] Nioutsikou E., Symonds-Taylor J.R.N., Bedford J.L. and S. Webb "Quantifying the effect of respiratory motion on lung tumor dosimetry with the aid of a breathing phantom with deforming lungs" Phys. Med. Biol. **51** 3359-3374 (2006).

[19] Flampouri S., Jiang S.B., Sharp G.C., Wolfgang J., Patel A.A. and N.C. Choi "Estimation of the delivered patient dose in lung IMRT treatment based on deformable registration of 4D-CT data and Monte Carlo simulations" Phys. Med. Biol. **51** 2763-2779 (2006).

[20] Rosu M., Chetty I.J., Balter J.M., Kessler M.L., McShan D.L. and R.K. Ten Haken "Dose reconstruction in deforming lung anatomy: Dose grid size effects and clinical implications" Med. Phys. **32** 2487-2495 (2005).

[21]. Rosu M., Chetty I.J., Tatro D.S. and R.K. Ten Haken "The impact of breathing motion versus heterogeneity effects in lung cancer treatment planning" Med. Phys. **34** 1462-1473 (2007).

[22] Yu C.X., Jaffray D.A. and J.W. Wong "The effects of intra-fraction organ motion on the delivery of dynamic intensity modulation" Phys. Med. Biol. **43** 91-104 (1998).

[23] Bortfeld T., Jokivarsi K., Goitein M., Kung J. and S.B. Jiang "Effects of intra-fraction motion on IMRT dose delivery: statistical analysis and simulation" Phys. Med. Biol. **47** 2203-2220 (2002).

[24] Ehler E.D., Nelms B.E. and W.A. Tome "On the dose to a moving target while employing different IMRT delivery mechanisms" Radiotherapy and Oncology **83** 49-56 (2007).

[25] Schaefer M. Munter M.W., Thilmann C., Sterzing F., Haering P., Combs S.E. and J. Debus "Influence of intra-fractional breathing movement in step-and-shoot IMRT" Phys. Med. Biol. **49** N175-179 (2004).

[26] Jiang S.B., Pope C., Al Jarrah K.M., Kung J.H., Bortfeld T. and G.T.Y. Chen "An experimental investigation on intra-fractional organ motion effects in lung IMRT treatments" Phys. Med. Biol. **48** 1773-1794 (2003).

[27] Duan J., Shen S., Fiveash J.B., Popple R.A. and I.A. Brezovich "Dosimetric and radiobiological impact of dose fractionation on respiratory motion induced IMRT delivery errors: A volumetric dose measurement study" Med. Phys. **33** 1380-1387 (2006).

[28] Seco J., Sharp G.C., Turcotte J., Gierga D., Bortfeld T. and H. Paganetti "Effects of organ motion on IMRT treatments with segments of few monitor units" Med. Phys. **34** 923-934 (2007).

[29] International Commission on Radiation Units and Measurements (ICRU), ICRU Report 60 "Prescribing, Recording, and Reporting Photon Beam Therapy (Supplement to ICRU Report 50)" ICRU, Bethesda MD (1999).

[30] Van Herk M. "Errors and margins in radiotherapy" Seminars in Radiation Oncology **14** 52-64 (2004).

[31] Craig T., Battista J., Moiseenko V. and J. Van Dyk "Considerations for the implementations of target volume protocols in radiation therapy" Int J Radiat. Oncol. Biol. Phys. **49** 241-250 (2001).

[32] Antolak J.A. and I. I. Rosen "Planning target volumes for radiotherapy: how much margin is needed?" Int. J. Radiat. Oncol. Biol. Phys. **44** 1165-1170 (1999).

[33] Stroom J.C., de Boer H.C.J., Huizenga H. and A.G. Visser "Inclusion of geometrical uncertainties in radiotherapy treatment planning by means of coverage probability" Int J Radiat. Oncol. Biol. Phys. **43** 905-919 (1999).

[34] van Herk M., Remeijer P., Rasch C. and J.V. Lebesque "The probability of correct target dosage: dose-population histograms for deriving treatment margins in radiotherapy" Int. J. Radiat. Oncol. Biol. Phys. **47** 1121-1135 (2000).

[35] Lagerwaard F.J., van Sornsen de Koste J.R., Nijssen-Visser M.R., Schuchhard-Schipper R.H., Oei S.S., Munne A. and S. Senan "Multiple "slow" CT scans for incorporating lung tumor mobility in radiotherapy planning" Int. J. Radiat. Oncol. Biol. Phys. **51** 932-937 (2001).

[36] Wurstbauer K., Deutschmann H., Kopp P. and F. Sedlmayer "Radiotherapy planning for lung cancer: Slow CTs allow the drawing of tighter margins" Radiotherapy and Oncology **75** 165-170 (2005).

[37] Shih H.A., Jiang S.B., Aljarrah K.M., Doppke K.P. and N.C. Choi "Internal target volume determined with expansion margins beyond composite gross tumor volume in three-dimensional conformal radiotherapy for lung cancer" Int. J. Radiat. Oncol. Biol. Phys. **60** 613-622 (2004).

[38] Ford E.C., Mageras G.S., Yorke E. and C.C. Ling "Respiration-correlated spiral CT: a method of measuring respiratory-induced anatomic motion for radiation treatment planning" Med. Phys. **30** 88-97 (2003)

[39] Vedam S.S., Keall P.J., Kini V.R., Mostafavi H., Shukla H.P. and R. Mohan "Acquiring a four-dimensional computed tomography dataset using an external respiratory signal" Phys. Med. Biol. **48** 45-62 (2003).

[40] Low D.A., Nystrom M., Kalini E., Parikh P., Dempsey J.F., Bradley J.D., Mutic S., Wahab S.H., Islam T., Christensen G., Politte D.G. and B.R. Whiting "A method for the reconstruction of four-dimensional synchronized CT scans acquired during free breathing" Med. Phys. **30** 1254-1263 (2003).

[41] Pan T., Lee T-Y., Rietzel E. and G.T.Y. Chen "4D-CT imaging of a volume influenced by respiratory motion on multi-slice CT" Med. Phys. **31** 333-340 (2004).

[42] Rietzel E., Pan T. and G.T.Y. Chen "Four-dimensional computed tomography: Image formation and clinical protocol" Med. Phys. **32** 874-889 (2005).

[43] Keall P.J., Starkschall G., Shukla H., Forster K.M., Ortiz V., Stevens C.W., Vedam S.S., George R., Guerrero T. and R. Mohan "Acquiring 4D thoracic CT scans using a multislice helical method" Phys. Med. Biol. **49** 2053-2067 (2004).

[44] Pan T. "Comparison of helical and cine acquisitions for 4D-CT imaging with mutlislice CT" Med. Phys. **32** 627-634 (2005).

[45] Sonke J-J., Zijp L., Remeijer P. and M. van Herk "Respiratory correlated cone beam CT" Med. Phys. **32** 1176-1186 (2005).

[46] Li T., Schreibmann E., Thorndyke B., Tillman G., Boyer A., Koong A., Goodman K. and L. Xing "Radiation dose reduction in four-dimensional computed tomography" Med. Phys. **32** 3650-3660 (2005).

[47] Rietzel E. and G.T.Y. Chen "Improving retrospective sorting of 4D computed tomography data" Med. Phys. **33** 377-379 (2006).

[48] Fitzpatrick M.J., Starkschall G., Antolak J.A., Fu J., Shukla H., Keall P.J., Klahr P. and R. Mohan "Displacement-based binning of time-dependent computed tomography image data sets" Med. Phys. **33** 235-246 (2006).

[49] Abdelnour A.F., Nehmeh S.A., Pan T., Humm J.L., Vernon P., Schoder H., Rosenzweig K.E., Mageras G.S., Yorke E., Larson S.M. and Y.E. Erdi "Phase and amplitude binning for 4D-CT imaging" Phys. Med. Biol. **52** 3515-3529 (2007).

[50] Lu W., Parikh P.J., Hubenschmidt J.P., Bradley J.D. and D.A. Low "A comparison between amplitude sorting and phase-angle sorting using external respiratory measurement for 4D CT" Med. Phys. **33** 2964-2974 (2006).

[51] George R., Chung T.D., Vedam S.S., Ramakrishnan V., Mohan R., Weiss E. and P.J. Keall "Audio-visual biofeedback for respiratory-gated radiotherapy: impact of audio instruction and audio-visual biofeedback on respiratory-gated radiotherapy" Int. J. Radiat. Oncol. Biol. Phys. **65** 924-944 (2006).

[52] Berlinger K., Sauer O., Vences L. and M. Roth "A simple method for labeling CT images with respiratory states" Med. Phys. 3**3** 3144-3148 (2006).

[53] Kleshneva T., Muzik K. and M. Alber "An algorithm for automatic determination of the respiratory phases in four-dimensional computed tomography" Phys. Med. Biol. **51** N269-276 (2006).

[54] Lu W., Parikh P.J., El Naqa I.M., Nystrom M.M., Hubenschmidt J.P., Wahab S.H., Mutic S., Singh A.K., Christensen G.E., Bradley J.D. and D.A. Low "Quantitation of the reconstruction quality of a four-dimensional computed tomography process for lung cancer patients" Med. Phys. **32** 890-901 (2005).

[55] Guckenberger M., Wilbert J., Meyer J., Baier K., Richter A. and M. Flentje "Is a single respiratory correlated 4D-CT study sufficient for evaluation of breathing motion?" Int. J. Radiat. Oncol. Biol. Phys. **67** 1352-1359 (2007).

[56] Gagne I.M., Robinson D.M., Halperin R. and W. Roa "The use of phase sequence image sets to reconstruct the total volume occupied by a mobile lung tumor" Med. Phys. **32** 2211-2221 (2005).

[57] Ragan D., Starkschall G., McNutt T. and M. Kauss "Semiautomated four-dimensional computed tomography segmentation using deformable models" Med. Phys. **32** 2254-2261 (2007).

[58] Underberg R.W.M., Lagerwaard F.J., Slotman B.J., Cuijpers J.P. and S. Senan "Benefit of respiration-gated stereotactic radiotherapy for stage 1 lung cancer: an analysis of 4DCT datasets" Int. J. Radiat. Oncol. Biol. Phys. **62** 554-560 (2005).

[59] Bradley J.D., Nofal A.N., El Nawa I.M., Lu W., Liu J., Hubenschmidt J., Low D.A., Drzymala R.E. and D. Khullar "Comparison of helical, maximum intensity projection (MIP), and average intensity (AI) 4D CT imaging for stereotactic body radiation therapy (SBRT) planning in lung cancer" Radiotherapy and Oncology **81** 264-268 (2006).

[60] Wolthaus J.W.H., Schneider C., Sonke J-J., van Herk M., Belderbos J.S.A., Rossie M.M.G., Lebesque J.V. and E.M.F. Damen "Mid-ventilation CT scan construction from four-dimensional respiration-correlated CT scans for radiotherapy planning of lung cancer patients" Int. J. Radiat. Oncol. Biol. Phys. **65** 1560-1571 (2006).

[61] Bosmans G., Buijsen J., Dekker A., Velders M., Boersma L, De Ruysscher D., Minken A. and P. Lambin "An "in silico" clinical trial comparing free breathing,

slow and respiration correlated computed tomography in lung cancer patients" Radiotherapy and Oncology **81** 73-80 (2006)

[62] Zhang T., Jeraj R., Keller H., Lu W., Olivera G.H., McNutt T.R., Mackie T.R. and B. Paliwal "Treatment plan optimization incorporating respiratory motion" Med. Phys. **31** 1576-1586 (2004).

[63] Chan T.C.Y., Bortfeld T. and J.N. Tsitsiklis "A robust approach to IMRT optimization" Phys. Med. Biol. **51** 2567-2583 (2006).

[64] Unkelbach J. and U. Oelfke "Inclusion of organ movements in IMRT treatment planning via inverse planning based on probability distributions" Phys. Med. Biol. **49** 4005-4029 (2004).

[65] Trofimov A., Rietzel E., Lu H-M., Martin B., Jiang S., Chen G.T.Y. and T. Bortfeld "Temporo-spatial IMRT optimization: concepts, implementation and initial results" Phys. Med. Biol. **50** 2779-2798 (2005).

[66] Li J.G. and L. Xing "Inverse planning incorporating organ motion" Med Phys. **27** 1573-1578 (2000).

[67] Coolens C., Evans P.M., Seco J., Webb S., Blackall J., Rietzel E. and G.T.Y. Chen "The susceptibility of IMRT dose distributions to intrafraction organ motion: An investigation into smoothing filters derived from four dimensional computed tomography data" Med. Phys. **33** 2809-2818 (2006).

[68] Lax I., Blomgren H., Naslund I. and R. Svanstrom "Stereotactic radiotherapy of malignancies in the abdomen. Methodological aspects" Acta. Oncol. **33** 577-683 (1994).

[69] Lax I., Blomgren H., Larson D. and I. Naslund "Extracranial stereotactic radiosurgery of localized targets" Journal of Radiosurgery **1** 135-148 (1998)

[70] McGarry R.C., Papiez L., Williams M. and R.D. Timmerman "Stereotactic body radiation therapy of early-stage non-small-cell lung carcinoma: Phase 1 study" Int. J. Radiat. Oncol. Biol. Phys. **63** 1010-1015 (2005).

[71] Wulf J., Hadinger U., Oppitz U., Olshausen B. and M. Flentje "Stereotactic radiotherapy of extracranial targets: CT-simulation and accuracy of treatments in the stereotactic body frame" Radiotherapy and Oncology **57** 225-236 (2000).

[72] Negoro Y., Nagata Y., Aoki T., Mizowaki T., Araki N., Takayama K., Kokubo M., Yano S., Koga S., Sasai K., Shibamoto Y. and M. Hiraoka "The effectiveness of an immobilization device in conformal radiotherapy for lung tumor: reduction of respiratory tumor movement and evaluation of the daily setup accuracy" Int. J. Radiat. Oncol. Biol. Phys. **50** 889-898 (2001).

[73] Lohr F., Debus J., Frank C., Herfarth K., Pastyr O., Rhein B., Bahner M.L., Schlegel W. and M. Wannenmacher "Noninvasive patient fixation for extracranial stereotactic radiotherapy" Int. J. Radiat. Oncol. Biol. Phys. **45** 521-527 (1999).

[74] Zhang T., Orton N.P. and W.A. Tome "On the automated definition of mobile target volumes from 4D-CT images for stereotactic body radiotherapy" Med. Phys. **32** 3493-3502 (2005).

[75] Yin F.F., Kim J.G., Haughton C., Brown S., Ajlouni M., Stronati M., Pamukov N. and J.H. Kim "Extracranial radiosurgery: immobilizing liver motion using high-frequency jet ventilation and total intravenous anesthesia" Int. J. Radiat. Oncol. Biol. Phys. **48** S361-362 (2000).

[76] Hanley J., Debois M.M., Mah D., Mageras G.S., Raben A., Rosenzweig K., Mychalczak B., Schwartz L.H., Gloeggler P.J., Lutz W., Ling C.C., Leibel S.A., Fuks Z. and G.J. Kutcher "Deep inspiration breath-hold technique for lung tumors: the potential value of target immobilization and reduced lung density in dose escalation" Int. J. Radiat. Oncol. Biol. Phys. **45** 603-611 (1999).

[77] Mah D., Hanley J., Rosenzweig K.E., Yorke E., Braban L., Ling C.C. and S.A. Leibel "Technical aspects of the deep inspiration breath-hold technique in the treatment of thoracic cancer" Int. J. Radiat. Oncol. Biol. Phys. **48** 1175-1185 (2000).

[78] Rosenzweig K.E., Hanley J., Mah D., Mageras G., Hung M., Toner S., Burman C., Ling C.C., Mychalzak B., Fukz Z. and S.A. Leibel "The deep inspiration breath-hold technique in the treatment of inoperable non-small-cell lung cancer" Int. J. Radiat. Oncol. Biol. Phys. **48** 81-87 (2000).

[79] Stock M., Kontrisova K., Dieckmann K., Bogner J., Poetter R. And D. Georg "Development and application of a real-time monitoring and feedback system for

deep inspiration breath hold based on external marker tracking" Med. Phys. **33** 2868-2877 (2006).

[80] Murphy M.J., Martin D., Whyte R., Hai J., Ozhasoglu C. and Q-T Le "The effectiveness of breath-holding to stabilize lung and pancreas tumors during radiosurgery" Int. J. Radiat. Oncol. Biol. Phys. **53** 475-482 (2002).

[81] Nakamura K., Shioyama Y., Nomoto S., Ohga S., Toba T., Yoshitake T., Anai S., Terashima H. and H. Honda "Reproducibility of the abdominal and chest wall position by voluntary breath-hold technique using a laser-based monitoring and visual feedback system" Int. J. Radiat. Oncol. Biol. Phys. **68** 267-272 (2007).

[82] Barnes E.A., Murray B.R., Robinson D.M., Underwood L.J., Hanson J. and W.H.Y. Roa "Dosimetric evaluation of lung tumor immobilization using breath hold at deep inspiration" Int. J. Radiat. Oncol. Biol. Phys. **50** 091-1098 (2001).

[83] Kim D.J.W., Murray B.R., Halperin R. and W.H.Y. Roa "Held-breath self-gating technique for radiotherapy of non-small-cell lung cancer: a feasibility study" Int. J. Radiat. Oncol. Biol. Phys. **49** 43-49 (2001).

[84] Onishi H., Kuriyama K., Komiyama T., Tanaka S., Sano N., Aikawa Y., Tateda Y., Araki T., Ikenaga S. and M. Uematsu "A new irradiation system for lung cancer combining linear accelerator, computed tomography, patient self-breath-holding, and patient-directed beam-control without respiratory monitoring devices" Int. J. Radiat. Oncol. Biol. Phys. **56** 14-20 (2003).

[85] Nelson C., Starkschall G., Balter P., Fitzpatrick M.J., Antolak J.A., Tolani N. and K. Prado "Respiration-correlated treatment delivery using feedback-guided breath hold: a technical study" Med. Phys. **32** 175-181 (2005).

[86] Kontrisova K., Stock M., Dieckmann K., Bogner J., Poetter R. And D. Georg "Dosimetric comparison of stereotactic body radiotherapy in different respiration conditions: a modeling study" Radiotherapy and Oncology **81** 97-104 (2006).

[87] Wong J.W., Sharpe M.B., Jaffray D.A., Kini V.R., Robertson J.M., Stromberg J.S. and A.A. Martinez "The use of active breathing control (ABC) to reduce margin for breathing motion" Int. J. Radiat. Oncol. Biol. Phys. **44** 911-919 (1999).

[88] Sarrut D., Boldea V., Ayadi M., Badel J-N., Ginestet C., Clippe S. and C. Carrie "Nonrigid registration method to assess reproducibility of breath-holding with ABC in lung cancer" Int. J. Radiat. Oncol. Biol. Phys. **61** 594-607 (2005).

[89] Stromberg J.S., Sharpe M.B., Kim L.H., Kini V.R., Jaffray D.A., Martinez A.A. and J.W. Wong "Active breathing control (ABC) for Hodgkin's disease: reduction in normal tissue irradiation with deep inspiration and implications for treatment" Int. J. Radiat. Oncol. Biol. Phys. **48** 797-806 (2000).

[90] Cheung P.C.F., Sixel K.E., Tirona R. and Y.C. Ung "Reproducibility of lung tumor position and reduction of lung mass within the planning target volume using active breathing control (ABC)" Int. J. Radiat. Oncol. Biol. Phys. **57** 1437-1442 (2003).

[91] Ohara K., Okumura T. and M. Akisada "Irradiation synchronized with respiration gate" Int. J. Radiat. Oncol. Biol. Phys **17** 853-857 (1989).

[92] Berson A.M., Emery R., Rodrigues L., Richards G.M., Ng T., S. Sanghavi and J. Barsa "Clinical experience using respiratory gated radiation therapy: comparison of free-breathing and breathe-hold techniques" Int. J. Radiat. Oncol. Biol. Phys. **60** 419-426 (2004).

[93] Engelsman M., Sharp G.C., Bortfeld T., Onimaru R. and H. Shirato "How much margin reduction is possible through gating or breath hold" Phys. Med. Biol. **50** 477-490 (2005).

[94] Starkschall G., Forster K.M., Kitamura K., Cardenas A., Tucker S.L. and C.W. Stevens "Correlation of gross tumor volume excursion with potential benefits of respiratory gating" Int. J. Radiat. Oncol. Biol. Phys. **60** 1291-1297 (2004).

[95] Kubo H.D. and B.C. Hill "Respiration gated radiotherapy treatment: a technical study" Phys. Med. Biol. **41** 83-91 (1996).

[96] Zhang T., Keller H., O'Brian M.J., Mackie T.R. and B. Paliwal "Application of the spirometer in respiratory gated radiotherapy" Med. Phys. **30** 3165-3171 (2003).

[97] Shirato H., Shimizu S., Kunieda T., Kitamura K., van Herk M., Kagei K., Nishioka T., Hashimoto S., Fujita K., Aoyama H., Tsuchiya K., Kudo K. and K. Miyasaka "Physical aspects of a real-time tumor-tracking system for gated radiotherapy" Int. J. Radiat. Oncol. Biol. Phys. **48** 1187-1195 (2000).

[98] Willoughby T.R., Forbes A.R., Buchholz D., Langen K.M., Wagner T.H., Zeidan O.A., Kupelian P.A. and S.L. Meeks "Evaluation of an infrared camera and X-ray system using implanted fiducials in patients with lung tumor for gated radiation therapy" Int. J. Radiat. Oncol. Biol. Phys. **66** 568-575 (2006).

[99] Li X.A., Stepaniak C. and E. Gore "Technical and dosimetric aspects of respiratory gating using a pressure-sensor motion monitoring system" Med. Phys. **33** 145-154 (2006).

[100] Vedam S.S., Keall P.J., Kini V.R. and R.Mohan "Determining parameters for respiration-gated radiotherapy" Med. Phys. **28** 2139-2146 (2001).

[101] Jin J-Y., Ajlouni M., Ryu S., Chen Q., Li S. and B. Movsas "A technique of quantitatively monitoring both respiratory and nonrespiratory motion in patients using external body markers" Med. Phys. **34** 2875-2881 (2007)

[102] Bert C., Metheany K.G., Doppke K. and G.T.Y. Chen "A phantom evaluation of a stereo-vision surface imaging system for radiotherapy setup" Med. Phys. **32** 2753-2762 (2005).

[103] Berbeco R.I., Mostafavi H., Sharp G.C. and S.B. Jiang "Towards fluoroscopic respiratory gating for lung tumors without radiopaque markers" Phys. Med. Biol. **50** 4481-4490 (2005).

[104] Tada T., Minakuchi K., Fujioka T., Sakurai M., Koda M., Kawase I., Nakajima T., Nishioka M., Tonai T. and T. Kozuka "Lung cancer: intermittent irradiation synchronized with respiratory motion – results of a pilot study" Radiology **207** 779-783 (1998).

[105] Cui Y., Dy J.G., Sharp G.C., Alexander B. and S.B. Jiang "Robust fluoroscopic respiratory gating for lung cancer radiotherapy without implanted fiducial markers" Phys. Med. Biol. **52** 741-755 (2007).

[106] Sawada A., Yoda K., Kobubo M., Kunieda T., Nagata Y. and M. Hiraoko "A technique for noninvasive respiratory gated radiation treatment system based on a real time 3D ultrasound image correlation: A phantom study" Med. Phys. **31** 245-250 (2004).

[107] Xu Q. and R.J. Hamilton "A novel respiratory detection method based on automated analysis of ultrasound diaphragm video" Med. Phys. **33** 916-921 (2006).

[108] Chi P-C M., Balter P., Luo D., Mohan R. and T. Pan "Relation of external surface to internal tumor motion studied with cine CT" Med. Phys. **33** 3116-3123 (2006).

[109] Koch N., Liu H.H., Starkschall G., Jacobson M., Forster K., Liao Z., Komaki R. and C.W. Stevens "Evaluation of internal lung motion for respiratory-gated radiotherapy using MRI: Part 1- correlating internal lung motion with skin fiducial motion" Int. J. Radiat. Oncol. Biol. Phys. **60** 1459-1472 (2004).

[110] Vedam S.S., Kini V.R., Keall P.J., Ramakrishnan V., Mostafavi H. and R. Mohan "Quantifying the predictability of diaphragm motion during respiration with a noninvasive external marker" Med. Phys. **30** 505-513 (2003).

[111] Berbeco R.I., Nishioka S., Shirato H., Chen G.T.Y. and S.B. Jiang "Residual motion of lung tumors in gated radiotherapy with external respiratory surrogates" Phys. Med. Biol. **50** 3655-3667 (2005).

[112] George R., Ramakrishnan V., Siebers J.V., Chung T.D. and P.J. Keall "Investigation of patient, tumor and treatment variables affecting residual motion for respiratory-gated radiotherapy" Phys. Med. Biol. **51** 5305-5319 (2006).

[113] Kini V.R., Vedam S.S., Keall P.J., Patil S., Chen C. and R. Mohan "Patient training in respiratory-gated radiotherapy" Medical Dosimetry **28** 7-11 (2003).

[114] Sharp G.C., Jiang S.B., Shimizu S. and H. Shirato "Prediction of respiratory tumor motion for real-time image-guided radiotherapy" Phys. Med. Biol. **49** 425-440 (2004).

[115] Shen S., Duan J., Fiveash J.B., Brezovich I.A., Plant B.A., Spencer S.A., Popple R.A., Pareek P.N. and J.A. Bonner "Validation of target volume and position in respiratory gated CT planning and treatment" Med. Phys. **30** 3196-3205 (2003).

[116] Lu W., Parikh P.J., Hubenschmidt J.P., Politte D.G., Whiting B.R., Bradley J.D., Mutic S. and D.A. Low "Reduction of motion blurring artifacts using respiratory gated CT in sonogram space: a quantitative evaluation" Med. Phys. **32** 3295-3304 (2005).

[117]. Sillanpaa J., Chang J., Mageras G., Riem H., Ford H., Todor D., Ling C.C. and H. Amols "Developments in megavoltage cone beam CT with an amorphous silicon EPID: reduction of exposure and synchronization with respiratory gating" Med. Phys. **32** 819-829 (2005)

[118] Kubo H.D. and L. Wang "Compatibility of Varian 2100C gated operations with enhanced dynamic wedge and IMRT dose delivery" Med Phys **27** 1732-1738 (2000).

[119] Ahunbay E. and X.A. Li "Investigation of the reliability, accuracy and efficiency of gated IMRT delivery with a commercial linear accelerator" Med. Phys. **34** 2928-2938 (2007)

[120] Murphy M.J. "Tracking moving organs in real time" Seminars in Radiation Oncology **14** 91-100 (2004).

[121] Schweikard A., Glosser G., Bodduluri M., Murphy M.J. and J.R. Adler "Robotic motion compensation for respiratory movement during radiosurgery" Computer Aided Surgery **5** 263-277 (2000).

[122] Seppenwoolde Y., Berbeco R.I., Nishioka S., Shirato H. and Heijman B. "Accuracy of tumor motion compensation algorithm from a robotic respiratory tracking system: a simulation study" Med. Phys. **34** 2774-2784 (2007).

[123] Keall P.J., Kini V.R., Vedam S.S. and R. Mohan "Motion adaptive x-ray therapy: a feasibility study" Phys. Med. Biol. **46** 1-10 (2001).

[124] Neicu T., Shirato H., Seppenwoolde Y. and S.B. Jiang "Synchronized moving aperture radiation therapy (SMART): average tumor trajectory for lung patients" Phys. Med. Biol. **48** 587-598 (2003).

[125] Tewatia D., Zhang T., Tome W., Paliwal B. and M. Metha "Clinical implementation of target tracking by breathing synchronized delivery" Med. Phys. **33** 4330-4336 (2006).

[126] Papiez L., "DMLC leaf-pair optimal control of IMRT delivery for a moving rigid target" Med. Phys. **31** 2742-2754 (2004).

[127] D'Souza W.D., Naqvi S.A. and C.X. Yu "Real-time intra-fraction-motion tracking using the treatment couch: a feasibility study" Phys. Med. Biol. **50** 4021-4033 (2005).

[128] Keall P.J., Joshi S., Vedam S.S., Siebers J.V., Kini V.R. and R. Mohan "Four-dimensional radiotherapy planning for DMLC-based respiratory motion tracking" Med. Phys. **32** 942-951 (2005).

[129] Alasti H., Cho Y.B., Vandermeer A.D., Abbas A., Norrlinger B., Shubbar S. and A. Bezjak "A novel four-dimensional radiotherapy method for lung cancer: imaging, treatment planning and delivery" Phys. Med. Biol. **51** 3251-3267 (2006).

[130] Vandermeer A.D., Alasti H., Cho Y-B. and B. Norrlinger "Investigation of the dosimetric effect of respiratory motion using four-dimensional weighted radiotherapy" Phys. Med. Biol. **52** 4427-4448 (2007).

[131] Keall P.J., Cattell H., Pokhrel D., Dieterich S., Wong K.H., Murphy M.J., Vedam S.S., Wijesooriya K. and R. Mohan "Geometric accuracy of a real-time target tracking system with dynamic mutlileaf collimator tracking system" Int. J. Radiat. Oncol. Biol. Phys. **65** 1579-1584 (2006).

[132] Neicu T., Berbeco R., Wolfgang J. and S.B. Jiang "Synchronized moving aperture radiation therapy (SMART): improvement of breathing pattern reproducibility using respiratory coaching" Phys. Med. Biol. **51** 617-636 (2006).

[133] Parikh P., Hubenschmidt J., Dimmer S., Vertatschitsch E., Eidens R., Wright J.N. and D.A. Low "4D verification of real-time accuracy of the Calypso system with lung cancer patient trajectory data" Int. J. Radiat. Oncol. Biol. Phys. **63** S26-27 (2005).

[134] Yan H., Yin F-F., Zhu G-P., Ajlouni M. And J.H. Kim "The correlation evaluation of a tumor tracking system using multiple external markers" Med. Phys. **33** 4073-4084 (2006).

[135] Ozhasoglu C. and M.J. Murphy "Issues in respiratory motion compensation during external-beam radiotherapy" Int. J. Radiat. Oncol. Biol. Phys. **52** 1389-1399 (2002).

[136] Ruan D., Fessler J.A., Balter J.M. and J-J. Sonke "Exploring breathing pattern irregularity with projection-based method" Med. Phys. **33** 2491-2499 (2006).

[137] Kakar M., Nystrom H., Aarup L.R., Nottrup T.J. and D.R. Olsen "Respiratory motion prediction by using the adaptive neuro fuzzy inference system (ANFIS)" Phys. Med. Biol. **50** 4721-4728 (2005).

[138] Isaksson M., Jalden J. and M.J. Murphy "On using an adaptive neural network to predict lung tumor motion during respiration for radiotherapy applications" Med. Phys. **32** 3801-3809 (2005).

[139] Murphy M.J. and S. Dieterich "Comparative performance of linear and nonlinear neural networks to predict irregular breathing" Phys. Med. Biol. **51** 5903-5914 (2006).

[140] Yan H, Yin F-F., Zhu G-P., Ajlouni M. and J.H. Kim "Adaptive prediction of internal target motion using external marker motion: a technical study" Phys. Med. Biol. **51** 31-44 (2006).

[141] Vedam S.S., Keall P.J., Docef A., Todor D.A., Kini V.R. and R. Mohan "Predicting respiratory motion for four-dimensional radiotherapy" Med. Phys. **31** 2274-2283 (2004).

[142] Vedam S., Docef A., Fix M., Murphy M. and P. Keall "Dosimetric impact of geometric errors due to respiratory motion prediction on dynamic multileaf collimator-based four-dimensional radiation delivery" Med. Phys. **32** 1607-1620 (2005).

# Chapter 3:

# Methods for incorporating organ motion in dose calculations

## 3.1 INTRODUCTION

The result of any anatomical variations over the course of radiotherapy delivery is a discrepancy between the planned and delivered dose distributions. In order to improve the accuracy of radiotherapy such patient variations should be accounted for during treatment planning. As discussed in Chapter 2, this requires a method to measure the motion (ie., serial images or a motion surrogate) as well as a dose calculation algorithm which uses this motion information to give an accurate estimate of the delivered dose. Such methods are required to assess the impact of patient motion, to design treatment plans that account for the motion and finally to assess how well a given plan or treatment method compensates for patient motion.

In this chapter we will review the development of dose calculation methods which incorporate information about patient anatomical variations. Such methods vary from modeling the rigid motion encountered in setup errors to the more complex deformations resulting from respiratory motion. Discussion of dose calculation methods are organized into three sections: (1) numerical methods; (2) convolution-based methods; and (3) dose warping methods based on non-linear image registration.

## 3.2 NUMERICAL METHODS

Goitein[1] attempted to estimate the uncertainty on the delivered dose distribution by calculating the dose at nominal and extreme values of quantities which affect the dose. The quantities which were investigated included motion of the field-defining aperture, variations in source intensity, changes in tissue-equivalent depth or tissue density and misregistration of the beam-modifying compensator. This method required three separate dose calculations to be performed for each parameter to be investigated. For this case,

patient motion was assumed to be equivalent to motion of the beam aperture. The method was independent of the dose calculation algorithm used and could be applied to any treatment modality (ie., external beam therapy, brachytherapy). The extreme values of dose variation at a given point could be used to determine the "error bars" on the dose estimation. However, the simplicity of the method limited its use for determining dose in deforming anatomy.

Killoran *et al.*[2] randomly simulated 3D displacements of the treatment beam relative to the patient to determine the dosimetric consequences of setup errors. Assuming a Gaussian probability distribution of setup errors the dose distribution was rotated and translated and then resampled to the original dose grid resolution. The fundamental assumptions of this method are that the patient motion is rigid and that the dose distribution is not affected by these motions. Similarly, Mackay *et al.*[3] derived surfaces from planning contours and projected them onto the daily CT image. The affine transformations resulting from alignment of these structures were used to shift the locations of sampled dose points within the planning structures.

Mageras *et al.*[4] extended the above method to use information about organ deformation determined from contours drawn on repeat CT scans to adjust the planned dose distribution for rigid and non-rigid motion. An initial rigid alignment of the repeat and planning CTs was performed first based on the bony anatomy. The remaining spatial differences between the contours were then resolved by means of a simple 3D contour-based deformable registration. Dose calculation points were placed in quasi-random locations inside each volume of interest on the planning scan. To estimate the dose received for a particular motion state, the position of each point inside the planning contour was shifted by an amount interpolated from the contour deformations and the dose at the new position taken from the treatment planning dose distribution. The dose calculation procedure was repeated for every repeat CT scan to estimate the dose uncertainty at a particular dose grid point over the course of radiotherapy. The method was applied to radiotherapy of the prostate in order to derive so-called "confidence level" DVHs (CL-DHVs) that indicate the possible range of variations in DVH due to patient motion. This method represented the first attempt at a "deformable" dose calculation method in which organ deformations, in addition to rigid motion, was taken into account.

A mathematical formalism for determination of dose in the presence of changing anatomy due to both setup errors and organ motion was defined by Yan *et al.*[5]. The dose received by a volume element *v* was estimated from the cumulative dose estimated on *m* samples of the anatomical motion:

$$D(v) \approx D(v,m) = \int_{\varepsilon} \int_{X} D\left(T\left(\varepsilon\right)\cdot X\right)\cdot \phi\left(v,X\right)\cdot \psi\left(\varepsilon,\mu,\sigma\right) dX d\varepsilon \,, \qquad (1)$$

where $\phi\left(v,X\right)$ is an organ motion probability distribution function (pdf) describing the frequency of finding the volume element *v* at the position *X* within the reference coordinate system of the patient's bony anatomy. Such a pdf can be determined from repeated daily scans. The setup errors $\epsilon$ are characterized by the Gaussian pdf $\psi\left(\varepsilon,\mu,\sigma\right)$ which is characterized by a mean ($\mu$) and standard deviation ($\sigma$) predicted from repeat measurements of the setup error. The composite effects of setup error and organ motion are then described by the joint probability distribution $\phi\left(v,X\right)\cdot\psi\left(\varepsilon,\mu,\sigma\right)$. Mathematically, the cumulative dose is given by the expectation value of dose matrix *D(v)* on the joint distribution describing the variations of the geometric position of *v*. This can be numerically solved by the following procedure: (1) sample an organ sub-volume $v_{\mathrm{i}}$; (2) randomly sample a displacement from the joint probability distribution; (3) transform the coordinate of the volume element; and (4) calculate the dose received at the new position $D\left(T\left(\varepsilon\right)\cdot X\right)$. Here it is assumed that the dose distribution is spatially invariant and was not significantly affected by changes in the patient anatomy. The authors noted that for large magnitudes of organ motion it might be necessary to recalculate the dose distribution on each sample of the motion *m* and then determine the cumulative dose as before but using each dose matrix $D_m$.

Two elegant methods for dose determination in the presence of motion were later presented by the same authors. The first method[6] was limited to modeling interfraction motion and deformation and could be used to determine either the minimum, maximum or mean dose received by a volume element *j* of a volume of interest (VOI) over *M* fractions. The cumulative dose delivered to *j* was given by

$$D_{\mathrm{t}}(j) = \frac{1}{M} \times \sum_{\mathrm{i}=1}^{M} D\left(\overline{VOI}_{\mathrm{i}}(j)\right), \qquad (2)$$

where $\left\{\overline{VOI}_{\mathrm{i}}\right\}_{\mathrm{i}=1}^{M}$ is the complete characterization of the interfractional patient geometric variations for that organ over *M* fractions. For each volume element a search region was defined which contained all manifestations of that volume element over the *M* fractions. Within this region occupancy values between 0 and 1 were assigned based on the relative number of fractions for which a volume element is present at a given position (see Figure 1). By searching the region for a particular endpoint (ie., minimum dose) in each occupancy region and weighting that value by the occupancy value for the voxel in which it occurs it is possible to estimate a dosimetric quantity for each volume element. The authors gave an example of determination of the minimum dose received by the prostate. They defined a volume discrepancy distribution (VDD) displaying the fraction of time a given voxel of the CTV is outside of the reference PTV volume, assuming that the PTV was always covered. For each voxel on the boundary of the VDD a search cylinder was constructed whose axis was normal to the PTV surface and radius was determined by the standard deviation of PTV motion. Within this cylinder they searched for the maximum dose variation from the planning dose which was weighted by the corresponding

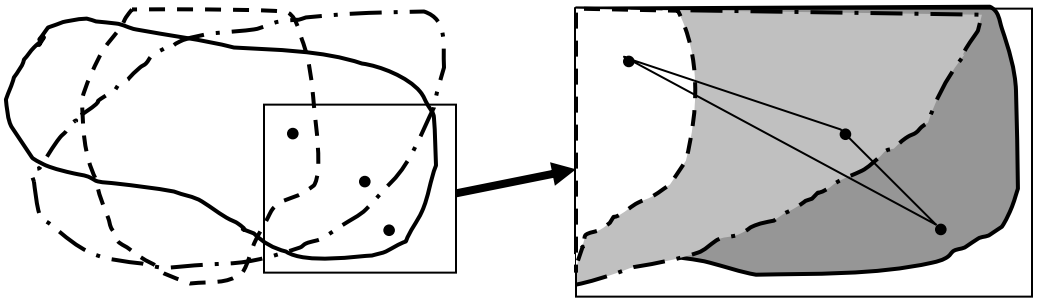

(a) Contours corresponding to three observations of a volume of interest. The corresponding locations of a volume element j are shown as black dots.

(b) Enlargement of box region in (a) where different grey levels represent occupancy values for each volume manifestation. The area enclosed by the connected black dots defines the search space for volume element j.

Figure 1. Method of defining occupancy values based on multiple observations of a volume of interest. [adapted from reference 6].

occupancy factors. A series of expected dose volume histograms (EDVH) were constructed for a different numbers of total fractions. A large variation between these EDVHs was found for a low number of fractions but they eventually converged as the number of fractions was increased. This indicated that a certain number of samples of anatomical variation were required to properly reconstruct the cumulative dose.

In a second approach[7], the temporal variation of the dose distribution was explicitly accounted for. Thus far this had not been modeled. Using a finite element model to derive a displacement map for the volume elements, the resulting dose deviations were separated into two components. The first component was deviations due to changes in the patient configuration and density while the second was due to positional displacements of the volume elements. The deviation between the delivered $D(v)$ and planned dose $D_P(v)$ was formulated as:

$$\Delta D(v) = D(v) - D_{\mathrm{P}}(v) = \sum_{\mathrm{t}=1}^{n} \left[ d_{\mathrm{t}}(x_0) - d_{\mathrm{P}}(v, x_0) \right] + \sum_{\mathrm{t}=1}^{n} \left[ d_{\mathrm{t}}(v, x_{\mathrm{t}}) - d_{\mathrm{t}}(x_0) \right], \qquad (3)$$

where $x_0$ is planning position of volume element $v$ and $x_t$ is the position of that element at time $t$. The first term is the sum of deviations between the planned dose $d_{\mathrm{P}}(v, x_0)$ for a particular volume element and the dose $d_{\mathrm{t}}(x_0)$ at the same position $x_0$ in the dose distribution at time $t$. This term represents the dose deviations resulting from the changing patient configuration at each time sample and was not considered for this study. The second term of Equation 3 represents dose deviations due to the changing position of the volume element $v$ at each time point compared to the dose at the planning position $x_0$. The deviations due to position displacements were considered to have a systematic $\mu(v, x_0)$ and random component $\xi_{\mathrm{t}}(v)$. The random component has a standard deviation $\sigma(\xi, n)$ defined along the three axes,

$$\mu(v, x_0) = \sum_{\mathrm{t}=1}^{n} \frac{x_{\mathrm{t}}(v)}{n} - x_0(v) \qquad (4)$$

$$\xi_{\mathrm{t}}(v) = x_{\mathrm{t}}(v) - \sum_{\tau=1}^{n} \frac{x_{\tau}(v)}{n} \ .$$

The dose deviation defined in the second half of Equation 3 was also considered to consist of a random and systematic component:

$$\Delta D(v) = \Delta D_s(v) + \Delta D_r(v) \tag{5}$$

which could be approximated as:

$$\Delta D(v) \approx \mu^T(x_0)\cdot n\cdot \overline{\nabla} d^T\left[x_0, x_0+\mu(x_0)\right] + \sigma^T\left(\xi_t, n\right)\cdot\frac{(n-1)}{2}\cdot\frac{\partial^2 d}{\partial x^2}^T\left(x_0+\mu(x_0)\right)\cdot\sigma^T\left(\xi_t, n\right) \tag{6}$$

where the $T$ superscript indicates a 3D vector.

The gradient and curvature terms in the above equation point to the fact that the cumulative dose distribution is very sensitive to the shape of the dose distribution instead of the shape of the subvolume displacements. This indicates that the effects of motion are important for critical organs which are commonly located in the beam penumbra where large dose gradients exist. The spectrum of dose deviations was found to have some dependence on the distribution of displacements in that a uniform distribution resulted in a broader spectrum of dose deviations compared to those resulting from a Gaussian distribution.

Another stochastic model for determining the effect of inter-fractional motion on the planned dose distribution was presented by Maleike *et al.*[8]. Their method used a Monte-Carlo approach to sample many possible volume element displacements from a Gaussian probability distribution and calculate the resulting dose distribution. Approximately 10,000 displacements were sampled to generate an expectation value and standard deviation of the dose in each volume element. The results of these simulations were used to display the probability of each element receiving dose within a user-specified interval for plan evaluation.

Webb[9] derived a simple mathematic model to determine the effect of density changes due to organ deformation. Incident fluence "bixels" *I(u,v)*, or pencil beams, were exponentially attenuated considering the radiological depth and density variations along the ray line connecting a voxel of interest (x,y,z) to that bixel. The total dose received over a breathing cycle was determined from the sum of the doses calculated at discrete time steps $D^{\text{delivered}}(t)$,

$$D^{\text{total}}_{\left[(x,y,z)(t_0)\right]_R} = \frac{1}{T}\int_0^T D^{\text{delivered}}_{\left[(x,y,z)(t)\right]_R}(t)dt \quad . \tag{7}$$

The density variations were calculated from volume changes determined from a voxel displacement map obtained from non-linear image registration as follows:

$$\rho_{\mathrm{dV(t)}} = \rho_{\mathrm{dV(t_0)}} \times \frac{dV(t_0)}{dV(t)} \quad . \tag{8}$$

The dose delivered at an infinitesimal time point *dt* was calculated as follows:

$$D^{\text{delivered}}_{\left[(x,y,z)(t)\right]_R}(t)\left(\frac{dt}{T}\right) = k \times I(u,v)_{\left[(x,y,z)(t)\right]_R} \times \left(\frac{dt}{T}\right) \times$$

$$\left[ \exp\left( -\frac{\mu}{\rho} \left( \int_{(u,v)_{\left[(x,y,z)(t)\right]_R}}^{\left[(x,y,z)(t)\right]_R} \rho\left[(x,y,z)(t)\right](t)d\underline{r} \right)_{\left[(x,y,z)(t)\right] in \left[(x,y,z)(t)\right]_R \, to \, (u,v)_{\left[(x,y,z)(t)\right]_R}} \right) \right] +$$

$$f\left(I(u,v), \rho\left[(x,y,z)(t)\right](t)\right)$$

. (9)

The scatter term *f* in Equation 9 was set to zero to simplify the calculation. The simplicity of this calculation limits its application to phantom studies but the work represented a first attempt to account for density variations in addition to voxel displacements.

Finally, a method of estimating the effect of interplay between MLC leaf motion in IMRT and intrafraction target motion was presented by Naqvi *et al*[10]. Using a Monte Carlo convolution/superposition dose calculation method particles were randomly sampled from a source model and transported through an MLC geometry randomly sampled from the delivery sequence. Upon sampling of each particle the isocenter of the CT-based phantom was shifted according to randomly sampled motion vectors. The method accounts only for rigid motion but could conceivably be extended to model organ deformation. A similar approach was proposed by Litzenberg *et al.*[11]

### 3.3 CONVOLUTION-BASED METHODS

Many of the aforementioned dose calculation techniques used shifting of the planning dose distribution to model the effect of patient motion. If the dose distribution can be assumed to be invariant when it is shifted relative to the patient anatomy and a large number of fractions (i.e., shifts) are performed it is equivalent to convolving the

dose distribution with a pdf describing the distribution of positional deviations. Leong[12] was the first to propose that the random component of set-up errors and organ motion could be modeled by convolution of the dose distribution:

$$D_{mot}(x',y',z') = \sum_{-Z}^{Z}\sum_{-Y}^{Y}\sum_{-X}^{X} D(x,y,z)\,g(x-x')\,h(y-y')\,k(z-z') \quad , \qquad (9)$$

where $g$, $h$ and $k$ are independent pdfs describing the beam position translations along the $x$, $y$ and $z$ directions, respectively. In the case of a rotation the pdf is a simultaneous function of $x$ and $y$. According to central limit theorem, for a large number of fractions the pdf can be described by a Gaussian function, however, the applicability of this theorem was thought to depend on the number of fractions and the shape of dose distribution.

Keall *et al.*[13,14] developed the convolution method of Leong with the assumption that the positional variations are normally distributed and the motion in the 3-dimensions were uncorrelated. The dose could then be estimated by convolution of the planned dose distribution with three separate motion kernels. An interface was developed with the CADplan treatment planning system (Varian Medical Systems, Palo Alto, CA) to estimate the effect of motion on the planned dose. By comparing with direct simulation (shifting of the dose distribution) it was found that a minimum of 15 fractions was required to get a reasonable estimate of the dose distribution by the convolution method. Bel *et al.*[15] used a similar convolution method to determine planning margins for the prostate from which they noted that the isodose lines tended to shrink after convolution was applied. The convolutions accounted for translation and rotations, assuming a normal distribution.

Lujan *et al.*[16,17] developed a similar method for modeling setup errors and extended it to modeling the effect of breathing motion on the dose distribution. Assuming the motion to be mainly in the superior-inferior direction they parameterized the organ motion as a function of time by a sinusoidal function:

$$z(t) = z_0 - b\cos^{2n}\left(\pi t/\tau - \phi\right), \qquad (10)$$

where $b$ is the breathing amplitude, $z_0$ is the position at exhale, $\tau$ is period, $\phi$ is starting phase of breathing cycle and $n$ determines the shape of the model. For most patient

breathing curves more time is spent at exhale than at inhale and the breathing model can be adjusted to reflect this.

A corresponding pdf, which ignores the starting phase, was derived from this expression.

$$p_{\mathrm{om}}(z)=\left\{nb\pi\left(\frac{z_0-z}{b}\right)^{(2n-1)/2n}\times\left[1-\left(\frac{z_0-z}{b}\right)^{1/n}\right]^{1/2}\right\}^{-1} \quad \text{for } z_0\text{-}b < z < z_0\,. \quad (11)$$

The convolution was applied to the entire dose grid and did not account for the fact that organs could have different motion characteristics.

The limitations of the dose convolution method were discussed by Craig *et al.*[18,19] in the context of modeling setup errors. The assumption of shift invariance of the dose distribution was found to be invalid near the patient surface and at tissue interfaces. Furthermore, an infinite number of fractions must be delivered in order to properly sample the motion pdf. However, the errors due to the actual finite number of delivered fractions was insignificant after 15 to 20 fractions.

The limitations of the dose convolution approach led to the introduction of the fluence convolution method by Beckham *et al.*[20]. Patient motion essentially results in the patient seeing a different incident fluence than for the static case. By reciprocity, convolution of the patient dose distribution should be equivalent to convolution of the incident beam fluence. The problem of shift invariance was then solved but the method was still limited by the assumption of an infinite number of fractions. The authors implemented fluence convolution into Monte Carlo calculations by shifting the particle positions in the phase space file according to a motion pdf. When comparing dose and fluence convolution in a heterogeneous phantom the dose convolution method was found to be inaccurate at the tissue interfaces. Chetty *et al.*[21,22] also compared the fluence and dose convolution methods for modeling respiratory motion effects on dose to the liver and lung using the DPM Monte Carlo code. They convolved the particle distribution obtained below the MLC with a 1D pdf describing respiratory motion. Particle positions and directions were modified according to the pdf. Differences between fluence and dose convolution methods were up to 5% which the authors attributed to the shift invariance assumption of the dose convolution method. A method of fluence convolution in the

context of a conventional treatment planning system was described by Kung *et al.*[23] where the physical fluence map determined by superposition of weighted subfields from a DMLC sequence file was transformed into an *effective incident fluence* (EIF) which accounted for periodic motion of the target. The EIF was then re-introduced into the planning system to re-calculate the motion-affected dose distribution. Note that the fluence convolution methods do not account for motion along the beam direction.

Van Herk *et al.*[24] considered both the systematic and random components of prostate motion. Systematic, or preparation, errors were defined as errors in imaging or delineation which resulted in a shift of the dose distribution. Random, or execution, errors tended to blur the dose distribution. Systematic errors were randomly generated and the convolved (blurred) dose distribution was rotated or translated accordingly. A cumulative dose was estimated by summing the dose for each sampled systematic error weighted by the probability of that error occurring.

## 3.4 DOSE WARPING METHODS (DEFORMABLE DOSE CALCULATIONS)

The convolution methods presented in the previous section were limited in that a single probability distribution function was assumed for the whole anatomy. It is known that motion amplitudes vary between and within organs. Three-dimensional information about differential organ motion can be obtained from non-linear image registration which outputs a voxel displacement or deformation vector map indicating the motion and volumetric changes of each voxel of the image grid. Recently, 4D dose calculation methods, which make use of non-linear image registration vectors, were developed that explicitly account for organ deformations. The general approach is to calculate the delivered dose on multiple samples of motion states. The problem with adding these dose distributions is that they are not calculated on the same geometry. A given voxel coordinate may contain a vastly different material density and composition from one motion state to the next. The solution is to use the deformation vectors to track how a voxel moves with time and to determine the dose received at each new location (see Figure 2). This is equivalent to mapping the dose distribution from a given motion state back to a common reference state on which all the contributions can be summed. For this reason these methods are also referred to as “dose warping”.

The use of non-linear registration for 4D dose calculation was first proposed by Brock *et al.*[25] who developed a finite element model to describe respiration-induced motion of the liver. The liver modeled consisted of 6000 tetrahedral elements for which the inhale-to-exhale centroid displacements were determined by finite element analysis. The dose received at an intermediate breathing phase $\phi$ (varies from 0 to 1) could be calculated from the inhale $D^{\mathrm{I}}$ and exhale $D^{\mathrm{E}}$ dose distributions at the corresponding position (x,y,z) of that volume element at those phases:

$$D_{\phi}(x,y,z) = D^{\mathrm{E}}(x,y,z)\phi + D^{\mathrm{I}}(x,y,z)(1-\phi) \ . \tag{12}$$

The cumulative dose was determined by a weighted sum of intermediate phase doses at phase increments of 0.2.

Schaly *et al.*[26] used deformation vectors from thin plate spline registration of daily CT images to map the dose distributions calculated on each CT image to the planning CT for comparison with the planned dose distribution. The warped dose distribution was formulated as:

$$d_{\mathrm{W_i}}(x_{\mathrm{i}},y_{\mathrm{i}},z_{\mathrm{i}}) = d_{\mathrm{i}}\left(T_{\mathrm{i}}(x_0,y_0,z_0)\right) \ , \tag{13}$$

where $d_{\mathrm{i}}$ is the dose distribution calculated for the i$^{\mathrm{th}}$ fraction, $(x_{\mathrm{i}},y_{\mathrm{i}},z_{\mathrm{i}})$ and $(x_0,y_0,z_0)$ are the treatment study coordinates for the i$^{\mathrm{th}}$ fraction and reference state respectively and $T_{\mathrm{i}}$ is transformation mapping the reference image to the i$^{\mathrm{th}}$ daily CT image. The warped

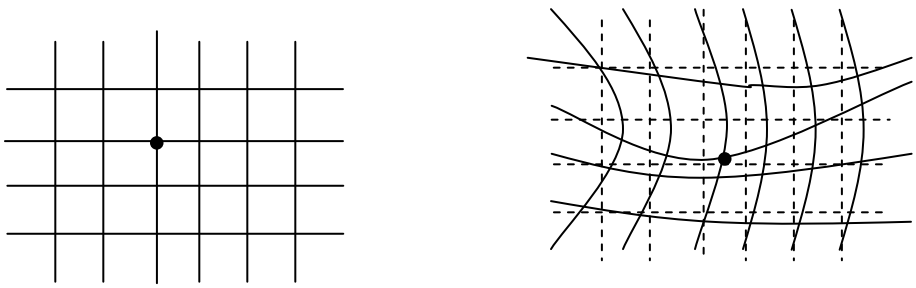

Reference dose grid. Warped reference dose grid superimposed on dose grid at motion state *i*.

Figure 2. Illustration of the concept of calculating warped dose distribution [adapted from reference 26].

dose $d_{W_i}(x_i, y_i, z_i)$ is determined from the dose at the corresponding position in $d_i$ which is determined by linear interpolation of the dose grid to the transformed voxel centroid $T_i(x_0, y_0, z_0)$.

Rosu *et al.*[27] investigated the effect of dose grid size on the remapped dose distribution. The dose distribution was calculated on breathe hold images acquired at exhale and inhale. A thin-plate spline registration was performed between these two images. The reconstructed cumulative dose was determined from the exhale dose and the dose at "tracked" locations in the inhale dose distribution were weighted with a pdf describing the fraction of time spent at each phase (70% and 30%, respectively). To eliminate the influence of registration errors, the authors calculated the dose distribution on the transformed exhale-like-inhale image instead of the inhale CT image. Two methods of estimating the reconstructed dose were used. In the first, the corresponding location of the center of mass (COM) of a reference voxel at inhale was determined and the dose at this point tri-linearly interpolated from surrounding voxels in the inhale dose distribution.

The authors pointed out that in the case of large volume changes the tracked exhale voxel may overlap several voxels of the inhale dose grid. If steep dose gradients exist in this region then the interpolated dose at the remapped COM may not be an accurate representation of the received dose. They proposed a second reconstruction method which accounts for this possibility by subdividing each reference voxel into octants. The dose received by each octant was reconstructed and then averaged. They compared the two reconstruction methods for 4 NSCLC patients with dose grid sizes of 3.5, 5 and 10 mm. As expected, differences in the reconstructed dose occurred in regions of steep dose gradients (penumbra) but no significant differences between the two methods were noted in terms of clinical endpoints (DVH, EUD). No significant dependence on grid size was noted.

In a second study[28] the authors examined how many phases of the respiratory motion were required to accurately reconstruct the cumulative dose and whether it is sufficient to linearly interpolate intermediate image states rather than acquire a 4D CT dataset for the whole breathing cycle. Compared to dose reconstructed from 20 breathing

states a "2-ave" state, reconstructed from the time weighted averaged breathing phases in the first and second half of the time intervals between exhale and inhale, and a "2-state" dose distribution reconstructed from weighted exhale and inhale dose distributions were found to differ by less than 2% in terms of dose in the lung. Motion between inhale and exhale was found to be essentially linear as no significant differences in dose distributions calculated on the interpolated or 4D CT images was noted.

The trilinear interpolation method has been used by other authors to assess cumulative dose in lung[29-31]. Flampouri *et al.*[32] used a simpler center-of-mass tracking method where the reconstructed dose is taken from the dose in the voxel which overlaps the corresponding location of the reference voxel COM without interpolation of the dose from neighbhouring voxels. The differences between trilinear interpolation and COM tracking are illustrated in Figure 3. Flampouri used B-spline registration vectors to determine a composite IMRT dose distribution from a 10 phase respiratory data set for three planning methods: uniform expansion of CTV by 5 mm or 10 mm and design of an ITV margin based on the union of contours drawn on all phases of the 4D CT dataset. They found that in 6 patients the composite dose distributions reconstructed from 5 phases, 99.5% of points within the CTV had a dose difference of less than 3% compared to the 10-phase reconstruction. Larger deviations were noted when fewer phases were used.

Coolens *et al.*[33] used a "reverse" approach to dose reconstruction by applying the non-linear transformations directly to the dose distributions to obtained the remapped dose distribution on the reference phase. Note that vice versa to previous methods this required registration vectors relating the image on which the dose was calculated to the reference phase.

All of the above mentioned dose remapping methods could be employed with any dose calculation algorithm, although most authors chose to calculate the dose distribution on each anatomical state with a Monte Carlo algorithm. Paganetti *et al.*[34] introduced a "4D Monte Carlo" method using the GEANT4 Monte Carlo code for simulation of time dependent geometries in proton therapy. After simulation of a set number of proton histories (corresponding to a 0.4 second delivery) the patient geometry was updated using one of 10 phases of a 4D data set imported into GEANT4. Voxel positions as a function

of time were tracked using voxel displacement maps from B-spline registration. Using COM tracking, pointers in the dose matrix were updated to properly accumulate dose as the voxels changed position.

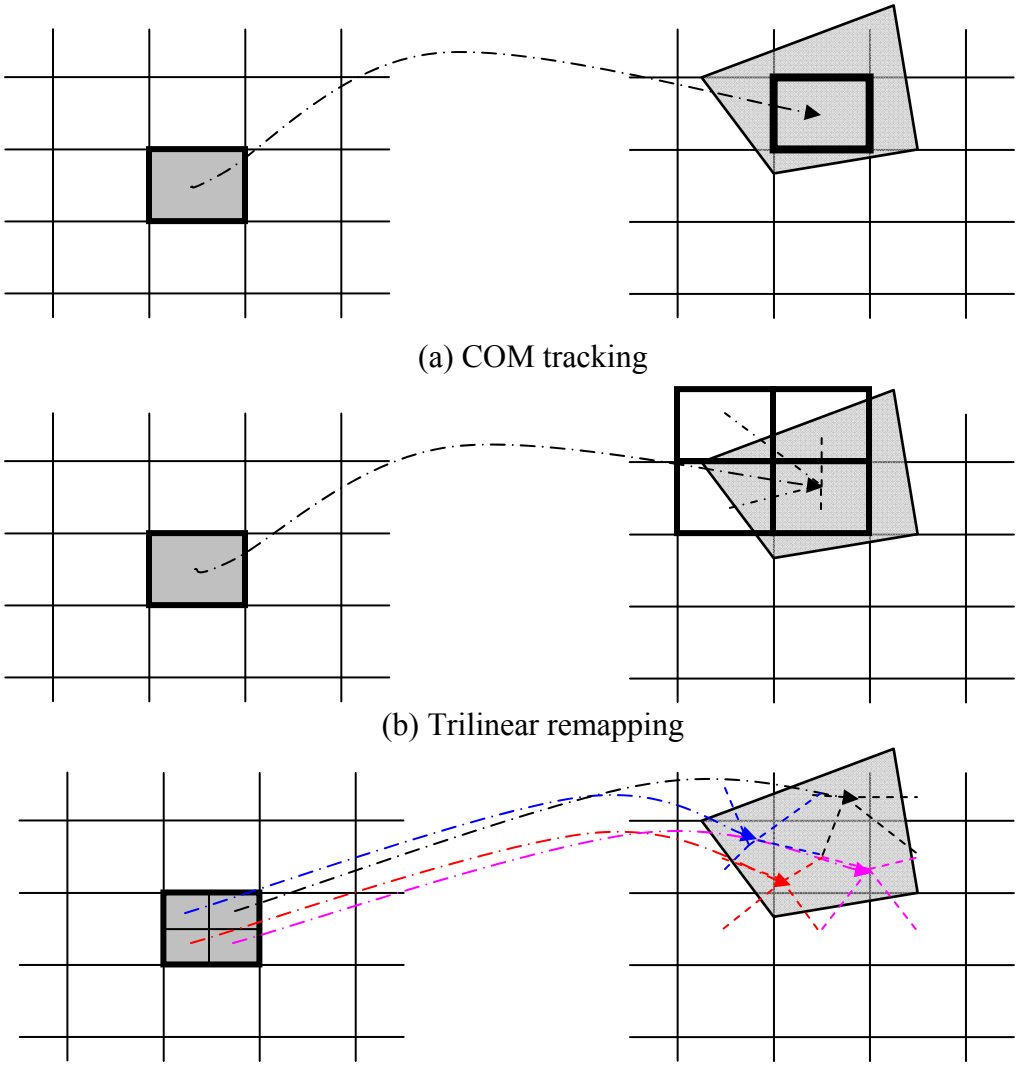

(a) COM tracking

(b) Trilinear remapping

(c) Trilinear remapping with octant subdivision

Figure 3: Illustration of different dose reconstruction methods. Shown in the left-hand column is the reference dose grid. On the right side is dose grid from which the dose is to be remapped to the reference phase. [parts of this figure were adapted from reference 27].

## 3.5 SUMMARY

Dose calculation methods which incorporate organ motion are required to evaluate the effects of inter- and intra-fraction patient motion as well as to evaluate the efficacy of

any motion compensation method. There exist three main approaches to dose calculation: numerical methods, convolution and dose warping. Only the latter method is able to account for dose deformation effects that occur with respiration-induced intra-fraction motion of the patient internal anatomy. These 4D dose calculations make use of deformation vectors from non-linear image registration to sum dose distributions calculated on multiple samples of the anatomical states in order to estimate a cumulative dose distribution. A limitation of this current approach is that interpolation of the dose distribution is required which may limit the accuracy of the dose calculation in regions of steep dose gradients and large deformations. Furthermore, the accuracy of these dose calculation methods is affected by the inherent accuracy of the non-linear image registration vectors, which requires evaluation.

## 3.6 REFERENCES


[1] Goitein M. "Calculation of the uncertainty in the dose delivered during radiation therapy" Med. Phys. **12** 608-612 (1985).

[2] Killoran J.H., Kooy H.M., Gladstone D.J., Welte F.J. and C.J. Beard "A numerical simulation of organ motion and daily setup uncertainties: implications for radiation therapy" Int. J. Radiat. Oncol. Biol. Phys. **37** 213-221 (1997).

[3] MacKay R I, Graham P.A., Moore C.J., Logue J.P., and P.J. Sharrock "Animation and radiobiological analysis of 3D motion in conformal radiotherapy" Radiotherapy and Oncology **52** 43-49 (1999).

[4] Mageras G.S., Kutcher G.J., Leibel S.A., Zelefsky M.J., Melian E., Mohan R. and Z. Fuks "A method of incorporating organ motion uncertainties into three-dimensional conformal treatment plans" Int. J. Radiat. Oncol. Biol. Phys. **35** 333-342 (1996).

[5] Yan D., Jaffray D.A. and J.W. Wong "A model to accumulate fractionated dose in a deforming organ" Int. J. Radiat. Oncol. Biol. Phys. **44** 665-675 (1999).

[6] Lockman D.M., Yan D. and J. Wong "Estimating the dose variation in a volume of interest with explicit consideration of patient geometric variation" Med. Phys. **27** 2100-2108 (2000).

[7] Yan D. and D.M. Lockman "Organ/patient geometric variation in external beam radiotherapy and its effects" Med. Phys. **28** 593-602 (2001).

[8] Maleike D., Unkelbach J. and U. Oelfke "Simulation and visualization of dose uncertainties due to interfractional organ motion" Phys. Med. Biol. **51** 223-2252 (2006).

[9] Webb S. "Does elastic tissue intrafraction motion with density changes forbid motion-compensated radiotherapy?" Phys. Med. Biol. **51** 1449-1462 (2006).

[10] Naqvi S.A. and W.D. D'Souza "A stochastic convolution/superposition method with isocenter sampling to evaluate intrafraction motion effects in IMRT" Med. Phys. **32** 1156-1163 (2005).

[11] Litzenberg D.W., Hadley S.W., Tyagi N., Balter J.M., Ten Haken R.K. and I.J. Chetty "Synchronized dynamic dose reconstruction" Med. Phys. **34** 91-102 (2007).

[12] Leong J. "Implementation of random positioning error in computerized radiation treatment planning systems as a result of fractionation" Phys. Med. Biol. **32** 327-334 (1987).

[13] Keall P.J., Beckham W.A., Booth J.T., Zavgorodni S.F. and M. Oppelaar "A method to predict the effect of organ motion and set-up variations on treatment plans" Australasian Physical and Engineering Sciences in Medicine **22** 48-52 (1999).

[14] McCarter S.D. and W.A. Beckham "Evaluation of the validity of a convolution method for incorporating tumour movement and set-up variations into the radiotherapy treatment planning system" Phys. Med. Biol. **45** 923-931 (2000).

[15] Bel A., van Herk M. and J.V. Lebesque "Target margins for random geometrical treatment uncertainties in conformal radiotherapy" Med. Phys. **23** 1537-1545 (1996).

[16] Lujan A.E., Larsen E.W., Balter J.M. and R.K. Ten Haken "A method for incorporating organ motion due to breathing into 3D dose calculations" Med. Phys. **26** 715-720 (1999).

[17] Lujan A.E., Ten Haken R.K., Larsen E.W. and J.M. Balter "Quantization of setup uncertainties in 3-D dose calculations" Med. Phys. **26** 2397 –2402 (1999).

[18] Craig T., Battista J. and J. Van Dyk "Limitations of a convolution method for modeling geometric uncertainties in radiation therapy. I. The effect of shift invariance." Med. Phys. **30** 2001-2011(2003).

[19] Craig T., Battista J. and J. Van Dyk "Limitations of a convolution method for modeling geometric uncertainties in radiation therapy. II. The effect of a finite number of fractions." Med. Phys. **30** 012-2020(2003).

[20] Beckham W.A., Keall P.J. and J.V. Siebers "A fluence-convolution method to calculate radiation therapy dose distributions that incorporate random set-up error" Phys. Med. Biol. **47** 3465-3473 (2002).

[21] Chetty I.J., Rosu M., Tyagi N., Marsh L.H., McShan D.L., Balter J.M., Fraass B.A. and R. Ten Haken "A fluence convolution method to account for respiratory motion in three-dimensional dose calculations of the liver: a Monte Carlo study" Med. Phys. **30** 776-1780 (2003).

[22] Chetty I.J., Rosu M., McShan D.L., Fraass B.A., Balter J.M. and R.K. Ten Haken "Accounting for center-of-mass target motion using convolution methods in Monte Carlo-based dose calculations of the lung" Med. Phys. **31** 925-932 (2004).

[23] Kung J.H., Zygmanski P., Choi N. and G.T.Y. Chen "A method of calculating a lung clinical target volume DVH for IMRT with intrafractional motion" Med. Phys. **30** 1103-1109 (2006).

[24] van Herk M., Remeijer P. and J.V. Lebesque "Inclusion of geometric uncertainties in treatment plan evaluation" Int. J. Radiation Oncol. Biol. Phys. **52** 1407-1422 (2002).

[25] Brock K.K., McShan D.L., Ten Haken R.L., Hollister S.J., Dawson L.A. and J.M. Balter "Inclusion of organ deformation in dose calculations" Med. Phys. **30** 290-295 (2003).

[26] Schaly B., Kempe J.A., Bauman G.S., Battista J.J. and J Van Dyk "Tracking the dose distribution in radiation therapy by accounting for variable anatomy" Phys. Med. Biol. **49** 91-805 (2004).

[27] Rosu M., Chetty I.J., Balter J.M., Kessler M.L., McShan D.L. and R. K. Ten Haken "Dose reconstruction in deforming lung anatomy: dose grid size effects and clinical implications" Med. Phys. **32** 2487-2495 (2005).

[28] Rosu M., Balter J.M., Chetty I.J., Kessler M.L., McShan D.L., Balter P. and R.K. Ten Haken "How extensive of a 4D dataset is needed to estimate cumulative dose distribution plan evaluation metrics in conformal lung therapy?" Med. Phys. **34** 233-245 (2006).

[29] Keall P.J., Siebers J.V., Joshi S. and R. Mohan "Monte Carlo as a four-dimensional radiotherapy treatment-planning tool to account for respiratory motion" Phys. Med. Biol. **49** 3639-3648 (2004).

[30]. Rietzel E., Chen G.T.Y., Choi N.C. and C.G. Willet "Four-dimensional image-based treatment planning: target volume segmentation and dose calculation in the presence of respiratory motion" Int. J. Radiation Oncol. Biol. Phys. **61** 1535-1550 (2005).

[31] Guerrero T., Zhang G., Segars W., Huang T-C., Bilton S., Ibbott G., Dong L., Forster K. and K.P. Lin "Elastic image mapping for 4-D dose estimation in thoracic radiotherapy" Radiation Protection Dosimetry **115** 497-502 (2005).

[32] Flampouri S., Jiang S.B., Sharp G.C., Wolfgang J., Patel A.A. and N.C. Choi "Estimation of the delivered patient dose in lung IMRT treatment based on deformable registration of 4D-CT data and Monte Carlo simulations" Phys. Med. Biol. **51** 2763-2779 (2006).

[33] Coolens C., Evans P.M., Seco J., Webb S., Blackall J., Rietzel E. and G.T.Y. Chen "The susceptibility of IMRT dose distributions to intrafraction organ motion: An investigation into smoothing filters derived from four dimensional computed tomography data" Med. Phys. **33** 2809-2818 (2006).

[34] Paganetti H., Jiang H., Adams J.A., Chen G.T. and E.Rietzel "Monte Carlo simulations with time-dependent geometries to investigate effects of organ motion with high temporal resolution" Int. J. Radiat. Oncol. Biol. Phys. **60** 942-950 (2004).

# Chapter 4:

# Non-linear Image Registration

## 4.1 INTRODUCTION

In radiotherapy planning, rigid image registration has been used for fusion of images[1] acquired with different modalities such at PET, MR and CT for the purpose of diagnosis or tumour delineation. Image registration is defined as the process of determining a spatial transformation which maps the features in a source image to those in a target image[2]. The *source image* is the image which will be transformed, the *target image* is the image that is fixed. The effect of applying the recovered transformation to the source image is to bring it into geometrical alignment with the target image, thus allowing the two images to be directly compared. However rigid registration methods are limited in their ability to full recover the spatial image misalignments which arise due to differences in patient posture during image acquisition and anatomical changes due to respiration, rectal filling, insertion of a brachytherapy applicator or pathological and treatment response. In such cases an additional non-rigid transformation is required to recover the residual image differences.

Non-linear image registration is a well established tool for neuroscience applications. Deformable registration of individual subject brains has allowed construction of normative atlases of brain anatomy which aid in automatic segmentation of brain anatomy and detection of pathological change. More recently, non-linear image registration has been used in 4D imaging and radiotherapy planning applications.

This chapter is organized as follows: first a summary of definitions and properties related to image registration is given; requirements and challenges for image registration specific to radiotherapy applications are discussed; this is followed by a review of voxel-based similarity metrics and transformation models which have been used in radiotherapy applications; and finally, methods of validation of image registration are discussed.

## 4.2 DEFINITIONS AND CLASSIFICATION

Image registration is a broad field with a large variety of implementations. A detailed classification of image registration techniques was reviewed in depth by Maintz[3] and van den Elsen[4] in which medical image registration methods were classified by their dimensionality, the nature of the registration basis, nature and domain of the transformation, optimization procedure, degree of automation, modalities and subjects involved.

In summary, the dimensionality of the transformation can be spatial in nature (e.g., 2D/2D or 3D/3D) or a time series (e.g., 4D CT set of 3D images). The registration matching may be based on extrinsic methods, such as a stereotactic frame, or intrinsic methods which rely on image information such as landmarks, segmented structures such as binary masks, surfaces, contours, or voxel properties. Voxel property methods may use the cross-correlation of image intensities, maximization of mutual information of both images or minimization of the sum of square image intensity differences, to name but a few. These metrics are discussed more extensively later in this chapter.

The nature or elasticity of the registration is generally classified as being rigid or non-linear. The main feature of rigid registration is that it preserves the geometry of the source object. A rigid transformation of coordinates is mathematically formulated as follows[3]:

$$\begin{bmatrix} x' \\ y' \\ z' \end{bmatrix} = \begin{bmatrix} & R & & \begin{matrix} t_x \\ t_y \\ t_z \end{matrix} \\ 0 & 0 & 0 & 1 \end{bmatrix} \begin{bmatrix} x \\ y \\ z \end{bmatrix} \quad , \tag{1}$$

where $\boldsymbol{R}$ represents rotations by angles $\alpha_1$, $\alpha_2$, and $\alpha_3$ and $t_x$, $t_y$ and $t_z$ represent translations along the x,y,z axis, respectively:

$$R = R^{(1)} R^{(2)} R^{(3)}$$

$$R^{(1)} = \begin{bmatrix} 1 & 0 & 0 \\ 0 & \cos\alpha_1 & -\sin\alpha_1 \\ 0 & \sin\alpha_1 & \cos\alpha_1 \end{bmatrix} \tag{2}$$

$$R^{(2)} = \begin{bmatrix} \cos\alpha_2 & 0 & \sin\alpha_2 \\ 0 & 1 & 0 \\ -\sin\alpha_2 & 0 & \cos\alpha_2 \end{bmatrix}$$

$$R^{(3)} = \begin{bmatrix} \cos\alpha_3 & -\sin\alpha_3 & 0 \\ \sin\alpha_3 & \cos\alpha_3 & 0 \\ 0 & 0 & 1 \end{bmatrix}.$$

An extension of rigid transformation is the affine transformation which can have up to 12 degrees of freedom, the extra 6 parameters describing scaling and shearing along each dimension.

In contrast, a nonlinear transformation contains a higher number of degrees of freedom in order to allow local deformation of the image. These could be parameterized by a relatively low-dimensional polynomial or a Fourier series, but also can be represented as a free-form deformation or vector field of local translations $T_{local}(x,y,z)$. These vector fields can be sparse, requiring a lower number of displacements defined at control points, or dense where a deformation vector is defined for each image element. In the case of a sparse vector field an interpolation method (e.g.; spline) is required to derive transformations at each image element. A rigid registration is usually performed as an initial estimate of the global transformation between the two images $T_{global}$ followed by a non-linear registration to recover the remaining local differences. The mapping of an image *A* to image *B* by the transformation T can be formulated as:

$$B(x,y,z) = TA(x,y,z) = (T_{global} + T_{local}(x,y,z))A(x,y,z). \qquad (3)$$

The optimization procedure refers to how the transformation parameters are determined. They can be either computed directly or determined using numerical methods to find an optimal solution in terms of image matching while respecting constraints of the transformation model. In both cases, care must be taken to ensure that the objective function is convex in nature so that a global minimum, and therefore a unique solution, exists.

Finally, registration methods may also be classified by the image modalities and subjects involved. Mono-modal image registration has been implemented in practically all image modalities. Multi-modal registration is employed in radiotherapy to aid in delineation of organs by combining functional and anatomical images (e.g.; PET-CT, MR-CT). Intra-subject registration involves comparing images of the same patient acquired with different image modalities or at different times (e.g.; portal image to DRR,

repeat CT scans over course of radiotherapy) while inter-subject registration is often used to compare healthy and diseased subjects.

## 4.3 CHALLENGES AND REQUIREMENTS FOR NON-LINEAR IMAGE REGISTRATION

Image registration in the context of medical imaging is challenging due to the possible non-existence of image correspondence. There may be features in the source image that do not necessarily have unique matching counterparts (unique correspondence) in the target image[5]. This can arise because of image artifacts, noise, partial volume effects, a change in voxel intensities, or anatomy that may be present in one image but not in another due to tissue motion or fluid flow between the image acquisitions. The fact that one-to-one correspondence does not exist means that there is no unique spatial transformation between images. The transformation model must then be appropriately designed so that the registration converges towards an anatomically realistic solution.

Some other considerations need to be made when designing a non-linear registration algorithm. The transformation should be symmetric so that the transformation of image A to B should be equal to the inverse of the transformation from image B to A. The transformation should also be continuous so that it preserves the topology of the source image without tearing. Such deformations are termed diffeomorphic, which means that they are one-to-one, continuous, differentiable, and maintain the image topology. The algorithm should be robust in the presence of image noise. This sensitivity to image noise is mainly determined by the similarity metric used. Ideally the registration implementation should be computationally efficient. The transformation should also be independent of the image resolution or scale on which it is estimated, however for many algorithms the magnitude of the recoverable deformation is limited by the resolution on which it is estimated. Thus multiresolution approaches, where registration is performed iteratively by estimating the deformation vectors at a low resolution scale and possibly a reduced image resolution[6], are often required. On each successive scale step the deformation vector map is refined using the previously estimated transformation as an initial estimate.

Non-linear image registration algorithms contain 3 distinct components: a similarity metric; optimization method; and a transformation model. The next sections will review voxel-based similarity metrics and transformation models used in image registration.

## 4.4 VOXEL-BASED SIMILARITY METRICS

The purpose of a similarity metric is to numerically determine how well two images are matched[2,7]. In a non-linear registration algorithm the similarity function is analogous to an external force which drives the deformation of the source image so that it matches the target image. The discussion here will be limited to voxel intensity-based metrics although similarity can be measured in terms of geometric features such as landmarks, curves or surfaces. In the case of landmark matching, if corresponding point landmarks can be extracted on both images the registration can be driven by minimization of the distance between landmark pairs. A similar approach may be applied to surface matching. The particular choice of which voxel-based similarity metric is used depends on whether registration is mono-modal or multi-modal and its robustness in the presence of noise.

The most basic approach is to minimize the sum of squared image intensity differences defined as:

$$SumSqrdDiff\left(A,B\right)=\frac{1}{N}\sum_{i}\left|A\left(\vec{x}_{\mathrm{i}}\right)-B\left(\vec{x}_{\mathrm{i}}\right)\right|^{2} \quad , \tag{4}$$

where $A$ and $B$ refer to source and target image intensities and $N$ is the number of image samples. This method assumes that the voxel intensities in both images have the same contrast and intensity level and differ only by Gaussian noise, therefore it cannot be applied to multi-modality registration or where image level or contrast is different between images. The sum of squared image intensity differences is also very sensitive to the presence of a small amount of outlier voxels which have large differences in image intensities.

If it can be assumed that intensities of the two images are related by a linear function (i.e., similar contrast, but not necessarily the same intensity level) then image similarity can be measured in terms of correlation (*xcorr)* of voxel intensities over the overlapping region of both images. The correlation coefficient (*corrcoeff*), or normalized

cross-correlation, is more robust with respect to non-preservation of image intensities. Both metrics are generally used for mono-modal registration:

$$xcorr(A,B) = \frac{\sum_i A(\vec{x}_i) B(\vec{x}_i)}{\sqrt{\sum_i A^2(\vec{x}_i) \sum_i B^2(\vec{x}_i)}} \quad , \tag{5}$$

$$corrcoeff = \frac{\sum_i \left(A(\vec{x}_i) - \bar{A}\right)\left(B(\vec{x}_i) - \bar{B}\right)}{\sqrt{\sum_i \left(A(\vec{x}_i) - \bar{A}\right)^2 \sum_i \left(B(\vec{x}_i) - \bar{B}\right)^2}} \quad , \tag{6}$$

where $\bar{A}$ and $\bar{B}$ denote the mean image intensities.

Efforts have been made to reduce the sensitivity of correlation metrics to localized variations in image intensities due to image artifacts through the use of robust correlation coefficient which reduces the effect of statistical outliers[8].

The sum of square difference and correlation metrics are commonly used in mono-modal registration of CT images[9], however they are not suitable for MR or when contrast is used in one image because of image intensity variations. In this case mutual information-based metrics are more appropriate.

Maximization of mutual information assumes that voxel intensities in the source and target images have a functional relationship. In this approach, the image voxel intensities are assumed to have a functional relationship. The amount of information in an image, or variation of anatomical features, can be quantified by the entropy *H(A)* or average information[10] contained in an image $A$ as:

$$H(A) = -\sum_{a \in A} p_A(a) \log p_A(a) \, , \tag{7}$$

where $p_A(a)$ is the probability of occurrence of a given voxel intensity $a$ within images $A$. The measure is averaged over all ranges of voxel intensities.

When two images are brought into alignment the entropy of the combined image will be minimized as the amount of repeated information is increased. Minimization of this joint entropy $H(A,B)$[11] can be used to drive image registration:

$$H(A,B) = -\sum_{b \in B} \sum_{a \in A} p_{AB}(a,b) \log p_{AB}(a,b) \quad , \tag{8}$$

where $p_{AB}(a,b)$ is probability of joint occurrence of a given voxel intensity $a$ in image A with an intensity $b$ in image B.

However, this metric is limited when large regions exist on both images whose overlap is not maximized when the images are perfectly registered[12]. In such cases the joint entropy will not be at a minimum when the images are registered. To overcome this limitation the concept of mutual information $I(A,B)$ was introduced simultaneously by Collignon[13] and Viola[14]. This approach minimizes the joint entropy while simultaneously maximizing the information content of both images in the region of overlap:

$$I(A,B) = H(A) + H(B) - H(A,B) = \sum_{b \in B} \sum_{a \in A} p_{AB}(a,b) \log \frac{p_{AB}(a,b)}{p_A(a)\, p_B(b)} \quad . (9)$$

It can be seen from the above formula that when the two images are statistically independent there is no correspondence between them so that

$$p_{AB}(a,b) = p_A(a)\, p_B(b) \quad , \qquad (10)$$

and the mutual information is zero. Mutual information still has some dependence on the amount of image overlap and Studholme[12] proposed a normalized mutual information (*NMI*) metric to overcome this. In this case, the mutual information is normalized to the join entropy of the overlapping volume as follows:

$$NMI(A,B) = \frac{I(A,B)}{H(A,B)} \quad . \qquad (11)$$

Normalized mutual information is used in multi-modality registration (e.g., PET-CT) and registration of MR images or images with and without contrast.

Many other similarity metrics exist, these include ratio of image uniformity, partitioned image intensity and correlation ratio[7]. It is also possible to combine different similarity metrics, such as voxel intensities and landmarks, in order to reduce the ambiguities of registration based on image intensities alone.

## 4.5 TRANSFORMATION MODELS

In theory, for a non-linear transformation represented by a set of free-form local deformations it is possible that all points in the source image could be mapped to a single point in the target image if no constraints are placed on the allowable deformations[15].

Deformation constraints or regularization of the vector field are defined by the transformation model. In the context of radiotherapy, transformation models based on splines, optical flow, elastic and fluid properties, diffusive and biomechanical models have been used in non-linear image registration.

### 4.5.1 Splines: Thin-plate and B-splines

A spline-based algorithm is a parametric transformation model which provides a sparse vector field based on displacements of control points. An interpolating function, the spline, is used to determine the displacements at all other points in the image. There are two types of commonly used spline interpolants: thin-plate splines and B-splines. They differ in their range of influence; thin plate splines have a global influence while B-splines have influence only in local region of control points.

Bookstein[16] introduced the concept of thin-plate splines (TPS) which model the deformation resulting from displacement of a control point as the bending of a thin metal sheet in its minimum energy configuration. The 2D basis function of the interpellant is :

$$z(x,y) = -U(r) = -r^2 \log r^2, \tag{12}$$

where $r^2 = x^2 + y^2$. The basis function *U(r)* in equation (12) is the fundamental solution of the biharmonic equation:

$$\nabla^4 U = \left( \frac{\partial^2}{\partial x^2} + \frac{\partial^2}{\partial y^2} \right)^2 U = 0 \ . \tag{13}$$

This equation represents the minimum bending energy configuration of a thin metal sheet fixed at (0,0).

For multiple control points, the shape and energy of the spline are given by the sum of interpellants which are each centered on the control point. At an infinite distance from each landmark the interpellant goes to zero. The accuracy of the registration depends on the number of control points. However, as the displacement of each control point has a global influence on the image deformation this approach is time consuming and usually not applied to registration of the whole image.

Brock *et al.*[17] used a thin-plate spline algorithm[18] for nonlinear registration of CT images of the liver acquired at inhale and exhale breathe holds. A contrast agent was used

for imaging and, as the spatial distribution of the contrast varies between the exhale and inhale images due to the time delay between their acquisition, a mutual-information based similarity metric was used. The registration process consisted of segmenting the liver and placing 24 control points on the exhale image using a probabilistic liver model derived from an average of images of 32 patients at exhale. Control points were placed with an approximately uniform density. A rigid registration was first performed using 4 control points and placing corresponding points at the same locations in the inhale images. The nonlinear registration initially used 12 control points whose displacements were determined by Nelder-Mead simplex optimization[19] in order to maximize the mutual information. After a control point displacement is sampled, the warp is interpolated to all other points in the liver and the mutual information of both images is calculated. A final optimization is then performed using all 24 control points. The complete registration required approximately 18700 iterations and 5.5 hrs on a Dec Alpha Server per subject. The accuracy of the registration was evaluated by comparing the transformed exhale coordinates of additional manually placed bifurcations to their corresponding coordinates at inhale. The accuracy was 0.13 cm (L/R) 0.15 cm (A/P) and 0.15 cm (S/I) which was comparable to reproducibility of the corresponding bifurcation identification.

Coselman *et al.*[20] used a mutual-information based thin-plate spline algorithm to register CT images of the lung acquired at inhale and exhale breath holds. Registration was performed on one lung only, using 30 control points placed on 6 planes along the inferior/superior direction. On each plane 4 control points were placed on the border of the lung and 1 point inside. An initial estimate of the deformation was determined by matching locations of the control points at exhale to approximately placed corresponding landmarks at inhale. Manual versus pseudo-random homologous landmark placement was investigated and it was determined that the random placement resulted in systematic errors during the registration. The control point displacements were refined by simplex optimization based on maximization of mutual information. An average accuracy of 1.7 (L/R), 3.1 (A/P) and 3.6 mm (I/S) was obtained, evaluated on vascular and bronchial bifurcations.

Schaly *et al.*[21,22] used a contour-driven TPS algorithm for registration of inter-fraction prostate images for the purpose of dose accumulation. Corresponding landmarks were automatically extracted from the prostate contours in additional to manual identification of bony anatomy landmarks. The registration procedure required 15 minutes on a 2.4 GHz processor and the average registration error for 10 clinical prostate cases was 3.0 mm.

Another application of thin-plate splines in non-linear image registration is as an interpellant for block-matching techniques[23,24]. Block matching is a locally rigid registration procedure which is performed on smaller sub-regions of the source image. A thin-plate spline is used to interpolate deformations between these rigidly registered sub-regions. Such algorithms have been demonstrated to be fast enough for online adaptive radiotherapy applications. Malsch *et al.*[23] used automatically selected control points in the source image along tissue boundaries. Corresponding points in the target image were determined by rigid registration of a region around each control point based on maximizing the normalized correlation coefficient of image intensities. Deformation vectors at all other image points were determined using a series of locally defined 3D thin plate splines. The time required for registration of repeat prostate, para-spinal and head and neck cases was less than 6 minutes on a 2.8 GHz Pentium IV processor. A similar implementation was used by Kostelec *e. al.*[24] for registration of brain MR images. The source image was first divided into quadrants which were rigidly registered to the target image. The registration was subsequently refined by subdividing each quadrant into further quadrants and repeating the registration.

In registration methods employing B-splines a mesh of regularly spaced control points is superimposed on the image. The free-form deformation at every point in the image $\mathrm{T}_{\mathrm{local}}(x,y,z)$ is given by the product of the control point displacements with the local cubic B-spline interpellants.

$$\mathrm{T}_{local}(x,y,z) = \sum_{\mathrm{l}=0}^{3}\sum_{\mathrm{m}=0}^{3}\sum_{\mathrm{n}=0}^{3} B_{\mathrm{l}}(u)\,B_{\mathrm{m}}(v)\,B_{\mathrm{n}}(w)\,\phi_{\mathrm{i+l,j+m,k+n}}\,, \qquad (14)$$

where $B_{\mathrm{i}}$ is the $\mathrm{i}^{\mathrm{th}}$ basis function of the B-spline and $\phi$ is an n x m x l mesh of control point displacements.

As the splines have local influence, changing the position of a control point will only affect the transformation in the local region. The number and spacing of the control points determines the magnitude and complexity of the recoverable deformation, at a cost of increased computing time. The registration process is therefore usually implemented in a multi-resolution process where the control grid spacing is iteratively refined[25]. An advantageous feature of B-splines is that they are refinable, that is the basis functions can be re-expressed in terms of one or more smaller basis functions[26] as more control points are added. These multiresolution approaches also improve the computational efficiency and reduce the likelihood of discontinuities or tearing of the deformation vector field. A non-uniform spacing of control points is also possible by designating the status of each point as active or passive[25].

The registration is driven by maximizing a similarity function $C_s$ at the control points while the deformations are constrained by a cost function $C_d$ which is analogous to the 3D bending energy of a thin plate of metal[27]:

$$C = -C_s(A, B^T) + \lambda C_d(T) \quad , \tag{15}$$

where the superscript $^T$ denotes a transformed image, λ is a regularization factor which determines the amount of smoothing and

$$C_d(T) = \frac{1}{V}\int_0^X \int_0^Y \int_0^Z \left[ \left(\frac{\partial^2 T}{\partial x^2}\right)^2 + \left(\frac{\partial^2 T}{\partial y^2}\right)^2 + \left(\frac{\partial^2 T}{\partial z^2}\right)^2 + 2\left(\frac{\partial^2 T}{\partial xy}\right)^2 + 2\left(\frac{\partial^2 T}{\partial xz}\right)^2 + 2\left(\frac{\partial^2 T}{\partial yz}\right)^2 \right] dxdydz \,, \tag{16}$$

where $V$ is the volume of the image domain. An important feature of this cost function is that it is differentiable, and therefore a gradient descent method[28] can be used to optimize the control point displacements.

B-spline algorithms have been used for non-linear registration of MR images of breast and liver with and without contrast[27], as well as PET to CT multimodal[29] and 4D PET[30] and CT lung monomodal images. Rueckert *et al.*[27] used a normalized mutual information based B-spline algorithm for non-linear registration of pre- and post-contrast breast MR images. They used a smoothing weight λ of 0.1 and tested control point spacings of 20 mm, 15 mm and 10 mm. The 10 mm control point spacing was found to be optimal as it allowed a higher flexibility in terms of deformation complexity. Rohlfing

*et al.*[31] applied B-spline registration to gated MR images of the liver at exhale and inhale. A multiresolution registration starting with a control point spacing of 4 cm and ending with a 2 cm spacing was used. The determinant of the Jacobian of the local deformations at each control point was monitored during the optimization and was forced to be positive everywhere to ensure a continuous transformation.

Rietzel *e. al.*[32] used a B-spline algorithm[33] for registration of 4D CT lung images starting with an initial control point spacing of 3 mm, refining this to a 0.75 mm spacing for the final resolution step. The average registration error based on manually identified landmarks in 5 patients was 2.1 mm. B-spline based registration of lung images has also been reported by Ruan *et al.*[34], Stancanello *et al.*[35] and Schreibmann *et al.*[36]. The first two authors introduced modifications to model the variation in stiffness of different tissues. Stancanello[35] allowed the smoothing weight to vary as a function of the CT number while Ruan[34] used a cost function to penalize changes in tissue element volumes based on the Jacobian determinant of the deformations in the region of each control point. McLelland *et al.*[37] presented an interesting application of B-spline registration to build a continuous 4D motion model of the lung based on B-spline fitting of control point displacements as a function of respiratory phase. This model allows reconstruction of the anatomy at any point in the breathing cycle with an accuracy of 1.6 mm. In their case a control point spacing of 2 cm was sufficient to obtain an average registration accuracy of 1.3 mm.

On average, computational time for B-spline registration has been reported to be a few hours[35]. Schreibmann[36] reduced the computation time to a few minutes by registering 5 or more control volumes which were placed in regions where local deformation was negligible and treating each control volume as spline control point. Each control volume was cubic or spherical in shape with a size of 1 to 2 cm. Additional control points were sometimes required to fully cover the image. The algorithm was tested on 4D CT lung images and a registration accuracy of 2 mm was obtained when using 2 cm size control volumes.

### 4.5.2 Optical flow

The optical flow method proposed by Horn and Schunck[38] registers two images by solving for the velocity distribution of bright objects moving from the source to target

image, based on object intensity. In the case of image registration only two time points, the two images, are considered so the velocity field is equivalent to the deformation field. The optical flow method has the underlying assumption that image intensities are essentially constant which limits its application to mono-modal registration. Based on the assumptions of constant image intensity $I(\vec{r},t)$ and small displacements, the velocity field $\vec{v}$ is solved from the following equation using the Taylor expansion:

$$I(\vec{r},t) \approx I(\vec{r}+\delta\vec{r},t+\delta t) \approx I(\vec{r},t) + \vec{\nabla} I \cdot \delta\vec{r} + \delta t \frac{\partial I}{\partial t} \quad . \tag{17}$$

Since image noise may cause small changes in image intensity from one image to the two intensity terms $I(\vec{r},t)$ do not cancel and are instead replaced by an error term $\varepsilon_b$.

Dividing both sides of Equation 17 by $\delta t$ we obtain:

$$\left(\vec{\nabla} I \cdot \vec{v} + \frac{\partial I}{\partial t}\right)(\vec{r},t) = \varepsilon_b \, . \tag{18}$$

The intensity of a moving point is considered to not change so that $\left(\frac{\partial I}{\partial t}\right)(\vec{r},t) = 0$ and:

$$\frac{\partial I}{\partial x} v_1 + \frac{\partial I}{\partial y} v_2 + \frac{\partial I}{\partial z} v_3 = \varepsilon_b \quad , \tag{19}$$

where $\frac{\partial I}{\partial x}$ etc. are the image intensity gradients along the x,y,z directions.

This expression alone is not enough for a unique determination of the velocity field. A regularization term $\varepsilon_s$ controlling the smoothness of the velocity field is added which minimizes the square magnitude of the optical flow velocity gradients:

$$\varepsilon_s^2 = \sum_{i=1}^{3} \left( \left(\frac{\partial v_i}{\partial x}\right)^2 + \left(\frac{\partial v_i}{\partial y}\right)^2 + \left(\frac{\partial v_i}{\partial z}\right)^2 \right) \quad . \tag{20}$$

The velocity field is then determined by minimizing the following expression over the whole image volume *V*:

$$\varepsilon^2 = \iiint_V \left( \alpha^2 {\varepsilon_b}^2 + {\varepsilon_s}^2 \right) \quad , \tag{21}$$

where α determines the relative importance of image matching and smoothness. The above equation is solved using variational calculus to get the following recursive equation of the velocities in each voxel:

$$\vec{v}(\vec{r})_{n+1} = \bar{v}(\vec{r})_n - \vec{\nabla} I(\vec{r}) \left( \frac{\bar{v}(\vec{r})_n \cdot \vec{\nabla} I(\vec{r}) + \frac{\partial I(\vec{r})}{\partial t}}{\alpha^2 + \left| \vec{\nabla} I(\vec{r}) \right|^2} \right) \quad , \tag{22}$$

where $\bar{v}_n$ is average velocity of nearest neighbours, $\frac{\partial I}{\partial t} = I_s{}^T - I_t$ is residual difference between the two images and n indicates the iteration number.

As previously mentioned, optical flow employs a small deformation assumption which means that this method can only recover deformations which are smaller or equal to the voxel size. For this reason a multiresolution strategy is needed, similar to that used for B-spline transformation. In this case the optical flow is estimated first on low-resolution images, then repeated on images of increasing intensity using the previously estimated transformation as a starting estimate for the next registration. An advantage of this method is its computational efficiency, requiring relatively few iterations to converge[2].

Guerrero *et al.*[39] used optical flow registration with an empirically determined smoothing weight of α=1.4 to estimate intrathoracic tumour motion based on breath hold CT data sets acquired at exhalation and inhalation. An rms error of less than 0.25 mm was reported for recovering a known thin-plate spline deformation. The recovered voxel displacements were used to compute a measure of ventilation[40] from the change in CT number of corresponding voxels in 4D data set. Optical flow has also been used in a multiresolution implementation for registration of 4D CT lung images[41]. El Naqa *et al.*[42] reported the use of a smoothing weight $\alpha(\vec{r})$ which adapts to local image features to register 4D CT lung images according to the function:

$$\alpha(\vec{r}) = \frac{\alpha_0}{2}\left(1 + \exp\left(-\left\|\nabla I(\vec{r})\right\| / T\right)\right), \tag{23}$$

where $T$ and $\alpha_0$ control the trade-off between smoothing and matching. $T$ is a cutoff point which was estimated from the histogram of the spatial gradients.

### 4.5.3 Demon's and diffusive models

The "Demon's" algorithm proposed by Thirion[43] models the image registration as a diffusion process. The target image may be thought of as possessing semi-permeable membranes which allow the source image (deformable model) to diffuse through the interfaces by the action of small "demons" located on the membranes. Points in the deformable model are attracted by all points in the target image which are similar. Thirion presented different implementations of this concept, one of which uses the optical flow equation to solve for the velocities of points within the deformable model:

$$\vec{v}(\vec{r})_{n+1} = \vec{v}(\vec{r})_{n} + \frac{\left(I_s(\vec{r}) - I_t(\vec{r})\right)\vec{\nabla} I_t(\vec{r})}{\left(\vec{\nabla} I_t(\vec{r})\right)^2 + \left(I_s(\vec{r}) - I_t(\vec{r})\right)^2} \quad . \tag{24}$$

Thirion stated that optical flow is similar to the demons since all pixels where the intensity gradient is non-zero behave as demons which force the images into alignment. In their implementation[43], the image velocities were solved using a sum of squared image intensity difference matching criterion and gradient descent minimization. After each iteration, the summed estimate of the velocities was smoothed in order to suppress the effects of noise and ensure continuity. Such regularization approximates the properties of a viscous fluid and large, discontinuous deformations are possible where the image gradients are small.

Cachier[44] and Pennec[15] used a modified implementation of the above equation to limit the maximum displacements to $\frac{1}{2\alpha}$ where $\alpha > 0$:

$$\vec{v}(\vec{r})_{n+1} = \vec{v}(\vec{r})_{n} + \frac{\left(I_s(\vec{r}) - I_t(\vec{r})\right)\vec{\nabla} I_t(\vec{r})}{\left(\vec{\nabla} I_t(\vec{r})\right)^2 + \alpha^2\left(I_s(\vec{r}) - I_t(\vec{r})\right)^2} \quad . \tag{25}$$

This modified version was used for registration of breathe hold images using weighting factors $\alpha$ of 0.5 to 0.65[45,46]. The summed estimate of the velocities on each iteration was smoothed with a Gaussian function. The registration was terminated after 150 iterations. A multiresolution registration process with a maximum resolution of 256x256 required 15 minutes on a Pentium 4 2.8 GHz processor. The authors demonstrated that the estimated velocity fields were continuous, however, the Gaussian regularization appeared to introduce a small number of discontinuities within the deformation vectors. The

registration was also tested for inverse consistency ($T_{ab}=T_{ba}$) and transitivity ($T_{ab}+T_{bc}=T_{ac}$). The mean consistency error was found to be 1.3 mm and the transitive error was 1.8 mm when estimating deformation vectors on a 2 mm resolution. Sarrut *et al.*[47] also used this implementation of the Demon's algorithm for temporal interpolation between inhale and exhale data sets for the purpose of reconstructing intermediate respiratory phases. As the sum of squared intensity difference metric assumes constant image intensity, modification of lung voxel intensities was required to account for lung density changes that occur with inhalation. This "a priori lung density modification" method improved the registration accuracy from 6.3 (3.8) mm to 2.7 (1.1) mm. Intermediate density images were generated using local volume changes approximated from the Jacobian determinant to modify the interpolated CT numbers.

Wang *et al.*[48,49] further modified the above implementation of the demon's algorithm to introduce an additional "active force" in order to improve the computational efficiency and allow large deformations. This additional force arises from Newton's third law as a reactive force in the diffusing image which acts on the static, target image:

$$\vec{v}(\vec{r})_{n+1} = \vec{v}(\vec{r})_{n} + \left(I_s(\vec{r}) - I_t(\vec{r})\right)\left[\frac{\vec{\nabla} I_t(\vec{r})}{\left(\vec{\nabla} I_t(\vec{r})\right)^2 + \alpha^2\left(I_s(\vec{r}) - I_t(\vec{r})\right)^2} + \frac{\vec{\nabla} I_s(\vec{r})}{\left(\vec{\nabla} I_s(\vec{r})\right)^2 + \alpha^2\left(I_t(\vec{r}) - I_s(\vec{r})\right)^2}\right]. \qquad (26)$$

The authors found that registration using this modified version converged more rapidly, requiring 40% fewer iterations. Full registration of a 256x256x61 image required 6 minutes on a 2.8 GHz Pentium processor. They used a weighting factor α of 0.4, Gaussian smoothing and a 3 step multiresolution approach for registration of a deformable pelvis phantom, as well as prostate and head and neck patient images deformed with thin-plate spline deformation fields. The mean magnitude difference between the simulated and recovered deformation vectors was 0.5 ± 1.5 mm for prostate images and 0.2 ± 0.6 mm for head and neck images. The registration recovered the motion of 23 embedded plastic beads inside the deformable pelvic phantom with a mean registration error of 0.8 ± 0.5 mm. The reported accuracy for registration of repeat pelvic CT images was 1 mm.

A non-linear image registration algorithm similar to the Demon's method was developed by Lu *et al.*[50]. The registration problem was formulated as solving for the displacement field $\vec{u}(\vec{r})$ that minimizes an energy functional $\varepsilon(\vec{u})$ which depends on the residual image difference $R(\vec{r},\vec{u})$ and the bending energy given by the sum of squared Laplacians of the deformation field:

$$\varepsilon(\vec{u}) = \int_{r\in V}\left[R^2(\vec{r},\vec{u}) + \lambda\sum_{i=1}^{3}\sum_{j=1}^{3}\left(\vec{v}(\vec{r})_j^i\right)^2\right]dr \quad , \tag{27}$$

where λ is a weighting factor for the regularization and controls tissue stiffness and was set to 0.1, $R(\vec{r},\vec{u}) = I_s(\vec{r}+\vec{u}) - I_t(\vec{r})$ is the residual of image intensities and $\vec{v}(\vec{r})_j^i \equiv \frac{\partial u(\vec{r})^i}{\partial x^j}$. The Laplacian regularization term $\nabla^2 u$ in Equation 27 is also known as the Tikhonov regularizer[51] and defines the registration as a diffusion-type process where the source image can be thought of as diffusing into the target image while driven by a similarity force defined by the image intensity residual.

This registration method was tested against known deformations using both synthetically deformed images and a deformable phantom. For small deformations on the of 3 to 4 mm the registration error was less than 1 mm. Non-linear registration of inter- and intra-fraction lung and prostate clinical images was performed for the purpose of automated contouring as well as comparison of daily MV cone-beam CT images to a planning kVCT image for deformable dose accumulation[52]. Registration required less than 3 minutes to register a 256x256x61 image on a 933 MHz Pentium III processor. This variational calculus method was also used for automated contouring[53] and determination of tumour motion envelopes[54] from 4D CT images.

A similar method was used by Gao *et al.*[55] for registration of serial images of the prostate. In this case, to avoid oversmoothing discontinuous regions where the image intensity gradient becomes infinite, a variable weight was used for the regularization:

$$\lambda = \lambda_0 f\left(I_s(\vec{r}+\vec{u}), I_t(\vec{r})\right) \quad , \tag{28}$$

where $\lambda_0$ was determined empirically and

$$f = \left|I_s(\vec{r}+\vec{u}) - I_t(\vec{r})\right|\sqrt{1+\left|\nabla I_s(\vec{r}+\vec{u})\right|^2} \quad . \tag{29}$$

The resulting partial differential equations were solved by a finite difference scheme and with a multiresolution approach.

### 4.5.4 Physical models: elastic and viscous fluid

For non-linear registration based on elastic models[56-58] the source image is modeled as an elastic continuum which is being deformed by an external driving force to match the target image. Similar to the previously discussed models, the image matching problem is formulated as the minimization of an objective function which penalizes deformations while maximizing image similarity. The image similarity is described as an external body force while the deformation penalty term is an internal force which resists deformation and is represented by the elastic strain energy. The minimum value of the objective function represents an equilibrium configuration where the total potential energy of the system reaches a minimum. Assuming small displacement gradients (ie., smooth deformations) this equilibrium is described by Navier's displacement equations:

$$0 = \mu\nabla^2\vec{u}(\vec{r}) + (\lambda+\mu)\vec{\nabla}\left(\vec{\nabla}\cdot\vec{u}(\vec{r})\right) + \vec{b} \qquad , \qquad (30)$$

where $\vec{b}$ is the body force, $\lambda$ and $\mu$ are the Lame elastic constants which control the stiffness of the elastic body and therefore the smoothness of the deformations.

This equation is highly nonlinear so numerical solutions are necessary. In practice, the Navier equation is solved iteratively on a finite grid of points using a finite difference scheme and the boundary condition that forces and displacements at the image boundary go to zero.

Bajcsy *et al.*[56] used an elastic registration algorithm to register CT images of brain to an atlas. They used normalized cross-correlation as a similarity metric with the body force proportional to the gradient of the similarity function. The elastic constant $\lambda$ was set to zero, allowing only longitudinal stretching but no lateral shrinking, and a multiresolution registration was used to overcome the small deformation limitation as well as to improve computational efficiency. Gee *et al.*[57,58] used an elastic model to register serial breath hold MRI lung images in order to study motion of lung tissue. Using normalized cross-correlation, they reported an average accuracy of 1.14 ± 0.93 pixels for a 3.5 mm image resolution. Christensen *et al.*[59] presented an elastic registration algorithm

which ensures inverse registration consistency by simultaneously estimating the forward and reverse transformation and placing a quadratic penalty term in the objective function which penalizes differences between the two transformations.

Due to the computation complexity and small deformation assumptions, the elastic registration models mentioned above have generally not found applications in radiotherapy. The exception is a somewhat different approach to elastic registration which was formulated by Pekar *et al.*[60]. This parametric model uses an adaptive grid of irregularly spaced control points. A Gaussian-shaped force is applied at each of these control points whose strength, direction and area of influence are parameters to be optimized in the registration process. From an analytic solution of Navier's equation for a Gaussian-shaped force the following expression for the displacement at the point of force application is derived:

$$\vec{u}\big|_{\mathrm{r}=0} = \frac{(5-6\nu)(1+\nu)}{3\left(\sqrt{2\pi}\right)^3 \sigma Y (1-\nu)} f \quad , \tag{31}$$

where σ is the Gaussian full-width at half maximum, $Y$ and ν are elastic constants and $f$ is the magnitude of the applied force. Using a sum of squared image intensity difference similarity function the control point location, σ and $f$ are optimized using a Levenberg-Marquardt optimization scheme[61]. Registration of a 3D prostate CT data set as well as thoracic PET and CT image registration required 1 hour using a multiresolution approach starting with a 3x3x2 regularly spaced control grid. Images appeared to correlate well by visual inspection though a quantitative analysis of the registration accuracy was not performed.

Viscous fluid models overcome the small deformation approximation of many registration algorithms to allow large, local nonlinear deformations while preserving image topology[62-65]. Time dependence is added to the displacement field $\vec{u}(\vec{r},t)$ between the deforming source image and the target image in an Eulerian reference frame. The velocity field $\vec{v}(\vec{r},t)$ describes the time rate of change of the displacement field and the two are linked by the material derivative:

$$\vec{v} = \frac{d\vec{u}}{dt} = \frac{\partial \vec{u}}{\partial t} + \sum_{\mathrm{i}=1}^{3} \vec{v}_{\mathrm{i}} \frac{\partial \vec{u}}{\partial r_{\mathrm{i}}} \quad . \tag{32}$$

In the Eulerian reference frame this displacement field maps points in the template to points in deforming continuum. A viscous-fluid analog of Hooke's law describes the forces resisting deformation of the image, however this differs from elastic models in that the stress induced as the image deforms is allowed to relax over time. Therefore the internal energy does not necessarily increase with increasing deformation and large deformations are allowed. Assuming a Newtonian fluid with a very low Reynold's number the Navier-Stokes equation describing the equilibrium velocity field is:

$$\mu\nabla^2\vec{v}+\left(\lambda+\mu\right)\vec{\nabla}\left(\vec{\nabla}\cdot\vec{v}\right)+\vec{b}\left(\vec{u}\right)=0 \quad , \tag{33}$$

where $\mu$ and $\lambda$ are viscosity constants and $\vec{b}\left(\vec{u}\right)$ is the body force which is given by:

$$\vec{b}\left[\vec{r},\vec{u}\right]=-\alpha\left(I_{\mathrm{s}}\left[\vec{r}+\vec{u}\right]-I_{\mathrm{t}}\left(\vec{r}\right)\right)\vec{\nabla}I_{\mathrm{s}}\Big|_{\vec{\mathrm{r}}+\vec{\mathrm{u}}} \quad . \tag{34}$$

The previous equations are evaluated directly with no small deformation approximation. Starting with an initial zero displacement field the body force is calculated and the linear PDE (Equation 33) is solved, using small time increments, for the instantaneous velocity at time *t* using a successive over-relaxation difference scheme which is a weighted average between previous iterate and computed Gauss-Seidel iterate[28]. Effectively the problem is four-dimensional but it is solved in 3D using Euler integration along the time dimension. Using an iterative form of material derivative the displacement field is then determined. Although the solution to the Navier-Stokes PDE is continuous, discontinuities can occur when it is solved on a finite grid. Therefore, the determinant of the Jacobian of transformation was evaluated on each iteration and when it falls below 0.5 a new deformed source image is propagated and registration is restarted. The final step of the registration process is to concatenate all these resulting transformations. This viscous-fluid model has been applied for registration of CT images acquired before and after insertion of brachytherapy catheter for purpose of dose mapping for multiple-insertion courses of intra-cavitary brachytherapy[62]. The registration of a 192x192x64 image required 4.5 hrs and 400 iterations on a 195 MHz processor. Keall *et al.*[66] also reported the use of this algorithm for registration of thoracic 4D CT images.

A similar implementation by Foskey *et al.*[67] used minimization of an energy functional $E\left(\vec{u}\right)$ based on the sum of squared image intensity differences and a

regularization term $L_{\text{reg}}$ which is a differential operator based on the Navier-Stokes equations. The PDE was solved for the deformation field similarly to the previously mentioned viscous fluid model using time integration of the velocity field:

$$E(\vec{u}) = \int_{V} \left( I_{\text{t}}(\vec{r}) - I_{\text{s}}\left(\vec{r} + \vec{u}(\vec{r},t)\right)\right)^2 dr + \int_{V,t} \left\| L_{\text{reg}} v(\vec{r},t) \right\|^2 drdt \quad . \qquad (35)$$

With variational calculus the problem reduces to the differential equation:

$$\left( I_{\text{t}}(\vec{r}) - I_{\text{s}}\left(\vec{r} + \vec{u}(\vec{r},t)\right)\right) \nabla I_{\text{s}}\left(\vec{r} + \vec{u}(\vec{r},t)\right) = L_{\text{reg}} \vec{v}(\vec{r},t) \qquad , \qquad (36)$$

where $L_{\text{reg}} \vec{v}(\vec{r},t) = \alpha \nabla^2 \vec{v}(\vec{r},t) + \beta \nabla\left(\nabla \cdot \vec{v}(\vec{r},t)\right) + \gamma \vec{v}(\vec{r},t) \qquad .$ (37)

The algorithm was applied for registration of pelvic images for use in automated segmentation and dose mapping in adaptive radiotherapy of the prostate. The authors introduced a novel method of image pre-processing to deflate regions of bowel gas which lead to discontinuities within the deformation field because they may be present in one image but not the other. By masking the bowel gas on a given image a velocity field is calculated, based on the image gradient, which collapses the masked region to a point:

$$\nabla I\left(\vec{u}_{\text{defl}}(\vec{r},t)\right) = L_{\text{reg}} \vec{v}(\vec{r},t) \qquad . \qquad (38)$$

The full transformation is then given by:

$$\vec{u}(x) = \vec{u}_{\text{s-defl}}\left(\vec{u}_{\text{defl}}\left(\vec{u}^{-1}_{\text{t-defl}}(\vec{r})\right)\right) + \tau \qquad , \qquad (39)$$

where τ is an initial rigid transformation, $\vec{u}_{\text{s-defl}}$ and $\vec{u}_{\text{t-defl}}$ are the transformations which collapse bowel gas on the source and target images, respectively, and $\vec{u}_{\text{defl}}$ is the transformation between the deflated source and target images.The following values were used for the regularization terms: α=0.01-0.02 β=0.01-0.02 γ=0.001-0.0001 depending on whether a coarse (4x), medium (2x) or fine resolution (full image resolution) was used for the deformation grid. The calculation time was 12.5 min for the full registration, for a final mesh size of 187x217x195, on a on a 3GHz Intel Xeon processor.

Pevsner *et al.*[68] used the same algorithm to register 4D CT images of non-small cell lung cancer patients and map tumour contours from end-exhale to end-inhale images. A three-dimensional distance-to-agreement between manual and automapped contours as well as 41 bronchial and vascular bifurcations was used to evaluate the registration. The maximum error was 3.2 mm in the superior-inferior direction which was limited by the

2.4 mm slice thickness. The mean contour and bifurcation error were 2.6 mm and 2.9 mm, respectively.

A combined fluid-landmark registration approach was proposed by Joshi *et al.*[69]. The landmark-based approach is more computationally efficient than a voxel-based viscous-fluid registration and, due to the lower dimensionality of the problem, there is no need to discretize the solution along the time dimension. The approach is similar to that of landmark matching by thin-plate splines however instead of the quadratic TPS penalty term a diffeomorphic energy functional $\|Lv\|^2$ based on fluid mechanics was used where $L = -a\nabla^2 + b\nabla(\nabla\cdot) + c$. The cost function to be minimized is then:

$$C(\vec{v}(\vec{r},t)) = \int_0^1 \int_V \left\|L\vec{v}(\vec{r},t)\right\|^2 drdt + \sum_{n=1}^{N} \beta_n \left\|\vec{x}_n(\vec{r}_n) - \vec{u}(\vec{r}_n,1)\right\|^2 \quad , \qquad (40)$$

where N is the number of landmarks, $\beta_n$ weights the balancing of the smoothness of velocity field against matching landmarks and $\vec{x}_n$ is the landmark displacement.

### 4.5.5 Biomechanical and finite-element based models (FEM)

Biomechanical models of organ deformation can be derived by the use of finite element analysis (FEA). In this method the organ to be modeled is divided into smaller volume elements and boundary conditions on the motion and deformation are derived from serial images. These boundary conditions define the forces acting on the volume elements from the source to target image. These forces induce displacement of each volume element according to Newton's first law and Hooke's law, using information about the elastic properties of the tissues. PDEs for each volume element must be solved numerically to determine the equilibrium deformed state, the final result being a 3D displacement for each volume element.

An FEM-based model of the rectum was first presented by Yan *et al.*[70]. Based on contours of the rectal wall drawn on daily CT images a 3D mesh of volume elements with 1 mm resolution was generated. The change in location of four fiducial points on the inner and outer rectal wall, determined on each CT slice, were used as boundary conditions. The displacements were solved using the ABAQUS finite-element modeling software assuming an elastic modulus of 0.5 N/m$^2$ and a compressibility of 0.3. The

authors used these displacements to determine the cumulative dose received by the rectal wall over the treatment course. Another FEM-based model of pelvic images was presented[71] for MR-guided brachytherapy where registration of the planning and intra-operative MR images is required to account for changes in the patient positioning. In this study the authors used different material properties for the central gland and peripheral zone of the prostate.

The accuracy of any biomechanical model is dependent on the accuracy of the selection of corresponding boundary points[72] as well as material properties. Chi *et al.*[73] studied the sensitivity of the accuracy of FEM-based registration to the uncertainty on the elastic properties of the rectal wall, prostate and bladder wall. For hollow, thin organs a 30% uncertainty in elastic properties led to a 1.3 mm registration error while for a solid organ an error of 4.5 mm was obtained. Another study[74] investigated the effect of variations in the elastic modulus and compressibility inside the liver and whether it is sufficient to assume homogeneous material properties.

Brock *et al.*[75-77] developed multi-organ 4D models for the abdomen and thorax based on inhale and exhale CT and MR images. The contours from the treatment planning system are first converted into triangulated smoothed surface meshes. Using the Hypermesh software a 4-node tetrahedral mesh with elemental volume of 0.03 $cm^3$ is created from these surface meshes. Material properties and surface interfaces are assigned to each element. A linear elastic material was assumed with homogeneous, isotropic organ properties. The HYPERMORPH software then determines the boundary conditions by aligning the organ surfaces from the source and target images. The finite-element analysis (ABAQUS) to solve for the displacements at each node of the tetrahedral mesh required 332 s for the abdomen and 495 s for the thorax on a 2.0 GHz P6600 processor. In the multi-organ model organs are defined as being explicitly deformed or implicitly deformed, in which case the organ deformations are determined by the displacements of explicitly deformed organs and the properties assigned to the organ surface interfaces. The average vector accuracy of the inhale-to-exhale registration was 0.44 cm and 0.24 cm for the lung and liver, respectively. A linear path of travel was assumed between these extreme states and intermediate states were created by fractional displacements of the mesh nodes.

A biomechanical breast model created for the VTK framework was also developed[78] to simulate breast deformations which occur during DCE-MR mammography. The breast tissue was segmented into fatty and fibroglandular tissues to which different elastic properties were assigned. Models using different volume element sizes, linear and hyperelastic tissue properties, varying compressibility and boundary conditions were investigated.

## 4.6 COMPARISON OF TRANSFORMATION MODELS

A comparison of the different transformation models discussed above, in terms of their degree of computational complexity, smoothness constraints and any limiting assumptions, is given in Table 1. The registration time required depends on the image size and processor, therefore average values from the literature are reported.

Table 1. Comparison of non-linear registration algorithms used in radiotherapy

| Model | Registration time | Smoothness constraint | Comments |
|---|---|---|---|
| Thin-plate spline | minutes-hours | Gradient of deformations | Suitable for single organ registration only |
| B-spline | minutes-hours | Gradient of deformations | |
| Optical flow | minutes | Gradient of velocity field | Small deformation assumption |
| Diffusive | minutes | Gradient of deformations | |
| Elastic | hours | Linear-elastic | Small deformation assumption |
| Viscous fluid | hours | Fluid Navier-Stokes | Diffeomorphic |
| FEM | minutes | Linear-elastic | |

## 4.7 VALIDATION OF IMAGE REGISTRATION

The accuracy of image registration can be assessed qualitatively and quantitatively. Visual inspection of a red-green image overlay or difference images of the deformed source and target image can be used to identify regions of mismatch. Quantitatively, the accuracy can be assessed based on metrics such as image similarity and distance to

agreement of point landmarks or contours. These metrics can be evaluated on actual patient data or by recovering simulated deformations of the patient images or images of a deformable phantom. The drawback of the former approach is that patient images are not necessarily artifact free. However, the latter method may not represent physically realistic deformations.

Image similarity metrics such as cross-correlation and mutual information may be used to quantitatively assess registration accuracy. These metrics provide a global measure of the image matching and are automatic and simple to compute. However, the fact that it is evaluated on the entire image volume means that no information is available about areas of local mismatch. A potential solution is to calculate the correlation over smaller regions. A novel metric similar to the gamma index[79] was proposed by Brock *et al.*[80] which is a combination of voxel intensity difference and minimum distance to voxel agreement.

Readily identifiable features such as vascular and bronchial bifurcations can be used as landmarks to assess a point-by-point distance to agreement. The accuracy of this metric is limited by the accuracy with which homologous landmarks can be identified on the source and target images. For this reason, observer landmark identification errors should be quantified.

Manual structure contours may also serve as a ground truth by which to evaluate the performance of image registration. An application of non-linear image registration in radiotherapy is to automate mapping of manual contours from one image to another. By comparing the automapped contour to a manual contour of the same structure on the target image a spatial distribution of distance to agreement (DTA) can be calculated. This can be performed in 2D or 3D, although the later approach is preferred to account for 3D motion that occurs in a 3D registration. It is also possible to calculate an area or volume overlap between the manual and auto-mapped contours. For a 3D calculation of DTA a 3D triangulated surface is determined from the 2D contours, where the size of the triangles influences the accuracy of the DTA calculation. Authors have differed in their approach to calculating the DTA between the surfaces; either as radial projections from the COM of one of the structures or along the surface normals of the triangles. The DTA can be analyzed as a 2D polar map[81,68] or a colormap superimposed on the organ

surface[36]. A possible drawback of the radial DTA approach is that it may give multiple values for DTA along a single rayline (see Figure 2).

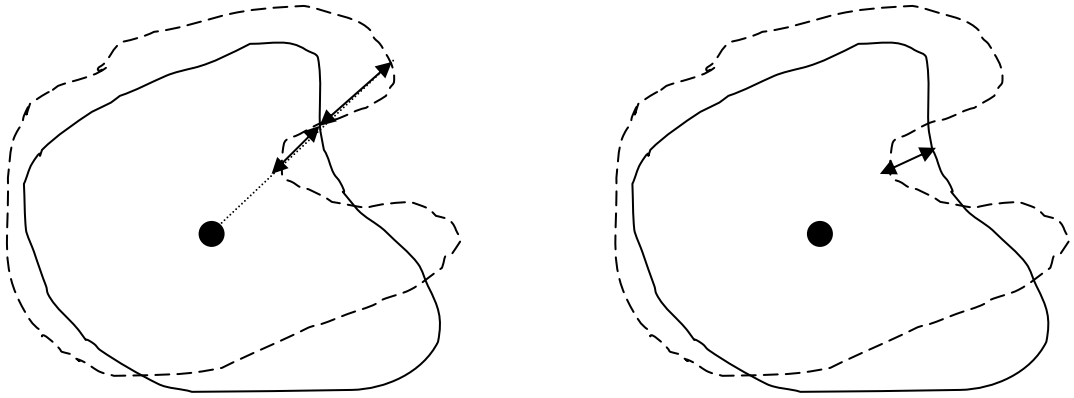

(a) (b)

Figure 2. Calculation of distance to agreement between two contours by (a) radial distance and (b) normal distance. A drawback of the radial distance approach in (a) is that it can return multiple intersection points along a particular rayline.

It is difficult to quantify image registration accuracy on patient data where image artifacts can occur. For this reason both rigid and deformable phantoms, where the geometry is exactly known, have been developed for validation of nonlinear image registration. Rigid motion phantoms[39] are obviously limited in their ability to produce deformations. A deformable phantom consisting of a silicon block with an embedded matrix of Teflon beads was developed for validation of FEM models[82]. Different loads were applied by a compression plate and measurable deformations of the beads compared to displacements from FEA. Lu *et al.*[83] designed a balloon phantom embedded in a gel matrix which was inflated by insertion of a heavy oil. About 300 plastic beads implanted around the balloon were used for verification of the registration. The achievable deformation was around 1 mm. The development of anthropomorphic deformable phantoms for validation of image registration has thus far been limited. Kashani *et al.*[84] used a rigid diagnostic thoracic phantom filled with compressible foam in which tumor-simulating inserts of varying sizes and composition were embedded. Deformations were

achieved by compression of the foam with a diaphragm plate. No investigation of registration accuracy was performed.

Mathematical breathing phantoms, such as the Nurbs-based Cardiac-Torso (NCAT) phantom[85,86], can be used to generate artifact-free 4D CT images. The software uses non-uniform rational B-splines (NURBS) to model the heart, spleen, stomach, kidneys, spine, liver, lungs, diaphragm and ribs. Motion of these organs is modeled by applying time-dependent translations to the control points defining the NURBS surface of each organ. NCAT models only anterior/posterior and inferior/superior respiratory-induced motion. 3D CT images of the phantom can be obtained at any intermediate phase of the breathing cycle at a resolution specified by the user by ray-tracing through the phantom at a given slice spacing. The phantom dimensions and breathing characteristics are adjustable through a series of parameters specified in an input file. Guerrero *et al.*[87] used the displacement vectors defined for each control point to validate deformation vectors predicted by a thoracic non-linear image registration.

## 4.8 SUMMARY

Image registration is the process of determining the spatial transformation which maps a source image as closely as possible to a target image. Registration algorithms are generally classified as rigid or non-linear, depending on whether the transformation is globally or locally defined. Non-rigid, or non-linear, registration algorithms are capable of recovering complex localized deformations. A non-linear registration method requires a similarity metric, optimization method and transformation model. Many different transformation models have been developed and they differ in terms of computational complexity, physical constraints and underlying approximations. Validation of non-linear registration can be performed qualitatively or quantitatively based on intrinsic image features. Because images may contain artifacts which affect determination of registration accuracy, validation may be best performed using anthropomorphic phantoms which undergo physically realistic deformations.

## 4.9 REFERENCES


[1] Rosenman J.G., Miller E.P., Tracton G. and T.J. Cullip "Image registration: an essential part of radiation therapy treatment planning" Int. J. Radiat. Oncol. Biol. Phys. **40** 197-205 (1998).

[2] Crum W.R., Hartkens T. and Hill D.L.G, "Non-rigid image registration: theory and practice", The British Journal of Radiology **77** S140-153 (2004).

[3] Maintz, J.B. and Viergever, M.A., "A survey of medical image registration", Medical Image Analysis **2** (1) 1-36 (1998).

[4] van den Elsen, P. Pol E.D. and Viergever, M.A. "Medical image matching – a review with classification", IEEE Engineering in Medicine and Biology 26- 39 (1993).

[5] Crum W.R., Griffin L.D., Hill D.L.G. and Hawkes D.J., "Zen and the art of medical image registration: correspondence, homology and quality" NeuroImage **20** 1425-1437 (2003).

[6] Florack L.M.J., Romeny B.M.H., Koenderink J.J. and M.A. Viergever "Scale and differential structure of images" Image Vision and Computing **10** 76-388 (1992).

[7] Hill D.L.G., Batchelor P.G., Holden M. and Hawkes D.J. "Medical image registration", Phys. Med. Biol. **36** R1-R45 (2001).

[8] Kim J. and Fessler J.A. "Intensity-based image registration using robust correlation coefficients" IEEE Transactions on Medical Imaging 23(11) pp. 1430-1444 (2004).

[9] Court L.E. and Dong L. "Automatic registration of the prostate for computed-tomography-guided radiotherapy" Med. Phys. **30** 2750-2757 (2003).

[10] Shannon C.E. "The mathematical theory of communication" Bell System Technical Journal **27** 379-423, 623-656 (1948).

[11] Collignon A., Vandermeulen D., Suetens P. and Marchal G. "3D multi-modality medical image registration using feature space clustering" Proceedings of the 1st International Conference on Computer Vision, Virtual Reality and Robotics in Medicine, Nice, France Springer, Berlin, 195-204 (1995).

[12] Studholme C., Hill D.G. and Hawkes D.J., "An overlap invariant entropy measure of 3D medical image alignment" Pattern Recognition **32** 71-86 (1999).

[13] Collignon A., Maes F., Delaere D., Vandermeulen D., Suetens P. and Marchal G.

”Automated multimodality medical image registration using information theory” Proceedings of the 14th International Conference on Information Processing in Medical Imaging” Vol 3. Computational Imaging and Vision pp. 263-274 (1995).

[14] Viola P. and Wells W.M. “Alignment by maximization of mutual information” Proceedings of the 5th International Conference on Computer Vision, Cambridge MA pp.16-23 (1995).

[15] Pennec X., Cachier P. and N. Ayache “Understanding the ‘demon’s algorithm’: 3D non-rigid registration by gradient descent” Proceedings of MICCAI 1999, LNCS 1679 pp.697-606 Springer-Verlag (1999).

[16] Bookstein F. “Principle warps: thin-plate splines and the decomposition of deformations” IEEE Transactions of Pattern Analysis and Machine Intelligence **11** 567-585 (1989).

[17] Brock K.K., Balter J.M., Dawson L.A. and Kessler M.L., “Automated generation of a four-dimensional model of the liver using warping and mutual information” Med. Phys. **30** 1128-1133 (2003).

[18] Meyer C.R., Boes J.L., Kim B., Bland P.H., Zasadny K.R., Kison P.V., Koral K., Frey K.A. and R.L. Wahl “Demonstration of accuracy and clinical versatility of mutual information for automatic multimodality image fusion using affine and thin-plate spline warped geometric deformations” Medical Image Analysis **1** 195-206 (1996).

[19] Nelder J.A. and Mead R. “A simplex method for function minimization” Computer Journal **7** 308-313 (1965).

[20] Coselman M.M., Balter J.M., McShan D.L. and Kessler M.L. “Mutual information based CT registration of the lung at exhale and inhale breathing states using thin-plate splines” Med. Phys. **31** 2942-2948 (2004).

[21] Schaly B., Kempe J.A., Baumann G.S., Battista J.J. and J. Van Dyk “Tracking the dose distribution in radiation therapy by accounting for variable anatomy” Phys. Med. Biol. **49** 791-805 (2004).

[22] Schaly B., Baumann G.S., Battista J.J. and J. Van Dyk “Validation of contour-driven thin-plate splines for tracking fraction-to-fraction changes in anatomy and radiation therapy dose mapping” Phys. Med. Biol. **50** 459-475 (2005).

[23] Malsch U., Thieke C., Huber P.E. and R. Bendl "An enhance block matching algorithm for fast elastic registration in adaptive radiotherapy" Phys. Med. Biol. **51** 4789-4806 (2006).

[24] Kostelec P.J., Weaver J.B. and D.M. Healy "Multiresolution elastic image registration" Med. Phys. **25** 1593-1604 (1998).

[25] Schnabel J.A., Rueckert D., Quist M, Blackall J.M., Castellano-Smith A.D., Hartkens T., Penney G.P., Hall W.A., Liu H.L., Truwitt C.L., Gerritsen F.A., Hill D.G. and Hawkes D.J. "A generic framework for non-rigid registration based on non-uniform multi-level free-form deformations" Proceedings of MICCAI 2001, LNCS 2208 Springer-Verlag, Berlin (2001).

[26] Forsey D.R. and R.H. Bartels "Hierarchical b-spline refinement" Computer Graphics **22** 205-212 (1988).

[27] Rueckert D., Sonoda L.I., Hayes C., Hill D.L.G., Leach M.O. and Hawkes D.J. "Nonrigid registration using free-form deformations: application to breast MR images" IEEE Transactions on Medical Imaging **18** 712-721 (1999).

[28] Burden R.L. and J.D. Faires "Numerical Analysis" pp.465-480 (2001).

[29] Mattes D., Haynor D.R., Vesselle H., Lewellen T.K. and Eubank W. "PET-CT image registration in the chest using free-form deformations" IEEE Transactions on Medical Imaging **22** 120-128 (2003).

[30] Li T., Thorndyke B., Schreibmann E., Yang Y. and L. Xing "Model-based image reconstruction for four-dimensional PET" Med. Phys. **33** 1288-1298 (2006).

[31] Rohlfing T., Maurer C.R., O'Dell W.G. and J. Zhong "Modeling liver motion and deformation during the respiratory cycle using intensity-based nonrigid registration of gated MR images" Med. Phys. **31** 427-432 (2004).

[32] Rietzel E. and G.T. Chen "Deformable registration of 4D computed tomography data" Med. Phys. **33** 4423-4430 (2006).

[33] Hartkens T. "Measuring, analyzing, and visualizing brain deformation using non-rigid registration" Ph.D. thesis dissertation, University of London (2003).

[34] Ruan D., Fessler J., Roberson M., Balter J. and M. Kessler "Deformable registration using regularization that accommodates local tissue rigidity" Med. Phys. **33** 2186 (2006).

[35] Stancanello J., Berna E., Cavedon C., Francescon P., Loeckx D., Cerveri P., Ferrigno G. and G. Baselli "Preliminary study on the use of nonrigid registration for thoraco-abdominal radiosurgery" Med. Phys. **32** 3777-3785 (2005).

[36] Schreibmann E., Chen G.T.Y. and L. Xing "Image interpolation in 4D CT using a Bspline deformable registration model" Int. J. Radiat. Oncol. Biol. Phys. **64** 1537-1550 (2006).

[37] McClelland J., Blackall J.M., Tarte S., Chandler A.C., Hughes S., Ahmad S., Landau D.B. and D.J. Hawkes "A continuous 4D motion model from multiple respiratory cycles for use in lung radiotherapy" Med. Phys. **33** 3348-3358 (2006).

[38] Horn B.K.P and Schunck B.G. "Determining optical flow" Artificial Intelligence **17** 185-204 (1981).

[39] Guerrero T., Zhang G., Huang T-C. and Lin K-P. "Intrathoracic tumour motion estimation from CT imaging using 3D optical flow method" Phys. Med. Biol. **49** 4147-4161 (2004).

[40] Guerrero T., Sanders K., Castillo E., Zhang Y., Bidaut L., Pan T. and R. Komaki "Dynamic ventilation imaging from four-dimensional computed tomography" Phys. Med. Biol. **51** 777-791 (2006).

[41] Zhang G., Guerrero T., Huang T-Z., Fitzpatrick M.J., Ibbott G., Lin K-P. and G. Starkschall "3D optical flow method implementation for mapping of 3D anatomical structure contours across 4D CT data" Proceedings of the 14th Conf. on the use of Computers in Radiation Therapy, Seoul pp.356-360 (2004).

[42] El Naqa I., Low D.A., Nystrom M., Parikh P., Lu W., Deasy J.O., Amini A., Hubenschmidt J. and S. Wahab "An optical flow approach for automated breathing motion tracking in 4D computed tomography" Proceedings of the 14th Conf. on the use of Computers in Radiation Therapy, Seoul pp.74-77 (2004).

[43] Thirion J.P. "Image matching as a diffusion process: an analogy with Maxwell's demons" Medical Image Analysis **2** .243-260 (1998).

[44] Cachier P., Pennec X. and N. Ayache "Fast non rigid matching by gradient descent: study and improvements of the "Demons" algorithm" INRIA report #3706, Institut National de Recherche en Informatique et en Automatique (1999).

[45] Boldea V., Sarrut D. and S. Clippe "Lung deformation estimation with non-rigid registration for radiotherapy treatment" Proceeedings MICCAI 2003, LNCS 2878 pp.770-777, Springer-Verlag, Berlin (2003).

[46] Sarrut D., Boldea V., Ayadi M., Badel J-N., Ginestet C., Clippe S. and C. Carrie "Nonrigid registration method to assess reproducibility of breath-holding with ABC in lung cancer" Int. J. Radiat. Oncol. Biol. Phys. **61** 594-607 (2005).

[47] Sarrut D., Boldea V., Miguet S. and C. Ginestat "Simulation of four-dimensional CT images from deformable registration between inhale and exhale breathe-hold CT scans" Med. Phys. **33** 605-617 (2006).

[48] Wang H., Dong L., O'Daniel J., Mohan R., Garden A.S., Ang K.K., Kuban D.A., Bonnen M., Chang J.Y. and R. Cheung "Validation of an accelerated "demons" algorithm for deformable image registration in radiation therapy" Phys. Med. Biol. **50** 2887-2905 (2005).

[49] Wang H., Dong L., Lii M.F., Lee A., Crevoisier d R., Mohan R., Cox J.D., Kuban D. and R. Cheung "Implementation and validation of a 3-dimensional deformable registration algorithm for targeted prostate cancer radiotherapy" Int. J. Radiat. Oncol. Biol. Phys. **61** 725-735 (2005).

[50] Lu W., Chen M-L., Olivera G.H., Ruchala K.J. and T.R. Mackie "Fast free-form deformable registration via calculus of variations" Phys. Med. Biol. **49** 3067-3087 (2004).

[51] Scherzer O. and J. Weickert "Relations between regularization and diffusion filtering" J. Math. Imaging Vision **12** 43-63 (2000).

[52] Lu W., Olivera G.H., Chen Q., Ruchala K.J., Haimerl J., Meeks S.L., Langen K.M. and P.A. Kupelian "Deformable registration of the planning image (kVCT) and the daily images (MVCT) for adaptive radiation therapy" Phys. Med. Biol. **51** 4357-4374 (2006).

[53] Lu W., Olivera G.H., Chen Q., Chen M-L. and K.J. Ruchala "Automatic re-contouring in 4D radiotherapy" Phys. Med. Biol. **51** 1077-1099 (2006).

[54] Zhang T., Orton N.P. and W.A. Tome "On the automated definition of mobile target volumes from 4D-CT images for stereotactic body radiotherapy" Med. Phys. **32** 3493-3502 (2005).

[55] Gao S., Zhang L., Wang H., de Crevoisier R., Kuban D.D., Mohan R. and L. Dong "A deformable image registration method to handle distended rectums in prostate cancer radiotherapy" Med. Phys. **33** 3304-3312 (2006).

[56] Bajcsy R. and Kovacic S. "Multiresolution elastic matching" Computer Vision, Graphics, and Image Processing **46** 1-21 (1989).

[57] Gee J.C. and R.K. Bajcsy "Elastic matching: continuum mechanical and probabilistic analysis" Brain Warping A.W. Toga Ed. Academic Press, San Diego (1999)

[58] Broit C. "Optimal registration of deformed images" PhD thesis, Department of computer and information science, University of Pennsylvania, Philadelphia (1981).

[59] Christensen G.E. and H.J. Johnson "Consistent image registration" IEEE Transactions on Medical Imaging **20** 568-582 (2001).

[60] Pekar V., Gladilin E. and K. Rohr "An adaptive irregular grid approach for 3D deformable image registration" Phys. Med. Biol. **51** 361-377 (2006).

[61] Marquardt D.W. "An algorithm for least-squares estimation of nonlinear parameters" Journal of the Society for Industrial and Applied Mathematics **11** 431-441 (1963).

[62] Christensen G.E., Carlson B., Chao K.S.C., Yin P., Grigsby P.W., Nguyen K., Dempsey J.F., Lerma F.A., Bae K.T., Vannier M.W. and J.F. Williamson "Image-based dose planning of intracavitary brachytherapy: registration of serial-imaging studies using deformable anatomic templates" Int. J. Radiat. Oncol. Biol. Phys. **51** 227-243 (2001).

[63] Christensen G.E., Joshi S.C. and M.I. Miller "Volumetric transformation of brain anatomy" IEEE Transactions on Medical Imaging **16** 864-877 (1997).

[64] Christensen G.E., R.D. Rabbitt and M.I. Miller "Deformable templates using large deformation kinematics" IEEE Transactions on Image Processing **5** 1435-1447 (1996).

[65] Christensen G.E., Rabbitt R.D. and M.I. Miller "3D brain mapping using a deformable neuroanatomy" Phys. Med. Biol. **39** 609-618 (1994)

[66] Keall P.J., Joshi S., Vedam S.S., Siebers J.V., Kini V.R. and R. Mohan "Four-dimensional radiotherapy planning for DMLC-based respiratory motion tracking" Med. Phys. **32** 942-951 (2005).

[67] Foskey M., Davis B., Goyal L., Changs S., Chaney E., Strehl N., Tomei S., Rosenman J. and S. Joshi "Large deformation three-dimensional image registration in image-guided radiation therapy" Phys. Med. Biol. **50** 5869-5892 (2005).

[68] Pevsner A., Davis B., Joshi S., Hertanto A., Mechalakos J., Yorke E., Rosenzweig K., Nehmeh S., Erdi Y.E. Erdi, Humm J.L., Larson S., Ling C.C. and G.S. Mageras "Evaluation of an automated deformable image matching method for quantifying lung motion in respiration-correlated CT images" Med. Phys. **33** 369-376 (2006).

[69] Joshi S.C. and M.I. Miller "Landmark matching via large deformation diffeomorphisms" IEEE Transactions on Image Processing **9** 1357-1370 (2000).

[70] Yan D., Jaffray D.A. and J.W. Wong "A model to accumulate fractionated dose in a deforming organ" int. J. Radiat. Oncol. Biol. Phys. **44** 665-675 (1999).

[71] Bharatha A., Hirose M., Hata N., Warfield S.K., Ferrant M., Zou K.H., Suarez-Santana E., Ruiz-Alzola J., D'Amico A., Cormack R.A., Kikinis R., Jolesz F.A. and C.M.C. Tempany "Evaluation of three-dimensional finite element-based deformable registration of pre- and interaoperative prostate imaging" Med. Phys. **28** 2551-2560 (2001)

[72] Liang J. and D. Yan "Reducing uncertainties in volumetric image based deformable organ registration" Med. Phys **30** 2116-2122 (2003)

[73] Chi Y., Liang J. and D. Yan "A material sensitivity study on the accuracy of deformable organ registration using linear biomechanical models" Med. Phys. **33** 421-433 (2006).

[74] Kim S., Jaffray D.A. and K.K. Brock "The effect of heterogeneous and nonlinear material properties on organ deformation" Med Phys. **32** 2143 (2005).

[75] Brock K.K., Sharpe M.B., Dawon L.A., Kim S.M. and D.A. Jaffray "Accuracy of finite element model-based multi-organ deformable image registration" Med. Phys. **32** 1647-1659(2005).

[76] Brock K.K., Hollister S.J., Dawson L.A. and J.M. Balter "Creating a four-dimensional model of the liver using finite element analysis" Med. Phys. **29** 1403-1405 (2002).

[77] Brock K.K., Dawson L.A., Sharpe M.B., Moseley D.J. and D.A. Jaffray "Feasibility of a novel deformable image registration technique to facilitate classification, targeting and monitoring of tumor and normal tissue" Int. J. Radiat. Oncol. Biol. Phys. **64** 245-1254 (2006).

[78] Tanner C.,Schnabel J.A., Hill D.L.G., Hawkes D.J., Leach M.O. and D.R. Hose "Factors affecting the accuracy of biomechnical breast models" Med. Phys. **33** 1758-1769 (2006).

[79] Low D.A., Harms W.B., Mutic S. and J.A. Purdy "A technique for the quantitative evaluation of dose distributions" Med. Phys. **25** 656-661 (1998).

[80] Brock K., Moseley J. and D. Jaffray "A novel metric for automatic assessment of deformable image registration accuracy" Med. Phys. **32** 1942 (2005).

[81] Remeijer P., Rasch C., Lebesque J.V. and M. van Herk "A general methodology for three-dimensional analysis of variation in target volume delineation" Med. Phys. **26** 931-940 (1999).

[82] Kerdok A.E., Cotin S.M., Ottensmeyer M.P., Galea A., Howe R.D. and S.L. Dawson "TruthCube: establishing physical standards for real time soft tissue simulation" Int. Workshop on deformable modeling and soft tissue simulation, Bonn, Germany (2001).

[83] Lu W. "Motion detection and correction for image guided radiation therapy" PhD Thesis University of Wisconsin-Madison (2001).

[84] Kashani R., Lam K., Litzenberg D. And J. Balter "Technical note: a deformable phantom for dynamic modeling in radiation therapy" Med. Phys. **34** 199-201 (2007).

[85] Segars W.P, Lalush D.S. and B.M.W. Tsui, "Modeling respiratory mechanics in the MCAT and spline-based MCAT phantoms," IEEE Trans. Nucl. Sci. **48** 89-97 (2001).

[86] Segars W.P., "Development and application of the new dynamic nurbs-based cardiac-torso (NCAT) phantom," PhD. dissertation, University of North Carolina (2001).

[87] Guerrero T., Zhang G., Segars W., Huang T-C., Bilton S., Ibbott G., Dong L., Forster K. and K.P. Lin "Elastic image mapping for 4-D dose estimation in thoracic radiotherapy" Radiation Protection Dosimetry **115** 497-502 (2005).

# Chapter 5:

# A direct voxel tracking method for 4-dimensional Monte Carlo dose calculations in deforming anatomy

## 5.1 INTRODUCTION

In this chapter we discuss the limitations of current 4D Monte Carlo dose calculation methods and present an alternative algorithm based on the EGSnrc/DOSXYZNRCNRC Monte Carlo dose calculation code. In this method, the same dose calculation grid is used for estimation of the dose received at each breathing phase. The dose calculation grid is deformed using the deformation vectors obtained from non-linear image registration. A procedure for validation of this 4D dose calculation method in simple deforming phantoms is presented.

The study presented in this chapter was previously published as the following paper "A direct voxel tracking method for four-dimensional Monte Carlo dose calculations in deforming anatomy" E. Heath and J. Seuntjens, Med. Phys. **33** 434-445 (2006).

## 5.2 LIMITATIONS OF CURRENT DOSE WARPING METHODS

Deformable dose calculation methods attempt to account for breathing motion effects by explicitly calculating the dose distribution received at intermediate phases of motion. For example, in the case of a lung treatment, 10 phases within the breathing cycle might be sampled. In order to determine the contribution of dose accumulated at these different geometries to the overall dose it is necessary to re-map the dose at each phase to a reference anatomy. To do this the correspondence between voxels at intermediate phase and the reference phase must be determined. Non-linear image registration algorithms produce a three-dimensional map of deformation vectors which describe the transformation required to map a source image to a target anatomy. Dose re-mapping methods using non-linear image registration have been reported in the literature, the

simplest approach being the center-of-mass (COM) remapping method which assumes a one-to-one correspondence between undeformed voxels at different phases. The deformation vectors are used to determine the new reference voxel indices to which the dose is translated[1,2]. However, the effect of applying these deformation vectors is to deform the voxels of the source image and, in the case of large deformations, the re-mapped, undeformed reference voxels do not necessarily exactly overlap the voxels of the dose grid at the phase from which the dose is to be remapped (see Figure 1). In such a situation it is incorrect to assume that the dose contribution to voxel *(i,j,k)* of the reference grid arises solely from the voxel *(i',j',k')* of the dose grid at phase *T* which contains the remapped dose point. Such deformations may occur in the thorax where the lung volume has been measured to change by 20% with normal respiration[3].

Such changes in volume imply that a one- to-one correspondence between the voxels in images at different respiratory phases does not necessarily exist. A more accurate estimate of the remapped dose can be obtained by tri-linear interpolation of dose from voxels in the vicinity of the transformed centre of mass of the reference voxel[4,5]. Rosu *et al.*[6] suggested refining this tri-linear interpolation method by sub-dividing voxels to improve the resolution of re-mapped dose points.

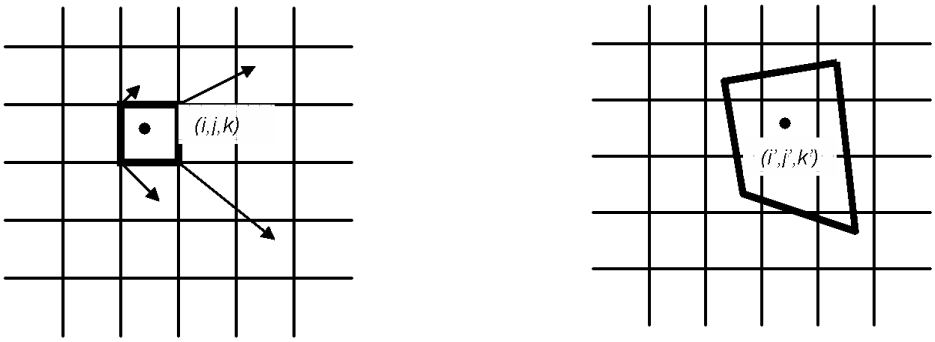


Figure 1: Illustration of possible voxel deformations which occur when remapping dose to a reference phase. Using deformation vectors relating the reference anatomy to the anatomy at phase *T* the center of mass of voxel (*i,j,k*) of the reference phase is mapped to voxel (*i',j',k'*) at phase *T*. Assuming a one-to-one voxel correspondence only the dose in voxel *(i',j',k')* at *T* will contribute to the dose in voxel *(i,j,k)* at the reference phase.

Any form of dose interpolation provides only an approximation of the remapped dose and the accuracy of such methods in regions of large dose gradients remains uncertain. Furthermore, these methods ignore the changes in voxel density which must occur as voxels are deformed if mass is conserved and, as different dose grids are used at each phase, preservation of tissue type on a voxel-by-voxel basis is also neglected. Therefore the accuracy of these techniques in regions of large deformations may also be limited.

## 5.3 MATERIALS AND METHODS

### 5.3.1 Proposed 4D Monte Carlo dose calculation method

The accuracy of 4D dose calculation methods could be improved if the dose distribution obtained on a phase of interest could be exactly remapped back to the reference phase. There are two possible approaches to this. The first would be to calculate a deposited energy per voxel on the phase of interest and then remap this to the reference grid, dividing by the mass of the reference voxels to obtain the remapped dose distribution. However, in order to accurately calculate the contributions of remapped dose to the reference grid the fractional overlap of the deformed voxels on the reference grid must be known. Methods for determining the volume overlap of non-rectangular voxels on a rectangular grid are very computationally expensive and may not be practical.

A second method would be to retain the same reference dose grid for calculation of the dose at the phase of interest but to deform these voxels to match the anatomy at different phases of the respiratory cycle. The voxel deformations would be obtained from deformation vectors resulting from non-linear image registration of the anatomy at inhalation to the exhalation (reference) phase. In this method energy deposition and hence, the dose distribution is exactly remapped to the reference phase. As voxel densities are adjusted as they deform, the total energy deposited in the phantom at a given phase is therefore inherently conserved when remapped to the reference phase.

We chose to implement a 4D Monte Carlo dose calculation algorithm based on this second approach. For this purpose we modified the EGSnrc/DOSXYZNRCnrc[7] Monte Carlo user code to perform particle transport in deforming voxels.

### 5.3.2 EGSnrc Monte Carlo code

The Electron Gamma Shower (EGS)[8] Monte Carlo code was initially developed at the Stanford Linear Accelerator for simulation of the interactions of high energy electrons. The code was later modified for applications to Medical Physics with the inclusion of low energy physics, simulation of photon interactions and improved transport and boundary crossing algorithms[9-12]. Based on this updated EGSnrc code, the BEAMnrc code[13] was subsequently developed for simulation of radiation beams produced in medical linear accelerators.

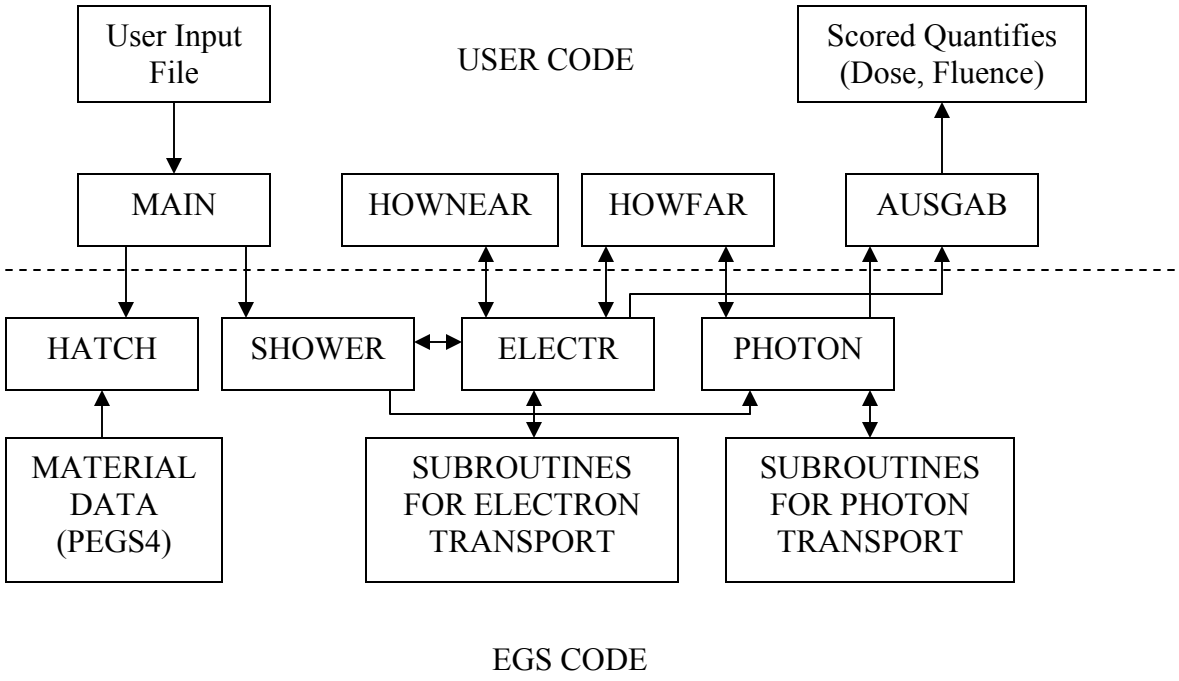


Figure 2: Structure of the EGSnrc Monte Carlo code [adapted from reference 11].

The EGSnrc code is written in MORTRAN which is a FORTRAN pre-processor code. The code structure, shown in Figure 2, is designed for easy modification by the user. The particle transport subroutines are contained within the main EGS code while the simulation geometry and quantities to be scored are specified by the user in the HOWNEAR, HOWFAR and AUSGAB subroutines in a separate *user code*. These user codes also interact with the HATCH and SHOWER subroutines of the EGS code which define properties of all materials in the simulation geometry and initialize particles for

transport, respectively. The latter can obtain particles from a built-in source type (i.e., isotropic point source, rectangular uniform source) or from a *phase space file* which contains the charge, energy, location and trajectory of particles generated from a BEAMnrc simulation of the treatment unit. The HOWFAR and HOWNEAR geometry checking routines[14] are used to determine if a particle will cross a subregion boundary on a particle transport step. Specifically, the HOWFAR subroutine calculates the distance to the nearest boundary along the current particle's trajectory while the HOWNEAR subroutine calculates the nearest perpendicular distance. The HOWFAR subroutine is used by the photon transport subroutine. The HOWNEAR subroutine is used by the PRESTA-I (Parameter Reduced Electron Step Transport Algorithm) electron transport algorithm but if the EXACT boundary crossing algorithm is used then at a specified distance to a region boundary the electron transport switches to single scattering mode and the HOWFAR subroutine is used to find the distance to the boundary.

The DOSXYZNRCnrc[7] Monte Carlo dose calculation code is an EGSnrc user code which simulates the transport of particles and scores their dose deposition in a Cartesian geometry. For calculation of dose deposition in a patient, a voxelized representation of the patient's geometry must be specified in an input *egsphant* file containing the dimensions, material and density of each voxel. This file is generated from patient CT images and a CT-to-electron density calibration curve. Material specification tables with known ranges of electron density ranges for different patient tissues are used to assign a material type to each voxel. The boundary checking process in DOSXYZNRCnrc is as follows. The HOWFAR subroutine is called for the current particle which is about to be transported by a distance USTEP, the straight line distance to the next interaction. The current voxel coordinates of a particle are determined based on its region number. The distance from the particle's current position to each of the 6 voxel faces is calculated. The minimum distance is then compared to USTEP to determine if the particle is to be transported to a new voxel or if it undergoes an interaction within the current voxel.

### 5.3.3 defDOSXYZNRC code

The EGSnrc/DOSXYZnrc[7,12] (NRCC, Ottawa) user code was modified to perform particle transport in deformed voxels as summarized in Figure 3(a). During initialization

of a simulation, the deformation vectors are read in and the volume of each deformed voxel is calculated by subdividing each voxel into 6 pyramids and calculating each sub-volume. Voxel densities obtained from the reference CT image are then modified to preserve the total voxel mass. These modified densities are used by the particle transport routines of EGSnrc. The geometry checking subroutines, HOWFAR and HOWNEAR, were modified to calculate distance from the current particle position to the nearest boundary in non-rectangular voxels. Voxel faces are sub-divided into 2 planes which are each defined by 3 nodes (see Figure 3(b)) as deformations may cause 4 nodes defining a voxel face to become non-coplanar. Based on the deformed nodes of the current voxel the distance either along the current trajectory (HOWFAR) or along a normal vector to plane (HOWNEAR) is calculated for all 12 planes. Planes to which the particle runs parallel to or away from are neglected.

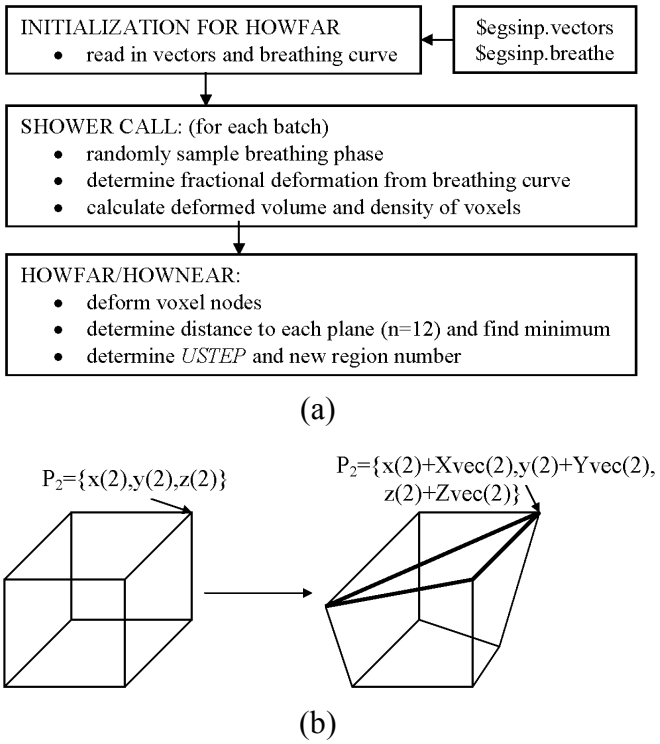


Figure 3: (a) Summary of modifications made to DOSXYZNRCnrc code. Nomenclature refers to the names of various subroutines in EGSnrc. (b) Plane definitions for deformed voxels.

Because the calculation of distance to a plane assumes infinite extent, it is necessary to test if the intersection point lies within the plane bounded by the three nodes. This was determined by comparing, at each node of the plane, the cross-product of the vectors formed by the intersection point and the adjacent node to the normal vector for the plane. If the intersection point is outside the plane bounded by the three nodes then the cross-product and normal vector will be at 180° with respect to each other for one of the plane nodes (see Figure 4). As this method involves only multiplication, it is fairly computationally efficient.

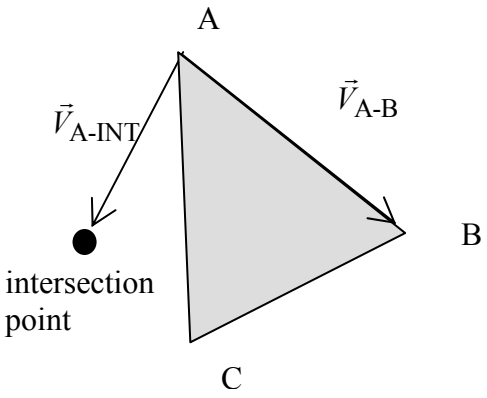


Figure 4. Method of testing if an intersection point lies on the plane bounded by points A,B,C. When testing node A, the cross-product formed the vectors $\vec{V}_{\text{A-B}}$ X $\vec{V}_{\text{A-INT}}$ is into the page, while the normal vector of the plane is out of the page.

From the true intersection points the minimum distance and corresponding plane number are determined. This is compared with the distance to the nearest interaction (USTEP) proposed by EGSnrc and in the case that the distance to the nearest plane is smaller, the new region number to which the particle is transported is determined based on the plane it intersects. Upon completion of a simulation, the energy deposited in each voxel is then divided by mass of the voxel to obtain the cumulative reference dose.

To initially determine the region number there must be a layer of undeformed voxels around the phantom through which particles pass. Therefore an additional shell of voxels is added to the phantom and the corresponding null vectors must be added to the deformation vectors matrix.

Automated accumulation of the dose received at multiple anatomical states is possible by randomly sampling the deformation vectors during the simulation from a

table describing fractional displacements as a function of breathing phase (indicated as $egsinp.breathe in Figure 3). As updating the geometry on each incident history can be time consuming the sampling can be implemented on a batch-by-batch basis where a number of histories are run for each geometry. Such a batch by batch vector-resampling may, at a later stage, also provide options for statistically optimizing the simulation as not all phases in the breathing cycle equally contribute to dose in the outlined volumes. However, enough samples to sufficiently reconstruct the breathing curve must be obtained. A measured breathing curve or an analytical model[15] is required for sampling the deformations. This approach assumes that intermediate displacements can be linearly and uniformly interpolated from the exhale-to-inhale displacements. This is not necessarily accurate, especially when hysteresis exists. A better method would be to parameterize the displacement vectors as a function of phase, as proposed by McClelland *et al.*[16]. However, their method was based on a B-spline algorithm which had a relatively sparse grid of control points (17x17 per slice) compared to our case where deformation vectors are estimated at a resolution equal to the dose grid resolution (typically128x128 per slice).

### 5.3.4 Validation

Calculations with the new defDOSXYZNRC code were initially tested with no deformations against calculations using DOSXYZNRCnrc. In the absence of deformation vectors the two dose calculations are expected to be identical to within the stochastic uncertainty of the Monte Carlo calculation.

The voxel deformation method was tested by comparing calculations in a static phantom with a second deforming phantom whose internal or external boundaries were deformed to match those of the static phantom. In the first test the deforming phantom consisted of two voxels whose inner boundary was deformed (see Figure 5 (a) and (b)). The dose in each voxel of both the static and deforming phantoms was calculated for a 1x1 $cm^2$ parallel beam of 6 MeV photons incident in the +z direction. In the second test a 6x6x6 $cm^3$ tissue phantom consisting of 1x1x1 $cm^3$ voxels was deformed to 6x6x3 $cm^3$ along the direction of the beam axis (see Figure 5 (c) and (d)). Dose profiles were calculated for a 2x2 $cm^2$ parallel beam of 2 MeV photons incident in the +z direction. The

dose profiles were compared with profiles in a static phantom with the same dimensions as the deformed phantom. In both cases the initial density of the voxels of the deforming phantom was chosen so that the density of the deformed voxels would match the density of the corresponding voxels in the static phantom.

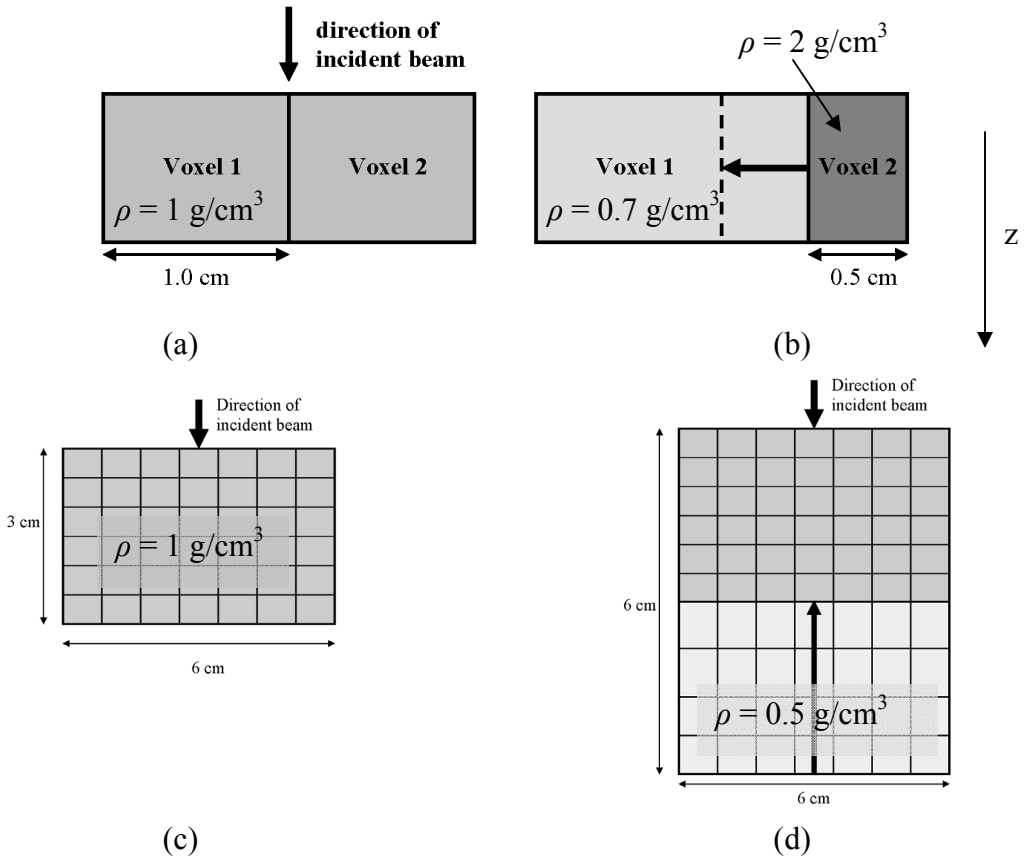


Figure 5: Geometry of deformation phantoms used for consistency check: (a) Test 1: static phantom (b) Test 1: deforming phantom with changing internal boundaries only (c) Test 2: static phantom (d) Test 2: deforming phantom where dimension along beam axis is compressed from 6 cm to 3 cm. The density of the deformed phantoms matches that of the static phantoms.

Another method used to test the internal consistency of the deforming voxel technique was to regenerate primary photons upon each interaction. The Fano theorem[17] states that under conditions of charged particle equilibrium the electron fluence is

independent of density variations. Therefore, if the primary photon fluence is constant, the deformations should have no effect on the dose in a phantom regardless of the deformation of any boundaries. The AUSGAB scoring subroutine was modified to discard scattered photons after interactions, regenerate the original photon and place it on the transport stack. Scattered electrons are also transported. The net result of all this is to create an equilibrium electron fluence throughout the deforming structure. Dose calculations were performed on a 5.5x5.5x16 $cm^3$ water phantom consisting of 0.5x0.5x0.5 $cm^3$. The phantom is surrounded by air. Only a column of 3x3 voxels centered on the beam axis undergo deformations. Each of the first 4 layers of voxels expand to 1 cm along the z direction, the next 6 layers are compressed to 0.375 cm and the next 4 layers are compressed to 0.25 cm along the z direction (see Figure 6). The outer phantom dimensions remain unchanged. Dose profiles in the deformed phantom were calculated with and without photon regeneration for a 4x4 $cm^2$ pencil beam of 2 MeV photons incident along the +z direction.

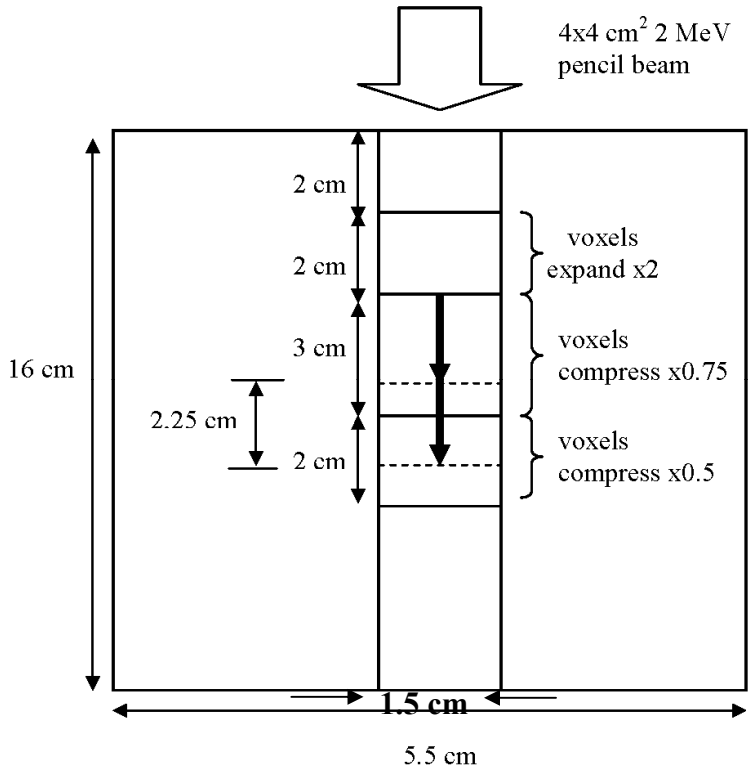


Figure 6. Phantom for testing internal consistency of voxel deformation technique.

## 5.4 RESULTS

### 5.4.1 Comparison with DOSXYZNRCnrc

A comparison of dose profiles calculated with DOSXYZNRCnrc and defDOSXYZNRC, with zero deformation vectors, is shown in Figure 7. Both calculations were performed with identical transport parameters. To simulate 100 million histories, the DOSXYZNRCnrc calculation required 4.1 hrs on a 1.7 GHz Pentium M processor. The defDOSXYZNRC calculation time was approximately 4 times longer. The average statistical uncertainty on the dose profiles shown in Figure 7 is 1%. The two calculations agree within 1%, on average, indicating that the modifications to DOSXYZNRCnrc have not introduced any statistically significant errors in particle transport in absence of deformations.

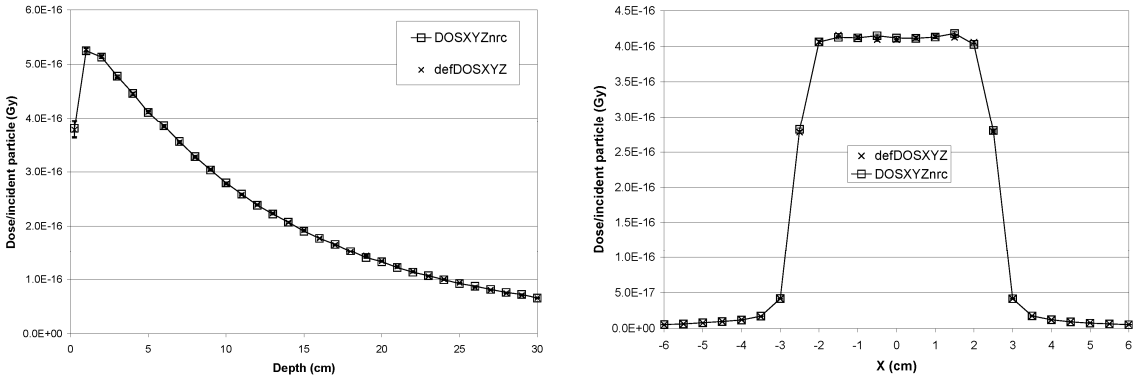


(a) (b)

Figure 7: Comparison of defDOSXYZ (without deformations) and DOSXYZnrc calculations in water phantom with 6 MV 10x10 $cm^2$ phase space (100 million histories) for (a) depth dose profiles at x=0 y=0 and (b) lateral profile at depth=5 cm.

### 5.4.2 Validation in simple deforming phantoms

#### *5.4.2.1 Phantom with internal boundary deformations*

The ratio of the dose in each voxel of the deforming phantom (shown in Figure 5 (a) and (b)), before and after deformations are applied, to the dose in corresponding voxel of the static phantom is reported in Table 1. Before the internal boundary deformations are applied the dose in the deformed phantom is lower than that of the static phantom due to differences in voxel density and dimensions. When deformations are applied to match

the deformed phantom boundaries to the static phantom the defDOSXYZNRC code reproduces the dose in the static phantom to within 1%.

Table 1: Ratio of dose in deformed phantom to static phantom (internal deformations)

| Phantom | Dose ratio in Voxel 1 | Dose ratio in Voxel 2 |
|---|---|---|
| before deformation | 0.87 ± 0.01 | 0.096 ± 0.002 |
| after deformation | 1.00 ± 0.01 | 0.992 ± 0.006 |

### *5.4.2.2 Phantom with external boundary deformations*

Dose profiles calculated in the phantom with external boundary deformations with and without deformations are shown in Figure 8. The average statistical uncertainty of the dose points is 1%. The defDOSXYZNRC calculation with deformations exactly reproduces the dose in the static phantom as calculated with DOSXYZNRCnrc. Therefore dose calculations within deforming phantoms were deemed to be accurate to within 1%.

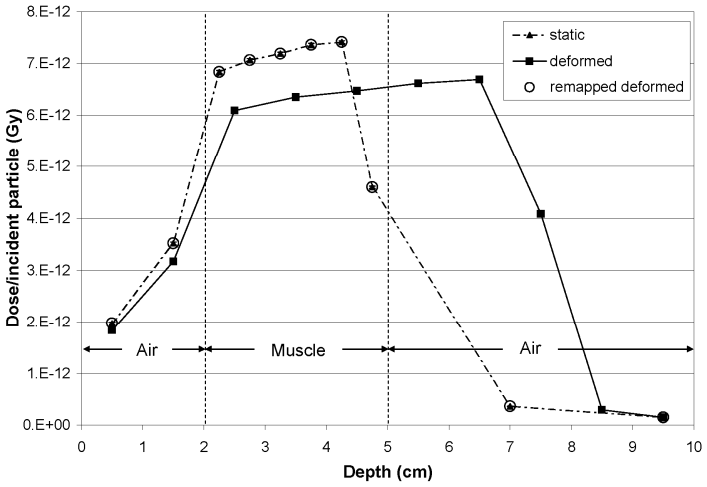


Figure 8. Comparison of central axis depth dose profiles in deformed and static phantoms for a 2x2 $cm^2$ incident beam of 2 MeV photons (10 M histories). "Deformed" refers to DOSXYZnrc calculations in the deforming phantom before deformations are applied. "Remapped deformed" refers to the defDOSXYZ calculation in the deforming phantom where deformations which map external boundaries to those of static phantom have been applied.

### 5.4.3 Internal consistency check using photon regeneration

A comparison of dose profile calculations in a phantom with internal deforming boundaries, with and without photon regeneration, is shown in Figure 9. A 4x4 $cm^2$ pencil beam of 2 MeV photons was incident on the phantom from the +z direction. With

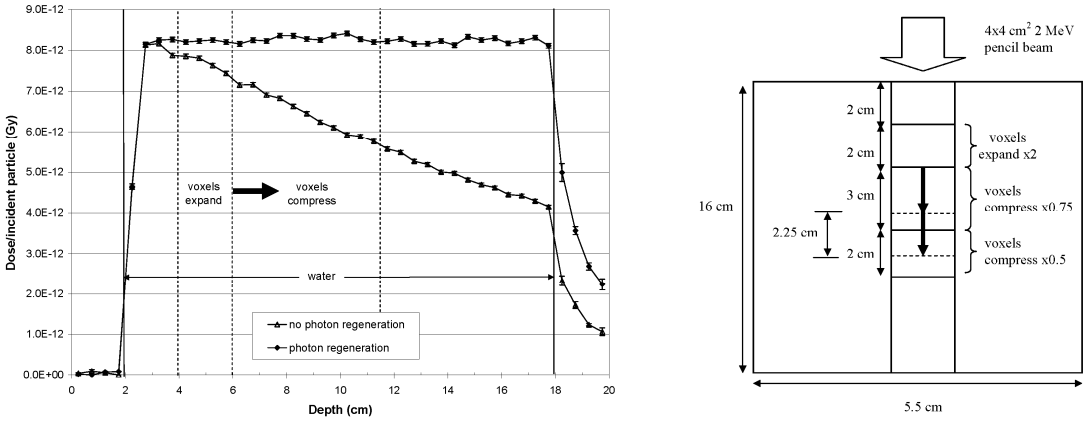


(a) (b)

Figure 9: (a) Depth dose profiles calculated with defDOSXYZ in deforming phantom with and without photon regeneration. (b) Geometry of deforming phantom in which a central column of voxels are alternately expanded and compressed.

photon regeneration the effects of the deformations are not apparent, therefore we have confidence that particle transport is correctly performed with the deforming boundaries.

## 5.5 DISCUSSION

Using the voxel deformation dose calculation method mass is conserved during the deformation process. Therefore we are calculating energy deposition in a conserved amount of tissue or material. In contrast to current dose remapping methods, the deformable dose calculation method provides a natural and accurate way to construct dose mass histograms[18] and the use of the latter concept for plan evaluation of time dependent treatment planning dose calculations should be investigated.

The current implementation assumes that a continuous deformation field can be obtained from non-linear registration. The continuity of voxel deformations is required to

determine the new region number when particles are transported across a deformed voxel boundary. However in the thorax it is known that the chest wall remains relatively stationary while the lungs slide along a thin membrane. Therefore modifications may be required to allow voxel faces which are shared by two voxels to be dislocated in such discontinuous regions.

A drawback of the current implementation of defDOSXYZ is the increased calculation time compared to the DOSXYZnrc code, approximately 4 times longer for the phantom geometries used in this validation study. This increase in calculation time is attributed to two main reasons: (1) a doubling of the number of planes defining a voxel thus doubling the number of distance to plane calculations to be performed on each particle transport step; and (2) additional coding to test particle-plane intersection points. There a number of ways to reduce the calculation time. For example, a more efficient coding which reduces the number of calculation steps could be implemented. Furthermore, by using knowledge of the previous plane that was crossed when entering the current voxel, the number of distance to plane calculations could be reduced. Variance reduction methods[19], which increase the efficiency of Monte Carlo simulations, can also be used to reduce defDOSXYZ simulation times.

## 5.6 SUMMARY

In this chapter we presented the development of an in principle exact method for the calculation of dose in deforming anatomy where incident particle trajectories and dose deposition are tracked in deforming voxels. The modified version of DOSXYZnrc, termed defDOSXYZ, was validated and calculations were found to be accurate to within 1% of the local dose. A comparison with conventional dose remapping methods is required to determine what clinical impact the approximations introduced by these 4D dose calculation methods may have on determination of the cumulative dose.

## 5.7 REFERENCES

[1] Paganetti H., Jiang H., Adams J.A., Chen G.T. and E. Rietzel, “Monte Carlo simulations with time-dependent geometries to investigate effects of organ motion

with high temporal resolution," Int. J. Radiat. Oncol. Biol. Phys. **60** 942-950 (2004).

[2] Brock K.K., McShan D.L., Ten Haken R.K., Hollister S.J., Dawson L.A. and J.M. Balter, "Inclusion of organ deformation in dose calculations," Med. Phys. **30** 290-295 (2003).

[3] Keall P.J., Starkschall G., Shukla H., Forster K.M., Ortiz V., Stevens C.W., Vedam S.S., George R., Guerrero T. and R. Mohan, "Acquiring 4D thoracic CT scans using a multislice helical method," Phys. Med. Biol. **49** 2053-2067 (2004).

[4] Schaly B., Kempe J.A., Bauman G.S., Battista J.J. and J. Van Dyk, "Tracking the dose distribution in radiation therapy by accounting for variable anatomy," Phys. Med. Biol. **49** 791-805 (2004).

[5] Keall P.J., Siebers J.V., Joshi S. and R. Mohan, "Monte Carlo as a four-dimensional radiotherapy treatment-planning tool to account for respiratory motion," Phys. Med. Biol. **49** 3639-3648 (2004).

[6] Rosu R., Chetty I., Balter J., Kessler M., McShan D. and R. Ten Haken, "Dose reconstruction in deforming anatomy: Dose grid size effects and clinical implications," Med. Phys. **32** 2487-2495 (2004).

[7] Walters B., Kawrakow I. and D.W.O. Rogers, "DOSXYZ Users Manual," NRCC Report PIRS-794revB (2005).

[8] Nelson W.R., Hirayama J. and D.W.O Rogers, "The EGS4 code system," Stanford Linear Accelerator Report SLAC-265 (1985).

[10] Bielajew A.F., Hirayama H., Nelson W.R. and D.W.O. Rogers "History, overview and recent improvements of EGS4," NRCC Report PIRS-0436, NRCC Canada (1994).

[11] Kawrakow I., "Accurate condensed history Monte Carlo simulation of electron transport. I EGSnrc, the new EGS4 version," Med Phys **27**, 485 – 498 (2000).

[12] Kawrakow I. and D.W.O. Rogers, "The EGSnrc Code System: Monte Carlo Simulation of Electron and Photon Transport," NRCC Reports PIRS-701, NRC Canada (2001).

[13] Rogers D.W.O., Faddegon B.A., Ding G.X., Ma C.M. and J. We, "BEAM: A Monte Carlo code to simulate radiotherapy treatment units", Med. Phys. **22** 503–524 (1995).

[14] Bielajew A.F., "HOWFAR and HOWNEAR: Geometry Modeling for Monte Carlo Particle Transport," NRCC Reports PIRS-0341 (1995).

[15] Lujan A.E., Balter J.M. and R.K. Ten Haken, "A method for incorporating organ motion due to breathing into 3D dose calculations in the liver: sensitivity to variations in motion," Med. Phys. **30** 2643-2649 (2003).

[16] McClelland J., Blackall J.M., Tarte S., Chandler A.C., Hughes S., Ahmad S., Landau D.B. and D.J. Hawkes "A continuous 4D motion model from multiple respiratory cycles for use in lung radiotherapy" Med. Phys. **33** 3348-3358 (2006).

[17] Fano U., "Note on the Bragg-Gray cavity principle for measuring energy dissipation," Radiat. Res. **1** 237 (1954).

[18] Nioutsikou E., Webb S., Panakis N., Bortfeld T. and U. Oelfke "Reconsidering the definition of a dose-volume histogram" Phys. Med. Biol. L17-9 (2005).

[19] Rogers D.W.O. and A.F. Bielajew "Monte Carlo techniques of electron and photon transport for radiation dosimetry" The Dosimetry of Ionizing Radiation Chapt. 5 Vol III (1990).

# Chapter 6:

# Quantification of accuracy of the Automated Nonlinear Image Matching and Anatomical Labeling (ANIMAL) non-linear registration algorithm for 4D CT images of lung

## 6.1 INTRODUCTION

In this chapter the ANIMAL non-linear image registration algorithm and its application to registration of 4D CT thoracic images for 4D Monte Carlo dose calculations is described. First, the features of the ANIMAL code and the various registration parameters which control the recoverable deformation field are presented. The concept of deformation vector discontinuities is then introduced and modifications to the ANIMAL code which minimize the incidence of these discontinuities are described.

A procedure for patient-specific optimization of registration parameters is described as well as three methods for evaluation of registration accuracy. A study of optimized registration parameters and the resulting accuracy for 5 lung patients is presented.

Finally, the issue of a further investigation of the use of tissue-dependent deformation stiffness factors is presented in an effort to obtain physically realistic deformations from non-linear image registration.

Some aspects of the work presented in this chapter was previously published as the following paper "Quantification of accuracy of the automated nonlinear image matching and anatomical labeling (ANIMAL) nonlinear registration algorithm for 4D CT images of lung" E. Heath, D.L. Collins, P.J. Keall, L. Dong and J. Seuntjens, Med. Phys. **34** 4409-4421 (2007).

## 6.2 ANIMAL NON-LINEAR IMAGE REGISTRATION ALGORITHM

### 6.2.1 Previous work with ANIMAL

The ANIMAL (Automated Nonlinear Image Matching and Anatomical labeling) non-linear registration algorithm was developed by Collins *et al.*[1,2,3] for automated segmentation of 3D MR images of brain by registration of a subject brain to a labeled stereotaxic atlas. With this method, previously labeled structures on the atlas can be transferred to the subject brain. The recovered deformation fields can also be used to quantify anatomic variability among the subjects to be registered. Registration of a subject (source) brain to a model (target) brain was iteratively refined using a multiresolution method where the image blurring and deformation grid size were reduced after each registration step.

In an initial study[2] the accuracy of non-linear registration was evaluated by comparing automated and manual segmentations of structures in a simple ellipsoid brain phantom, a more complex digital brain phantom and 11 normal volunteers. In the first two studies the phantom images were deformed by a known thin-plate spline warp. The percentage volume difference as well as volume overlap of the true and segmented structures was evaluated. For the simple brain phantom a structure overlap of better than 99% was achieved. This was reduced to 97% for the digital brain phantom and 87% for the human MRI data. A further study[3] evaluated the registration accuracy by comparing a recovered transformation to a known deformation for a human brain image. An rms error of 2 mm was reported for recovery of deformation of up to 19.7 mm.

### 6.2.2 Characteristics of ANIMAL registration algorithm

The ANIMAL code recovers a 3D mesh of deformation vectors which match as closely as possible a source image *S* to a target image *T*. Displacements *d* at each node of the deformation lattice are determined independently using 3D simplex optimization[4] which minimizes an objective function $S(I_s, I_t; \boldsymbol{N})$ (Equation 1a) consisting of an image similarity function $R(I_s, I_t; \boldsymbol{N}, \vec{x})$ and a cost function $C(\boldsymbol{N}, \vec{x})$ (Equation 1b). A number of voxel intensity-based similarity functions are available within the ANIMAL code including: image difference; sum of squared image difference; normalized cross-correlation; and the correlation coefficient. It is also possible to use image intensity

gradient data as an additional feature volume with the cross-correlation similarity function. The relative importance of the cross-correlation of gradient images in the overall objective function is determined by a weighting factor which is greater than 1. In this work we used the correlation coefficient of image intensities (Equation 1c) as a similarity function:

$$S(I_S, I_t; \boldsymbol{N}) = \frac{1}{n} \sum_{\vec{x} \in L} \left[ \alpha R(I_s, I_t; \boldsymbol{N}, \vec{x}) + (1-\alpha) C(\boldsymbol{N}, \vec{x}) \right] \quad , \qquad 1(a)$$

$$C(\boldsymbol{N}, \vec{x}) = \begin{cases} \dfrac{0.2 d^{3/2}}{d_{\max}^3 - d^{3/2}} & \text{if} \quad d^{3/2} \le d_{\max}^3 \\ \infty & \text{otherwise} \end{cases} \quad , \qquad 1(b)$$

$$R(I_s, I_t; \boldsymbol{N}, \vec{x}) = \frac{\sum_{v \in V_{\vec{x}}} I_s(v) I_t(\boldsymbol{N}(v)) - \overline{I}_s(v) \overline{I}_t(\boldsymbol{N}(v))}{\sqrt{\left[ \sum_{v \in V_{\vec{x}}} (I_s(v))^2 - \overline{I}_s(v) \overline{I}_t(\boldsymbol{N}(v)) \right] \left[ \sum_{v \in V_{\vec{x}}} (I_t(\boldsymbol{N}(v)))^2 - \overline{I}_s(v) \overline{I}_t(\boldsymbol{N}(v)) \right]}} \quad . \qquad 1(c)$$

In these equations $\boldsymbol{N}$ is the non-linear transformation between the source and target images and $\vec{x}$ represents the $n$ nodes of the deformation lattice $L$. The behavior of the cost function $C(\boldsymbol{N}, \vec{x})$, an empirically determined function, is very flat until the displacement $d$ approaches $d_{max}$, the 3D spacing of the undeformed deformation lattice nodes. Therefore only deformations approaching $d_{\max}$ are penalized. The constant factor of 0.2 in equation 1(c) was chosen by trial and error to avoid over-penalizing small deformations[1]. The image similarity function $R(I_s, I_t; \boldsymbol{N}, \vec{x})$ is based on maximizing the correlation coefficient of the source image intensities $I_s(v)$ and the corresponding target image intensities $I_t(\boldsymbol{N}(v))$ over $n$ samples in a local sublattice of elements $v \in V_{\vec{x}}$ in the vicinity of each node $\vec{x}$. The relative importance of image similarity versus the extent to which large deformations are constrained is determined by the similarity-cost ratio α as shown in Equation 1(a).

### 6.2.3 Registration parameters

The ANIMAL code is highly flexible due to the large number of registration parameters that can be varied including: deformation lattice spacing, *lattice diameter (LatDia)*, *sublattice (SubLat)*, *iteration weight (IW)*, and *smoothing weight (SW)*.

The deformation lattice spacing defines not only the resolution of the recovered deformable field but also the radius of the 3D simplex, therefore limiting the amount of deformation that can be recovered on a single iteration of the registration optimization. The user-specified lattice spacing is super-sampled by a factor of two prior to estimation of deformations. The *lattice diameter* and *sublattice* parameters are related to the evaluation of the image similarity as illustrated in Figure 1. The *lattice diameter* defines

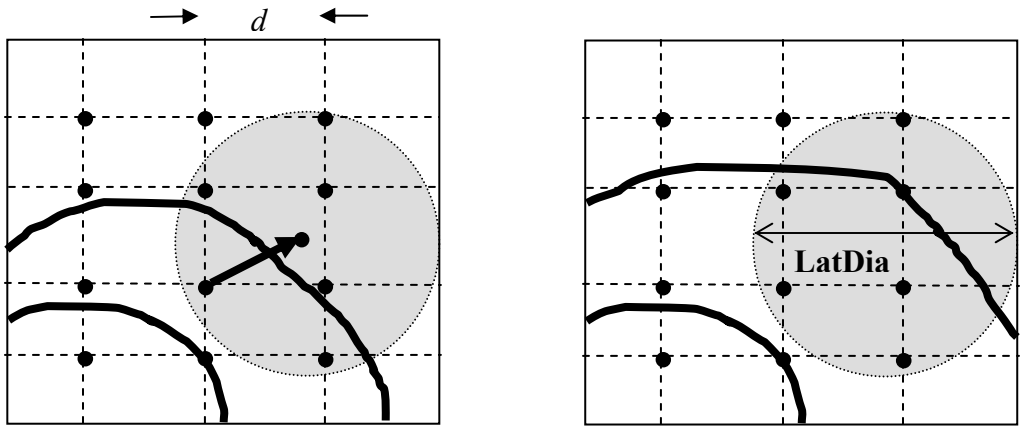


Figure1: Illustration of deformation lattice with lattice spacing *d* superimposed on target and source images. Lattice nodes are represented by filled circles. Image similarity is evaluated over a region defined by the lattice diameter (LatDia) in the vicinity of a deformed lattice node. The sublattice defines the number of samples used within this region, measured as the number of samples across the region diameter.

the region in the vicinity of each lattice node over which the image similarity is evaluated. Generally it should be large enough to cover residual motion between the source and target image. The *sublattice* parameter defines the number of nodes within the lattice diameter at which image similarity is measured, (i.e., sublattice = 3 specifies that

image similarity is measured on a 3x3x3 grid) and should be chosen such that the node spacing is greater than or equal to the image resolution.

The smoothness of the recovered deformation map is controlled by the *iteration* and *smoothing weight* parameters. The *iteration weight* (IW) determines the fraction of the deformation estimated on the current iteration that is added to the sum of previously estimated deformations. A lower IW can result in a smoother estimate of the deformation field but requires more iterations and may result in an incomplete recovery of the deformation field. The *smoothing weight* (SW) is a global regularization factor which controls the smoothness of the recovered deformation field by specifying the relative fraction of the deformation which is averaged with its 26 local neighbors:

$$\vec{d}\left(\vec{x}_{\mathrm{i}}\right) = SW\vec{d}\left(\vec{x}_{\mathrm{i}}\right) + (1-SW)\left\langle d\left(\vec{x}_{\mathrm{i}}\right)\right\rangle \quad , \tag{2}$$

where $\left\langle d\left(\vec{x}_{\mathrm{i}}\right)\right\rangle$ denotes the average deformations in the neighborhood of node $\vec{x}_{\mathrm{i}}$ (i.e., 26 nodes). An SW of 1.0 means that the deformation at a given node is the average of its neighbours while a weight of 0.0 specifies no smoothing (see Equation 2)

Two implementations of deformation vector smoothing are possible: global and local smoothing. In the global smoothing method, after addition of the current estimation of the remaining deformation, smoothing is applied to the sum of currently estimated vectors on each iteration of the registration process. This smoothing strategy emulates the properties of a linear-elastic medium. In contrast, when using the local smoothing method only the current estimate is smoothed. No smoothing is applied after addition of the current to the previous summed estimate of the deformation field. This method models the image as a visco-elastic medium since it is possible to recover larger deformations. In this work we used the global smoothing implementation as it results in a more continuous deformation field.

## 6.3 METHODS AND MATERIALS

### 6.3.1 Deformation vector discontinuities

To our knowledge, the ANIMAL algorithm has not yet been applied to the registration of 4D CT lung images. There are a few features of this type of registration which require consideration. First, we wish to obtain deformation vector fields for input

to the defDOSXYZ 4D Monte Carlo code. Therefore, we require deformation vectors to be defined for each voxel of the dose calculation grid which relate the position of this reference voxel to its position at the target phase. Secondly, large deformations of up to 2 to 3 cm are expected when registering between extreme breathing phases. The magnitude of the recoverable deformations is limited by the deformation lattice spacing in ANIMAL. Given the relative scale of the anatomical deformations compared to a typical dose grid spacing (e.g., 5 mm or less) a multi-resolution registration method will be necessary. Finally, for accurate particle transport with defDOSXYZ through the deformed reference geometry, the deformation vectors must preserve the topology of the anatomy. This requires that the ordering of voxel nodes should be respected which implies that the deformation field is continuous. An example of discontinuous deformation vectors applied to a dose voxel is shown in Figure 2. If the applied deformation vectors cause the node ordering for a particular voxel to be inconsistent the opposing planes of the resulting deformed voxel can intersect causing the voxel to be "collapsed". This causes errors for the 4D dose calculation because the volume element in which energy deposition is scored becomes ill-defined.

Discontinuities or "tearing" within the deformation field can occur as a result of physical reasons such as discontinuous motion between different tissues, as may occur at the chest wall/lung boundary or between the lobes of the lung. In this case discontinuities in the deformation field are unavoidable if we wish to correctly model the tissue motion.

Discontinuities can also be caused by inconsistencies in the source and target image features caused by anatomy which is present in one image but not in the other or caused by image artifacts. Thirdly, discontinuities can occur as a result of the registration process within ANIMAL. Since deformations are estimated at each node independently, it is possible for neighboring deformation vectors to overlap. It is these erroneously introduced discontinuities which we wish to minimize.

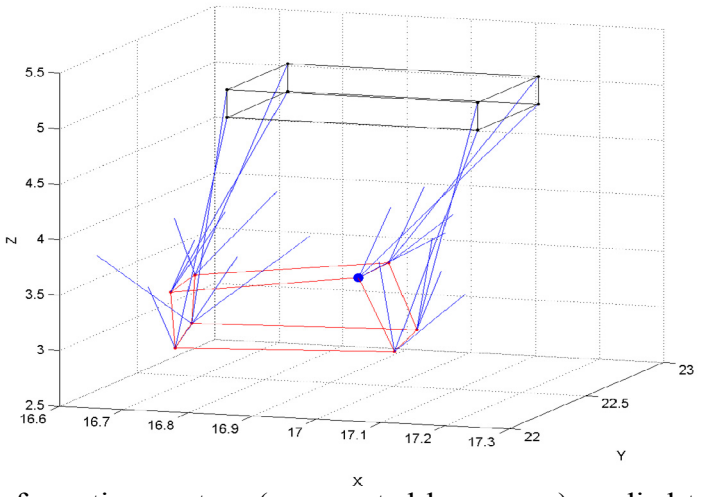


(a) Example of deformation vectors (represented by arrows) applied to reference voxel (in black) where voxel node ordering is not maintained. The deformed voxel (in red) is turned inside out.

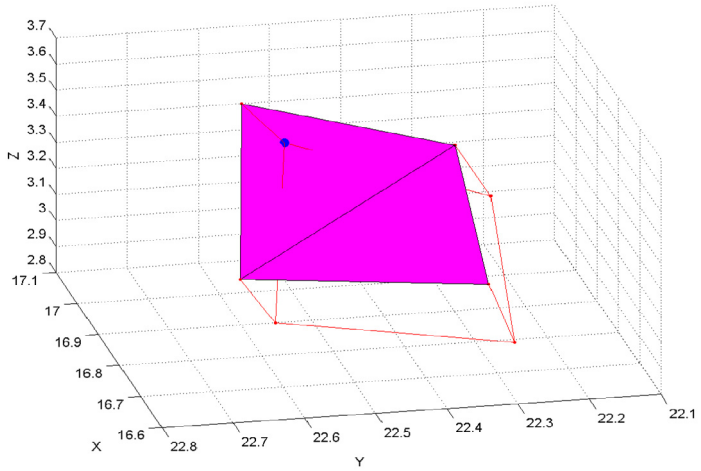


(b) Example of "collapsed" voxel. The front plane intersects the back plane of the voxel (intersection point shown as blue dot).

Figure 2. Creation of a "collapsed" voxel due to application of discontinuous deformation vectors.

### 6.3.2 Modifications to regularize deformation vector discontinuities

Deformation vector discontinuities can be minimized by increasing the smoothing weight parameter (SW). However, as this is a global regularization parameter the

registration accuracy at all points in the image may be penalized. Another option is to explicitly test and correct for discontinuities in the estimated deformation field during the optimization process. The ANIMAL code was modified so that after each iteration of the registration process the determinant of the Jacobian matrix of the non-linear transformation *N(x)* in the local neighbourhood of each node is calculated, as shown in Equation 3.

$$\det\left(Jac\left(\vec{N}\left(\vec{x}\right)\right)\right)=\begin{vmatrix}\frac{\partial N_x}{\partial x} & \frac{\partial N_x}{\partial y} & \frac{\partial N_x}{\partial z}\\ \frac{\partial N_y}{\partial x} & \frac{\partial N_y}{\partial y} & \frac{\partial N_y}{\partial z}\\ \frac{\partial N_z}{\partial x} & \frac{\partial N_z}{\partial y} & \frac{\partial N_z}{\partial z}\end{vmatrix}=\begin{vmatrix}\frac{\partial u_x}{\partial x}+1 & \frac{\partial u_x}{\partial y} & \frac{\partial u_x}{\partial z}\\ \frac{\partial u_y}{\partial x} & \frac{\partial u_y}{\partial y}+1 & \frac{\partial u_y}{\partial z}\\ \frac{\partial u_z}{\partial x} & \frac{\partial u_z}{\partial y} & \frac{\partial u_z}{\partial z}+1\end{vmatrix}, \qquad (3)$$

where $u_x$,$u_y$ and $u_z$ are the components of the displacement vectors $\vec{u}$ comprising the non-linear transformation at node $\vec{x}$, $N(\vec{x})=\vec{x}+\vec{u}$.

The determinant of the Jacobian matrix provides an estimate of the local volume change. A negative value indicates a discontinuity[5,6] at that node. In the modified ANIMAL code the deformations at nodes which are identified as discontinuous are replaced by an average of the deformations of the 26 local neighbors.

Any discontinuities which remain after the optimization process are removed by local or global smoothing of the deformation vectors with a Gaussian kernel. The kernel full-width half maximum (FWHM) was chosen as a multiple of the image resolution (usually 2 to 4) which, when applied to the deformation vectors, removed all remaining discontinuities.

### 6.3.3 Registration process and optimization of registration parameters

The image data to be registered consisted of 4D CT images of the thorax acquired at the MD Anderson Cancer Centre using the axial mode of a PET-CT scanner (Discovery ST, GE Medical Systems, Milwaukee, WI)[7]. Scans were retrospectively sorted into ten breathing phases with an image resolution of 0.98 mm and slice thickness of 2.5 mm. Details on patient GTV motion, tumor location, source and target phases are summarized

in Table 1. The exhale or inhale phases were selected as reference phase. As these extreme phases represent the largest displacements to be recovered, registration between these phases represents the most stringent test of registration accuracy. Therefore the registration was performed between the inhale and exhale phases except for Patients 1 and 3 where registration was also performed between the reference and intermediate phases. The patient anatomy was masked on the target and source images to exclude the CT couch and other objects around the patient from the registration.

Table 1: Characteristics of tumor motion for 4D CT patients

| Patient # | GTV size ($cm^3$) | GTV location | Max GTV motion* (cm) | Source phase | Target phase |
|---|---|---|---|---|---|
| 1 | 5.2 | upper L lobe | 1.2 | Inhale | Exhale |
| 2 | 1.4 | mediastinum | 1.1 | Exhale | Inhale |
| 3 | 5.2 | mid R lobe | 2.1 | Exhale | Inhale |
| 4 | 106.4 | lower R lobe | 0.9 | Inhale | Exhale |
| 5 | 17.0 | upper L lobe | 1.6 | Exhale | Inhale |

*measured as change in centre of mass of GTV between exhale and inhale

As the deformation lattice spacing controls the maximum amount of recoverable deformation on each step size, rather than determining the deformation field at a single resolution it is more computationally efficient to use a multiresolution approach to the registration. A multiresolution registration consists of performing the registration on blurred images to recover the gross features of the deformation field, followed by registration at increasing resolution to recover more localized details of the deformations. Such an approach minimizes the number of iterations required to recover a given scale of deformation and also results in a smaller chance of getting caught in local minima in objective function or creating discontinuities within the deformation field[8].

The multiresolution registration process was initiated with a deformation lattice spacing of 16 times the image resolution. For each subsequent iteration, the deformation lattice spacing was decreased by a factor of two, using the transformation recovered on the previous step as a starting estimate. The images are blurred using a Gaussian kernel

with a FWHM equal to the deformation lattice spacing. This effectively downsamples the image resolution so that the features are on the same scale as the resolution at which vectors are estimated. The use of a Gaussian kernel for such purposes is desirable as it is isotropic and does not introduce any spurious details in the blurred images. During optimization of the registration the deformation vectors are "super-sampled" or estimated at a resolution twice that of the user specified deformation lattice spacing. Therefore the Nyquist criterion of sampling the deformation field at 2 times the underlying resolution is satisfied. Four resolution steps were used for the registration, on the last step the registration is effectively performed on the original image resolution due to deformation lattice super-sampling. The image resolution was kept non-isotropic, as in the original images.

The lattice diameter, sublattice, iteration and smoothing weights were determined for each registration step by systematically testing many possible combinations to see which resulted in a stable objective function with the lowest minimum. The process was automated by using a script which generates the command lines for running ANIMAL with variable parameter combinations. For the lattice diameter the search space consisted of values between 1x and 4x the deformation lattice spacing with steps of 0.5. Sublattice values between 5 and 10 were tested with steps of 1.0. The search process is summarized in Figure 2. First an initial estimate of the lattice diameter (LatDia) and sublattice (SubLat) is performed using an iteration weight (IW) of 1.0 and a smoothing weight (SW) of 0.5 for 5 iterations. Based on these optimized values the optimum iteration and smoothing weights are determined for 30 iterations. Using these values, the lattice diameter and sublattice are optimized again. If the values are not the same as initial estimate the parameter optimization is repeated until convergence is reached.

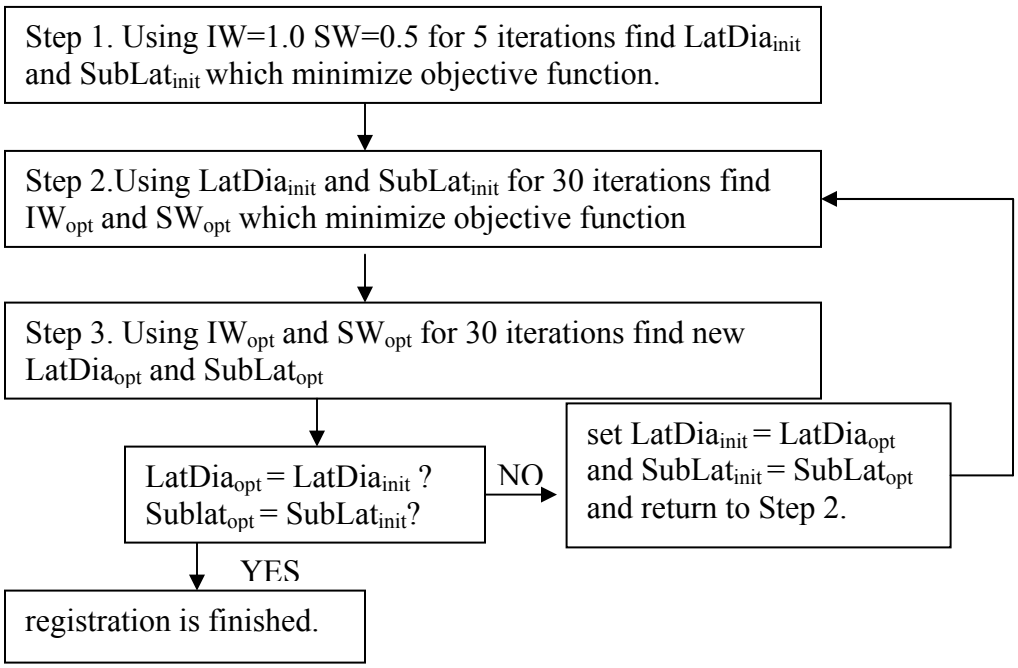


Figure 2: Process for determination of optimum registration parameters $IW_{opt}$, $SW_{opt}$, $LatDia_{opt}$ and $SubLat_{opt}$. IW is the iteration weight, SW is the smoothing weight, LatDia is the lattice diameter and SubLat is the sublattice size. For the lattice diameter the search space consisted of values between 1x and 4x the deformation lattice spacing with steps of 0.5. Sublattice values between 5 and 10 were tested with steps of 1.0.

### 6.3.4 Analysis of registration accuracy

The registration accuracy between the transformed and target images was evaluated after each resolution step of the registration process by 3 metrics: image cross-correlation, distance-to-agreement (DTA) of manually identified landmarks and DTA of 3D surfaces derived from contoured planning structures.

#### *6.3.4.1 Image correlation*

Image correlation was evaluated by first applying the recovered non-linear transformation to the source image and re-sampling the image intensities on the original voxel grid by tri-linear interpolation. The normalized cross-correlation of image intensities, between this transformed image and the target image, was calculated as per Equation 4:

$$xcorr = \frac{\sum I_s I_t}{\sqrt{\sum I_s^2}\sqrt{\sum I_t^2}} \quad , \tag{4}$$

where $I_s$ is the resampled transformed source image intensity and $I_t$ is the target image intensity. Note that the cross-correlation was calculated for voxels inside the masked patient anatomy only.

#### *6.3.4.2 Landmark analysis*

Registration accuracy was also determined using manually identified homologous landmarks on the source and target images including vascular and bronchial bifurcations, fiducial markers, and bony anatomy. Examples of anatomical landmarks are shown in Figure 3. Typically 20-30 landmarks were identified for each patient image set which were well distributed throughout the patient volume. The displacement of these landmarks was compared to the estimated displacements at the same locations interpolated from the recovered deformation vectors. The differences between the actual and predicted displacements were compared along each direction as well as summed in

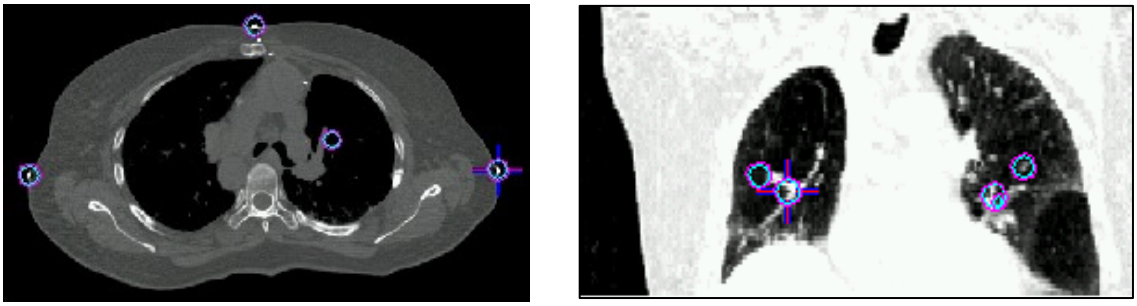

(a) (b)

Figure 3. Examples of landmarks (indicated by circles) used for registration accuracy analysis.

quadrature as a 3D vector error. The accuracy with which homologous landmarks were identified was quantified by having three independent observers identify the corresponding landmarks on the target image for one patient.

#### *6.3.4.3 3D DTA analysis*

A 3D DTA analysis based on planning contours was also performed. The GTV, spinal cord, heart and lungs were manually contoured on the source and target images. The same window and level were used for contouring on both images to improve contouring consistency. Repeated contouring of the GTV and heart by 3 independent observers for one patient data set was used to quantify reproducibility of manual contours. Automatic contouring based on image intensity thresholds was also used to see if this improved contouring consistency of the GTV between phases. 3D surface meshes were created from these contours by one of two methods. For Patients 2 and 7 the smoothed triangulated meshes were extracted from Pinnacle (Philips Medical Systems, Andover, MA) contour (.roi) files[9]. For the remaining patients triangulated surfaces were created using a method of connecting points on adjacent contours within a specified angular interval as illustrated in Figure 4.

First contour points are interpolated at a desired in-slice resolution (e.g.,1 mm for spinal cord, 2 mm for GTV and heard, 5 mm for lungs). Triangles connecting two adjacent slices are constructed by connecting the first points on each slice. The third vertex is formed by the next point on one of the two slices, whichever falls within the angular interval specified by the desired resolution. The structure ends are closed by triangulating the first and last slice in a "bicycle wheel" fashion formed by connecting the contour center of mass and the contour points.

For each structure the triangulated surface for the source image is deformed using the recovered deformations by tri-linear interpolation of deformations at each triangle vertex. The center of mass of this deformed surface and the target surface is compared. A 3D DTA was calculated by averaging the minimum distance between the deformed and target surface for each triangle of the deformed surface along its normal. The DTA along the surface normals was used instead of the radial distance used by other authors[9,10] as it avoids incorrect identification of the closest surface point where concavities exist. For each structure an average 3D DTA and COM shift were determined. The distribution of the DTA could be visualized by assigning a color map to the triangles of the deformed surface based on the calculated DTA for each triangle.

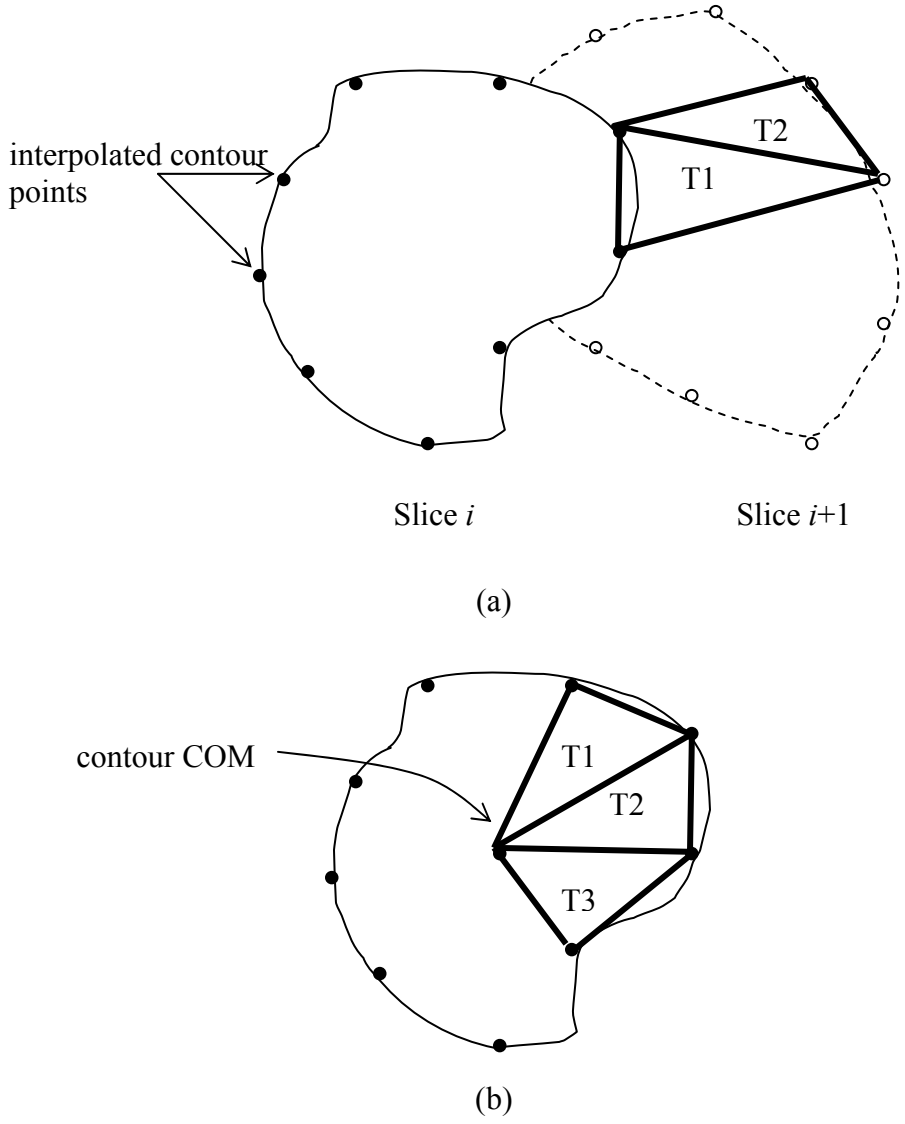


Figure 4. Triangulation of contour points. Contour points are first interpolated at desired in-slice resolution. (a) Connection of interpolated points on adjacent contours that lie within a user-specified angular interval. (b) Triangulation of end contours by connecting contour center-of-mass (COM) with contour points.

### 6.3.5 Investigation of mass conservation in image registration

It has been pointed out by some Rietzel *et al.*[11] that the transformations obtained from non-linear image registration do not conserve mass, instead it is image intensities that are preserved. This has implications for the accuracy of the defDOSXYZ Monte

Carlo code in which voxels are deformed using these non-linear transformations and their densities are adjusted to conserve the mass, especially when comparing with other dose remapping techniques in which dose is calculated on the transformed image.

To investigate the extent to which mass is not conserved by the non-linear transformations obtained from ANIMAL we compared density matrices obtained from the transformed reference image against density matrices derived from the reference image in which the voxels were deformed using the deformation vectors and then remapped by trilinear interpolation with octant subdivision[12] back to the rectangular image grid. In the latter case, voxel densities were adjusted to conserve mass as voxel volumes changed with deformation.

### 6.3.6 Modifications to allow multiple smoothing weights

To enforce realistic tissue deformations it is desirable to incorporate information about tissue elastic properties into the choice of registration parameters. Ruan *et. al.*[13] used a tissue specific non-rigidity penalty in the cost function to reduce bone warping in non-linear image registration. The non-stiffness of the warping was determined from the determinant of the Jacobian matrix of the local deformations.

In the ANIMAL algorithm, the smoothing weight effectively controls the amount of recoverable deformation. We modified the code to allow specification of two smoothing weights, one for all tissues, excluding the lungs, identified in a mask file and another value for the lung tissue. All deformation lattice nodes which were inside the tissue mask were assigned a smoothing weight of 1.0. The smoothing weight for the other tissues was optimized as mentioned previously. The registration of Patient 1 was repeated with the modified code and the deformation vectors were compared to the previously obtained vectors in terms of volume changes which occur within the masked tissues.

### 6.3.7 Dependence of 4D dose calculation accuracy on non-linear image registration accuracy

To investigate how non-linear image registration accuracy affects the accuracy of 4D dose calculations which use the deformation vectors, dose calculations were performed on the Patient 1 images using deformation vectors recovered at the 2 mm, 4

mm, 8 mm and 16 mm deformation lattice spacings. A two-field 3D conformal treatment plan was created on the inhale image and using the defDOSXYZ code the dose received at the exhale phase was calculated. The dose grid size was 3.90624 x 3.90624 x 2.5 $mm^3$, each set of deformation vectors were resampled to match the dose grid resolution. More details of the treatment plan and Monte Carlo dose calculations are given in Chapter 8. The resulting inhale-exhale dose distributions were compared in terms of dose volume histograms for target volumes and organs at risk.

## 6.4 RESULTS

### 6.4.1 Influence of registration parameters on objective function

The effect of registration parameters on the behavior of the objective function for inhale to exhale registration on a deformation lattice spacing of 16,16,40 mm for Patient 1 is summarized in Figure 5.

For this patient the optimal registration parameters were selected to be a lattice diameter of 60 mm, sublattice of 5 nodes, an iteration weight of 1.0 and the smoothing weight 0.2. From Figure 5 it can be seen that a sub-optimal selection of some registration parameters can lead to an unstable objective function. For example, if the lattice diameter is too large compared to the image resolution and deformations to be recovered then the similarity function evaluated at each node becomes insensitive to changes in image features because they are averaged out (see Figure 5 (a)). Likewise, a lattice diameter which is smaller than the image resolution will not be able to distinguish any features for registration. The choice of sublattice is dependent on the lattice diameter but it can be seen that an increased number of sublattice nodes, and hence increasing number of samples of image similarity, is preferred, however, this comes at a cost of longer registration times.

The influence of iteration and smoothing weights are shown in Figures 5(c) and (d). For this particular registration a lower iteration weight resulted in underestimation of the deformations to be recovered. With no regularization of the deformations (smoothing weight=0) the objective function is not stable, but if the smoothing weight is set at 1.0 then ANIMAL is not able to completely recover the deformations required to optimize the objective function value.

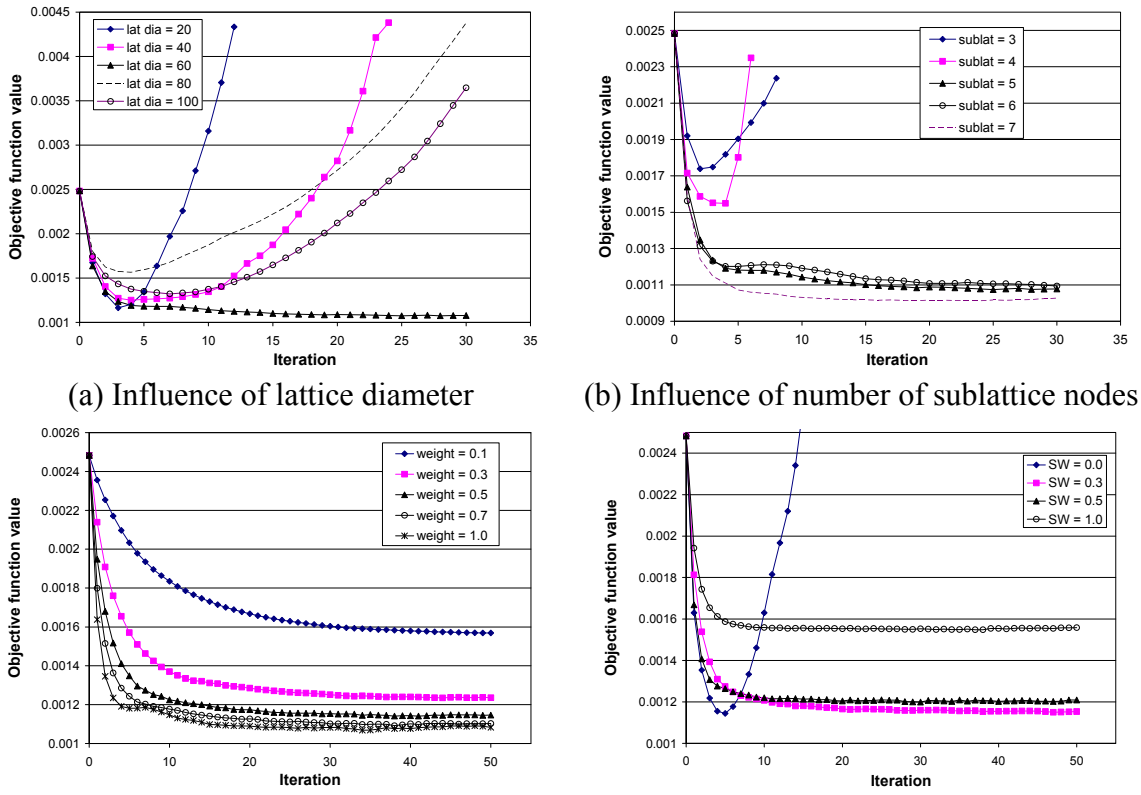


(a) Influence of lattice diameter

(b) Influence of number of sublattice nodes

(c) Influence of iteration weight

(d) Influence of smoothing weight

Figure 5. Influence of registration parameters on objective function

### 6.4.2 Optimized registration parameters for 4D CT patients

The optimized registration parameters determined on each registration step for all phases between inhale and exhale on Patient 1 are summarized in Table 2. A similarity-cost ratio between 0.98 and 1.0 was used as a balance between maximizing image correlation and minimizing the number of discontinuities. This is consistent with values reported in a study on optimizing ANIMAL parameters for inter-subject registration of brain[14].

Some general trends were noted in the optimized parameters, namely that as the deformation lattice spacing decreased, the iteration weight decreased and smoothing weight increased. This indicates that as lattice nodes become more closely spaced a higher amount of smoothing is needed to ensure continuity of the deformations. On the 2 mm registration step, the optimized iteration weight was significantly lower than on previous steps; this is discussed further in Section 6.4.6.

Table 2: Optimized registration parameters for Patient 1. The reference phase is T0 (Inhale).

| Target Phase | GTV motion (mm) | Lattice Spacing (mm) | Lattice Diameter (mm) | # Sublattice nodes | Iteration Weight | Smoothing weight | Number of iterations |
|---|---|---|---|---|---|---|---|
| T5 | 12.0 | 16,16,40 | 60 | 5 | 1.0 | 0.2 | 30 |
| | | 8,8,20 | 40 | 7 | 0.9 | 0.3 | 50 |
| | | 4,4,10 | 25 | 9 | 0.9 | 0.5 | 7 |
| | | 2,2,5 | 15 | 5 | 0.5 | 0.6 | 10 |
| | | | | | | | |
| T4 | 12.0 | 16,16,40 | 50 | 9 | 1.0 | 0.2 | 20 |
| | | 8,8,20 | 35 | 8 | 0.9 | 0.3 | 20 |
| | | 4,4,10 | 20 | 10 | 1.0 | 0.6 | 4 |
| | | 2,2,5 | 20 | 5 | 0.3 | 0.5 | 15 |
| | | | | | | | |
| T3 | 10.0 | 16,16,40 | 50 | 9 | 1.0 | 0.2 | 40 |
| | | 8,8,20 | 35 | 8 | 0.9 | 0.3 | 40 |
| | | 4,4,10 | 25 | 9 | 1.0 | 0.5 | 30 |
| | | 2,2,5 | 20 | 5 | 0.4 | 0.5 | 10 |
| | | | | | | | |
| T2 | 7.0 | 16,16,40 | 40 | 10 | 1.0 | 0.2 | 30 |
| | | 8,8,20 | 35 | 8 | 1.0 | 0.3 | 30 |
| | | 4,4,10 | 30 | 9 | 0.8 | 0.5 | 15 |
| | | 2,2,5 | 15 | 5 | 0.5 | 0.7 | 5 |
| | | | | | | | |
| T1 | 3.0 | 16,16,20 | 40 | 10 | 0.9 | 0.2 | 30 |
| | | 8,8,20 | 35 | 8 | 0.9 | 0.3 | 15 |
| | | 4,4,10 | 35 | 8 | 1.0 | 0.8 | 50 |
| | | 2,2,5 | 20 | 5 | 0.2 | 0.3 | 30 |

The optimized lattice diameter size relative to the deformation lattice spacing also increased as the deformation lattice spacing decreased indicating that a large amount of residual motion relative to the lattice spacing remained to be recovered on these steps. Comparing optimized registration parameters for registration of different phases we noted that lattice diameter size decreased on registering phases where the amount of GTV motion decreased.

The optimized registration parameters determined for registration between the extreme phases for all patients are listed in Table 3. Note that registration was not performed on the 2 mm lattice spacing for all patients, the reasons for this are discussed

later. From this table it is evident that there is some inter-patient variation in the optimized registration parameters due to differences in breathing motion and patient geometry.

Table 3: Optimized registration parameters registration between extreme phases of all patients.

| Patient# | GTV motion (mm) | Lattice spacing (mm) | Lattice Diameter (mm) | # Sublattice nodes | Iteration Weight | Smoothing weight | Number of iterations |
|---|---|---|---|---|---|---|---|
| 1 | 12.0 | 16,16,40 | 60 | 5 | 1.0 | 0.2 | 30 |
| | | 8,8,20 | 40 | 7 | 0.9 | 0.3 | 50 |
| | | 4,4,10 | 25 | 9 | 0.9 | 0.5 | 7 |
| | | 2,2,5 | 15 | 5 | 0.5 | 0.6 | 10 |
| | | | | | | | |
| 2 | 11.2 | 16,16,40 | 60 | 6 | 0.8 | 0.2 | 20 |
| | | 8,8,20 | 50 | 7 | 0.9 | 0.4 | 35 |
| | | 4,4,10 | 40 | 8 | 0.9 | 0.4 | 20 |
| | | 2,2,5 | 20 | 8 | 0.8 | 0.7 | 20 |
| | | | | | | | |
| 3 | 21.3 | 16,16,40 | 100 | 9 | 0.9 | 0.2 | 40 |
| | | 8,8,20 | 40 | 8 | 1.0 | 0.4 | 10 |
| | | 4,4,10 | 40 | 8 | 1.0 | 0.6 | 30 |
| | | | | | | | |
| 4 | 12.5 | 16,16,40 | 50 | 6 | 1.0 | 0.2 | 3 |
| | | 8,8,20 | 35 | 7 | 0.7 | 0.3 | 30 |
| | | 4,4,10 | 20 | 10 | 1.0 | 0.7 | 40 |
| | | 2,2,5 | 20 | 10 | 0.5 | 0.6 | 30 |
| | | | | | | | |
| 5 | 17.5 | 16,16,40 | 100 | 10 | 0.9 | 0.2 | 60 |
| | | 8,8,20 | 50 | 9 | 0.9 | 0.3 | 10 |
| | | 4,4,10 | 16 | 8 | 1.0 | 0.6 | 70 |

### 6.4.3 Sensitivity of registration accuracy to registration parameters

Although lattice diameter and sublattice varied between registrations of different phases for individual patients, the relative consistency of iteration and smoothing weights in Table 2 led us to question the sensitivity of the registration accuracy to the choice of registration parameters. It would speed up the registration process if the parameters need to be optimized only for registration between the extreme phases and these values could be used for all other phases. Thus, for Patients 1 and 3 the registration of the intermediate

phases was repeated using the optimized parameters determined for the registration of the extreme phases. The registration accuracy was determined using the individual phase optimized parameters and the extreme phase optimized parameters, as shown in Tables 4(a) and (b).

Table 4a: Sensitivity of registration accuracy to registration parameters for Patient 1. Reference phase is T0 (inhale). One standard deviation on the mean DTA is quoted in brackets.

| Lattice Spacing (mm) | Optimized parameters | | | | Image xcorr | 3D Bif error (mm) | T0-T5 parameters | | | | Image xcorr | 3D Bif error (mm) |
|---|---|---|---|---|---|---|---|---|---|---|---|---|
| Target Phase = T1 | | | | | | | | | | | | |
| | LatDia | SubLat | IW | SW | | | LatDia | SubLat | IW | SW | | |
| 16,16,40 | 40 | 10 | 0.9 | 0.2 | 0.9968 | 1.3 (1.4) | 60 | 5 | 1.0 | 0.2 | 0.9966 | 1.2 (1.4) |
| 8,8,20 | 35 | 8 | 0.9 | 0.3 | 0.9979 | 1.0 (0.9) | 40 | 7 | 0.9 | 0.3 | 0.9978 | 1.0 (1.0) |
| 4,4,10 | 35 | 8 | 1.0 | 0.8 | 0.9981 | 0.8 (0.9) | 25 | 9 | 0.9 | 0.5 | 0.9975 | 0.7 (1.0) |
| Target Phase = T4 | | | | | | | | | | | | |
| | LatDia | SubLat | IW | SW | | | LatDia | SubLat | IW | SW | | |
| 16,16,40 | 50 | 9 | 1.0 | 0.2 | 0.9908 | 3.6 (4.3) | 60 | 5 | 1.0 | 0.2 | 0.9905 | 4.1 (5.4) |
| 8,8,20 | 35 | 8 | 0.9 | 0.3 | 0.9955 | 2.1 (1.6) | 40 | 7 | 0.9 | 0.3 | 0.9952 | 1.9 (1.9) |
| 4,4,10 | 20 | 10 | 1.0 | 0.6 | 0.9956 | 1.3 (1.6) | 25 | 9 | 0.9 | 0.5 | 0.9956 | 1.3 (1.6) |

Table 4b: Sensitivity of registration accuracy to registration parameters for Patient 3. Reference phase is T5 (exhale). One standard deviation on the mean DTA is quoted in brackets.

| Lattice Spacing (mm) | Optimized parameters | | | | Image xcorr | 3D Bif error (mm) | T0-T5 parameters | | | | Image xcorr | 3D Bif error (mm) |
|---|---|---|---|---|---|---|---|---|---|---|---|---|
| Target Phase = T1 | | | | | | | | | | | | |
| | LatDia | SubLat | IW | SW | | | LatDia | SubLat | IW | SW | | |
| 16,16,40 | 100 | 9 | 1.0 | 0.2 | 0.9928 | 3.5 (3.1) | 100 | 9 | 0.9 | 0.2 | 0.9938 | 2.8 (2.5) |
| 8,8,20 | 50 | 7 | 1.0 | 0.4 | 0.9952 | 1.6 (1.5) | 40 | 8 | 0.9 | 0.4 | 0.9952 | 1.6 (1.7) |
| 4,4,10 | 40 | 8 | 1.0 | 0.4 | 0.9962 | 1.3 (1.3) | 40 | 8 | 1.0 | 0.6 | 0.9962 | 1.3 (1.2) |
| Target Phase = T4 | | | | | | | | | | | | |
| | LatDia | SubLat | IW | SW | | | LatDia | SubLat | IW | SW | | |
| 16,16,40 | 100 | 9 | 1.0 | 0.3 | 0.9979 | 1.1 (1.2) | 100 | 9 | 0.9 | 0.2 | 0.9978 | 1.2 (1.2) |
| 8,8,20 | 50 | 6 | 1.0 | 0.6 | 0.9983 | 1.1 (1.2) | 40 | 8 | 0.9 | 0.4 | 0.9983 | 1.2 (1.2) |
| 4,4,10 | 40 | 7 | 1.0 | 0.5 | 0.9981 | 0.9 (1.0) | 40 | 8 | 1.0 | 0.6 | 0.9986 | 1.0 (1.0) |

Abbreviations:

3D Bif error = 3D bifurcation registration error LatDia = Lattice diameter

SubLat = number of sublattice nodes IW = iteration weight

SW = smoothing weight

Using these registration parameters instead of optimizing on each individual phase was found to have no significant effect on the registration accuracy despite significant changes in the lattice diameter and sublattice. This insensitivity is attributed to the relative smoothness of the deformation fields which means that the recovered deformations are not significantly affected by changes to the registration parameters.

### 6.4.4 Summary of registration accuracy in 4D CT thoracic images

An example of triangulated GTV contours at the reference phase, a deformed GTV surface and the resulting colour map of DTA when compared with a target phase GTV is shown in Figure 6. The colour map in Figure 6(c) displays DTA between the two surfaces

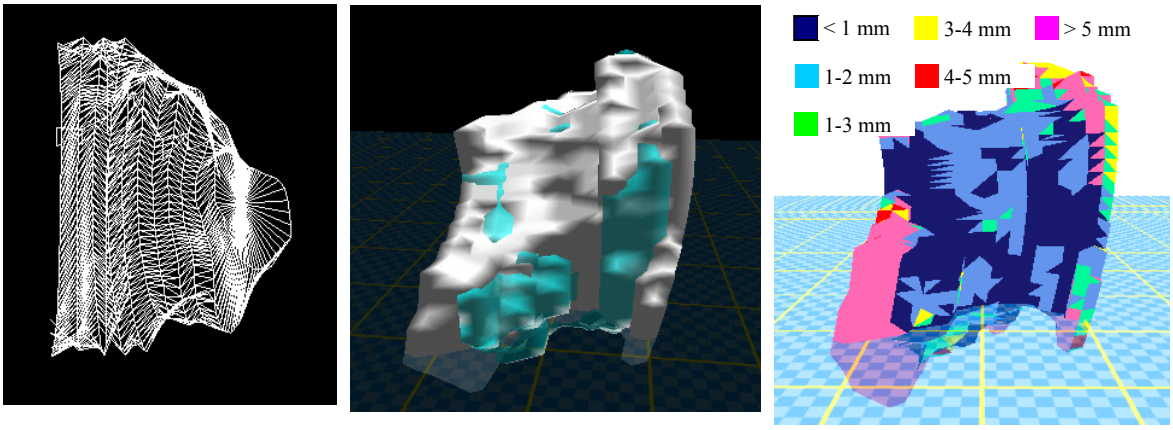


(a) (b) (c)

Figure 6. (a) Example of triangulated GTV. (b) Deformed (white) and target (blue) triangulated surfaces from Pinnacle contour file (c) colour map of DTA for surfaces in (b). Pink regions of colour map indicate that distance-to-agreement between surfaces is greater than 5 mm.

super-imposed on the deformed surface. In this case, colors were assigned to each triangle of the deformed surface using 1 mm DTA bins. The pink regions indicate triangles where the distance to the target structure exceeds 5 mm. Note that most of the surface is aligned with less than 2 mm error. Large discrepancies between the deformed and target surfaces may be noted at the same location in Figure 6(b).

The registration accuracy as evaluated on the 4 mm registration step for each patient is summarized in Table 5. The reproducibility of the homologous landmark identification on the exhale and inhale phases for Patient 5 as determined from identification of 22 landmarks by three independent observers was 1.7 mm (0.6 mm SD). For the same patient, the reproducibility of the manual contours of the GTV was 1.6 mm (0.7 mm SD) in DTA and 3.4 mm (2.3 mm SD) in COM shift. For the heart, the average vector DTA between manual contours drawn by three independent observers was 1.7 mm (0.4 mm SD) and the COM shift was 1.7 mm (0.7 mm SD). The average vector (3D) bifurcation error was 1.6 mm (0.3 mm SD) for all 5 patients. On average, the COM shift and 3D DTA between the transformed and target GTV contours was 2.0 mm (0.4 mm SD) and 1.6 mm (0.3 mm SD), respectively. The average 3D DTA between transformed and target structures for the GTV, heart, spinal cord and lungs was 1.8 mm (0.4 mm SD).

For the 3D surface DTA analysis of Patient 2 the lung contours were omitted because the full extent of both lungs was not present in the exhale and inhale images. The registration accuracy results shown in Table 5 are within the range of the uncertainty of the bifurcation and contour DTA analysis. Using auto-contoured structures resulted in an improved registration accuracy compared to manually contoured structures (data not shown). This was expected as the image registration is driven by matching image intensities and the contouring reproducibility is superior to manual contouring. For Patients 1 and 3, a similar or improved registration accuracy for all metrics was obtained for registration between the reference and intermediate phases.

Table 5. Final registration accuracy on inhale-exhale registration (deformation lattice spacing= 4,4,10 mm). One standard deviation on the mean DTA is quoted in brackets.

| Patient # | 3D bifurcation error (mm) | | Original Image xcorr | | GTV COM shift (mm) | | GTV DTA (mm) | | Average DTA (mm) | |
|---|---|---|---|---|---|---|---|---|---|---|
| | Prereg. | Postreg. | Prereg. | Postreg. | Prereg. | Postreg. | Prereg. | Postreg. | Prereg. | Postreg. |
| 1 | 4.6 (5.4) | 1.5 (1.4) | 0.982 | 0.998 | 12.5 | 1.8 | 7.3 (5.2) | 1.8 (1.3) | 4.6 (2.4) | 2.0 (0.6) |
| 2 | 6.8 (4.7) | 1.4 (1.4) | 0.978 | 0.994 | 11.2 | 2.0 | 4.3 (3.5) | 1.2 (0.8) | 5.4 (4.1) | 1.2 (0.8) |
| 3 | 8.7 (7.5) | 1.6 (1.3) | 0.980 | 0.995 | 21.3 | 2.7 | 16.0 (6.5) | 1.6 (0.7) | 6.7 (5.7) | 2.1 (1.0) |
| 4 | 4.2 (3.7) | 1.3 (1.1) | 0.985 | 0.995 | 9.0 | 2.1 | 5.9 (0.9) | 2.0 (0.6) | 4.3 (1.9) | 2.1 (0.7) |
| 5 | 10.3 (9.0) | 2.0 (1.6) | 0.980 | 0.995 | 16.3 | 1.6 | 10.0 (8.0) | 1.4 (0.1) | 7.1 (3.8) | 1.8 (0.9) |
| **avg** | **6.9 (2.8)** | **1.6 (0.6)** | **0.981** | **0.995** | **14.1 (4.8)** | **2.0 (0.4)** | **8.7 (2.4)** | **1.6 (0.4)** | **5.6 (1.7)** | **1.8 (0.4)** |

### 6.4.5 Dependence of registration accuracy on deformation lattice spacing

The intermediate registration step results were analyzed by the three registration accuracy metrics for Patient 1 (see Table 6). Most of the image difference measured in terms of bifurcation and contour DTA was recovered by the 4 mm registration step with little significant improvements on the 2 mm step size. Similar results were noted for Patient 3. The registration on the 4 mm deformation lattice spacing required approximately 5 min/iteration on a 2.2 GHz Athlon processor with 2 GB of RAM and this increased to 40 min/iteration, mainly due to memory swapping, at the 2 mm step size, 10-30 iterations were required for these step sizes.

Table 6: Registration accuracy for inhale-exhale registration for Patient 1 evaluated at different deformation lattice spacings. One standard deviation on the mean DTA is quoted in brackets.

| Lattice Spacing (mm) | Xcorr | 3D Bif error (mm) | GTV COM shift (mm) | GTV DTA (mm) | Avg DTA (mm) |
|---|---|---|---|---|---|
| Initial | 0.982 | 4.6 (5.4) | 12.5 | 7.3 (5.2) | 4.6 (2.4) |
| 16,16,40 | 0.990 | 4.2 (5.3) | 7.3 | 5.6 (0.6) | 3.2 (1.6) |
| 8,8,20 | 0.993 | 1.9 (1.9) | 3.0 | 2.5 (1.2) | 2.3 (0.8) |
| 4,4,10 | 0.998 | 1.5 (1.4) | 1.8 | 1.8 (1.3) | 2.0 (0.6) |
| 2,2,5 | 0.997 | 1.2 (1.2) | 0.9 | 1.7 (1.7) | 1.8 (0.6) |

### 6.4.6 Incidence of deformation vector discontinuities

The location of the discontinuous nodes in the deformation vectors recovered on the 2 mm resolution step for Patient 2 is shown in Figure 7. Discontinuities were found to occur at the interfaces between sliding tissues, such as the chest wall and lung or diaphragm boundary, as well as in the heart and in the lung in the vicinity of 4D CT artifacts. The large number of discontinuities in the region of the diaphragm is also attributed to the fact that the diaphragm was not present in the inhale image therefore the

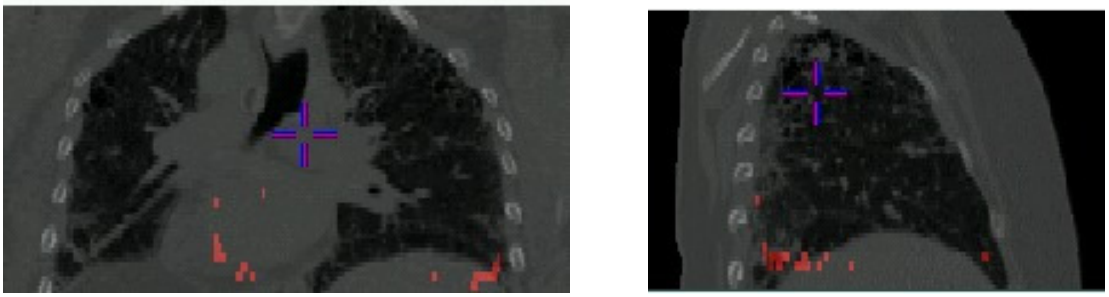

(a) (b)

Figure 7. Location of discontinuities in deformation vectors from exhale to inhale for Patient 2 relative to anatomy. Discontinuous regions are indicated in red.

anatomy was inconsistent. For the other four patients discontinuities were noted at similar locations but the incidence of discontinuities was lower.

The incidence of vector discontinuities for Patient 2, with and without the modification of ANIMAL for interpolation of discontinuous nodes, is summarized in Table 7. The modification resulted in a reduced number of discontinuous nodes only on the 8 mm and 4 mm steps. Similar results were noted for the other four patients.

Table 7: Incidence of deformation vector discontinuities for exhale-to-inhale registration of Patient 2 with and without modifications to ANIMAL for interpolation of discontinuous nodes.

| Lattice spacing (mm) | Number of discontinuous nodes (% of deformation lattice) | |
|---|---|---|
| | Without interpolation | With interpolation |
| 16,16,40 | 3 (0.05%) | 4 (0.07%) |
| 8,8,20 | 3 (0.007%) | 2 (0.004%) |
| 4,4,10 | 327 (0.09%) | 197 (0.05%) |
| 2,2,5 | 852 (0.03%) | 926 (0.03%) |

The fraction of deformation lattice nodes which were discontinuous increased as deformation lattice spacing was decreased. This is in part attributed to the larger spacing between the nodes as well as the increased amount of image blurring which is performed at the lower resolution registration steps which tends to blur out image artifacts. It is

interesting to note that the incidence of discontinuities along the chest wall/lung interface was relatively low. This may be due to a lack of high contrast features in the lung adjacent to the stationary chest wall which undergo large displacements as well as sufficient regularization of the vectors. The exception is near the diaphragm, which slides along the chest wall.

From Table 7 it is apparent that the modifications to the ANIMAL code did not completely remove all discontinuities. This is because only the local neighborhood of a node which is identified as being discontinuous is used for interpolation of the deformation vector at that node. If the deformation vectors at one or more of the surrounding nodes are also inconsistent with respect to its neighbors, which is more likely to occur as the deformation lattice spacing is reduced, the interpolated deformation vector will likely be discontinuous and the original discontinuity is not removed. This could be resolved by interpolating over a larger number of nodes. For the 2 mm registration step, interpolating over a 124-node local neighborhood reduced the number of discontinuities to 759. The relatively low optimized iteration weight obtained at the 2 mm deformation lattice spacing is attributed to the large number of discontinuities which occur at this step size.

Up to and including the 4 mm resolution step, the remaining discontinuities could be removed by a smoothing with a Gaussian kernel of FWHM of two times the deformation lattice spacing over a region of radius 3 x FWHM in the immediate neighborhood of the discontinuous node. This had a lesser impact on registration accuracy compared to increasing the smoothing weight. On the 2 mm resolution step, global smoothing of the deformation vectors was required to remove the discontinuities. The registration accuracy was not found to be significantly affected by this smoothing. For Patient 1 the bifurcation error on the 2 mm resolution step was 1.5 mm (1.1 mm SD) without smoothing and 1.2 mm (1.2 mm SD) after smoothing with a Gaussian kernel with FWHM of 7.8 mm for the X and Y components of the deformations and 10.0 mm for Z component.

### 6.4.7 Issues of mass conservation in image registration

The transformed and deformed density matrices at the exhale phase for Patient 1 are shown in Figure 8(a) and (b). The density difference between these two images, normalized to the density of tissue (1.0 g/cm$^3$) is shown in Figure 8(c) and a corresponding histogram of percentage density differences for all voxels within the patient are shown in Figure 7(d). The mean density difference inside the patient was 16% (22% SD) with differences up to 600% occurring in the heart and diaphragm. As more of the diaphragm is present in the exhale image than in the inhale image, the resulting registration vectors stretch the diaphragm from which leads to a reduction in the density when mass conservation is enforced. Similarly, the large density differences in the heart are attributed to image artifacts, induced by cardiac motion, which cause inconsistencies

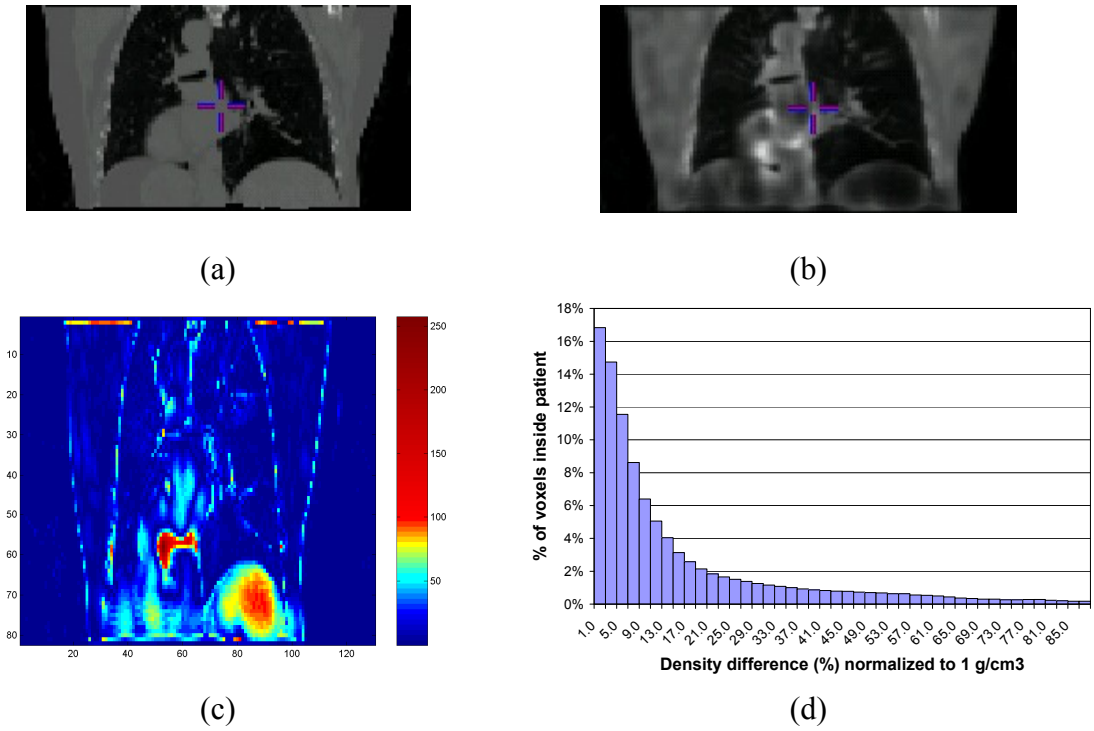


Fig 8. (a) Transformed exhale image, (b) Deformed exhale image that is remapped to the rectangular grid using trilinear interpolation with octant subdivision, (c) percentage density difference map normalized to maximum density of (a) and (d) histogram of density differences. Image size has been downsampled to 128x128x80. Maximum density of image (b) is 3.4 g/cm$^3$.

in the anatomy and are consequently modeled as tissue compression by the ANIMAL deformation vectors. The effect of these density differences on the calculated dose distribution depends on a number of factors including beam geometry and extent of density discrepancies and needs to be investigated further.

It should be noted, however, that mass is not necessarily conserved in 4D CT images. Particularly in the lung the mean density of lung tissue changes between inhale and exhale. In this work we did not account for the change in density, though other authors have modified the lung densities of the source image so that the densities are consistent[15].

### 6.4.8 Results of assigning multiple smoothing weights

The mask used to define tissues to be assigned a different smoothing weight is shown in Figure 9. The tumor, heart, chest wall and mediastinum are included in the tissue mask. These structures were segmented automatically based on image intensity values. The previously optimized registration parameters were used, however, the number of iterations was re-optimized. Different smoothing weights for the masked tissues were investigated, though a smoothing weight of 1.0 was found to minimize volume deformations in these tissues. For the unmasked regions the previously optimized values for the smoothing weights were used: 0.2 for the 16,16,40 mm step, 0.3 for the 8.8,20 mm step and 0.5 for the 4,4,10 mm step. Generally more iterations were required when using the tissue masking but it is likely that this could change if the registration parameters for the deforming structures were re-optimized.

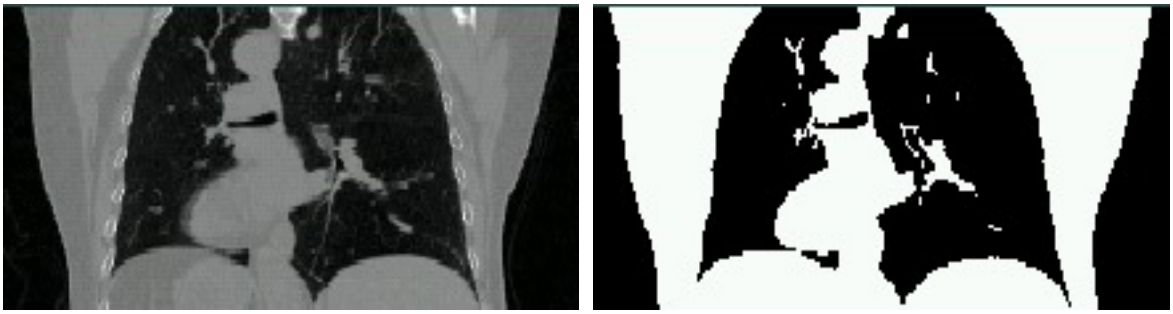

Inhale (source) image Tissue mask

Figure 9. (a) Source image and (b) corresponding binary tissue mask. All tissues included in the mask appear in white.

The registration accuracy, evaluated as a 3D landmark error vector, along with the number of discontinuous nodes and number of nodes with volume changes greater than 5%, are summarized in Table 8. For the results shown in this table, the smoothing weight for masked tissues was 1.0. The tissue masking significantly reduced the deformations which occurred in these tissues. The number of discontinuous nodes on the 4,4,10 mm step was decreased which indicates that this tissue masking technique may be a useful approach for regularizing discontinuities. No significant changes in the registration

Table 8. Registration accuracy for Patient 1 inhale-to-exhale registration with and without tissue masking evaluated by landmark analysis. (SW = 1.0 for masked tissues, SW = 0.2 (16,16,40), 0.3 (8,8,20) and 0.5 (4,4,10) for unmasked tissues).

| Step Size (mm) | No tissue mask | | | With tissue mask | | |
|---|---|---|---|---|---|---|
| | N. disc nodes | N. vol changes > 5% | 3D Bif error (mm) | N. disc nodes | N. vol changes > 5% | 3D Bif error (mm) |
| 16,16,40 | 0 | 317 (5%) | 3.2 (3.4) | 0 | 102 (2%) | 3.3 (3.9) |
| 8,8,20 | 0 | 3064 (6%) | 2.0 (2.0) | 0 | 1734 (4%) | 1.7 (1.9) |
| 4,4,10 | 1 | 22275 (6%) | 1.5 (1.4) | 0 | 14854 (4%) | 1.3 (1.4) |

accuracy were noted, which was expected as most of the landmarks were located within the lung and the landmarks in the bony anatomy undergo very little motion.

To see how the tissue masking affected registration of organs within the mask the 3D DTA analysis of deformed and target planning contours was repeated for the tissue masking registration (see Table 9). A small, but not statistically significant, improvement in registration accuracy was noted when using tissue masking.

The comparison of transformed and deformed density images was repeated for the transformations recovered on the 4,4,10 mm registration step. As seen in Figure 10(c) the use of tissue masking reduces the magnitude of tissue deformations which occur in the lung and diaphragm. The maximum difference between the transformed and deformed density images was reduced from 30.7 g/cm$^3$ to 12.5 g/cm$^3$ while the mean density

difference was reduced from 0.33 g/cm$^3$ to 0.25 g/cm$^3$. Since the registration parameters are the same for the lung there is little change in lung deformations; however, if the parameters were re-optimized it is possible that the reduced volume deformations in tissue may result in increased lung deformations.

Table 9. Registration accuracy for Patient 1 inhale-to-exhale registration with and without tissue masking evaluated on planning contours.

| Step Size (mm) | No Tissue mask | | | With tissue mask | | |
|---|---|---|---|---|---|---|
| | GTV COM shift (mm) | GTV DTA (mm) | Avg DTA (mm) | GTV COM shift (mm) | GTV DTA (mm) | Avg DTA (mm) |
| 16,16,40 | 7.3 | 5.6 (0.6) | 3.2 (1.6) | 7.7 | 5.5 (1.5) | 3.0 (1.6) |
| 8,8,20 | 3.0 | 2.5 (1.2) | 2.3 (0.8) | 2.3 | 2.3 (1.4) | 2.1 (0.6) |
| 4,4,10 | 1.8 | 1.8 (1.3) | 2.0 (0.6) | 1.2 | 1.8 (1.8) | 1.9 (0.5) |

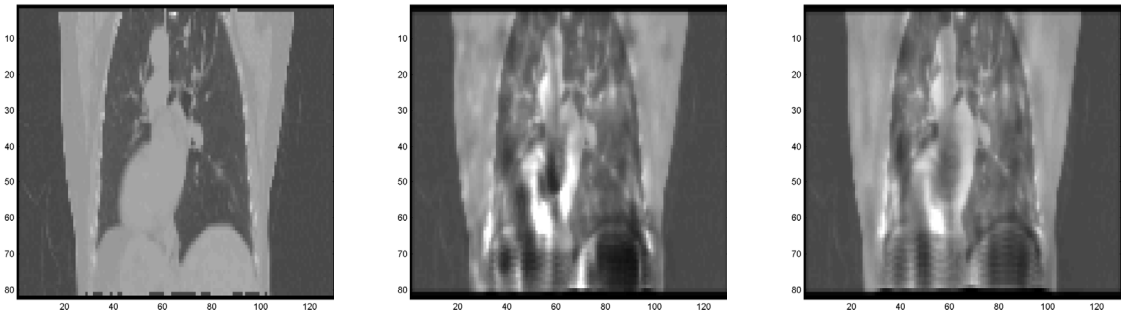

(a) Transformed source image (b) Deformed density image no mask (c) Deformed density image with mask

Figure 10. (a) Transformed Inhale-to-Exhale density image and corresponding deformed Inhale density images without (b) and with (c) tissue masking.

### 6.4.9 Dependence of dose calculation accuracy on image registration accuracy

The dose-volume histograms for the clinical target volume (CTV) for Patient 1 are shown in Figure 11. The registration accuracy corresponding to each set of deformation vectors is listed in Table 6. It can be seen that the deformation vectors recovered on the 8 mm, 4 mm and 2 mm steps result in very similar DVHs. The average statistical uncertainty of the dose in the CTV was 3%. The mean dose error in the CTV was 4% for the vectors recovered on the 16 mm step vectors compared to the 2 mm step vectors. The 16 mm step deformation vectors registration error exceeds the dose grid resolution. For the 8 mm and 4 mm step vectors the mean difference in the CTV dose compared to the 2 mm step vector calculation was 2% or less.

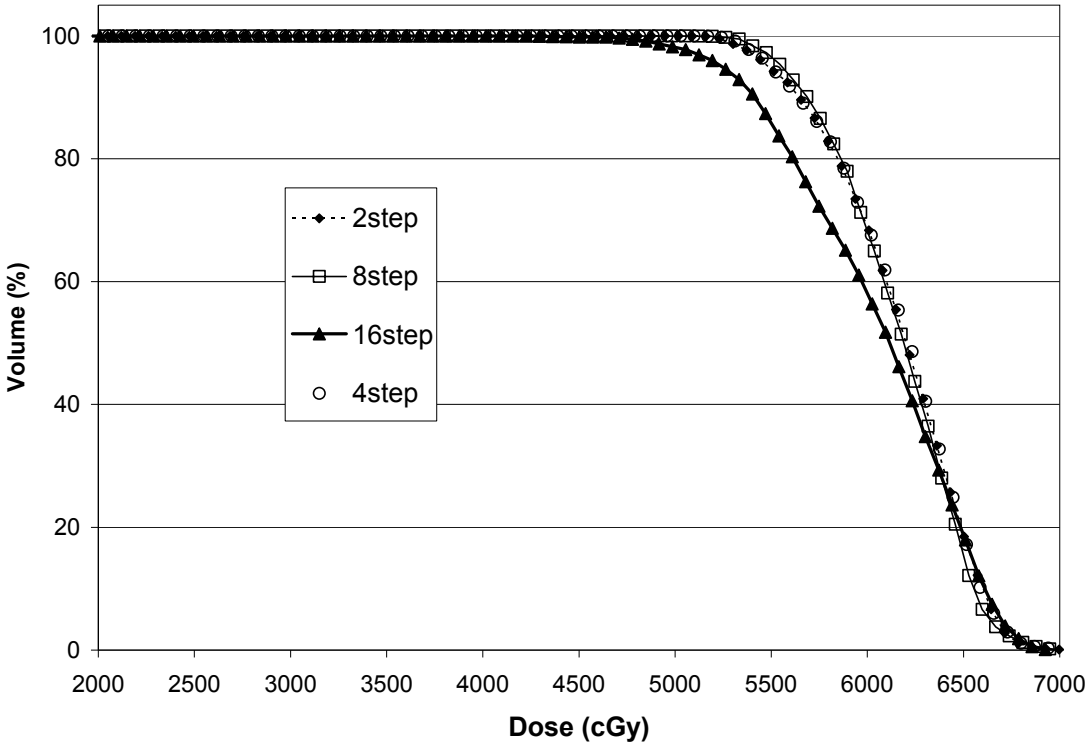


Figure 11. Inhale-to-Exhale dose volume histograms for Patient 1 CTV.

Rosu *et al*[16] investigated the sensitivity of the cumulative dose distribution to registration accuracy in lung. They found no significant effect on the dose when the registration accuracy was smaller than the dose grid size, however, dose discrepancies of a few Gray occurred for relatively small registration errors in regions of steep dose

gradients. More investigation of the dependence of 4D dose calculation accuracy on the image registration accuracy is needed.

## 6.5 DISCUSSION

The registration accuracy obtained with ANIMAL for all 5 patients using a deformation lattice spacing of 4 times the image resolution (4 mm) was comparable to the uncertainty of the registration accuracy evaluation metrics. The modest improvement in registration accuracy on the 2 mm deformation lattice spacing as well as the increased number of discontinuities and increased interpolation required to remove them leads us to question whether it is necessary to perform the registration on this final resolution step. Ultimately the requirements for image registration accuracy should be determined by its influence on the 4D dose calculation accuracy which, in turn, is limited to the inherent image resolution.

Among the different accuracy metrics used, each had its advantages and disadvantages. Image cross-correlation offers a global measure of registration accuracy which is simple to compute and automatic. However, because it is a global measure no information can be discerned about local regions of disagreement and the values are not very intuitive, especially for predicting the resultant 4D dose calculation accuracy. Homologous landmarks give a point-to-point measure of the registration accuracy but are limited by the accuracy with which they can be identified and the registration accuracy can be quantified only in those regions where suitable landmarks can be found.

It should also be noted that the assessment of the image registration accuracy using readily identifiable landmarks is biased due to the fact that these high-contrast objects are more easily brought into alignment by a similarity function based on matching image intensities. Distance to agreement of planning contours is a less accurate metric than using landmarks as it does not involve matching homologous points, but provides a better coverage over a structure surface and gives an intuitive measure of registration accuracy in regions where the dose calculation accuracy is of interest.

To account for the discontinuous motion which occurs at the chest wall/lung boundary, other groups[11] have registered the lungs separately. However, the requirement for a continuous deformation field for the 4D Monte Carlo dose calculation is not

compatible with the use of two separate sets of deformation vectors which are likely to be discontinuous across their boundaries unless a boundary matching criterion is used. In our case, acceptable registration accuracy with a limited number of discontinuities was obtained by masking and registering all tissues simultaneously. However, the patient images that were used in this study contained tumors that were not in close proximity to the chest wall. In the case where the tumor appears to slide along the chest wall we would expect that registration of both stationary and moving tissues together would limit the ability of ANIMAL to recover the motion of the tumour as the algorithm assumes a continuous deformation field.

The regularization of vector discontinuities could be partially accomplished by interpolation of deformations at discontinuous nodes which modestly reduced the number of discontinuities within the deformation field. The limitation of this regularization method is that it is applied after the estimate of the deformation vector is obtained. Therefore, if the deformation vector estimated at a particular node on each iteration is consistently discontinuous, despite the interpolation correction, the final sum of corrected estimates may still be discontinuous. An alternative, and more native, approach to regularizing discontinuities would be to implement a penalty term within the objective function which is based on the Jacobian determinant value at each node[17]. Such an approach can be used to control different levels of stiffness for tissues[13] as well as enforcing conservation of mass. In its current implementation, mass conservation is not enforced by the ANIMAL algorithm. This must be considered when using the recovered deformation vectors for input to our defDOSXYZ 4D Monte Carlo dose calculation code.

A drawback of the ANIMAL algorithm in its current implementation is the large number of registration parameters that need to be tuned and the significant inter-patient variation in the optimized values for these parameters. Before this algorithm can be implemented for clinical use, further work is needed to examine the sensitivity of the registration accuracy to these parameters and to determine a set of global parameters which can be applied to all or readily identifiable subsets of 4D CT patients. On the other hand, the flexibility of the algorithm presents a number of advantages including a possibility of using image gradient data as an additional similarity feature for registration,

the availability of numerous similarity functions and the relative ease of algorithm modification.

## 6.6 SUMMARY

In this chapter we discussed the application of the ANIMAL non-linear image registration algorithm was used for registration of thoracic 4D CT images using a multiresolution strategy. The code was modified to interpolate deformations at nodes where discontinuities in the deformation vectors occur. Image registration accuracy was evaluated by cross-correlation of transformed and target images, distance-to-agreement analysis of anatomical landmarks and triangulated surfaces constructed from manual contours. On average, the 3D DTA of transformed and target landmarks was 1.6 mm. Comparing transformed and target 3D triangulated surfaces derived from planning contours, the average GTV COM shift was 2.0 mm and the 3D DTA was 1.6 mm. An average DTA of 1.8 mm was obtained for all planning structures. All accuracy metrics were within the uncertainty of the landmark and contour analysis. With the code modification, the number of discontinuities was unchanged or modestly reduced, except on the final resolution step. Issues such as level of registration accuracy required and mass conservation in image registration need to be addressed for application of non-linear registration for 4D dose calculation.

## 6.7 REFERENCES


1 Collins D.L. "3D Model-based segmentation of individual brain structures from magnetic resonance imaging data" Ph.D. dissertation, Department of Biomedical Engineering, McGill University (1994).

2 Collins D.L., Holmes C.J., Peters T.M. and A.C. Evans "Automatic 3-D model-based neuroanatomical segmentation" Human Brain Mapping 3 pp. 190-208 (1995).

3 Collins D.L. and A.C. Evans "ANIMAL: validation and applications of nonlinear registration-based segmentation" Int. J. Pattern Recognition and Artificial Intelligence **11** 1271-1294 (1997).

4 Bazaraa M.S. "Linear programming and network flows 3rd ed." J. Wiley (2005).

[5] Rey D., Subsol G., Delingette H. and N. Ayache "Automatic detection and segmentation of evolving processes in 3D medical images: Application to multiple sclerosis" Medical Image Analysis **6** 163-179 (2002).

[6] Christensen G.E., Rabbitt R.D. and M.I. Miller "Deformable templates using large deformation kinematics" IEEE Transactions on Image Processing **5** 1435-1447 (1996).

[7] Pan T., Lee T-Y., Rietzel E. and G.T.Y. Chen "4D-CT imaging of a volume influenced by respiratory motion on multi-slice CT" Med. Phys. **33** 333-340 (2006).

[8] Schnabel J.A., Rueckert D., Quist M, Blackall J.M., Castellano-Smith A.D., Hartkens T., Penney G.P., Hall W.A., Liu H.L., Truwitt C.L., Gerritsen F.A., Hill D.G. and Hawkes D.J. "A generic framework for non-rigid registration based on non-uniform multi-level free-form deformations" Proceedings of MICCAI 2001, LNCS 2208 Springer-Verlag, Berlin (2001).

[9] Pekar V., McNutt T.R. and M.R. Kauss "Automated model-based organ delineation for radiotherapy planning in prostatic region" Int. J. Radiat. Oncol. Biol. Phys. **60** 973-980, (2004).

[10] Pevsner A., Davis B., Joshi S., Hertanto A., Mechakalos J., Yorke E., Rosenzweig K, Nemeh S., Erdi Y.E., Humm J.L., Larson S., Ling C.C. and G.S. Mageras "Evaluation of an automated deformable image matching method for quantifying lung motion in respiration-correlated CT images" Med. Phys. **33** 369-376 (2006).

[11] Rietzel E. and G.T. Chen, "Deformable registration of 4D computed tomography data" Med. Phys. **33** 4423-4430 (2006).

[12] Rosu M., Chetty I.J., Balter J., Kessler M., McShan D. and R. Ten Haken "Dose reconstruction in deforming anatomy: dose grid size effects and clinical implications" Med. Phys. **32** 2487-2495 (2005).

[13] Ruan D., Fessler J., Robertson M., Balter J. and M. Kessler "Deformable registration using regularization that accommodates local tissue rigidity" Med. Phys. **33** 2186 (2006).

[14] Robbins, S., Evans A.C., Collins D.L. and S. Whiteside "Tuning and comparing spatial normalization methods" Proceedings of MICCAI 2003 pp. 910-917 (2003).

[15] Sarrut D., Boldea V., Miguet S. and C. Ginestet "Simulation of four-dimensional CT images from deformable registration between inhale and exhale breathe-hold CT scans" Med. Phys. **33** 05-617 (2006).

[16] Rosu M., Chetty I.J., Kessler M.L. and R.K. Ten Haken "Monte Carlo non-adaptive 4D treatment planning in conformal radiation therapy: why, how and what to look for", Integrating new technologies into the clinic: Monte Carlo and image-guided radiation therapy, Proceedings of theAAPM summer school, Windsor, Canada pp. 293-310 (2006).

[17] Noblet V., Heinrich C., Heitz F., and J-P. Armspach "3-D deformable image registration: a topology preservation scheme based on hierarchical deformation models and interval analysis optimization" IEEE Trans. Image Processing 14(5) pp.553-566 (2005).

# Chapter 7:

# A non-linear image registration-based correction method for motion artifacts in 4D-CT

## 7.1 INTRODUCTION

In this chapter we review sources of image artifacts in 4D CT image acquisition and present a method for correction of these artifacts using interpolation of adjacent image data. A temporal interpolation method is investigated which uses non-linear image registration of temporally adjacent artifact-free breathing phases. The temporal interpolation method was validated by simulating 4D binning artifacts using a mathematical breathing phantom. The method was also applied to correction of artifacts in patient 4D CT images.

## 7.2 IMAGE ARTIFACTS IN 4D CT

As mentioned previously in Chapter 2 section 2.6.1.1, although 4D CT by definition decreases motion artifacts by labeling acquired slices by the breathing state significant artifacts can still occur in 4D image data sets due to binning artifacts and motion during slice acquisition. An example of a 4D CT artifact is shown in Figure 1. In these images the anatomy appears discontinuous as it is reconstructed from image slices acquired at

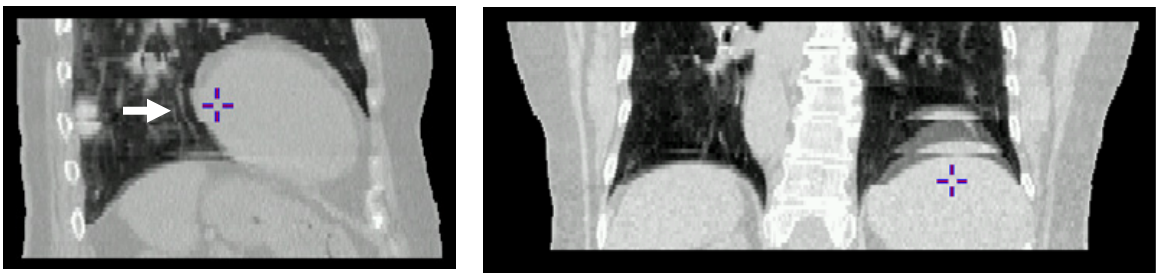

Figure 1. Examples of image artifacts occurring in 4D CT images.

different breathing amplitudes.

Binning artifacts can occur due to improper identification of the breathing phase[1,2] or because the patient breathing amplitude varies from one respiratory cycle to the next. These artifacts can be minimized by the use of amplitude-based 4D CT image sorting[4,5] or by retrospectively sorting phase-binned data by breathing amplitude[1-3]. The effectiveness of the latter method is limited by the temporal resolution of the phase bins and is not possible if the original patient breathing trace is unavailable. It is still possible to have artifacts in amplitude-binned data if image data is missing for a particular breathing amplitude or if the range of each amplitude bin is large. To exactly reconstruct the CT image at a given breathing level it is necessary to use projections acquired at exactly the same breathing state.

Artifacts in 4D-CT images affect organ delineation, non-linear registration and dose calculations performed on these images. In the case of non-linear registration image artifacts may cause discontinuities within the recovered deformation field because an artifact present on the source image is not present on the target image. Such discontinuities could potentially be used to identify image artifacts. Mutaf *et. al.*[6] reported the effect of phase binning errors on the volume of a moving spherical phantom determined from 4D CT images as well as average and maximum intensity pixel images generated from the same data. Volumetric deviations of up to 40% were noted when the motion amplitude approached the phantom dimensions.

## 7.3 MATERIALS AND METHODS

### 7.3.1 4D-CT artifact correction method

We propose a method for correcting artifacts in 4D CT images when the original raw image data and breathing curve are not available. The correction method replaces the artifact-containing region by CT numbers interpolated from adjacent artifact-free images. For artifacts with small spatial extent (ie., confined to one slice) it would be possible to use spatial interpolation. However, it is not always clear what is the true anatomical representation. Furthermore, spatial interpolation is not possible at remote image locations where neighboring slices are not present.

Temporal interpolation of adjacent artifact-free 4D-CT images is possible using non-linear image registration to determine the anatomical deformations which occur between the images to be interpolated (see Figure 2). By determining an appropriate weighting factor for the deformation vectors and applied this to the source image, it is possible to reconstruct the corrupted intermediate image. To improve the registration accuracy, and hence the image interpolation, it may be preferable to segment the anatomy of interest and perform registration on that region alone instead of the entire image. An example where this method is advantageous is when some parts of the anatomy may undergo large displacements whereas adjacent anatomy is stationary (ie., lungs and chest wall). Segmentation may also be necessary for a registration algorithm such as ANIMAL, where the deformation regularization parameters are globally defined.

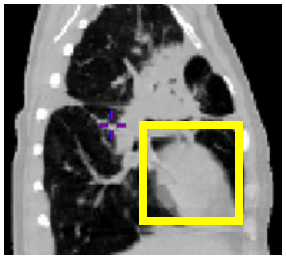

Step 1. Identify image artifact on current phase $T$.

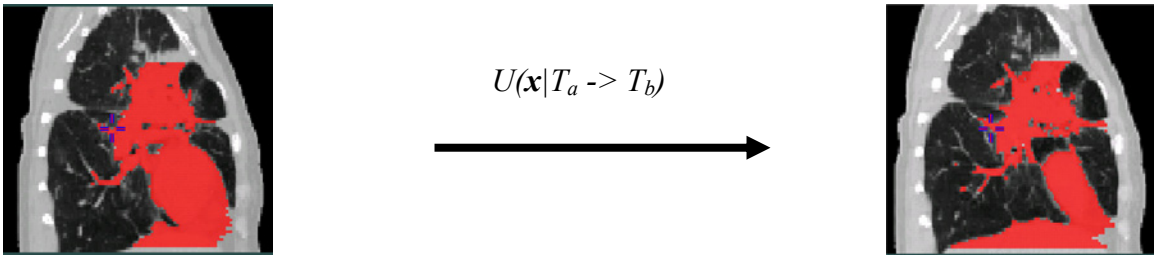


Step 2: Identify temporally adjacent artifact-free images Phase $T_a$ and $T_b$ and segment anatomy to be reconstructed. Determine non-linear transformation $U(\mathbf{x}|T_a \rightarrow T_b)$ from Phase $T_a$ to $T_b$.

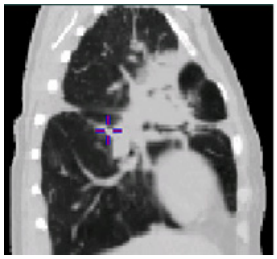

Phase $T_a(w^* U(\mathbf{x}|T_a \rightarrow T_b))$

Step 3: Determine weighting factor $w$ which most closely reproduces Phase $T$ and apply to Phase $T_a$.

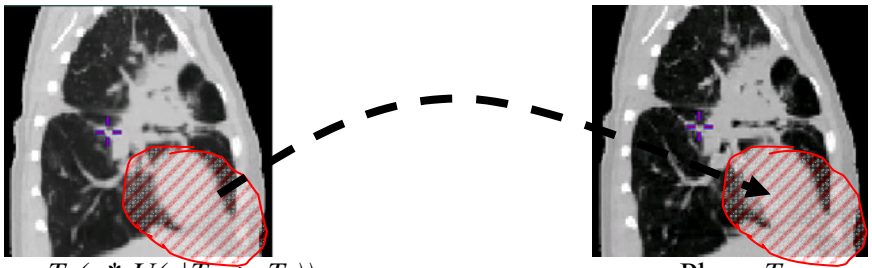

Phase $T_a(w^* U(\mathbf{x}|T_a \rightarrow T_b))$ Phase $T$

Step 4: Replace the CT numbers in region containing artifacts on Phase $T$ with corresponding region from reconstructed image.

Figure 2. Procedure for artifact correction method using temporal interpolation.

### 7.3.2 Validation using NCAT phantom

The artifact correction method was validated by synthesizing binning artifacts in CT data generated using the NCAT v1.12 mathematical breathing phantom[7,8]. These images are artifact-free by definition and can serve as objective ground truth. Artifacts were introduced in an image corresponding to 10% of full inhalation by combining image data generated for this phase at three different magnitudes of diaphragm motion (0.5 cm, 2.0 cm and 4.0 cm) as shown in Figure 3(b). CT images were generated with an image size of 256x256, a pixel size of 1.953 mm and a slice thickness of 2.5 mm.

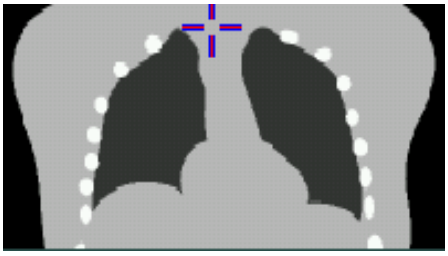

(a) Simulated CT image at 10% inhalation, diaphragm displacement = 2 cm

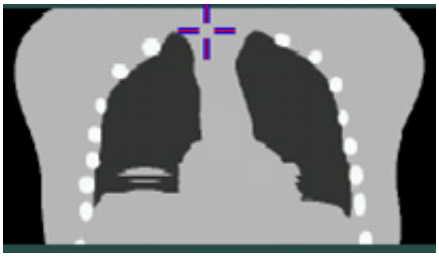

(b) Simulated 4D-artifact image by replacing image slices in (a) with slices from images generated for 2 cm and 4 cm diaphragm displacement

Figure 3. NCAT phantom images at 10% inhalation with and without simulated artifacts.

Non-linear registration was performed between the adjacent artifact-free images, generated for a maximum 2 cm diaphragm displacement, at full exhalation (0% inhalation) and 20% of full inhalation. Registration was performed in four steps using deformation lattice spacing of 32 mm, 16 mm, 8 mm and 4 mm respectively. On each registration step the phantom images were blurred with a Gaussian kernel of FWHM equal to the deformation lattice spacing. The registration parameters are summarized in Table 1.

The 10% inhalation image was reconstructed by empirically determining a weighting factor for the deformation vectors which resulted in a transformed image most closely matching the 10% inhale image. The best match was determined both visually and quantitatively from the difference image between the transformed and target image.

Table 1. ANIMAL parameters for registration of NCAT full exhalation to 20% inhalation

| Deformation lattice spacing (mm) | Iteration weight | Smoothing weight | Lattice diameter (mm) | Sublattice | iterations |
|---|---|---|---|---|---|
| 40,32,32 | 1.0 | 0.7 | 140 | 9 | 3 |
| 20,16,16 | 1.0 | 0.3 | 70 | 9 | 10 |
| 10,8,8 | 0.7 | 0.6 | 30 | 7 | 15 |
| 5,4,4 | 0.6 | 0.6 | 20 | 6 | 10 |

The accuracy of the image interpolation method was evaluated by comparing the correlation and voxel intensity difference between the artifact-containing and artifact-free data before and after correction.

### 7.3.3 Application to patient data

We applied the artifact correction method to two sets of patient 4D CT data containing motion artifacts in the heart and tumor, respectively (see Figures 4 and 5). The accuracy and efficiency of the registration in these cases was improved by segmenting only these structures for registration between the adjacent phases. The improvement in image quality was evaluated visually.

#### *7.3.3.1 Patient 1*

4D-CT images for Patient 1 contained a significant image artifact in the tumor where it appears to be split into two parts on the 20% and 40% exhalation images (phase 1 and 2). As the tumor did not appear to undergo any deformation between the adjacent inhale and 60% exhalation images it was decided that a rigid transformation would best describe the motion between these images.

The source and target images were first downsampled to a 256x256 resolution. The tumor was then segmented on the source and target images and the resulting masks were used for a rigid registration with a resolution of 0.97656 x 0.97656 x 1.25 $mm^3$.

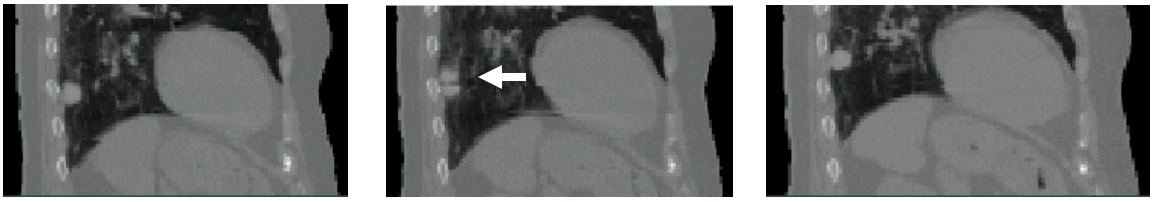

(a) Inhale (Phase 0) Source image

(b) 20% Exhale (Phase 1) Image to be interpolated

(c) 60% Exhale (Phase 3) Target image

Figure 4. 4D CT images for Patient 1 showing artifact-containing image (b) and temporally adjacent artifact-free images (a) and (c). Image size is 256x256x56. Location of the image artifact is indicated by arrow.

The segmented tumor at Phase 0 was linearly displaced using the rigid transformation with different weighting factors and the transformed tumor position was compared to the inferred correct tumor location on the original Phase 1 image. Using image manipulation methods available with the MNI Brain Imaging Toolbox the region of Phase 1 containing the corrupted tumor representation was replaced with the interpolated tumor image.

***7.3.3.2 Patient 2***

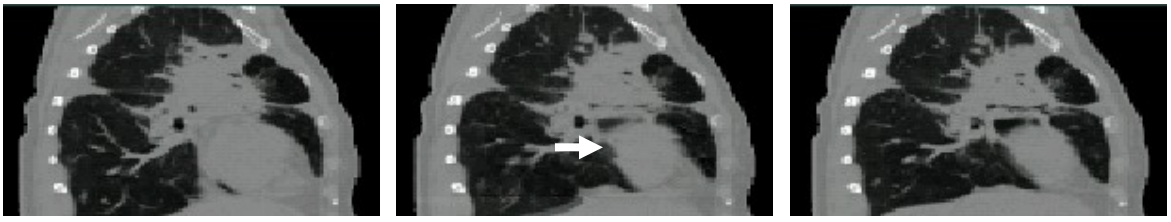

(a) Inhale (Phase 0) Source image

(b) 40% Exhale (Phase 2) Image to be interpolated

(c) 60% Exhale (Phase 3) Target image

Figure 5. 4D CT images for Patient 2 showing artifact-containing image (b) and temporally adjacent artifact-free images (a) and (c). Image size is 256x256x88. The location of the image artifact is indicated by the arrow.

Images at Phases 1 and 2 for Patient 2 contained a binning artifact in the heart (see Figure 5b). The heart and mediastinum were segmented on the source and target images

using image intensity thresholds. Non-linear registration between these images was performed with ANIMAL using the masks on 5 resolution steps ranging from 32 mm to 2 mm for the deformation lattice spacing. The registration parameters are listed in Table 2.

Table 2. ANIMAL parameters for registration of Patient 2 inhale to 60% exhalation

| Deformation lattice spacing (mm) | Iteration weight | Smoothing weight | Lattice diameter (mm) | Sublattice | iterations |
|---|---|---|---|---|---|
| 40,32,32 | 1.0 | 0.1 | 80 | 5 | 2 |
| 20,16,16 | 0.5 | 0.5 | 60 | 9 | 10 |
| 10,8,8 | 0.5 | 0.5 | 30 | 7 | 10 |
| 5,4,4 | 0.2 | 0.6 | 20 | 6 | 10 |
| 5,2,2 | 0.2 | 0.5 | 20 | 8 | 5 |

Similar to Patient 1, a weighting factor for the non-linear transformation was determined which, when applied to the source image, reconstructed the Phase 2 image as closely as possible. As shown in Step 4 of Figure 2, the voxel intensities were copied from the interpolated image to the original Phase 2 image for the region of the heart containing the artifacts.

## 7.4 RESULTS

### 7.4.1 Validation with NCAT phantom

The transformed target image resulting from non-linear registration of the NCAT images at 0% and 20% inhalation is shown in Figure 6 (b). A difference image formed by subtracting the transformed and target images is shown in Figure 6 (c).

From this image it can be seen that a good match between the transformed and target images is obtained. Some regions of discrepancy exist at tissue boundaries, due to interpolation of the transformed image, and in the ribs. The poor registration of the ribs could be improved by segmenting moving and stationary tissues and performing registration of each region separately. The cross-correlation of the source and target images before and after registration was 0.9527 and 0.9945, respectively.

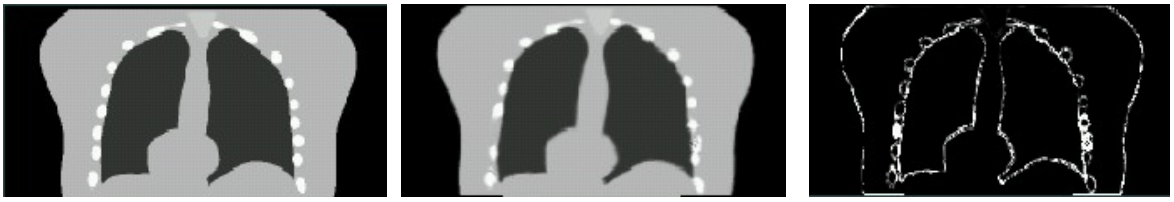

(a) target image (20% Inhalation) (b) transformed exhale image (c) difference image abs(transformed-target)

Figure 6. Comparison of target and transformed NCAT images at 20% Inhalation. The absolute difference in image intensities in shown in (c). Regions in white have voxel intensity difference > 10% of the maximum voxel intensity in (a).

10% inhalation images were generated by weighting this non-linear transformation with factors ranging from 0.3 to 0.5, the resulting differences images between the artifact-containing 10% inhalation and interpolated images are shown in Figure 7. Although the highest correlation (xcorr) was obtained for a weight of 0.5 visual inspection of the left diaphragm region indicates that a weight of 0.4 results in the closest reconstruction of the 10% inhalation image. Image correlation calculated over the whole anatomy is influenced by large differences in the regions containing artifacts, a more quantitative determination of the weighting factor could be determined by calculating correlation in an artifact-free region of interest.

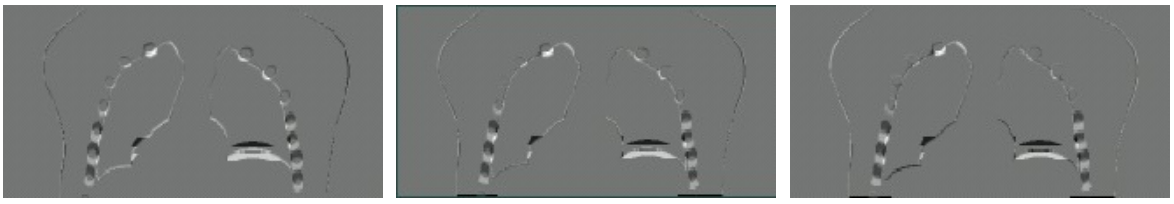

(a) Weight = 0.3 (xcorr=0.9903) (b) Weight = 0.4 (xcorr=0.9927) (c) Weight = 0.5 (xcorr=0.9928)

Figure 7. Absolute image intensity difference images at 10% inhalation (interpolated-original) for different weighting factors.

Figure 8 shows the 10% inhalation image before and after the artifact correction method was applied. Correlation of the artifact-free (Figure 8c) and corrupted images (Figure 8a) improved from 0.971 to 0.992 after artifact correction. The corresponding difference images also confirmed removal of the artifacts. However, some small areas of discrepancy are introduced at the tissue boundaries of the left lung due to an imperfect registration in this region.

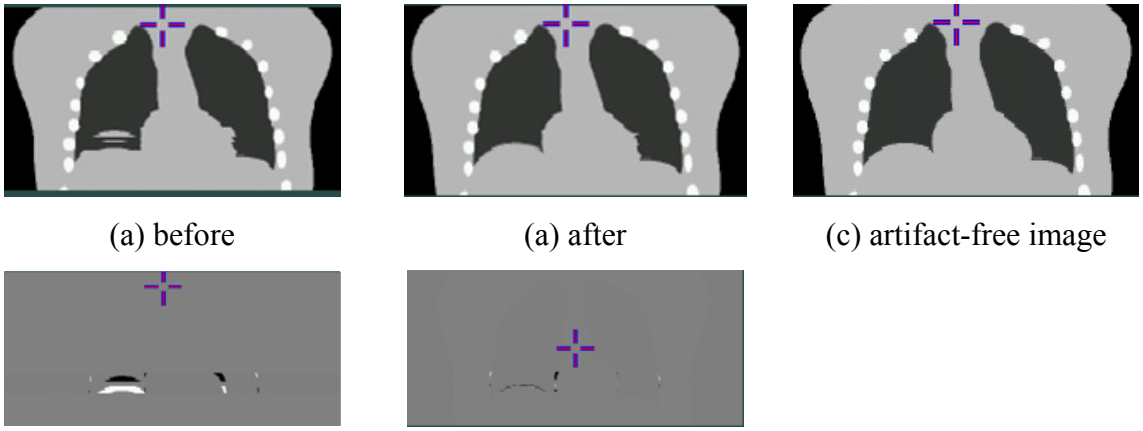

(a) before (a) after (c) artifact-free image

(c) difference image before (d) difference image after

Figure 8. 10% inhalation and differences images (a) before and (b) after artifact correction method is applied.

### 7.4.2 Correction of Patient 1 images

(a) location of segmented tumor before registration on 60% exhale image

(b) location of segmented after linear registration on 60% exhale image

(c) interpolated tumor position on 20% exhale image

Figure 9. Linear registration of segmented tumor. Original (a) and transformed tumor image (b) is superimposed on the target 60% exhale image, (c) interpolated tumor position (weight = 0.3) superimposed on 20% exhale image.

In Figures 9 (a) and (b) the segemented source and transformed tumor images are shown superimposed on the target 60% exhale image. The cross-correlation of the transformed and target segmented tumor is 0.8853. The translation of the tumor position determined from the linear registration was scaled by a factor of 0.3 to match the presumed tumor location on the 20% exhale image. The determination of the weighting factor in this case was somewhat subjective, however, the inference of the correct tumor position on this phase was guided by examining the tumor location of the adjacent phase images.

The 20% exhale (phase 1) images before and after artifact correction are shown in Figure 10 with the physician delineated contours. It can be seen that the presence of the artifact affected the tumor delineation and if a corrected image had been available the target volume would be reduced.

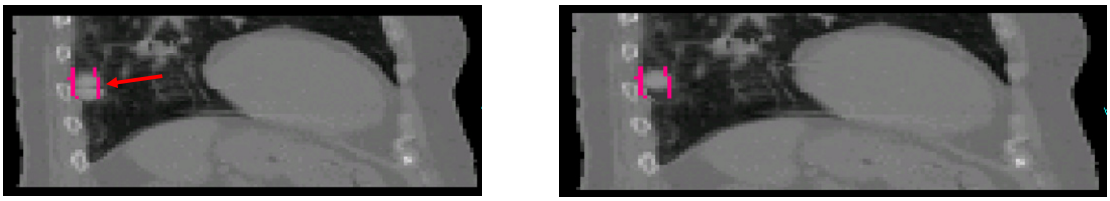

(a) original 20% exhale image (b) corrected 20% exhale image

Figure 10. 20% exhale image for Patient 1 before and after artifact correction was applied. Physician delineated target volume contours are shown in pink.

### 7.4.3 Correction of Patient 2 images

The segmented inhalation and 40% exhalation images are shown in Figures 11 (a) and (b). Initial cross-correlations of these two images, evaluated on the target image mask, was 0.9842. After non-linear image registration the correlation improved to 0.9917.

A weighting factor of 0.9 for the non-linear transformation was determined to best match the original 40% exhale image (see Figure 12). The corrected image in Figure 13(b) was formed by replacing image voxel intensities in the original 40% exhale image with values from the interpolated image in the region around the heart (as illustrated in Step 4 of Figure 2).

(a) Source image (b) Target image (c) Transformed image

Figure 11. (a) Segmented inhalation (source) and (b) 40% exhale images (target) with (c) transformed image resulting from non-linear registration of segmented images.

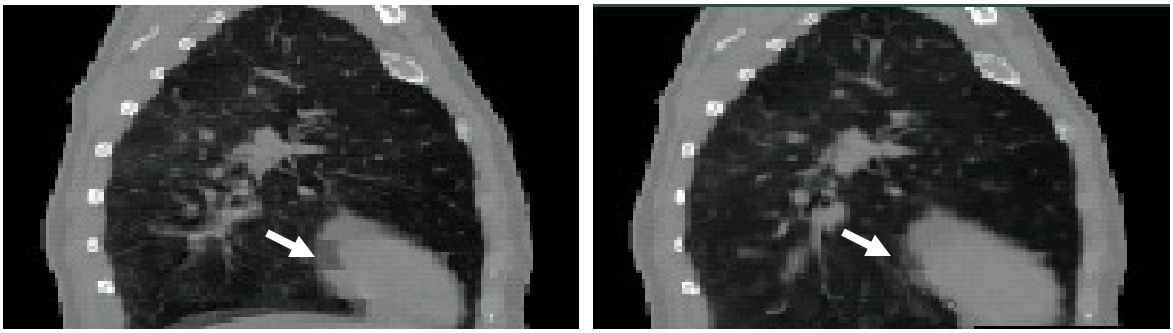

(a) 40% exhale image (b) Interpolated 40% exhale image

Figure 12. Original and interpolated 40% exhale images. The interpolated image in (b) was determined using a weighting factor of 0.9. The artifact indicated by the white arrow is not present in the interpolated image.

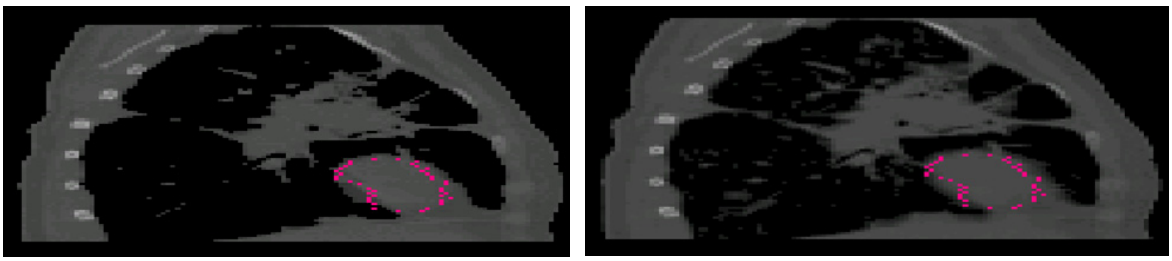

(a) 40% exhale image before correction (b) 40% exhale image after correction

Figure 13. 40% exhale image before and after artifact correction. Physician delineated heart contours shown in pink.

## 7.5 DISCUSSION

### 7.5.1 Limitations of the correction method

The artifact correction method requires temporally adjacent artifact free images. As the image data in the 4D CT data set consists of binned image sets, possibly corresponding to different breathing levels, these images may not be entirely free of artifacts. In this chapter the method was applied to visually identified artifacts however additional image artifacts may not be readily detectable and affect the accuracy of the temporal interpolation method. It may, however, be possible to detect image artifacts by registering two datasets as any inconsistencies in the anatomy would result in discontinuities in the recovered deformation field.

Another aspect of the artifact correction method that requires further investigation is the selection of the weighting factor for interpolation of the image data at the phase to be corrected. It is not sufficient to determine the weighting factor from the phase indices. Ideally the breathing amplitude at the phase of interest and the neighboring phases could be obtained from the patient's breathing curve measured at the time of image acquisition. The fractional displacement would provide a good estimate of the weighting factor. In the absence of such information the weighting factor could be determine by maximizing correlation between the original and interpolated images in a region of interest close to the region to be corrected. Furthermore, the accuracy of temporal extrapolation to end of phase images may be limited.

Finally, in order to quantify the accuracy of the correction method on patient data organ contours which estimate the correct anatomy are required. The physician must identify image artifacts and consider the location and shape of the anatomy on neighbouring phases when delineating organs.

### 7.5.2 Other artifact correction methods employing image registration

Our proposed artifact correction method makes use of reconstructed image data for interpolation. An alternate approach would be to use the raw projection data to interpolate slices at exactly the same breathing level. Ehrardt *et. al.*[9] used optical flow-based registration between scans acquired at neighboring respiratory states to interpolate images at the desired breathing level. The tidal volume measured by digital spirometry during

image acquisition was used to weight the velocity field given by the image registration. The method was implemented for an axial multi-slice CT acquisition so that interpolations were performed on scan segments acquired at each couch position. The optical flow-based interpolation was shown by visual inspection and quantitative measures to be superior to simple nearest neighbor linear interpolation.

## 7.6 SUMMARY

In this chapter we presented a method to correct 4D CT artifacts which occur due to errors in phase binning. The method does not require the patient breathing curve from the CT acquisition and relies instead on temporal interpolation of adjacent artifact-free CT data based on the non-linear transformation between these images. The method was demonstrated to improve image quality while reconstructing anatomy with a reasonable accuracy in both simulated and patient 4D CT images. Such correction methods have the potential to improve accuracy of organ delineation, image registration and dose calculations which use of 4D CT data.

## 7.7 REFERENCES


1 Rietzel E. and G.T.Y. Chen "Improving retrospective sorting of 4D computed tomography data" Med. Phys. **33** 377-379 (2006).

2 Fitzpatrick M.J., Starkschall G., Antolak J.A., Fu J., Shukla H., Keall P.J., Klahr P. and R. Mohan "Displacement-based binning of time-dependent computed tomography image data sets" Med. Phys. **33** 235-246 (2006).

3 Abdelnour A.F., Nehmeh S.A., Pan T., Humm J.L., Vernon P., Schoder H., Rosenzweig K.E., Mageras G.S., Yorke E., Larson S.M. and Y.E. Erdi "Phase and amplitude binning for 4D-CT imaging" Phys. Med. Biol. **52** 3515-3529 (2007).

4 Lu W., Parikh P.J., Hubenschmidt J.P., Bradley J.D. and D.A. Low "A comparison between amplitude sorting and phase-angle sorting using external respiratory measurement for 4D CT" Med. Phys. **33** 2964-2974 (2006).

5 Lu W., Nystrom M.M., Parikh P.J., Fooshee D.R., Hubenschmidt J.P., Bradley J.D. and D.A. Low "A semi-automatic method for peak and valley detection in free-breathing respiratory waveforms" Med. Phys. **33** 3634-3636 (2006).

[6] Mutaf Y.D., Antolak J.A. and D.H. Brinkmann "The impact of temporal inaccuracies on 4DCT image quality" Med. Phys. **34** 1615-1622 (2007).

[7] Segars, W., "Development and application of the new dynamic nurbs-based cardiac-torso (NCAT) phantom", Ph.D. dissertation, University of North Carolina, 2001.

[8] Segars W.P., Lalush D.S. and B.M.W. Tsui, "Modeling respiratory mechanics in the MCAT and spline-based MCAT phantoms," IEEE Trans Nucl Sci **48** 89-97 (2001).

[9] Ehrardt J., Werner R., Saring D., Frenzel D., Lu W., Low D. and H. Handels "An optical flow based method for improved reconstruction of 4D CT data sets acquired during free breathing" Med. Phys. **34** 711-721 (2007).

# Chapter 8:

# A comparison of dose warping methods for 4D Monte Carlo dose calculations in lung

## 8.1 INTRODUCTION

Dose calculation methods which incorporate tissue motion are an important tool for evaluating the effect of respiratory motion on the delivered dose distribution. A 4D dose calculation method uses a sum of remapped doses calculated on 4D CT images of the patient at different respiratory phases to determine the cumulative dose received over the entire respiratory cycle. Non-linear image registration is used to track how tissue elements move and deform from a reference phase to each imaged phase. A number of methods for remapping the dose to the reference phase have been proposed, including center-of-mass (COM) tracking[1] and trilinear interpolation[2]. In this chapter we compare calculations of dose distributions remapped between extreme breathing phases against the 4D Monte Carlo dose code defDOSXYZ in which the reference dose grid voxels deform to match anatomical deformations at the phase of interest. Remapped dose distributions are compared in geometries ranging from simple deforming phantoms to 4D CT patient data. Thus far, only the grid size dependence of dose remapping methods has been discussed in the literature[1]. No comparison of the trilinear remapping method and the simpler COM remapping method has been made. Such a study is required to determine what errors are introduced by the use of simpler dose warping methods and the potential improved accuracy using the defDOSXYZ code.

Some aspects of the work presented in this chapter was previously published as the following paper "A direct voxel tracking method for four-dimensional Monte Carlo dose calculations in deforming anatomy" E. Heath and J. Seuntjens, Med. Phys. **33** 434-445 (2006).

## 8.2 METHODS AND MATERIALS

### 8.2.1 Dose remapping methods

Three methods of 4D Monte Carlo dose calculation were compared: warping dose distributions calculated with DOSXYZnrc using COM remapping, using Trilinear remapping with octant subdivision and dose calculations using the deformable voxel tracking code defDOSXYZ. For all comparisons performed in this study the DOSXYZnrc and defDOSXYZ simulations used the same phase space file, transport parameters and number of histories. ECUT and PCUT were set to 0.7 MeV and 0.001 MeV, respectively and the EXACT boundary crossing algorithm with a skin depth of 3 electron mean free paths was used.

#### *8.2.1.1 Trilinear remapping*

In this study we implemented the dose remapping technique using tri-linear interpolations which was described by Rosu *et al.*[1]. The dose is calculated on the anatomy at a given breathing phase (*T*) or deformed state from which we wish to remap the dose to the reference anatomy. The voxel correspondence of the reference grid to this phase is then obtained from registration of the reference anatomy to the deformed anatomy at phase *T*. Each reference voxel is subdivided into octants and the translation of the center of mass of each octant from the reference phase to the deformed state is determined by interpolating from the deformation vectors at the voxel nodes (see Figure 1). After the center of each octant is remapped to the dose calculation grid, the dose at this point in the deformed state is interpolated from the dose in the neighbouring voxels. The dose in each reference voxel is then determined from the average of the re-mapped dose in each octant.

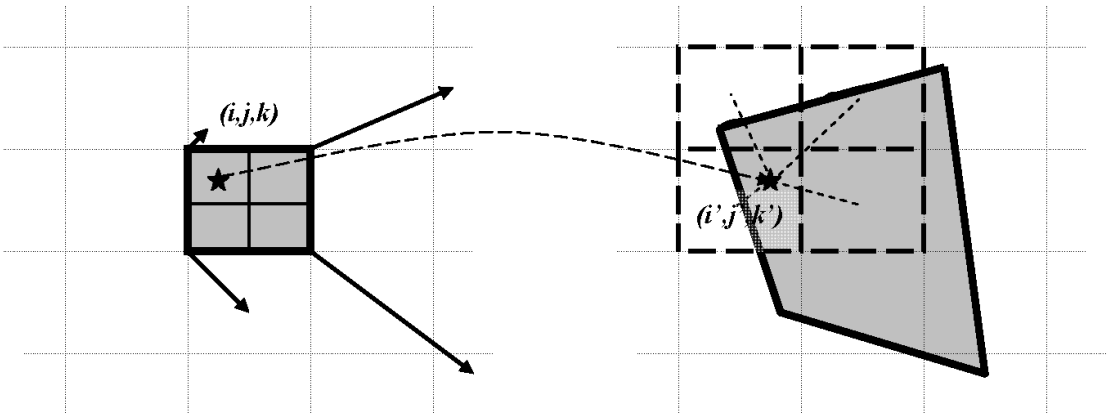


Reference dose grid Dose grid at phase *T*

Figure 1: Illustration of trilinear dose re-mapping method where reference voxels are subidivided into octants. The center of mass of each octant is mapped to the dose grid at phase *T* and the dose contribution to this point is interpolated from neighbouring voxels (indicated by dashed lines). Adapted from Figure 2(b) of Reference 1.

#### *8.2.1.2 COM remapping*

A COM dose remapping method, similar to that of Flampouri *et. al.*[2], was developed based on the above trilinear dose remapping without octant subdivision and with no dose interpolation. In this case the remapped dose in each reference voxel *(i,j,k)* is taken from the voxel *(i',j',k')* at phase *T* which overlaps the corresponding mapped location of the reference voxel center of mass. The differences between the COM and TL dose remapping approaches are illustrated in Figure 3 of Chapter 3.

### 8.2.2 Comparison of dose warping methods in simple deforming phantom

Dose calculations with the defDOSXYZ code were compared with calculations remapped from "exhale" to "inhale" using the trilinear interpolation method in simple rectangular phantoms with voxel sizes ranging from 1.0 cm to 0.25 cm and deformations from 10% to 50% (see Figure 2). The densities of voxels in the deformed "exhale" phantom were adjusted to ensure conservation of mass.

Dose profiles along the z axis of the phantom were calculated for beam incidence along the z axis (parallel to the deformations) and with the beam oriented 90 degrees to

the z axis (perpendicular to deformations). In the latter case the central axis of the beam was aligned along the distal edge of the deformed phantom in order to test the accuracy of the dose remapping in a region of high dose gradient. For the trilinear remapping method, the dose was calculated using DOSXYZnrc on the exhale geometry and then the dose was remapped to the inhale geometry. For the defDOSXYZ method the calculation used the inhale geometry as the reference dose grid and deformed this grid using the vectors relating the inhale to exhale geometry.

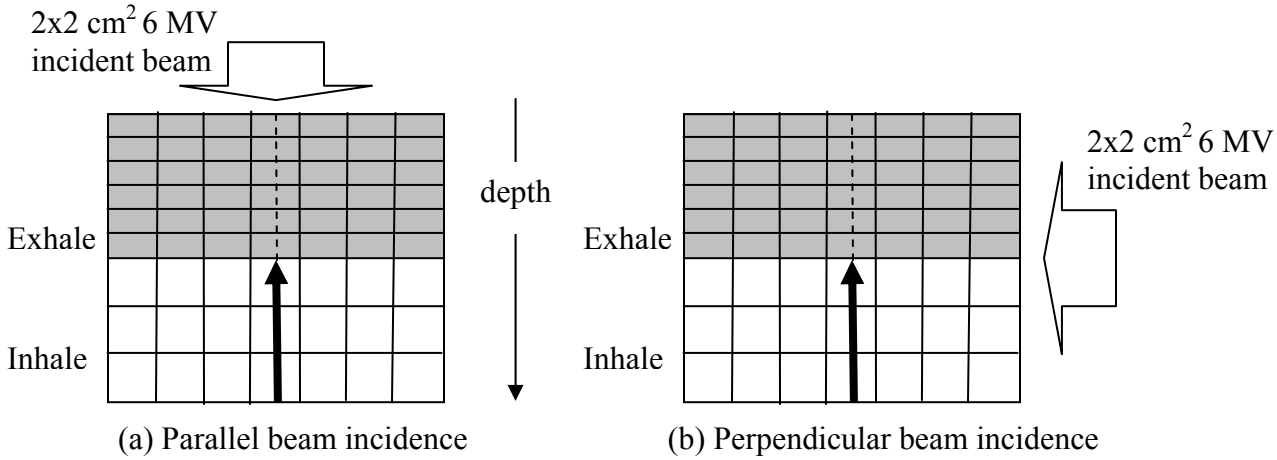


Figure 2. Geometry of deforming phantom. Voxel densities are 0.5 g/cm$^3$ at the inhale phase and 1.0 g/cm$^3$ at the exhale phase (indicated by grey shading). Dashed line indicates location of dose profiles.

### 8.2.3 Comparison of dose warping methods in anatomical breathing phantom

To investigate the nature of dose discrepancies that could be expected when using a tri-linear interpolation dose remapping method for patient calculations the defDOSXYZ and trilinear dose remapping methods were compared using 4D CT images generated using the NCAT mathematical breathing phantom[3,4]. A breathing period of 4 seconds, a maximum AP expansion of 1.2 cm and a 2 cm diaphragm motion were specified which is consistent with normal breathing. 3D CT images were created at exhale (phase=0) and inhale (phase=0.455) with a voxel size of 0.3125 cm and 160x160x160 pixels with no cardiac motion.

The exhale image of the NCAT phantom was registered to the inhale image using the ANIMAL non-linear registration algorithm. Registration of the exhale NCAT image

to the inhale image was carried out starting at a deformation lattice spacing of 2.5 cm and reducing the step size by a factor of two for each subsequent registration. The transformation determined at the previous step size was used as starting estimate for the next step size. The correlation coefficient of image intensities was used as a measure of image similarity. The smoothing weight was set to 1.0 to maximize the smoothness of the estimated deformations. At each step size the optimum combination of registration parameters (lattice diameter, sublattice and similarity) were determined based on the final objective function value. The correspondence of the target image and the transformed source image was also inspected visually and their cross-correlation was calculated. The deformation maps were also tested for discontinuities which cause collapsed or overlapping voxels. As a preliminary validation of the registration accuracy the deformation maps were compared to the respiratory motion vectors defined for each control point in the NCAT phantom. At the end of the registration process the deformation vectors were interpolated to the resolution of the dose calculation grid to obtain the vectors at the nodes of each voxel and written to a file for input to the defDOSXYZ code.

If the image registration is not perfect, then the deformed exhale anatomy will not exactly reproduce the inhale anatomy. Therefore the deformed anatomies on which the defDOSXYZ and trilinear remapping calculations are performed will not be identical. In order to minimize the effects of registration errors on the comparison of defDOSXYZ and the trilinear dose mapping method, the density matrix on which the inhale dose calculation was based was generated by transforming the exhale density matrix with the exhale-to-inhale transformation. This transformed exhale density image was then resampled to the original grid resolution using trilinear interpolation. For the trilinear remapping approach, a dose distribution was calculated on the transformed exhale anatomy using DOSXYZnrc with 1 billion histories from a 10x10 $cm^2$ 6 MV phase space file incident anteriorly. The dose contribution from this phase to the reference exhale image was then determined using the Exhale-to-Inhale deformation vectors. For the defDOSXYZ calculation, the dose contribution from the inhale phase to the reference exhale anatomy was calculated using the same Exhale-to-Inhale vectors for the same

incident beam. The resolution of the dose grid for all calculations was equal to the CT voxel resolution.

### 8.2.4 Comparison of dose warping methods in 4D CT patient data

#### *8.2.4.1 Patient data*

4D CT images for 2 lungs patients were used to compare COM remapping, Trilinear remapping and defDOSXYZ calculations. Patient 1 had a 5.2 cc tumour (GTV) located in the upper left lobe which underwent a displacement of approximately 1.2 cm between exhale and inhale (see Figure 3(a)). Patient 2 had a 112 cc primary target volume (GTV) located in the right lower lobe with mediastinal nodal involvements of 63 cc and 12 cc, respectively (see Figure 3(b)). The primary target volume underwent a maximum breathing excursion of 9 mm.

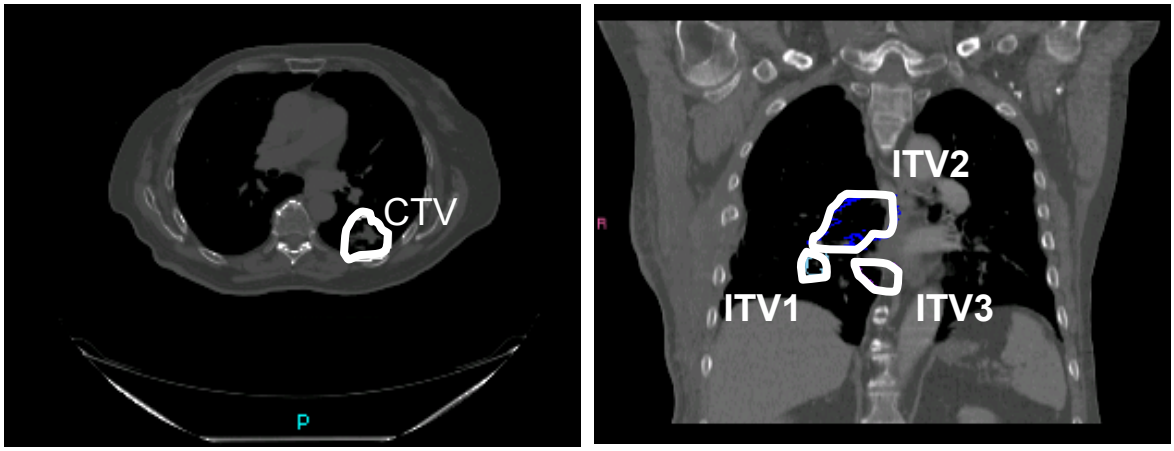


(a) Patient 1 (b) Patient 2

Figure 3. Location of target volumes for 4D CT Patient 1 and 2.

Thoracic 4D CT images for Patient 1 were acquired at the MD Anderson Cancer Centre using the axial mode of a Discovery ST PET-CT scanner (GE Medical Systems, Milwaukee, WI). Scans were retrospectively sorted into ten breathing phases with an image resolution of 0.98 mm and slice thickness of 2.5 mm. Images for Patient 2 were acquired at the Massachusetts General Hospital using a Lightspeed Qx/I 4-slice CT scanner (GE Medical Systems, Milwaukee, WI).

#### *8.2.4.2 Non-linear image registration*

Non-linear image registration was performed between the extreme breathing phases. For Patient 1 the reference phase was Inhale and the target phase was Exhale. Registration was performed using the ANIMAL code using a multiresolution process ending with a deformation lattice spacing equal to the image resolution. The average registration accuracy for this patient was evaluated to be 1.2 ± 1.2 mm based on manually identified landmarks. For Patient 2, registration between the exhale and inhale phase was performed using a B-splines method[5] with a 50 mm control point spacing. Based on expert identified homologous points the average accuracy of deformable registration in the lungs was 4.21 ± 2.42 mm.

#### *8.2.4.3 Treatment plans*

Three different treatment planning scenarios were considered. Patient 1 was planned using a 2-field 18 MV 3D-CRT plan using the CADplan treatment planning software (Varian Medical Systems, Palo Alto, CA). The target was delineated on the reference inhale phase and a 7 mm margin was added for microscopic extent. No additional margins for setup uncertainties were used. Two planning strategies were considered for this patient: (1) tracking and (2) no motion compensation. For the tracking case a treatment plan was defined on the target exhale phase and for the non-motion compensated case the plan was defined on the inhale phase with no additional margins to account for the inhale-exhale tumor motion. In both cases the dose received at the exhale phase remapped to the inhale phase was evaluated. The prescription dose was 60 Gy, delivered in 15 fractions.

Patient 2 was planned using a 5-field IMRT plan with the CORVUS (NOMOS Corp., Cranberry Township, PA)) treatment planning software. Internal target volume (ITV) margins were determined based on fusion of target volumes drawn on separate phases of the 4D CT image set and a further 8 mm expansion was added for the planning target volume. The prescribed dose was 63 Gy delivered in 35 fractions. Characteristics of the three planning strategies are summarized in Table 1.

Table1: Planning scenarios considered for 4D CT patient data

| Planning scenario | Patient | Maximum GTV motion (mm) | Plan type | Margins | Reference phase |
|---|---|---|---|---|---|
| ITV margin | Patient 2 | 9 | IMRT | ITV + 8 mm | Exhale |
| Tracking | Patient 1 | 12 | 3D-CRT on exhale phase | GTV + 7 mm | Inhale |
| No motion compensation | Patient 1 | 12 | 3D-CRT on inhale phase | GTV + 7 mm | Inhale |

#### *8.2.4.4 Dose calculations*

Phase space files were generated using a BEAMnrc model of the linear accelerator. For Patient 1 particles were tracked through the linear accelerator jaws to a scoring plane 70 cm below the target. For Patient 2 particles were tracked to a scoring plane above the jaws. Transport through the jaws and MLC was performed using a model developed by Siebers *et al.*[6] which was modified to model multiple Compton scatter interactions[7].

Two separate patient dose calculations were performed. For the dose calculations employing dose remapping, the DOSXYZnrc code was used to calculate the dose distribution on a patient density matrix generated from the transformed reference anatomy. Similarly to the calculations in the anatomical breathing phantom, for these calculations we use the transformed anatomy instead of the target phase anatomy to eliminate errors introduced by registration inaccuracies. The dose distribution was then remapped to the reference geometry using both COM and trilinear (TL) remapping methods. A second dose calculation was performed using the defDOSXYZ code to determine the dose received by the deformed reference-to-target geometry. The dose calculation process is summarized in Figure 4. Note that the dose between the extreme phases only was calculated. For all calculations a nominal dose grid size of one-quarter image resolution was used (4x4x2.5 $mm^3$), however different dose grid spacings were investigated for Patient 1 to determine the influence of dose grid size on discrepancies between the different dose calculation methods.

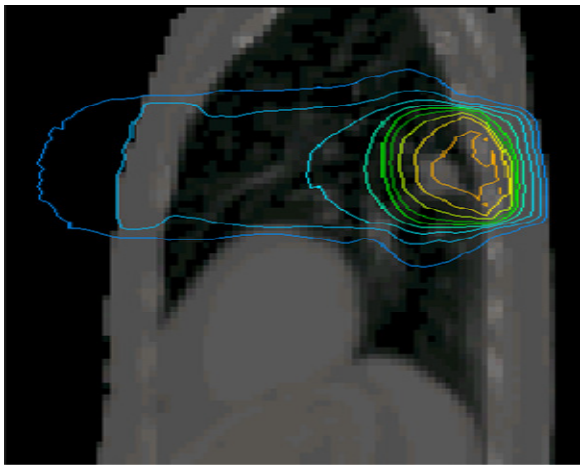

1. Calculate dose on transformed reference anatomy

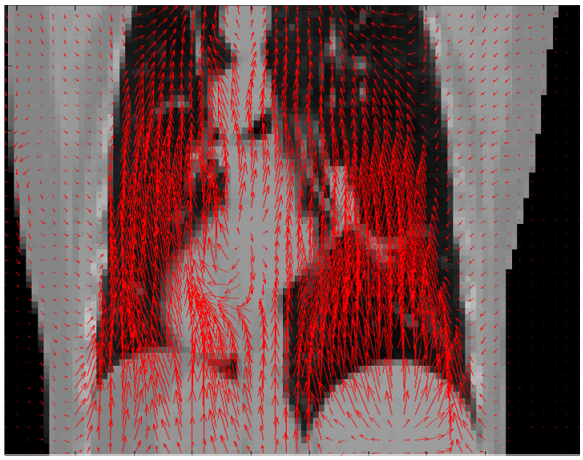

1. defDOSXYZ calculation on reference anatomy using deformation vectors

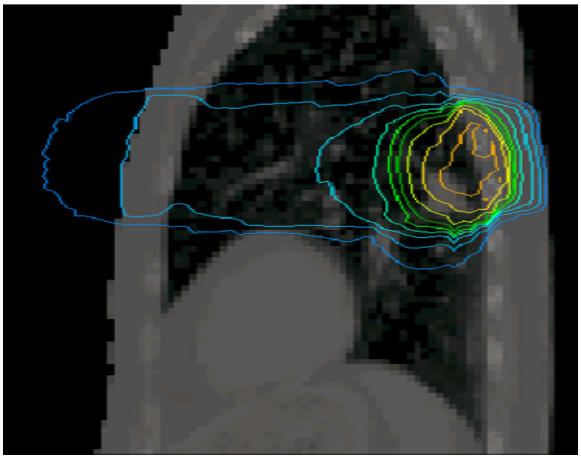

2. Remap dose distribution to reference phase using COM or TL remapping

(a) Dose remapping calculation

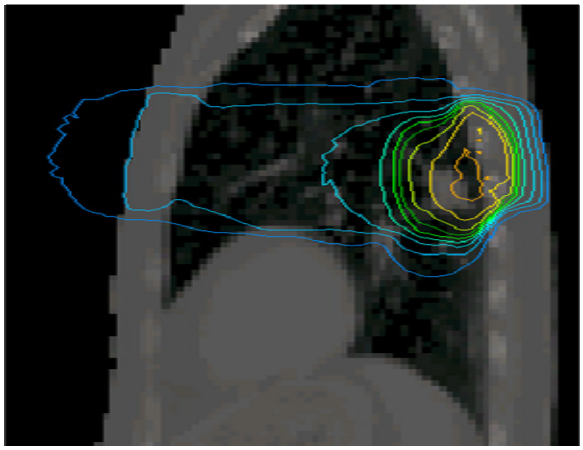

2. Dose calculated on deformed anatomy on reference voxel grid.

(b) defDOSXYZ calculation

Figure 4. Illustration of dose remapping and defDOSXYZ dose calculation process.

#### *8.2.4.5 Evaluation*

The dose distributions calculated by the three methods: defDOSXYZ, remap COM and remap TL were compared in terms of dose volume histograms determined for all the planning structures as well as dose difference maps. Dose difference maps were compared with dose gradients, deformation magnitude and volume changes to investigate their influence on any discrepancies between the 4D dose calculation methods.

## 8.3 RESULTS

### 8.3.1 Comparison of deformable dose calculation methods in simple deforming phantoms

#### *8.3.1.1 Simulation times and incidence of boundary crossing errors*

DOSXYZnrc and defDOSXYZ simulations were run with sufficient incident histories to obtain a statistical uncertainty of less than 1% for the dose inside the water phantom. For the DOSXYZ simulations this required simulation times ranging from 3 minutes to 26 hours on a 1.7 GHz Pentium M processor for voxel sizes of 1.0 cm to 0.1 cm, respectively. The defDOSXYZ simulation times were 4 to 11 times longer, depending on the voxel size. This increase in the ratio of simulation times was attributed to an increased incidence of boundary crossing errors as the voxel size was reduced.

Boundary crossing errors occur when the boundary crossing algorithm incorrectly determines that a voxel boundary has been crossed. On the subsequent particle transport step, the inconsistent assignment of the current voxel index relative to the actual particle position causes the HOWFAR subroutine to return a negative minimum distance to the next particle boundary. These errors are known to occur in DOSXYZnrc simulations and are attributed to two sources. First, truncation of calculated distances occurs when storing these quantities in a 4-byte floating point representation. These "round-up" errors can lead to uncertainty in determining whether a particle has crossed a boundary when the distance is on the order of $10^{-5}$ cm or less. The increased number of calculation steps in defDOSXYZ leads to a higher potential for round-up errors. Second, the PRESTA-I electron transport algorithm uses an approximation of the distance to the voxel boundary which has been demonstrated to generate boundary crossing errors[8]. An increased incidence of such errors in defDOSXYZ simulations is attributed to the complex nature of the deformed geometries. It should be noted that for dose calculations in an undeformed geometry, the incidence of negative distances in defDOSXYZ was consistent with that for DOSXYZnrc.

The incidence of these boundary crossing errors was minimized by two approaches. First, we used an 8-byte floating point representation for all quantities calculated by the HOWFAR and HOWNEAR subroutines. Second, the EXACT boundary crossing algorithm, which employs a more accurate distance to boundary calculation, was used for

all simulations. A skin depth of 3 electron mean free paths, at which the boundary crossing algorithm switches to the PRESTA-I algorithm, was found to minimize the incidence of boundary crossing errors.

The occurrence of boundary crossing errors was handled in the same manner as for the DOSXYZnrc code. When HOWFAR returned a negative distance on the order of $10^{-4}$ cm or smaller the distance to the boundary was reset to zero and the particle was moved to the voxel boundary. When a negative distance which is larger in magnitude than this cutoff occured the particle was discarded.

#### *8.3.1.2 Dose profiles*

The comparison of the two dose remapping methods in simple deforming phantoms is summarized in Figures 5 through 12. In Figure 5 depth dose profiles are compared for a 50% voxel deformation as a function of voxel size for a 2x2 $cm^2$ 6 MV phase space incident along the depth direction, parallel to the deformations. The trilinear remapping method underestimates the remapped dose in the inhale phantom by 25%, on average, for 1 cm voxels, 3.7%, 2.0% for 0.5 cm and the 0.25 cm voxels, respectively and 1% for the 0.1 cm voxel size. Larger discrepancies of up to 31% exist in the regions of steep dose gradients at the entrance and distal surfaces of the phantom. The very large discrepancies for the 1 cm voxel size are attributed to the (rather unrealistically) large voxel size relative to the beam dimensions (2x2 $cm^2$) which causes dose along the central axis to be interpolated from points laterally outside the beam when using the trilinear remapping method. The voxels of the phantom are arranged such that the beam central axis coincides with a lateral voxel boundary. The results for this voxel size are expected to be sensitive to the location of the voxel boundaries with respect to the beam central axis.

Figure 6 shows the same calculations repeated for perpendicular beam incidence. The dose profiles for the inhalation phase are shifted to deeper depths as the voxels shift along the depth direction with expansion from exhale to inhale. Due to the steep dose gradients that exist in the beam penumbra (up to 60%/2.5 mm) the discrepancies with the trilinear method are more significant than for parallel beam incidence but improve with smaller voxel size. Excluding the penumbra, the trilinear method underestimates the

remapped dose by 29%, 8.0% and 0.2%, on average, for the 1 cm, 0.5 cm and 0.25 cm voxel sizes. Discrepancies in the penumbra region are significantly larger than for the

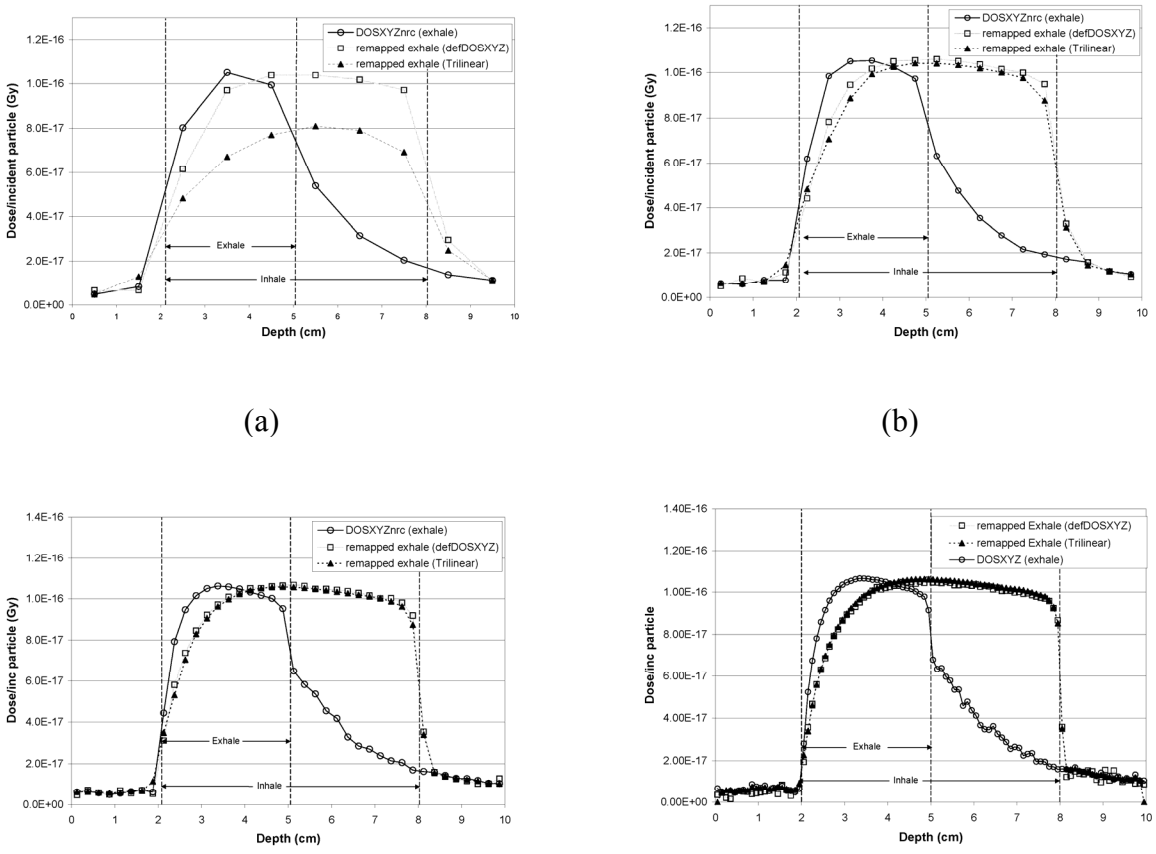


Figure 5. Depth dose profiles for beam incidence parallel to deformations for different voxel sizes: (a) 1 cm voxels 50% deformation (b) 0.5 cm voxels 50% deformation (c) 0.25 cm voxels 50% deformation and (d) 0.1 cm voxels 50% deformation. Dashed lines indicate phantom boundaries at inhale and exhale phases. The material beyond the phantom boundaries is air.

case with parallel beam incidence. As expected, a better estimation of the remapped dose is obtained when interpolating over a finer grid resolution. However, the accuracy in regions where dose gradients exist is limited by the dose averaging over contributions of neighbouring voxels when interpolation is performed. Furthermore, since the compression of the reference voxels to the exhale phase is accounted for by defDOSXYZ the calculation of dose on the

exhale phase is performed at a higher resolution than in the case of the trilinear remapping method. This is the reason why the trilinear remapping still shows some averaging in the high

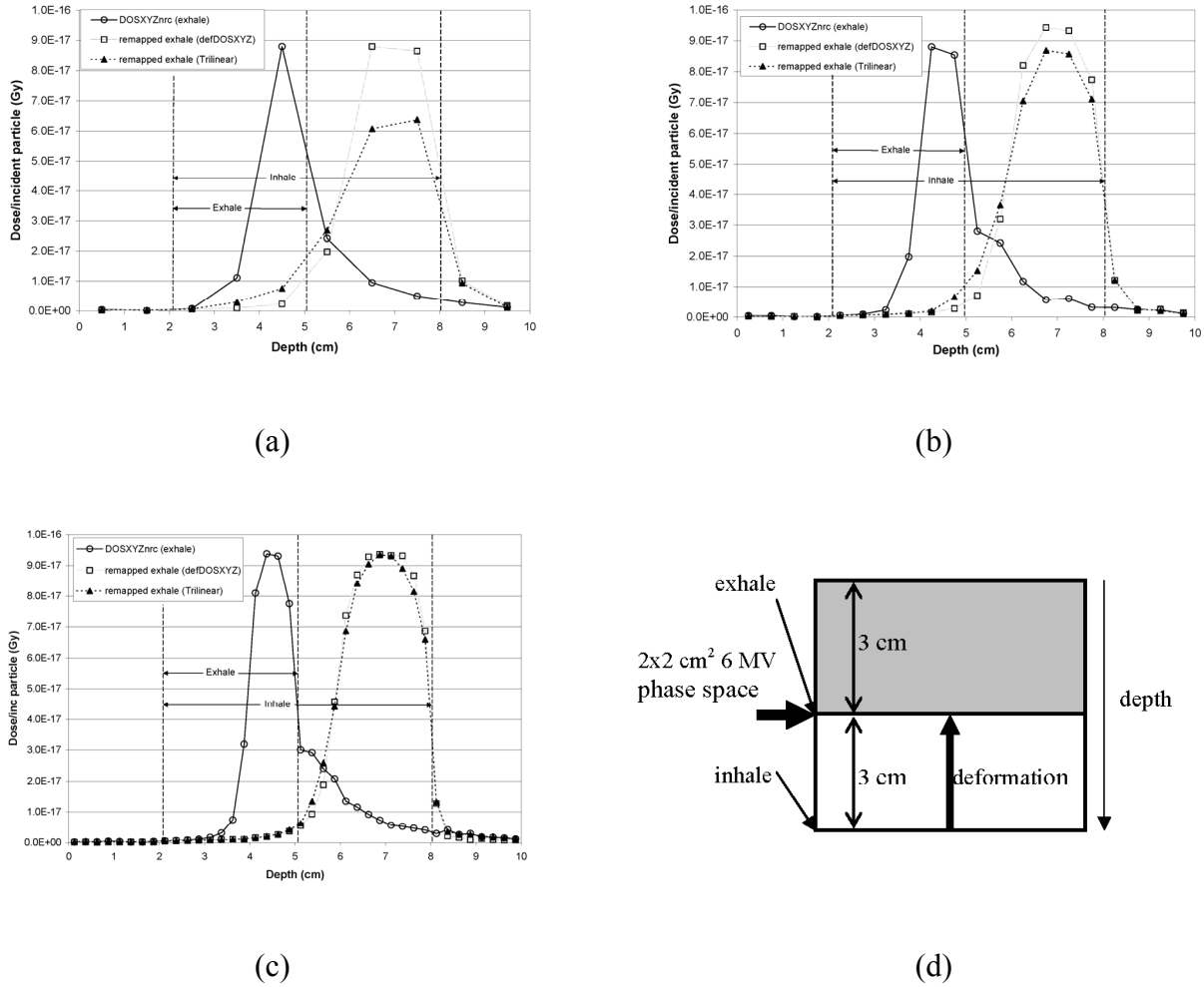


Figure 6. Depth dose profiles for beam incidence perpendicular to deformations for different voxel sizes: (a) 1.0 cm voxels 50% deformation (b) 0.5 cm voxels 50% deformation (c) 0.25 cm voxels 50% deformation and (d) phantom geometry. Dashed lines indicate phantom boundaries at inhale and exhale phases. The material beyond the phantom boundaries is air.

gradient areas even as the voxel size is reduced.

In Figure 7 depth dose profiles are compared in a phantom consisting of 0.25 cm voxels for different deformation magnitudes. Note that for the 10% deformation case it was necessary

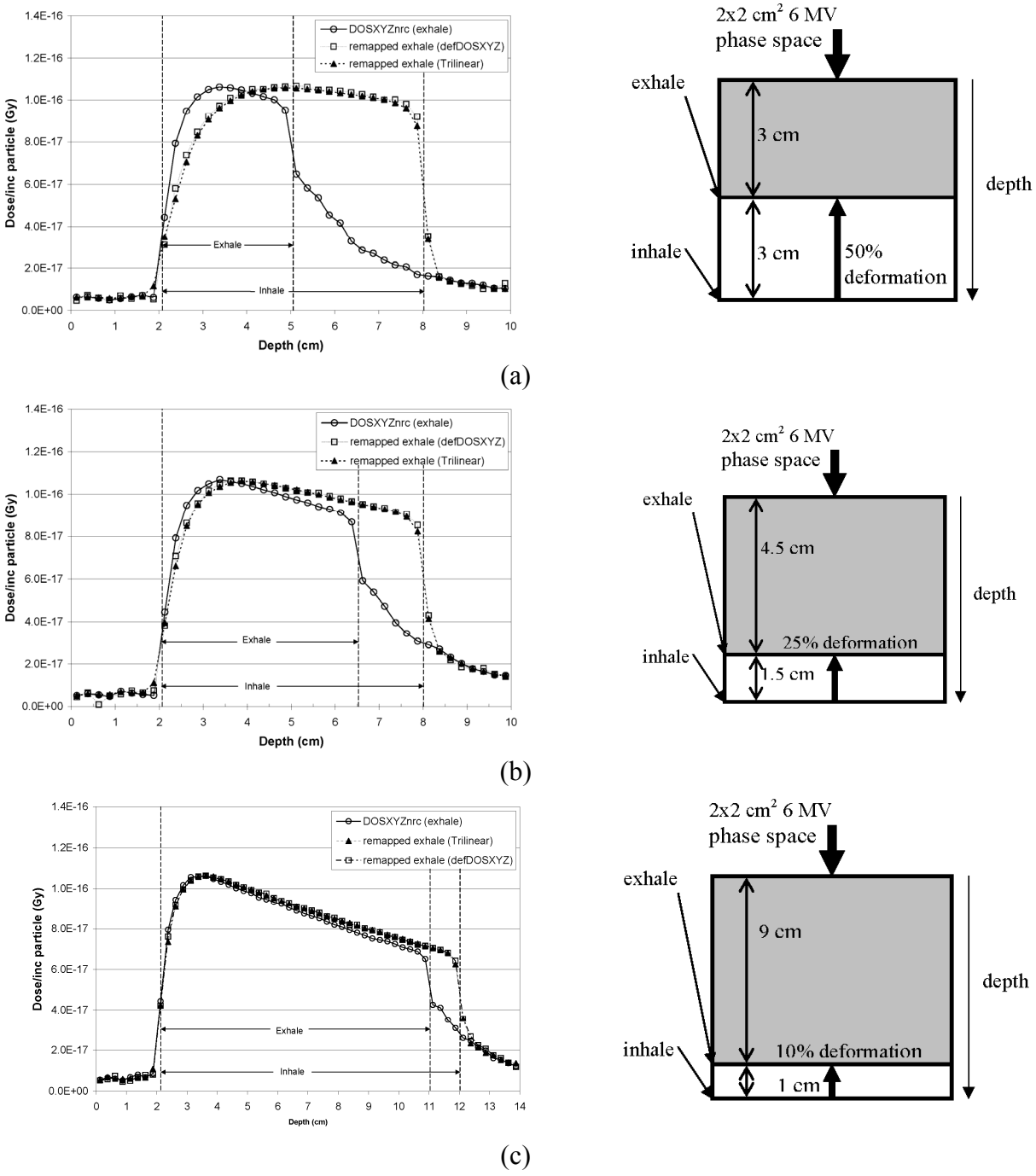


Figure 7. Depth dose profiles for 0.25 cm voxel phantom with parallel beam incidence for different deformation magnitudes: (a) 50% deformation (b) 25% deformation and (c) 10% deformation. Dashed lines indicate phantom boundaries at inhale and exhale phases. The material beyond the phantom boundaries is air.

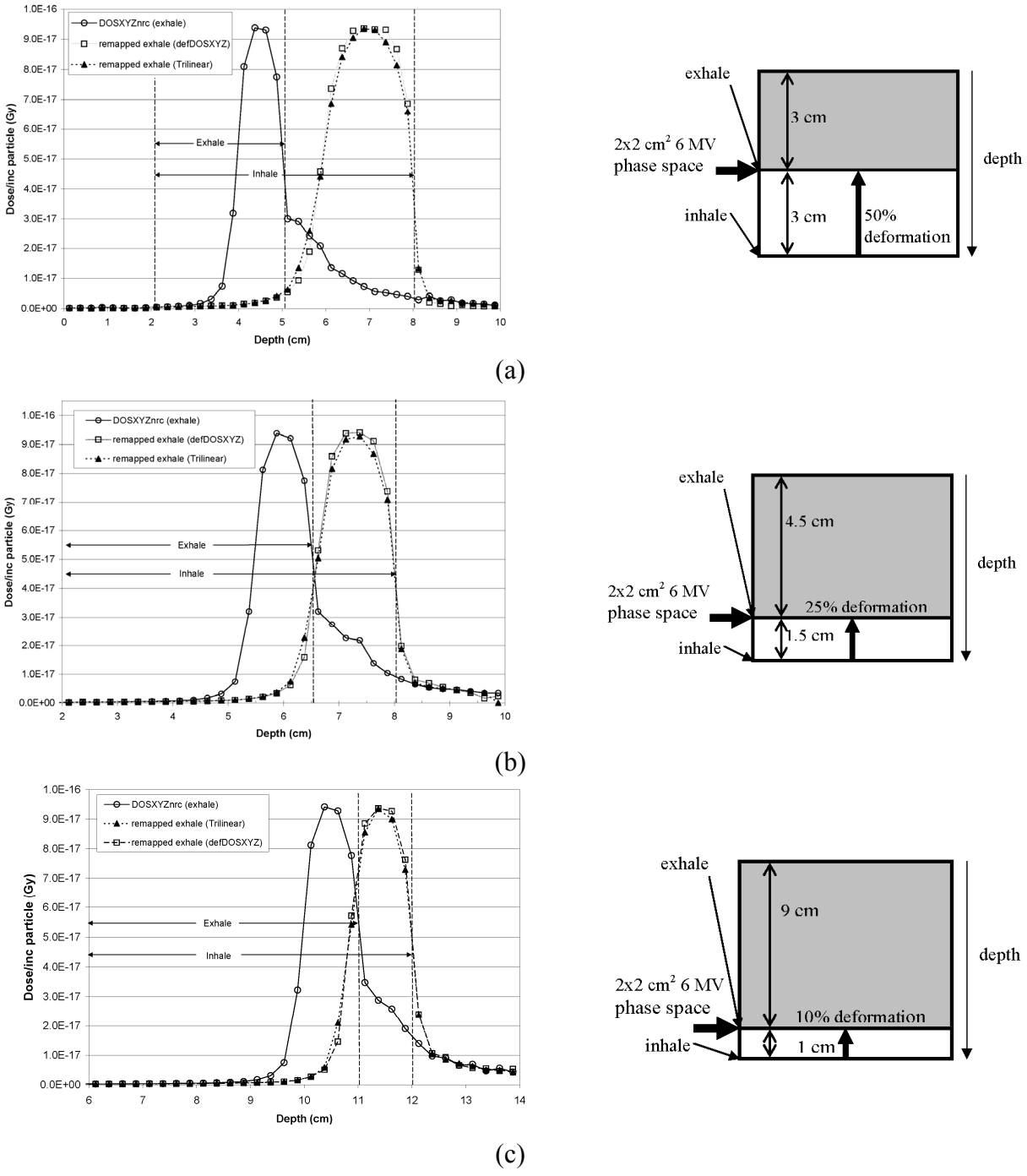


Figure 8. Depth dose profiles for 0.25 cm voxel phantom with parallel beam incidence for different deformation magnitudes: (a) 50% deformation (b) 25% deformation and (c) 10% deformation. Dashed lines indicate phantom boundaries at inhale and exhale phases. The material beyond the phantom boundaries is air.

for the inhale phantom to be extended to 10 cm in depth, compared to 6 cm for the 50% and 25% deformation. The trilinear method underestimates the remapped dose on average by 2.0% for a 50% deformation to 1.0% for the 25% and 0.5% for the 10% deformations. The magnitude of the deformation has an impact on how well the deformed voxels are aligned with the reference grid. The larger the deformation the more the remapped dose point at inhale deviates from the center of the exhale voxel to which it is mapped and the more the dose is interpolated from dose in neighbouring voxels. In the case of perpendicular incidence (see Figure 8) the accuracy of the trilinear interpolation method does not appear to be significantly affected by the magnitude of voxel deformations. Instead, the discrepancies between the defDOSXYZ calculation and the trilinear method appear to be mainly due to the steep dose gradients which exist for this configuration.

### 8.3.2 Comparison of deformable dose calculation methods in anatomical breathing phantom

Overall, the magnitude and general direction of the estimated deformation vectors agreed with how the respiratory motion is modeled in NCAT which leads us to conclude that ANIMAL can recover deformations on the order of those introduced by respiratory motion. However, a more rigorous validation of ANIMAL for such applications is required. The optimized registration parameters are summarized in Table 2.

Table 2: Optimized parameters for ANIMAL non-linear registration of NCAT phantom inhale and exhale images.

| Step Size (mm) | Lattice diameter (mm) | Sub lattice (nodes) | Similarity-cost ratio | Iterations | Final cross-correlation |
|---|---|---|---|---|---|
| Initial cross-correlation: 0.988 | | | | | |
| 25 | 80 | 10 | 0.3 | 10 | 0.995 |
| 12.5 | 40 | 8 | 0.8 | 6 | 0.997 |

Due to how respiratory motion is modeled in the NCAT phantom at the chest surface large gradients in the deformations exist and registration could be performed only down to a minimum lattice resolution of 12.5 mm (deformations are subsampled at a 6.25 mm lattice spacing then averaged) otherwise collapsed voxels occurred. The use of this relatively large step

size limits the accuracy of the registration. However, using the transformed Exhale image for the trilinear remapping method ensures that comparison of the dose calculation methods is independent of the registration accuracy. The majority of voxel deformations calculated by the defDOSXYZ code as the anatomy is transformed from Exhale to Inhale are less than 10%. However, 26 voxels (0.001% of the phantom voxels) underwent volume deformations (compressions) of 200%.

The dose distribution calculated on the transformed exhale anatomy with DOSXYZnrc is shown in Figure 9(a). The remapped dose distributions at exhale determined using trilinear interpolation and the defDOSXYZ code, respectively, are shown in Figures 9 (b) and (c). The DOSXYZnrc calculation required 5.2 hours when split on 5 processors while the defDOSXYZ calculation required 12 hours. Dose deformations at the chest surface are visible which correspond to the inf/sup motion at these points. The percentage dose difference normalized to the maximum remapped Inhale (defDOSXYZ) dose, is shown in Figure 9(d). The maximum dose difference, on the order of 57% of the maximum remapped dose, occurs at the surface. This region of large dose discrepancy consists of a layer of 1 voxel thickness, which may be attributed to interpolation errors which occur when the transformed Exhale image is resampled to the original image grid resolution. However, beyond this surface layer the dose in the buildup region is underestimated by approximately 10%. This is consistent with the results in the simple deforming phantom study for which the deformations were perpendicular to the direction of beam incidence (see Figure 6). Otherwise, dose differences on the order of 10-20% occur in the penumbra, particularly on the inferior beam edge.

The majority of the deformations (see Figure 10) are along the AP direction, parallel to the incident beam, however where the largest dose discrepancies occur there are also significant deformations along the inf/sup direction. This is again consistent with the observed dose differences in the simple deforming phantoms where larger discrepancies are obtained with perpendicular beam incidence.

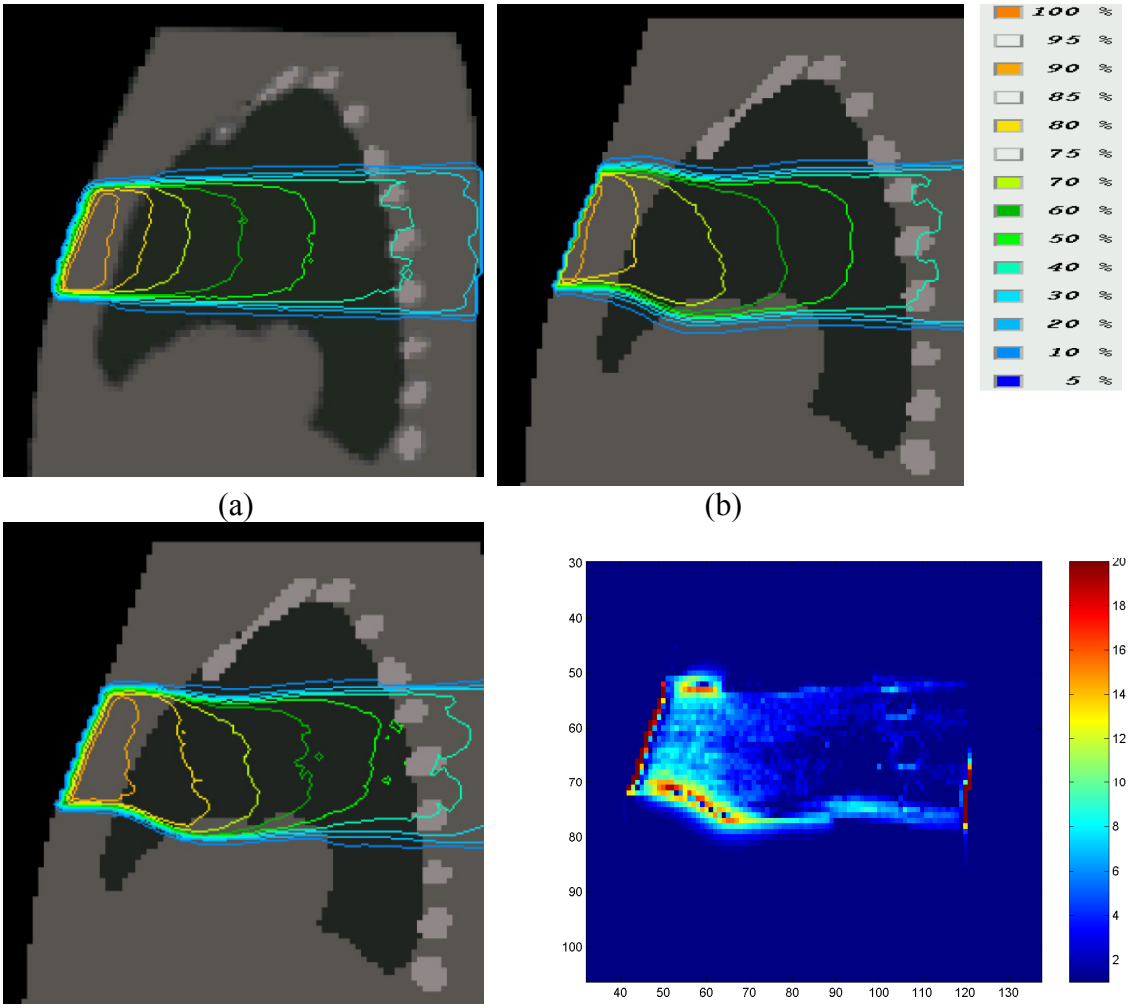


Figure 9. Comparison of remapped inhale dose in NCAT phantom (a) dose calculated on Transformed Exhale anatomy with DOSXYZnrc (b) Transformed Exhale dose remapped to Exhale (reference) phase using trilinear interpolation with octant remapping method (c) Inhale dose remapped to Exhale (reference) phase calculated with defDOSXYZ (d) difference map (defDOSXYZ-Trilinear)/max(defDOSXYZ). The dose grid resolution is 3.125x3.125x3125 $mm^3$.

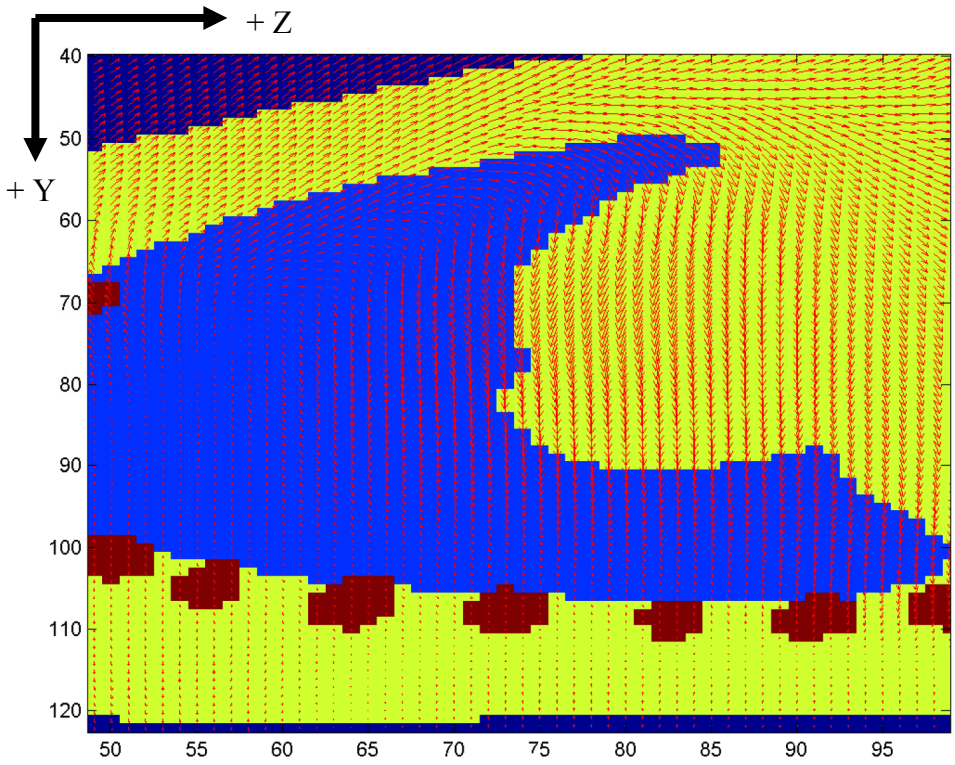


Figure 10: ANIMAL Exhale-to-inhale deformation vectors corresponding to Figure 9.

### 8.3.3 Comparison of deformable dose calculations in 4D CT lung patients

#### *8.3.3.1 Patient 1 2-field 3D CRT plan: tracking scenario*

***(a) DVH comparison for nominal dose grid size***

The Inhale-Exhale dose-volume histogram for the CTV is shown for the three different dose calculation methods in Figure 11. The dose calculated on the transformed inhale (target) anatomy, which is the planned dose distribution, is included to illustrate the effect of remapping the dose to the reference phase. Five hundred million histories were calculated for each beam, requiring 30 hrs for a DOSXYZnrc calculation when split among five 3 GHz processors. The time for defDOSXYZ simulations were approximately 10 times slower than for DOSXYZnrc. The average statistical uncertainty on the dose calculated in the CTV was approximately 3%. Note that the ICRU requirement[9] of 95% coverage of the target volume by the prescription dose was not met because the treatment plan was generated using a dose calculation algorithm (CADplan) which assumed a homogeneous water composition for the patient. This does not predict the loss of lateral electronic equilibrium in the low density lung tissue which results in a lower dose to the tumour.

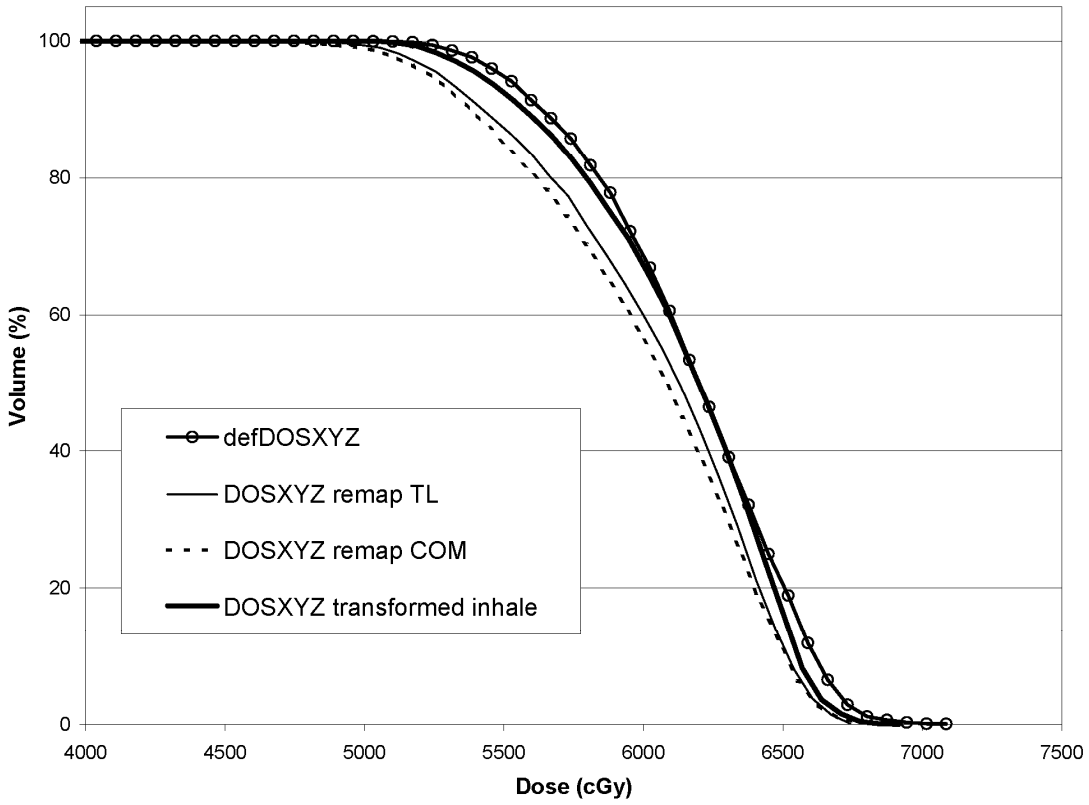


Figure 11. CTV DVH for Patient 1 tracking case. Dose grid size is 128x128x80 (4x4x2.5 $mm^3$).

Though at first it appears to be not statistically significant, there is a systematic 2-3% offset in the CTV dose between defDOSXYZ and remapping calculations. Comparison of the deformed density image, on which defDOSXYZ calculations are performed, and the transformed density images, on which DOSXYZnrc calculations are performed and then remapped to the reference phase, revealed an average 2% difference in density between these images. This investigation was similar to that carried out in Chapter 6 section 6.4.7. The deformation vectors obtained from ANIMAL do not conserve mass which caused the lung density to be higher in the deformed inhale images compared to the transformed inhale images. The increased lung density explains why the defDOSXYZ calculations are systematically higher. The presence of more tissue results in an increased generation and interactions of secondary electrons which leads to more dose deposition.

We therefore decided to repeat the defDOSXYZ calculations without modifying the voxel

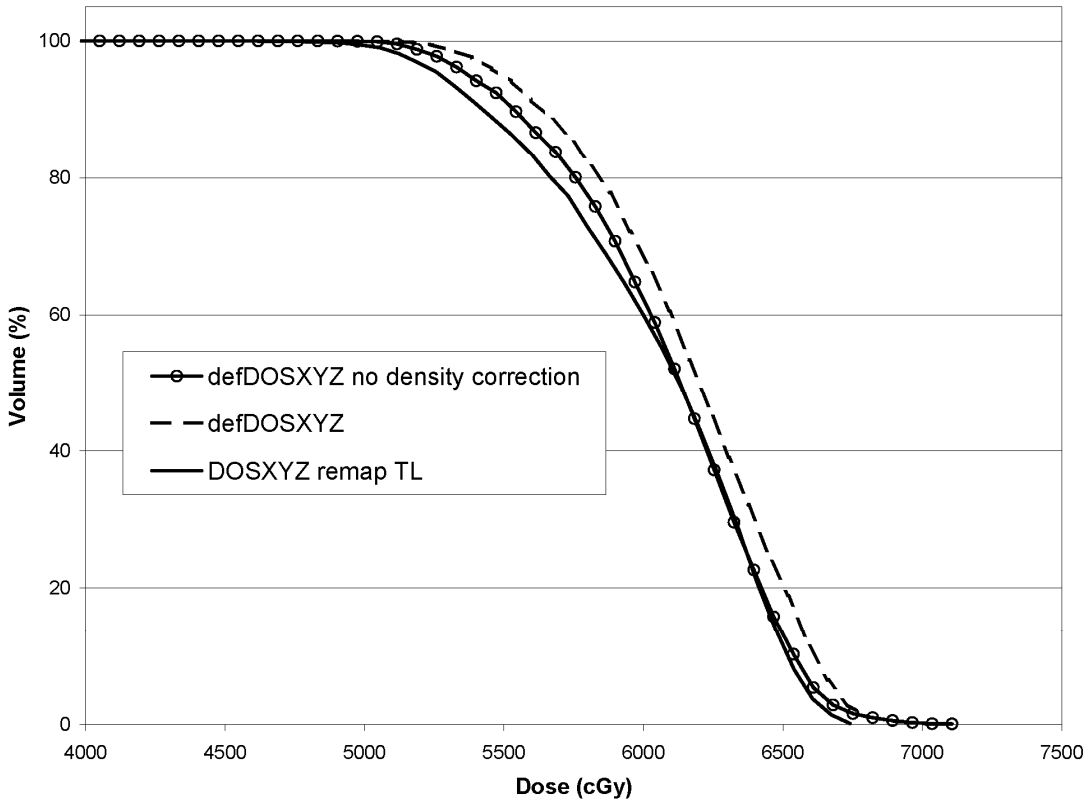


Figure 12. CTV DVH for Patient 1 for defDOSXYZ calculation with no density modification for mass conservation. Dose grid size is 128x128x80 (4x4x2.5 $mm^3$).

densities as they were deformed (see Figure 12). In this case the mass of the deformed voxel image was verified to be equal to the mass of transformed image. The removal of the mass conservation from defDOSXYZ calculations resulted in a 1% decrease in the mean dose and improved the agreement with dose remapping calculations. For all subsequent comparisons we used these non-density adjusted dose calculations.

A comparison of corresponding dosimetric parameters including the mean dose ($D_{mean}$), minimum dose ($D_{min}$), maximum dose ($D_{max}$), the dose which covers 95% of the target volume ($D_{95\%}$) and the highest dose to 5% of the target volume ($D_{5\%}$) is listed in Table 3. No statistically significant differences between defDOSXYZ and the remapping methods were noted for any dosimetric parameters in Table 3 .The mean difference in the dose calculated in the CTV by the remapping methods compared to defDOSXYZ was 3%.

Table 3. Comparison of dosimetric parameters for Patient 1 CTV.

| Parameter | DefDOSXYZ (Gy) | Remap COM (Gy) | Remap TL (Gy) |
|---|---|---|---|
| $D_{mean}$ | 60.5 | 59.7 | 60.1 |
| $D_{95\%}$ | 53.7 | 52.3 | 52.7 |
| $D_{5\%}$ | 66.2 | 65.8 | 65.9 |

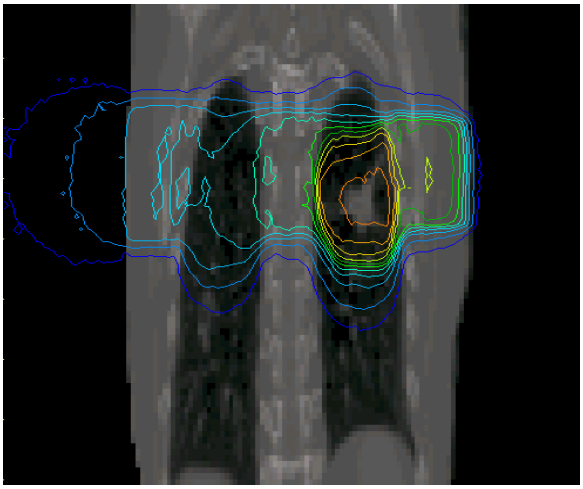

(a) defDOSXYZ

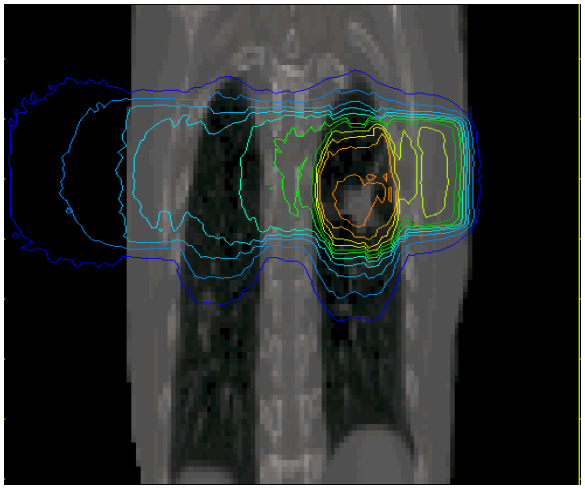

(b) COM remapping

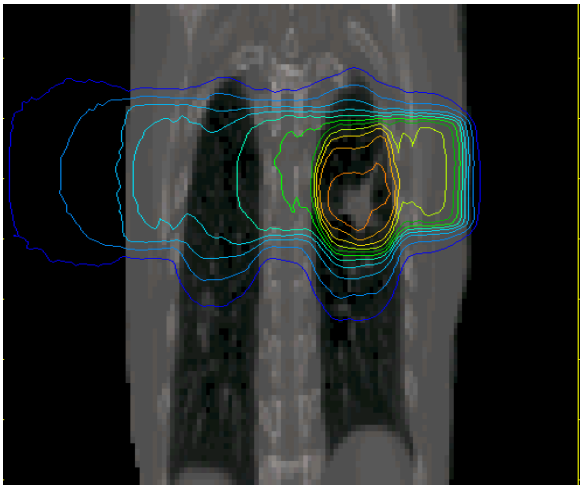

(c) TL remapping

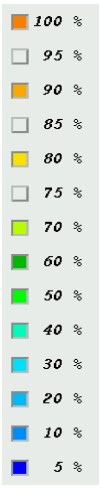


(d) legend for isodose lines

Figure 13. Dose distributions for Patient 1 tracking case on reference (inhale) phase. Dose distributions are normalized to the prescription dose of 60 Gy. Dose grid size is 128x128x80 (4x4x2.5 $mm^3$).

The dose distributions for the three methods are shown in Figures 13 (a) through (c). Two main observations can be made. First, there is more "warping" of the defDOSXYZ dose distribution along the superior/inferior direction compared to the TL and COM remapped dose distributions. This is because the higher 80-90% isodose lines extend more inferiorly into the lung for the defDOSXYZ calculation. However the extent of the low dose isodose lines is approximately consistent between the calculation methods. The discrepancies in the high dose regions can be attributed to the limitations of interpolation methods in regions where dose gradients exist, an effect which was already demonstrated in the simple deforming phantoms (see Figure 5(b)). The second observation is that there exist localized regions of discrepancy at tissue interfaces, for example at the right edge of the tumour and the chest wall/lung interfaces. These discrepancies are attributed to differences in the deformed geometries, used by the dose remapping methods compared to defDOSXYZ, on which the dose is calculated. For the dose remapping methods the dose distribution is calculated on the transformed image which has to be resampled to a rectangular grid. Partial volume averaging of voxel intensities leads to inconsistencies in the patient representation in such regions of sharp density gradients. In the case of the tumour/lung interface, this contributes to the reduced shoulder of the CTV DVH for the remapping methods compared to defDOSXYZ. The comparison of remapped dose in such regions is influenced by the voxel size, as partial volume averaging also occurs in defDOSXYZ calculations depending on the voxel size and location of voxel boundaries with respect to tissue boundaries.

A 0.6% difference in the mean dose between the trilinear and COM remapping methods was noted. Essentially the DVH for the COM remapping calculation appears to be a lower resolution version of the TL remapping calculation. This result is intuitive since the TL remapping uses octant subdivision the resolution of this method is inherently higher compared to COM remapping. The dose distributions for the remapping methods are similar, although in the case of TL remapping the dose distribution is smoother because interpolation of the remapped dose is performed.

Dose volume histograms for the planning organs at risk are shown in Figure 14. There is 10% reduction in the maximum spinal cord dose for the defDOSXYZ calculations compared to the remapping calculations. This can be attributed to the discrepancies in the dose deformations at the lung/chest wall interfaces evident in Figure 13. No significant differences can be

discerned between the calculation methods for the heart but the remapping methods underestimate the mean dose and the volume receiving at least 20 Gy ($V_{20Gy}$) in the left tumour-containing lung by 0.8 Gy and 4 cGy, respectively. These observations are consistent with the larger extent of the higher isodoses for defDOSXYZ calculations compared to remapping calculations.

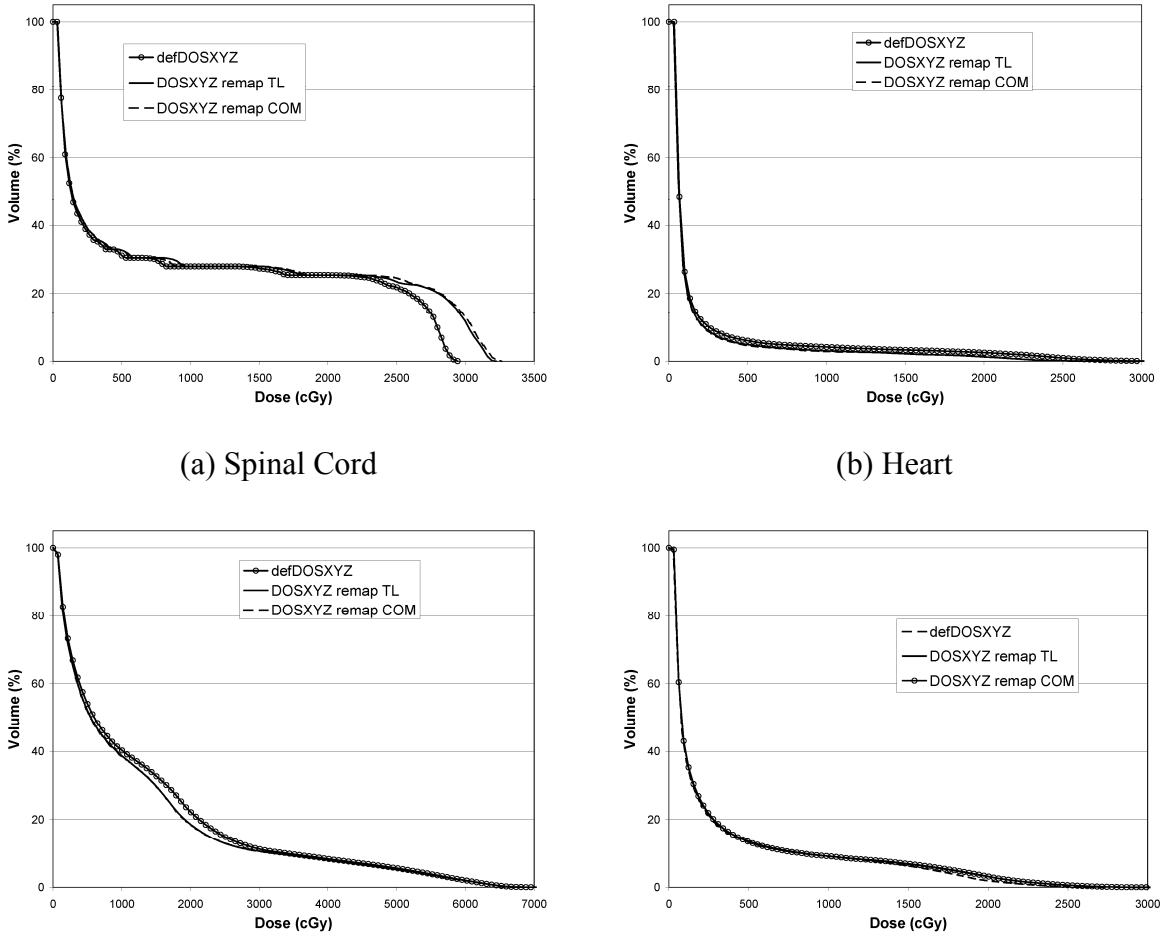


(a) Spinal Cord (b) Heart

(c) Left Lung (d) Right Lung

Figure 14. Dose volume histograms for organs at risk for Patient 1 tracking scenario. Dose grid size is 128x128x80 (4x4x2.5 $mm^3$).

***(b) Investigation of dose difference correlations***

To determine the factors which lead to differences between the remapping and defDOSXYZ calculations we studied the correlations between dose differences and deformation magnitude, volume change and dose gradient (see Figure 15). The normalized cross-correlation

between the percentage local dose difference (Figures 15(a) and (b)) and the gradient of the defDOSXYZ dose distribution (Figure 15(c)), the vector magnitude of the exhale-to-inhale deformations (Figure 15(d)) and the fractional volume change, calculated as the determinant of the Jacobian of the local deformations vectors for each voxel, (Figure 15(e)) was calculated over the whole dose grid (128x128x80). The influence of statistical uncertainties was

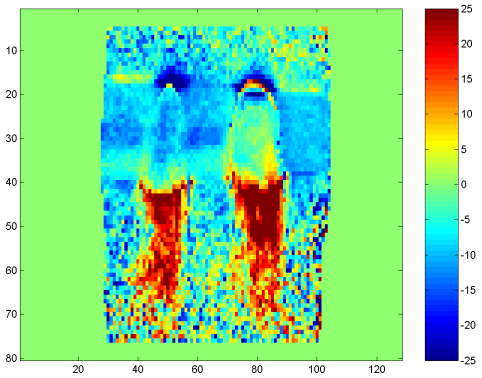

(a) local percentage dose difference 100*(defDOSXYZ-COM)/defDOSXYZ

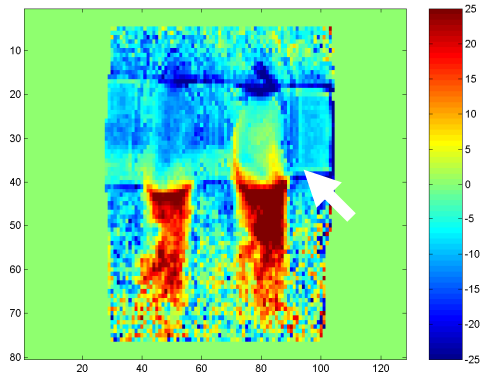

(b) local percentage dose difference 100*(defDOSXYZ-TL)/defDOSXYZ

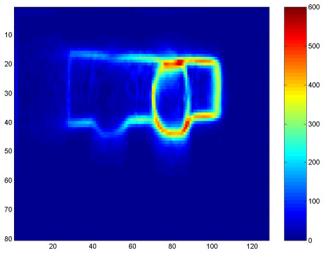

(c) dose gradient map (cGy/mm)

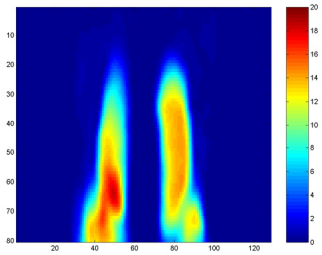

(d) deformation magnitude map (mm)

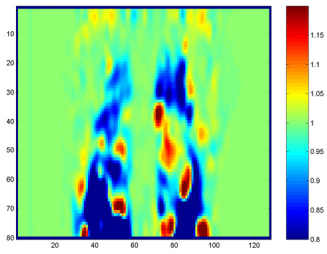

(e) fractional volume change map

Figure 15. Sagittal sections through isocenter (corresponding to Figure 13) of local dose differences ((a) and (b)) and (c) local dose gradient, (d) deformation magnitude and (e) fractional volume change for Patient 1 tracking case. Resolution of images is 4x4x2.5 $mm^3$.

minimised by considering only voxels with a statistical uncertainty of 10% or less. This corresponded to a local dose threshold of 10 Gy. Therefore, for these voxels, only local dose differences greater than 10% were considered significant and were included in the calculation of the correlation values shown in Table 4.

Visually, the dose difference maps appear to correlate with both dose gradient and deformation magnitude although calculation of cross-correlation values reveals that for COM remapping discrepancies compared to defDOSXYZ are more strongly influenced by deformation magnitude. For TL remapping discrepancies are most strongly correlated with dose gradient.

Table 4. Normalized cross-correlations for TL and COM remapping evaluated over voxels in 3D 128x128x80 image with statistical uncertainty of 10% or less and a local dose difference of greater than 10% for Patient 1 tracking case.

| | defDOSXYZ – TL | defDOSXYZ - COM |
|---|---|---|
| Deformation magnitude | 0.203 | **0.241** |
| Dose gradient | **0.212** | 0.108 |
| Volume change | 0.051 | 0.090 |

For COM remapping it can be expected that as the deformation magnitude increases deformed voxels are increasingly less aligned with the rectangular voxels of the dose distribution to be remapped. In this case, due to lack of interpolation, simple point dose remapping does not accurately estimate the remapped dose. Similarly, it is interesting to note that the correlation with deformed voxel volume change is stronger for COM remapping than for TL remapping. This could be attributed to the reference voxel subdivision used for the latter method which is better able to account for voxel volume changes.

The correlation of TL remapped dose discrepancies and dose gradient is consistent with the previous comparisons in simple deforming phantoms. The TL remapping method appears to introduce more artifacts in the remapped dose distribution in the beam penumbra (indicated by white arrow in Figure 15(b)) compared to the COM remapping method. It was already demonstrated in the deforming phantoms that deformation size (ie. volume change and deformation magnitude) had a limited influence on differences between TL remapping and defDOSXYZ (see Figure 7).

***(c) Dependence on dose calculation grid resolution***

CTV dose volume histograms are shown in Figure 16 for two different dose grid

resolutions: 4x4x5 $mm^3$ (128x128x40) and 2x2x2.5 $mm^3$ (256x256x80). Agreement between defDOSXYZ and the remapping calculations is improved when the voxel size was reduced. Furthermore, agreement between COM and TL calculations is improved. This is consistent with the observation of improved agreement between defDOSXYZ and TL calculations in the deforming phantoms.

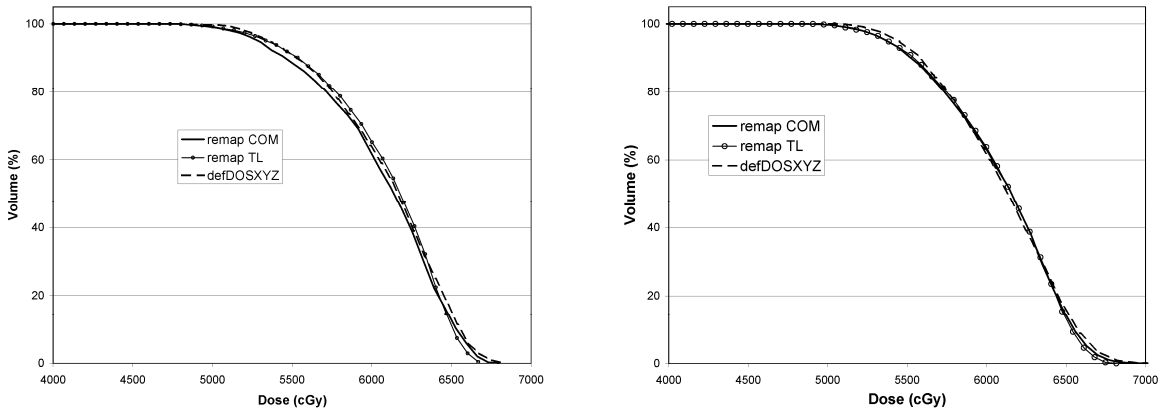


(a) 128x128x40 dose grid (b) 256x256x80 dose grid

Figure 16. Comparison of CTV DVHs for two dose grid resolutions (a) 4x4x5 $mm^3$ and (b) 2x2x2.5 $mm^3$.

### *8.3.3.2 Patient 1 2-field 3D-CRT plan: no motion compensation*

***(a) DVH comparison***

A comparison of CTV dose volume histograms for the no motion compensation scenario is shown in Figure 17. The number of simulated histories per beam and the calculation times were the same as for the tracking case. The static dose calculations on the transformed (i.e., delivered dose) and reference (i.e., planned dose) are included to illustrate the magnitude of the motion effect. Note that the defDOSXYZ calculations discussed here do not employ density modifications to conserve mass, for reasons discussed in the previous section. In this case the plan was not designed to cover the tumour in the target phase so there are significant dose gradients across the CTV which is manifested as a reduced shoulder of the DVH ($D_{95\%}$) compared to the tracking scenario. In this case defDOSXYZ calculations predict a 13% and 16% reduction in the $D_{95\%}$ compared to COM and TL remapping, respectively (see Table 5). The mean dose difference in the CTV for the remapping methods is 5% which is significant compared to

the 3% statistical uncertainty for the dose in this region. The corresponding dose distributions are shown in Figure 18. It can be seen that the sharp dose gradients are washed out in the remapping calculations which leads to prediction of better perceived tumour coverage and hence an enhanced $D_{95\%}$. When an intermediate breathing phase is considered, to estimate the cumulative dose, the discrepancies between in the $D_{95\%}$ calculated by defDOSXYZ and COM and TL remapping are reduced to 4% and 5%, respectively. For the organs at risk the results were similar to those reported for the tracking scenario.

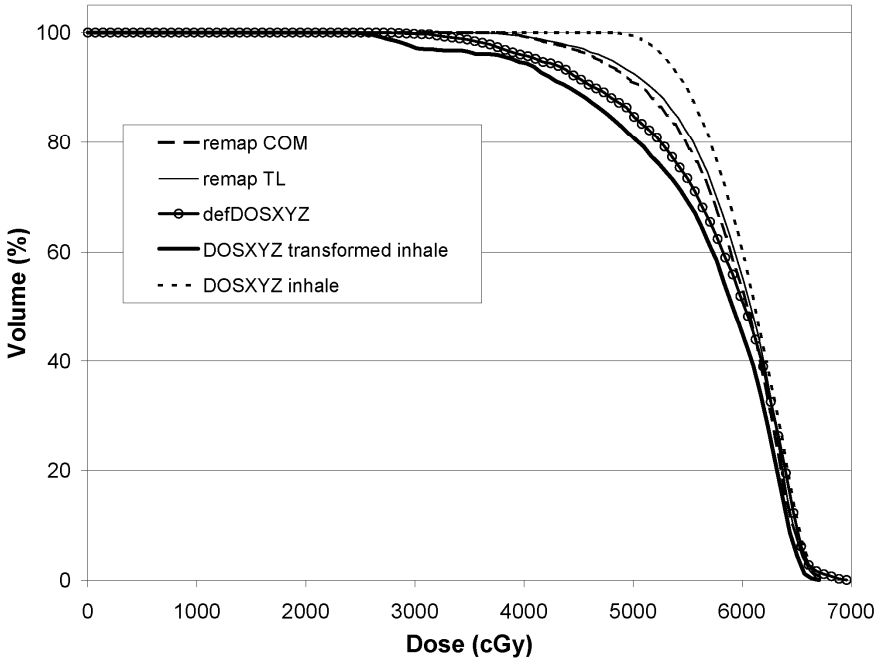


Figure 17. CTV dose volume histogram for Patient 1 no motion compensation scenario. Dose grid size is 128x128x80 (4x4x2.5 $mm^3$).

Table 5. Comparison of dosimetric parameters for Patient 1 CTV for no motion compensation planning scenario.

| Parameter | defDOSXYZ (Gy) | Remap COM (Gy) | Remap TL (Gy) |
|---|---|---|---|
| $D_{mean}$ | 57.5 | 58.6 | 59.0 |
| $D_{95}$ | 41.3 | 46.9 | 48.0 |
| $D_5$ | 65.7 | 65.6 | 65.4 |

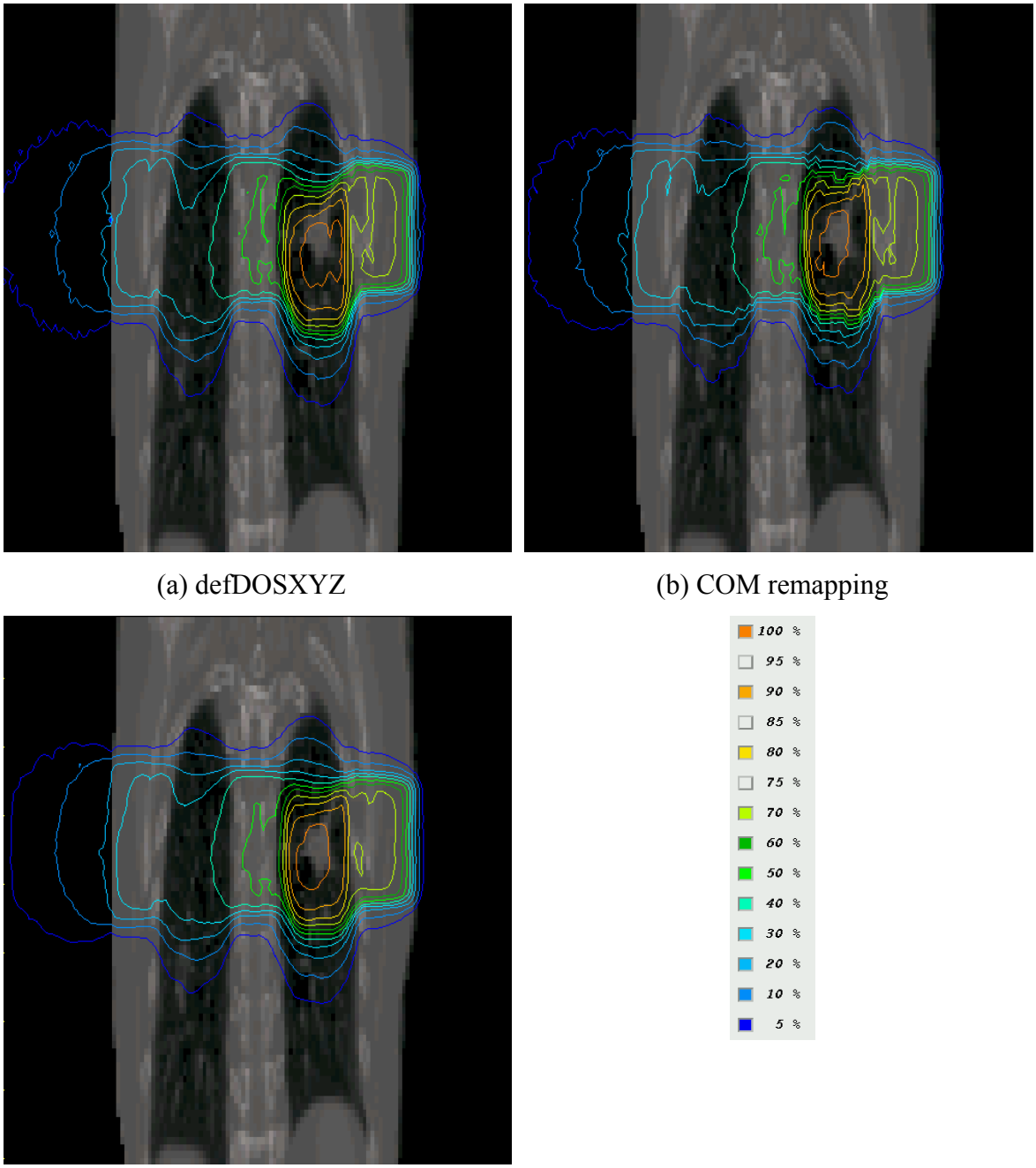


(a) defDOSXYZ (b) COM remapping

(c) TL remapping (d) legend for isodoses

Figure 18. Dose distributions for Patient 1 plan with no motion compensation on reference (inhale) phase. Dose distributions are normalized to prescription dose of 60 Gy. Dose grid size is 128x128x80 (4x4x2.5 $mm^3$).

***(b) Correlations of dose differences***

The local dose difference maps are shown in Figure 19. As motion effects are larger for this planning scenario the discrepancies between defDOSXYZ and the remapping calculations are increased and hence correlations with dose gradient, deformation magnitude and volume change are enhanced (see Table 6). For both remapping methods, dose discrepancies correlated most strongly with the dose gradient.

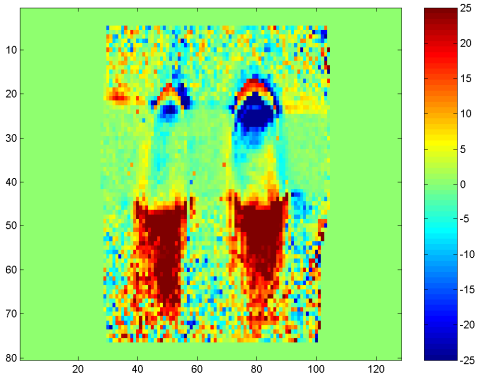

(a) local percentage dose difference 100*(defDOSXYZ-COM)/defDOSXYZ

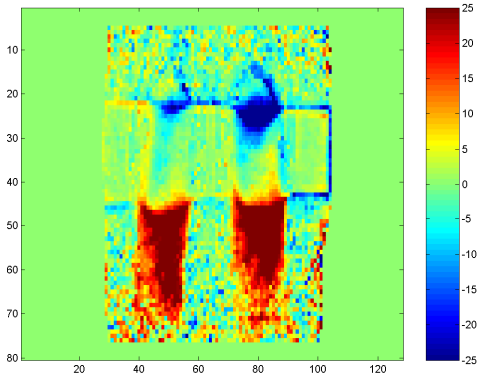

(a) local percentage dose difference 100*(defDOSXYZ-TL)/defDOSXYZ

Figure 19. Sagittal sections of local dose difference maps through isocenter (corresponding to Figure 18) for COM and TL remapping compared to defDOSXYZ for the no motion compensation scenario. Dose grid size is 128x128x80 (4x4x2.5 $mm^3$).

Table 6. Normalized cross-correlations for TL and COM remapping evaluated over voxels in 3D 128x128x80 image with statistical uncertainty of 10% or less and a local dose difference of greater than 10% for Patient 1 no motion compensation case.

| | defDOSXYZ – TL | defDOSXYZ - COM |
|---|---|---|
| Deformation magnitude | 0.532 | 0.549 |
| Dose gradient | **0.750** | **0.768** |
| Volume change | 0.095 | 0.101 |

#### *8.3.3.3 Patient 2 7-field IMRT plan: ITV scenario*

***(a) DVH comparison***

A comparison of dose volume histograms for the three target volumes is shown in Figure 20. Dose calculated on the transformed reference (exhale) phase is included to indicate the magnitude of target motion. Two hundred million histories were simulated for each beam, resulting in an average statistical uncertainty of 5% in the ITV. Similar to Patient 1, a systematic offset between remapping and defDOSXYZ calculations was noted. On average, there was a 5% difference in density between the deformed and transformed reference density matrices. defDOSXYZ calculations repeated without density adjustments are indicated by open circles in Figure 20. A corresponding comparison of dosimetric parameters for ITV1 is listed in Table 7. Although the re-calculation of defDOSXYZ dose distributions resulted in a 2% decrease in mean dose and improved agreement with

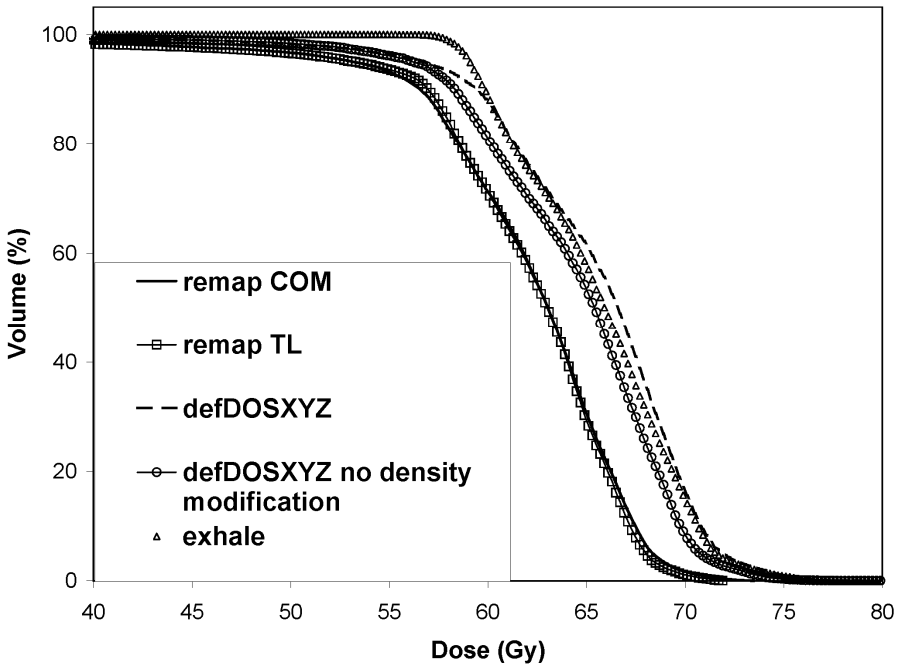


(a) ITV1

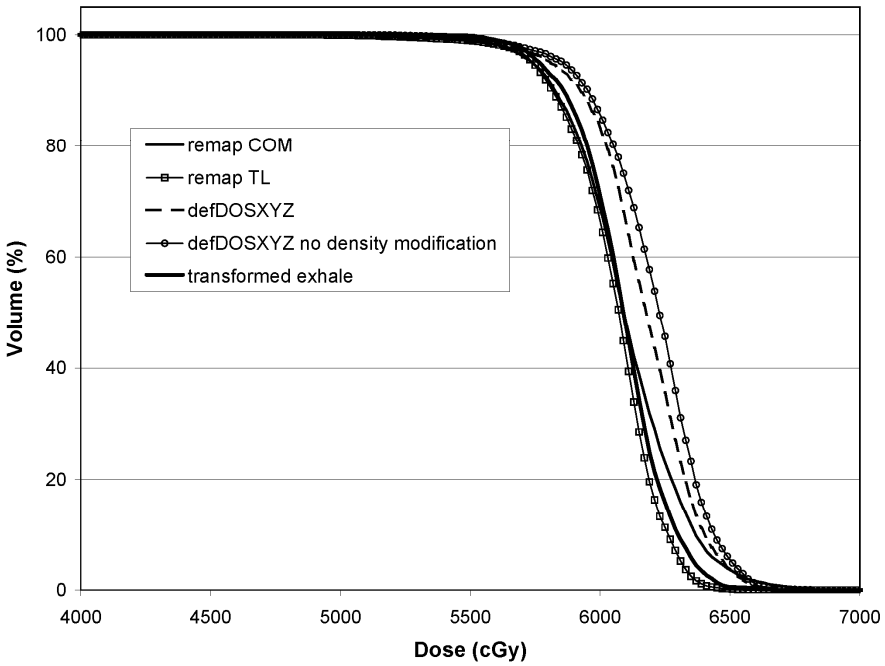


(b) ITV2

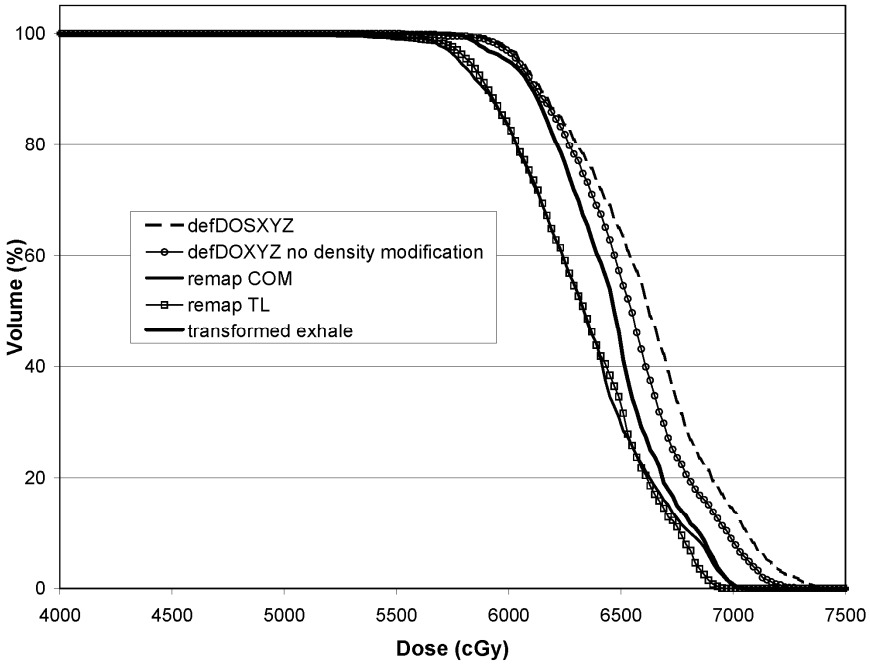


(c) ITV3

Figure 20. Comparison of target volume DVHs for Patient 2. Dose grid size is 128x128x80 (4x4x2.5 $mm^3$).

Table 7. Comparison of dosimetric parameters for Patient 2 ITV1.

| Parameter | defDOSXYZ (Gy) | defDOSXYZ no density correction (Gy) | Remap COM (Gy) | Remap TL (Gy) |
|---|---|---|---|---|
| $D_{mean}$ | 65.5 | 64.4 | 61.9 | 61.9 |
| $D_{95}$ | 56.7 | 56.2 | 53.2 | 53.3 |
| $D_5$ | 71.9 | 70.7 | 68.4 | 68.0 |

remapping methods there was a greater than 5% discrepancy in the $D_{95\%}$, minimum and maximum doses calculated by these methods.

The dose remapping methods underestimated these parameters compared to the defDOSXYZ calculation. Though such results are somewhat consistent with errors introduced by interpolation there still appeared to be a systematic offset between remapping calculations and defDOSXYZ. The dose distributions shown in Figure 21 indicate the defDOSXYZ calculation predicts more coverage of the tumour by the prescription (100%) isodose line. Steeper dose gradients are also more evident in the defDOSXYZ calculation.

Significant offsets in the mean target volume doses were noted for the fields at gantry angles of 120° and 250°. Investigation of the deformation vector magnitude Jacobian map of volume change revealed sharp gradients in the deformation magnitude and complex pattern of localized volume changes (see Figure 23) in the region transected by the these fields. Such deformations are clearly not physically realistic. Note that in contrast to the Patient 1 dose calculations, the deformation vectors used for Patient 2 calculations were obtained from a B-spline image registration algorithm. There is possibly some correlation between the dose difference and Jacobian maps but this is not conclusive. The location of the planning structures is indicated in Figure 22(e). The target volumes are located in a region of large localized volume expansions. These regions also coincide with areas of significant dose gradients in the defDOSXYZ dose distribution.

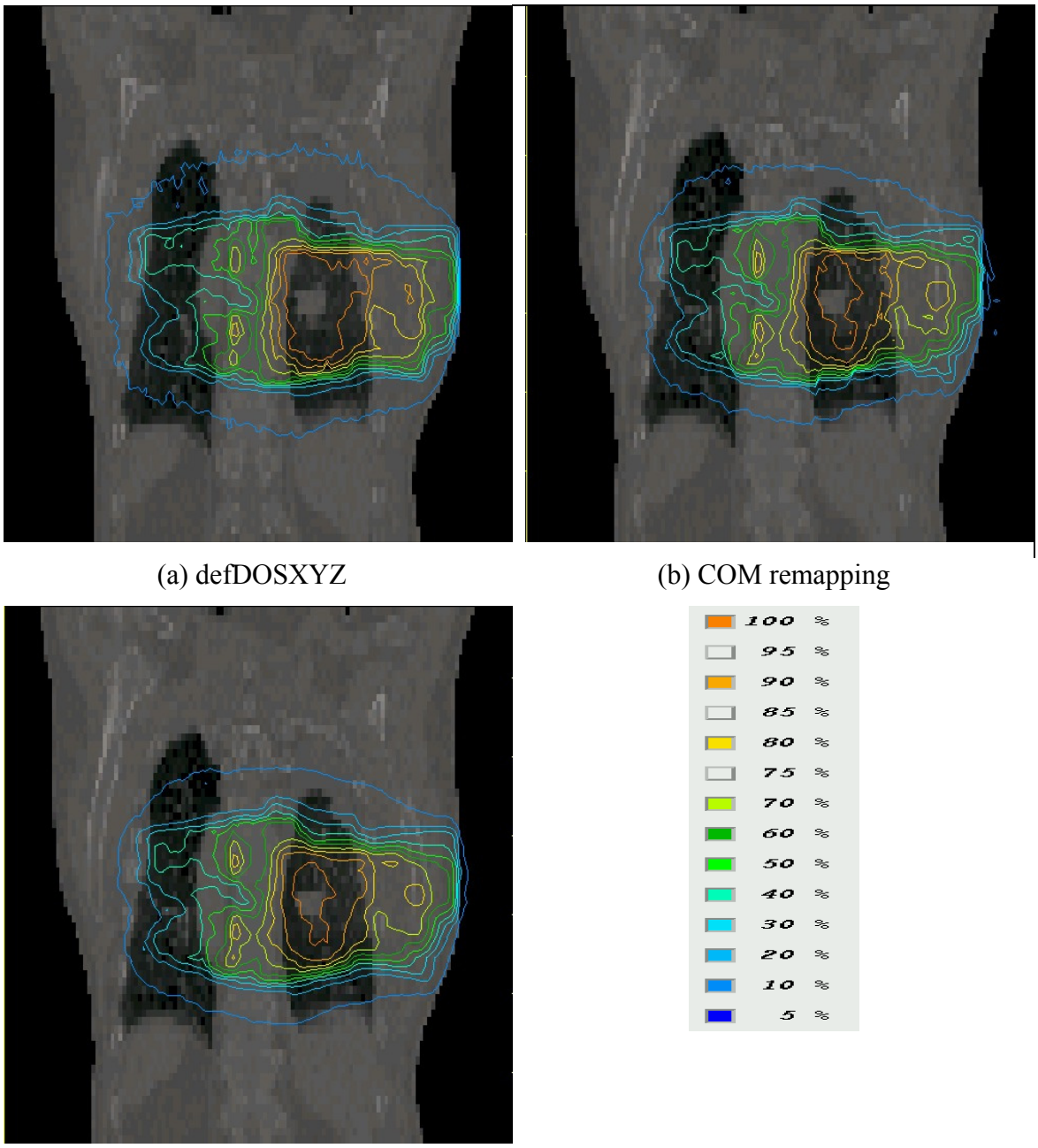


(a) defDOSXYZ (b) COM remapping

(c) TL remapping (d) isodose legend

Figure 21. Dose distributions normalized to prescription dose of 63 Gy. Dose grid size is 128x128x80 (4x4x2.5 $mm^3$).

We therefore hypothesized that the systematic offset of the defDOSXYZ calculations is due to these localized regions of large volume expansion and shrinkage. This hypothesis was tested by smoothing the deformation vectors with a Gaussian kernel

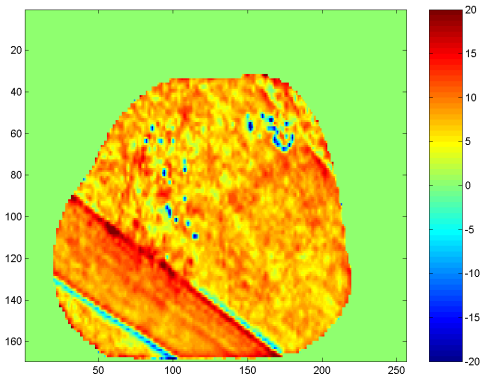

(a) percent local absolute dose differences 100*(defDOSXYZ-TL)/defDOSXYZ (%)

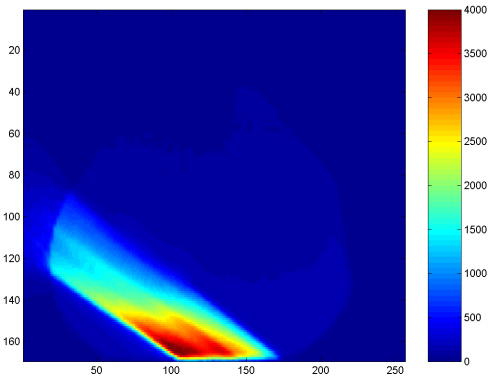

(b) defDOSXYZ dose distribution (cGy)

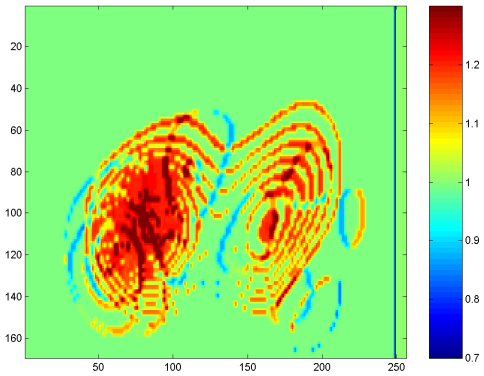

(c) Jacobian map of fractional volume change

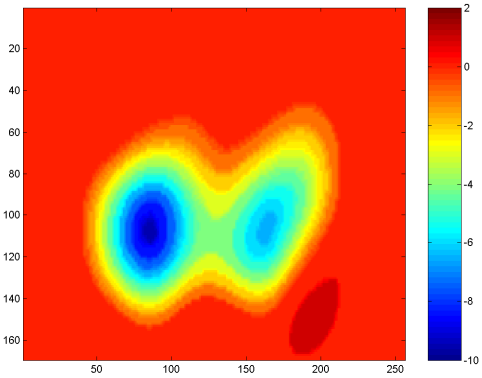

(d) Z component of deformation vectors (mm)

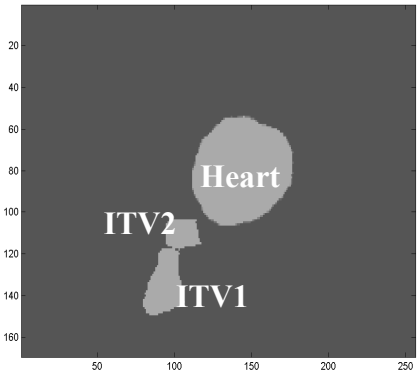


(e) location of target and heart contours

Figure 22. Illustration of correspondence between regions of large dose differences (a) and dose gradient (b) in axial slices of 120° field with complex deformation vectors volume change (c) and magnitude (d) distributions and (e) location of target volumes and heart. Resolution of images is 2x2x2.5 $mm^3$.

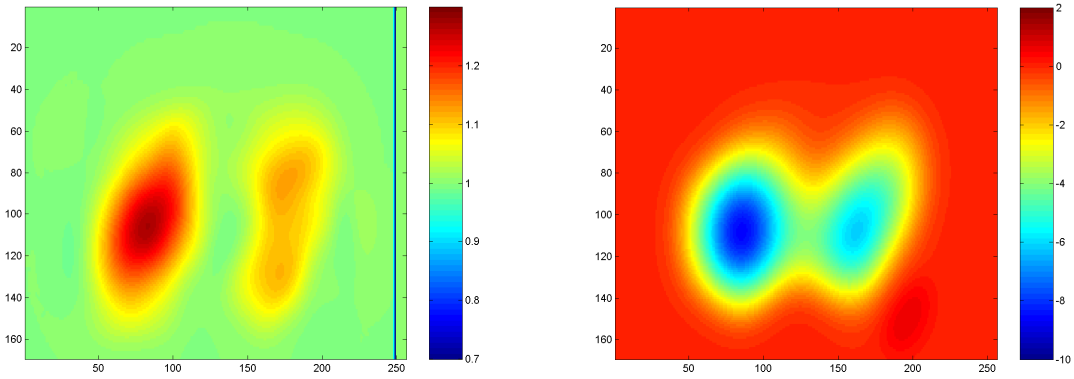


(a) Jacobian map of fractional volume change

(d) Z component of deformation vectors (mm)

Figure 23. Volume change and Z component of magnitude of smoothed inhale-to-exhale deformation vectors in axial slice corresponding to Figure 23(c) and (d).

of FWHM = 32,32,40 mm and repeating the calculations. Note that a new transformed image for remapping calculations was generated using the smoothed vectors. The magnitude of the Z component and Jacobian map of the smoothed vectors is shown in Figure 24.

The resulting DVHs for ITV1 before and after smoothing are shown in Figure 25. The smoothing does not significantly affect the mean value of the deformations and volume changes but rather the magnitudes of the minima and maxima are reduced. When the deformation vectors are smoothed there are no differences between the defDOSXYZ, remap TL and remap COM calculations (see Figure 25(b)). The original defDOSXYZ using the unsmoothed vectors has been included for comparison. It is interesting to note that the defDOSXYZ DVH is unchanged by vector smoothing compared to the remapping methods. It is possible that the changes in the dose distribution induced by smoothing the deformation vectors are not resolvable for the current dose grid size. Furthermore, in the absence of tissue boundaries, the dose distribution is expected to be inherently smooth. Conversely, the dose distributions obtained by point dose remapping appear to be sensitive to not only the magnitude but also to localized gradients in the deformation vectors. It could be postulated that artifacts in the remapped dose distribution could be induced by interpolation of the remapped dose obtained by

discontinuous point displacements. It is important to note that when a physically realistic deformation field is used, the discrepancies between defDOSXYZ and dose remapping methods are resolved. As in the case of mass conservation in image registration, this demonstrates the importance of determining a physically realistic and continuous deformation field for deformable dose calculations even if they are performed using interpolation methods.

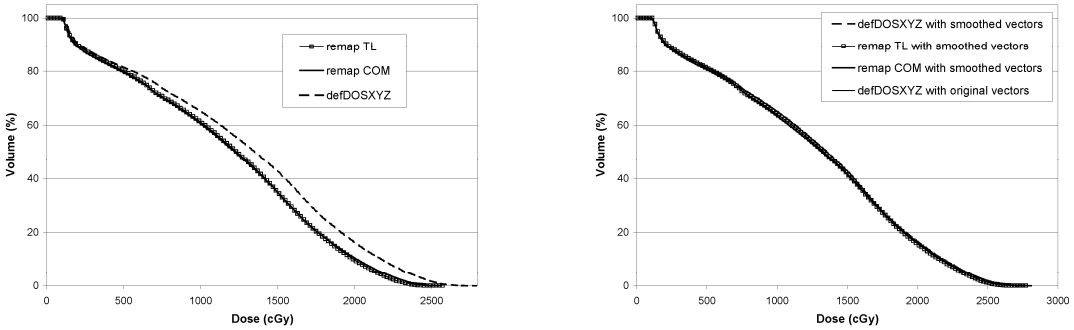


(a) original ITV1 DVH

(b) ITV1 DVH for calculation with smoothed vectors

Figure 24. ITV1 dose volume histograms for 120° field with and without smoothing of deformation vectors.

Dose volume histograms for the organs at risk are shown in Figure 25. Generally, the effects of motion, and therefore discrepancies between dose calculation methods, were smaller for these organs as they have larger volumes compared to the targets and hence localized dose differences and even motion effects are averaged out. As with the target volumes evidence of a systematic offset between defDOSXYZ and remapping calculations can be seen. Again we postulate that these are due to the complex deformation maps, however since dose is averaged over a larger volumes the effects of large localized dose discrepancies is reduced.

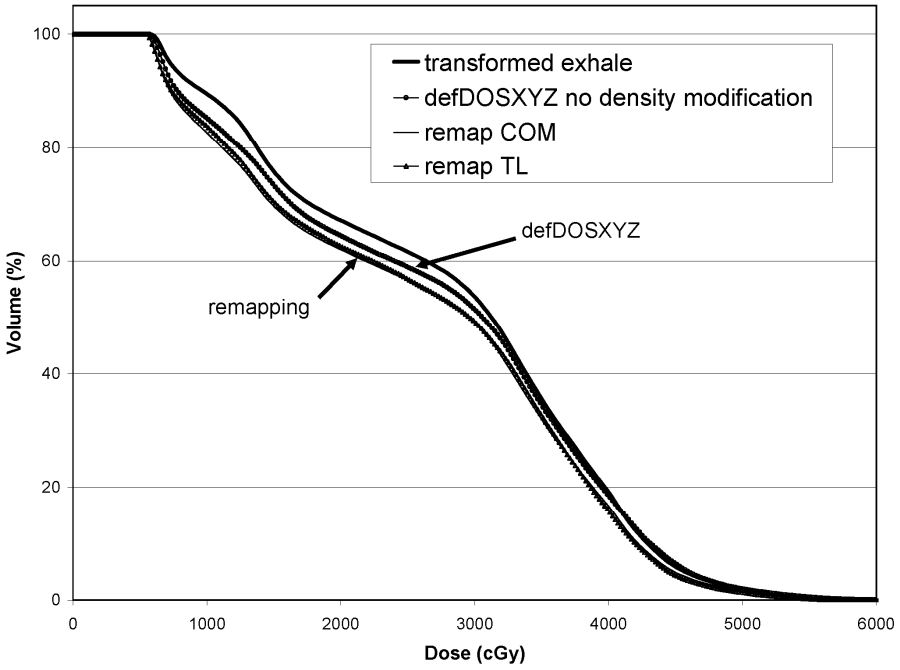


(a) Heart

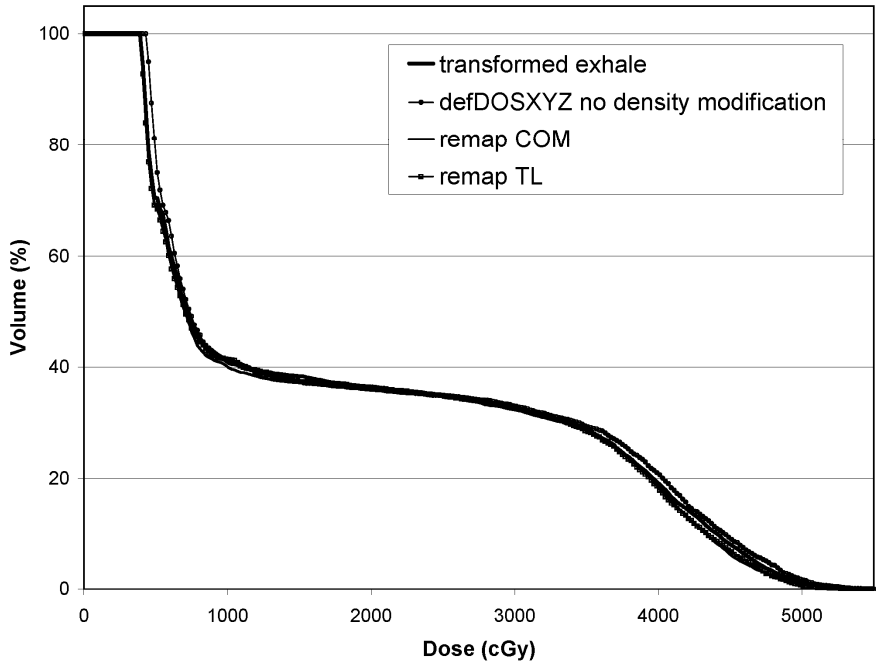


(b) Spinal Cord

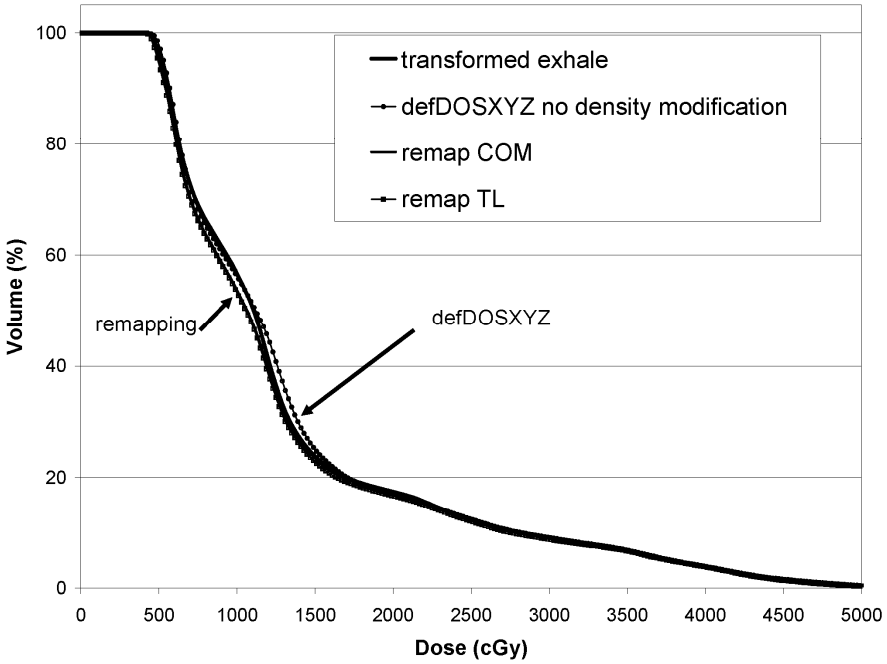


(c) Left Lung

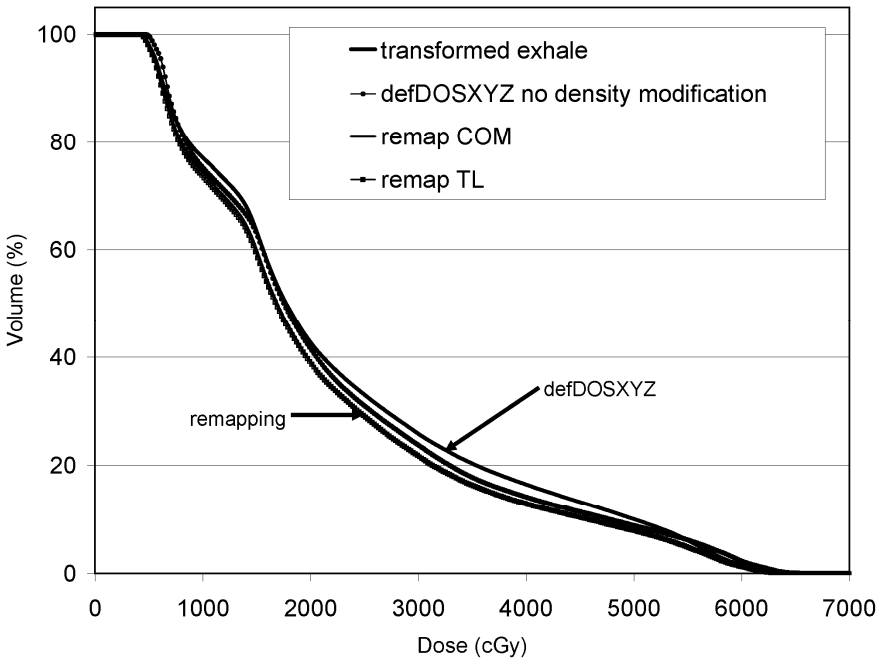


(d) Right Lung

Figure 25. Dose volume histograms for organs at risk. Dose grid size is 128x128x80 (4x4x2.5 $mm^3$).

No statistically significant differences were noticed in dosimetric parameters including mean and maximum dose, $V_{20Gy}$ and $V_{30Gy}$ for these organs, with the exception of the minimum dose. The minimum organ dose was however overestimated in the left lung by 12% and 13% for the COM and TL remapping methods, respectively, and underestimated by 9% by both methods for the spinal cord.

***(b) Investigation of dose differences correlations***

A comparison of dose difference maps, dose gradient, fractional volume change and deformation magnitude is shown in Figure 26. The corresponding normalized correlation values are shown in Table 6. For both remapping methods dose discrepancies were most strongly correlated with dose gradients. Again, fractional volume change had more significant correlation for COM remapping compared to TL remapping.

Table 6. Correlations of local dose differences evaluated over voxels in 3D 128x128x68 image with statistical uncertainty of 10% or less and a local dose difference of greater than 10% for Patient 2 ITV plan.

| Parameter | COM-defDOSXYZ | TL-defDOSXYZ |
|---|---|---|
| Def mag | 0.114 | 0.302 |
| Vol change | 0.079 | 0.023 |
| Dose grad | **0.324** | **0.543** |

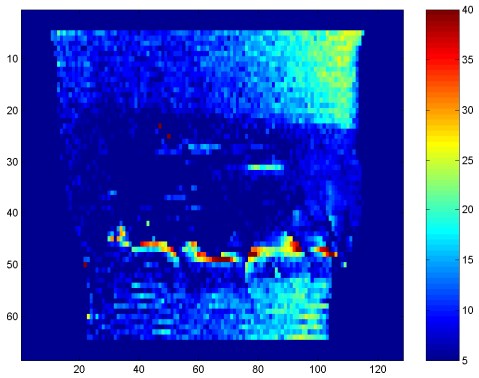

(a) local percentage dose difference 100*abs(defDOSXYZ – COM)/defDOSXYZ

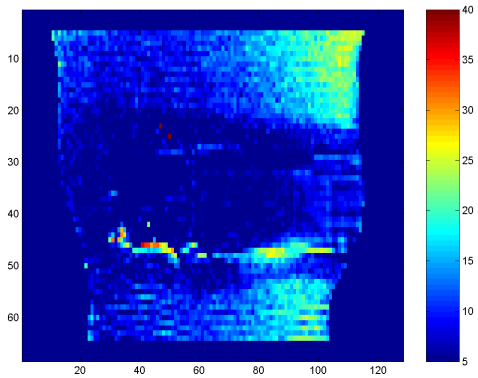

(b) local percentage dose difference 100*abs(defDOSXYZ – TL)/defDOSXYZ

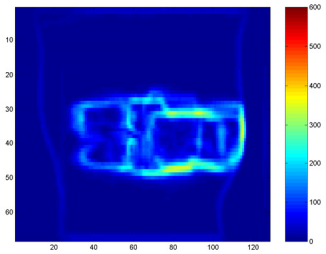

(c) dose gradient (cGy/mm)

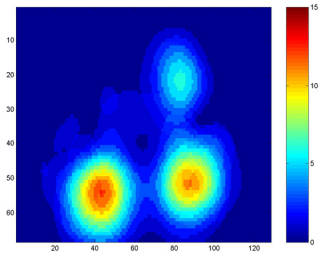

(d) deformation magnitude (mm)

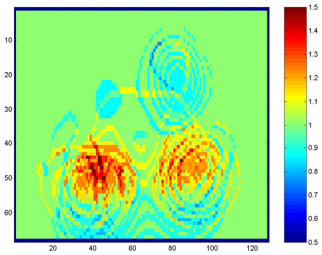

(e) fractional volume change

Figure 26. Correlations between dose difference maps ((a) and (b)) compared to and (c) local dose gradient, (d) deformation magnitude and (e) fractional volume change for Patient 2. Resolution of images is 4x4x2.5 $mm^3$ (128x128x80).

## 8.4 DISCUSSION

The results of comparing defDOSXYZ calculations with dose remapping methods indicate that the latter methods tend to underestimate the dose in regions where steep dose gradients and large deformations exist. The dose calculation methods converge if the dose grid resolution is increased but for clinically relevant dose grid sizes the remapping methods lead to local dose differences in excess of 25% in penumbral regions for a realistic patient plan. For a well designed plan which accounts for motion the location of these gradients should be such that they had little influence on the planning structure dose volume histograms. However this might not be the case if we are evaluating the effect of motion on a conformal static treatment plan in order to assess the

efficacy of a motion mitigation device or for calculation of a motion kernel to be used in 4D inverse planning. The results presented in this chapter represent the maximum possible deviations as only extreme breathing phases were considered. The calculation of a cumulative dose distribution, including intermediate phases for which there is less motion, would tend to reduce these discrepancies. This requires further investigation.

For the deforming geometries considered in this study, defDOSXYZ simulations required a 5 to 11 increase in calculation time compared to DOSXYZnrc calculations. A important contribution to this increased calculation time was an increase in the incidence of boundary crossing errors which occur when calculating dose in deformed geometries.

A significant issue in this study was that the ability to conserve mass with the defDOSXYZ calculation method could not be exploited as deformation vectors from non-linear registration of patient 4DCT images did not conserve mass. In the deforming phantoms this was not an issue as the voxel densities were adjusted to ensure that the dose was being calculated on exactly the same voxel density and composition for all calculation methods. Discontinuous deformation vector patterns can cause systematic effects, as demonstrated for the ITV plan case, further reinforcing the sensitivity of deformable dose calculation methods on the deformation vectors. It is essential that a physically realistic, continuous, deformation field is used for these dose calculations.

Finally, no statistically significant differences between the COM and TL remapping methods could be discerned for patient 4DCT data although the latter method most closely approximated the dose predicted by defDOSXYZ. The TL remapping method with octant subdivision is in theory better able to account for voxel volume changes but was also found to introduce more errors in penumbral regions due to interpolation. As both methods are computationally efficient to implement it would be preferable to use the TL remapping approach.

## 8.5 SUMMARY

In this chapter we presented a comparison of three dose calculation methods in deforming anatomies ranging from homogeneous phantoms which are compressed along their Z axis, to a mathematical breathing phantom and 4D CT patient data. The defDOSXYZ 4D dose calculation code was compared with dose remapping methods

employing center-of-mass tracking and trilinear interpolation. The trilinear method underestimated the dose by up to 26% within the field for a phantom consisting of 1 cm voxels and a 2x2 $cm^2$ incident beam. Larger discrepancies occured in the penumbra region. The discrepancies were reduced with decreasing voxel size and deformation magnitude. A comparison of dose remapping from Inhale to Exhale in a mathematical breathing phantom revealed dose discrepancies of up to 16% in the penumbra region and 8% near the surface where significant deformations occur. For realistic treatment planning scenarios no clinically significant differences were noted between dose remapping and defDOSXYZ calculations. However, for an extreme case where target motion was not included in the plan, the target volume coverage was underestimated by up to 16% by remapping methods. Definitive conclusions about the discrepancies between dose calculation methods requires further investigation with a larger patient set and calculation of cumulative dose rather than considering only extreme phases. Dose discrepancies between defDOSXYZ and remapping methods were found to correlate most strongly with the gradient of the dose distribution. The accuracy of all the dose remapping methods was influenced by the continuity of deformation vector fields as determined by non-linear image registration.

## 8.6 REFERENCES


1 M. Rosu, I. Chetty, J. Balter, M. Kessler, D. McShan and R. Ten Haken, "Dose reconstruction in deforming anatomy: Dose grid size effects and clinical implications," Med. Phys. **32** 2487-2495 (2005).

2 Flampouri S., Jiang S.B., Sharp G.C., Wolfgang J., Patel A.A. and N.C. Choi "Estimation of the delivered patient dose in lung IMRT treatment based on deformable registration of 4D-CT data and Monte Carlo simulations" Phys. Med. Biol. **51** 2763-2779 (2006).

3 Segars W.P., Lalush D.S. and B.M.W. Tsui, "Modeling respiratory mechnics in the MCAT and spline-based MCAT phantoms," IEEE Trans. Nucl. Sci. **48** 89-97 (2001).

[4] Segars W.P., "Development and application of the new dynamic nurbs-based cardiac-torso (NCAT) phantom," PhD. dissertation, University of North Carolina (2001).

[5] Wu Z., E. Rietzel, V. Boldea, D. Sarrut and G.C. Sharp "Evaluation of deformable registration of patient lung 4DCT with sub-anatomical region segmentations" Med. Phys. in review (2007).

[6] Siebers J.V., P.J. Keall, J.O. Kim and R. Mohan "A method for photon beam Monte Carlo multileaf collimator particle transport" Phys. Med. Biol. **47** 3225-3249 (2002).

[7] Seco J., Sharp G.C., Wu Z., Gierga D., Buettner and H. Paganetti "Dosimetric impact of motion in free-breathing and gated lung radiotherapy: a 4D Monte Carlo study of intra/inter fraction effects" Med. Phys. **35** 356-366 (2008).

[8] Walters B.R.B. and I. Kawrakow "Technical note: Overprediction of dose with default PRESTA-I boundary crossing in DOSXYZnrc and BEAMnrc" Med. Phys. **34** 647-650 (2007).

[9] International Commission on Radiation Units and Measurements (ICRU), ICRU Report 50 "Prescribing, Recording, and Reporting Photon Beam Therapy" ICRU, Bethesda MD (1993).

# Chapter 9:

# Conclusions and Outlook

## 9.1 SUMMARY AND CONCLUSIONS

Thus far, the efficacy of radiotherapy in the treatment of lung cancer has been limited by the inability of current treatment planning approaches to account for the significant tumour motion induced by respiration that occurs during imaging and delivery. Research efforts aimed at minimizing these motion have resulted in a new 4D treatment planning methodology based on 4D imaging, non-linear image registration and 4D dose calculation. The final accuracy of a 4D plan is dependent on the inherent accuracy with which each of these steps is carried out. Non-linear image registration is not yet a clinical tool as there are many issues which remain to be addressed, including how to evaluate the registration accuracy and its influence on dose calculation accuracy. Finally, current 4D dose calculations methods employ a number of approximations which brings into question their accuracy in regions of steep dose gradients and large deformations.

A 4D Monte Carlo dose calculation code, defDOSXYZ, was developed which calculates the cumulative dose received in a deforming voxel grid. This is a more natural approach to deformable dose calculation as the energy deposition is determined in a conserved density and atomic number characterized amount of tissue. In contrast to conventional methods where mapping or interpolation of the dose to a reference state is required, defDOSXYZ utilizes the same dose scoring grid for all states of motion. We validated defDOSXYZ calculations by comparison with the DOSXYZ Monte Carlo code and by consistency checks performed in deforming phantoms. The accuracy of these calculations was demonstrated to be within 1%.

To obtain the deformation vectors necessary to track how voxels deform from one motion state to the next we implemented the ANIMAL algorithm for non-linear registration of thoracic 4D CT images. A registration procedure was developed whereby the optimal combination of the many parameters controlling the registration could be

determined. Registration accuracy was measured by three methods including image correlation, landmark analysis and distance to agreement of planning structures. ANIMAL required a number of modifications before the resulting deformation vectors could be used for 4D dose calculation. A method for testing and regularizing deformation vector discontinuities was implemented to ensure a continuous deformation field. It was determined that the non-linear transformations did not conserve voxel mass; therefore an initial investigation into the assignment of tissue specific deformation regularization parameters was performed. A quantification of registration accuracy in five 4D CT lung patients demonstrated that this modified version of ANIMAL is capable of an average registration accuracy within 2 mm. An investigation of the influence of registration accuracy on 4D dose calculation accuracy concluded that a registration accuracy which less than the dose grid resolution is required. This indicates that ANIMAL is capable of registering 4D CT images with an accuracy acceptable for clinical dose calculations.

A potential application of non-linear registration is the correction of artifacts in 4D CT images. These artifacts affect the accuracy of any subsequent image registration or dose calculation. An interpolation method based on non-linear image registration of temporally adjacent artifact-free images was developed using the ANIMAL algorithm. The accuracy of the artifact correction method was evaluated by simulating binning artifacts in images generated using a mathematical breathing phantom. The correlation between the corrupted and original artifact-free images improved from 0.971 to 0.992 after artifact correction. The method was used to interpolate artifact-containing regions in two 4D CT data sets. The image quality was improved after correction though quantification was difficult as the ground truth was not known.

Deformable dose calculations using the defDOSXYZ code were compared with two conventional deformable dose calculation methods employing center-of-mass (COM) dose remapping and dose remapping with trilinear (TL) interpolation. The dose deformed between extreme breathing phases was compared in a simple deforming phantom for different voxel sizes and deformation magnitudes. The TL remapping approach was found to underestimate the dose within the field by up to 29% for a voxel size of 1.0 cm with larger discrepancies occurring in penumbral regions. The discrepancies were reduced with decreasing voxel size and deformation magnitude. For more clinically

realistic voxel sizes of 0.5 cm and 0.25 cm the TL remapping approach underestimated the dose by 8% and 0.2%, respectively. A comparison of dose remapping from Inhale to Exhale in a mathematical breathing phantom revealed dose discrepancies of up to 16% in the penumbra region and 8% near the surface where significant deformations occurred perpendicular to the direction of beam incidence. The TL and COM remapping methods were compared to defDOSXYZ calculation of dose deformed between inhale and exhale for 3 different treatment planning scenarios in 4D CT lung patient images. Large discrepancies of more than 25% occurred in the beam penumbra and dose deformation at tissue interfaces were underestimated by the remapping methods. Generally, no statistically significant differences in clinically relevant plan evaluation parameters, such as dose volume histograms, were noted with the exception of the motion evaluation case where the $D_{95\%}$ was underestimated by up to 16%. Discrepancies between defDOSXYZ and remapping calculations were determined to correlate most strongly with the magnitude of the dose gradients. In one patient, complex deformation gradients led to a systematic 2 Gy underestimation of the mean target volume doses. These discrepancies were resolved when smoothing was applied to the deformation vectors.

The non-linear transformations for both 4D CT patients were determined to not conserve image mass and therefore the assumption of mass conservation for defDOSXYZ calculations was found to result in a systematic offset compared to dose remapping calculations because the density matrices on which the dose was calculated were not consistent. A rigorous accuracy evaluation of these dose calculation methods requires a consistent approach to mass conservation for both image registration and dose calculation. The assumption of mass conservation is not valid in all dose accumulation scenarios and the comparison between dose calculation methods requires site specific evaluation.

For clinically-relevant planning scenarios with motion compensation, conventional dose remapping methods were determined to have no significant dose discrepancies when compared with defDOSXYZ. However, when motion effects are large dose remapping methods fail to accurately predict the cumulative dose which may be important for 4D inverse planning methods which incorporate motion effects into the treatment planning process.

A limitation of the 4D dose calculation method comparison presented here is that only extreme breathing phases were considered in the calculation of the cumulative dose. The magnitude of the dose discrepancies is expected to be smaller for intermediate phases where there is less motion and therefore the overall magnitude of cumulative dose differences will be reduced.

The relatively long simulation times required for the current implementation of defDOSXYZ hinders its application to clinical 4D dose calculation. Although future revisions will attempt to improve calculation efficiency in its current form the code presents a useful tool for validating faster dose remapping methods. For example, defDOSXYZ and dose remapping calculations can be compared to quantify the limit of accuracy of the former methods for a given voxel size and anatomical deformations.

## 9.2 OUTLOOK

Accurate representation of the dose deposition in a deforming anatomy requires a physically realistic model of the changing patient anatomy. The current implementation of the defDOSXYZ code assumes a continuous deformation field which may limit its application to sites where discontinuities exist in the vicinity of planning structures. Further modification to transport particles across discontinuous voxel boundaries is required in order to accurately model the discontinuous tissue motion which occurs at the lung/chest wall interface. This would allow the image registration to be performed separately on segmented moving and non-moving structures potentially improving the registration accuracy in these regions.

The lack of mass conservation in image registration is currently a significant problem which limits its application to accurate 4D dose calculations in lung. Currently there is much investigation into obtaining physically realistic deformations from non-linear image registration. For future 4D dose calculations it might be preferable to use a finite-element model-based registration algorithm which models physical properties of tissues. Incorporation of tissue-specific regularization parameters into ANIMAL is also another possibility.

Currently, non-linear image registration using ANIMAL requires the optimization of a large number of registration parameters. For implementation of routine patient 4D

CT registration the determination of parameter class solutions is required. Such a study would require a large number of patient data sets to study how optimized registration parameters vary as a function of pathology, anatomical variability and patient motion.

Many interesting issues were brought to light by the comparison of dose remapping methods and defDOSXYZ in 4D CT patient data. The study performed here was only preliminary and further investigation of the differences between the dose calculations needs to be performed to understand the influence of the deformation maps, dose distribution (i.e., 3D CRT vs. IMRT planning), target volume location, the number of treatment fields, accumulation over multiple breathing phases and the influence on dose in organs at risk.

Finally, to evaluate the total uncertainty of the 4D dose calculation process, including image acquisition and registration accuracy, a comparison of dose calculations in a deformable anthropomorphic phantom is required.

The 4D dose calculation method developed in this thesis could easily be extended to other anatomical sites such as the abdomen and to the evaluation of inter-fraction motion effects. The fact that it is based on a Monte Carlo dose calculation code also allows the study of interplay effects by linking time-dependent treatment head simulations to the time-dependence of the patient dose calculation[1].

4D radiotherapy dose calculation methods are an essential tool for future radiotherapy developments. Currently, the trend in radiotherapy development is towards individualization of patient treatment to reflect differences in individual patient geometries, tissue functional status, radiosensitivity and tumour characteristics, as well as organ motion. 4D dose calculation methods can be used to assess the delivered dose distribution on an individual patient basis in order to determine the most appropriate planning and motion compensation method. Furthermore, 4D dose calculation methods are needed to evaluate the application of emerging radiotherapy techniques, such as scanned heavy ion beams, in sites known to be affected by respiratory motion. Finally, important progress in the refinement of dose-outcome models essential to radiotherapy planning has been made by improving dose calculation accuracy. The additional accuracy gains offered by 4D dose calculation methods now make possible significant

improvements to these models and potentially improved outcomes of patients receiving radiotherapy treatment.

## 9.3 REFERENCES

[1] Paganetti H., Jiang H., Adams J.A., Chen G.T. and E.Rietzel "Monte Carlo simulations with time-dependent geometries to investigate effects of organ motion with high temporal resolution" Int. J. Radiat. Oncol. Biol. Phys. **60** 942-950 (2004).

# Bibliography


Abdelnour A.F., Nehmeh S.A., Pan T., Humm J.L., Vernon P., Schoder H., Rosenzweig K.E., Mageras G.S., Yorke E., Larson S.M. and Y.E. Erdi "Phase and amplitude binning for 4D-CT imaging" Phys. Med. Biol. **52** 3515-3529 (2007)……..…*(24,155)*.

Ahunbay E. and X.A. Li "Investigation of the reliability, accuracy and efficiency of gated IMRT delivery with a commercial linear accelerator" Med. Phys. **34** 2928-2938 (2007)……..*(29)*.

Alasti H., Cho Y.B., Vandermeer A.D., Abbas A., Norrlinger B., Shubbar S. and A. Bezjak "A novel four-dimensional radiotherapy method for lung cancer: imaging, treatment planning and delivery" Phys. Med. Biol. **51** 3251-3267 (2006)…….*(31)*.

Antolak J.A. and I. I. Rosen "Planning target volumes for radiotherapy: how much margin is needed?" Int. J. Radiat. Oncol. Biol. Phys. **44** 1165-1170 (1999)……..…*(22)*.

Armstrong J. and C. McGibney "The impact of three-dimensional radiation on the treatment of non-small cell lung cancer" Radiotherapy and Oncology **56** 157-167 (2000)……*(8)*.

Arnfeld M., Siantar C.H., Siebers J., Garmon P., Cox L. And R. Mohan "The impact of electron transport on the accuracy of computed dose" Med Phys. **27** 266-1274 (2000)…….…...*(8)*.

Bajcsy R. and Kovacic S. "Multiresolution elastic matching" Computer Vision, Graphics, and Image Processing **46** 1-21 (1989)…….……*(83)*.

Balter J.M., Ten Haken R.K., Lawrence T.S., Lam K.L. and J.M. Robertson "Uncertainties in ct-based radiation therapy treatment planning associated with patient breathing" Int. J. Radiation Oncology Biol. Phys. **36** 167-174 (1996)……...…*(16)*.

Barnes E.A., Murray B.R., Robinson D.M., Underwood L.J., Hanson J. and W.H.Y. Roa "Dosimetric evaluation of lung tumor immobilization using breath hold at deep inspiration" Int. J. Radiat. Oncol. Biol. Phys. **50** 1091-1098 (2001)……..…*(27)*.

Bazaraa M.S. "Linear programming and network flows 3rd ed." J. Wiley (2005)……..…*(119)*.

Beckham W.A., Keall P.J. and J.V. Siebers "A fluence-convolution method to calculate radiation therapy dose distributions that incorporate random set-up error" Phys. Med. Biol. **47** 3465-3473 (2002)……..*(56)*.

Beckmann G.K., Kolbl O., Krieger T., Wulf J. and M.P. Flentje "How can we further improve radiotherapy for stage-III non-small-cell lung cancer?" Lung Cancer **45** S125-132 (2004)……..……...*(8)*.

Bel A., van Herk M. and J.V. Lebesque "Target margins for random geometrical treatment uncertainties in conformal radiotherapy" Med. Phys. **23** 1537-1545 (1996)……..*(55)*.

Belderbos J.S.A., Heemsbergen W.D., De Jaeger K., Baas P. and J.V. Lebesque "Final results of a Phase I/II dose escalation trial in non-small-cell lung cancer using three-dimensional conformal radiotherapy" Int. J. Radiat. Oncol. Biol. Phys. **66** 126-134 (2006)……...…….*(8)*.

Berbeco R.I., Nishioka S., Shirato H., Chen G.T.Y. and S.B. Jiang "Residual motion of lung tumors in gated radiotherapy with external respiratory surrogates" Phys. Med. Biol. **50** 3655-3667 (2005)……*(28)*.

Berbeco R.I., Mostafavi H., Sharp G.C. and S.B. Jiang "Towards fluoroscopic respiratory gating for lung tumours without radiopaque markers" Phys. Med. Biol. **50** 4481-4490 (2005)……..*(28)*.

Berlinger K., Sauer O., Vences L. and M. Roth "A simple method for labeling CT images with respiratory states" Med. Phys. **33** 3144-3148 (2006)……..*(25)*.

Berson A.M., Emery R., Rodrigues L., Richards G.M., Ng T., S. Sanghavi and J. Barsa "Clinical experience using respiratory gated radiation therapy: comparison of free-breathing and breathe-hold techniques" Int. J. Radiat. Oncol. Biol. Phys. **60** 419-426 (2004)……..….*(28)*.

Bert C., Metheany K.G., Doppke K. and G.T.Y. Chen "A phantom evaluation of a stereo-vision surface imaging system for radiotherapy setup" Med. Phys. **32** 2753-2762 (2005)……...…*(28)*.

Bharatha A., Hirose M., Hata N., Warfield S.K., Ferrant M., Zou K.H., Suarez-Santana E., Ruiz-Alzola J., D'Amico A., Cormack R.A., Kikinis R., Jolesz F.A. and C.M.C. Tempany "Evaluation of three-dimensional finite element-based deformable

registration of pre- and interaoperative prostate imaging" Med. Phys. **28** 2551-2560 (2001)……..*(88)*.

Bielajew A.F., Hirayama H., Nelson W.R. and D.W.O. Rogers "History, overview and recent improvements of EGS4," NRCC Report PIRS-0436, NRCC Canada (1994)……..*(105)*.

Bielajew A.F. "HOWFAR and HOWNEAR: Geometry Modeling for Monte Carlo Particle Transport," NRCC Reports PIRS-0341 (1995)…….*(106)*.

Boldea V., Sarrut D. and S. Clippe "Lung deformation estimation with non-rigid registration for radiotherapy treatment" Proceeedings MICCAI 2003, LNCS 2878 pp.770-777, Springer-Verlag, Berlin (2003)……..…..*(80)*.

Bookstein F. "Principle warps: thin-plate splines and the decomposition of deformations" IEEE Transactions on Pattern Analysis and Machine Intelligence **11** 567-585 (1989)……..….*(73)*.

Bortfeld T., Jokivarsi K., Goitein M., Kung J. and S.B. Jiang "Effects of intra-fraction motion on IMRT dose delivery: statistical analysis and simulation" Phys. Med. Biol. **47** 2203-2220 (2002)……....*(20)*.

Bortfeld T., Jiang S.B. and E. Rietzel "Effects of motion on the total dose distribution" Seminars in Radiation Oncology **14** 41-51 (2004)…….*(17,19)*.

Bosmans G., Buijsen J., Dekker A., Velders M., Boersma L, De Ruysscher D., Minken A. and P. Lambin "An "in silico" clinical trial comparing free breathing, slow and respiration correlated computed tomography in lung cancer patients" Radiotherapy and Oncology **81** 73-80 (2006)…….*(25,26)*.

Bradley J., Thorstad W.L., Mutic S., Miller T.R., Dehdashti F., Siegel B.A., Bosch W. and R.J. Bertrand "Impact of FDG-PET on radiation therapy volume delineation in non-small cell lung cancer" Int. J. Radiat. Oncol. Biol. Phys. **59** 78-86 (2004)……...*(9)*.

Bradley J.D., Nofal A.N., El Nawa I.M., Lu W., Liu J., Hubenschmidt J., Low D.A., Drzymala R.E. and D. Khullar "Comparison of helical, maximum intensity projection (MIP), and average intensity (AI) 4D CT imaging for stereotactic body radiation therapy (SBRT) planning in lung cancer" Radiotherapy and Oncology **81** 64-268 (2006)……..…*(25)*.

Brock K.K., Hollister S.J., Dawson L.A. and J.M. Balter "Creating a four-dimensional model of the liver using finite element analysis" Med. Phys. **29** 1403-1405 (2002)…….*(88)*.

Brock K.K., McShan D.L., Ten Haken R.L., Hollister S.J., Dawson L.A. and J.M. Balter "Inclusion of organ deformation in dose calculations" Med. Phys. **30** 290-295 (2003)……...*(58,103)*.

Brock K.K., Balter J.M., Dawson L.A. and Kessler M.L., "Automated generation of a four-dimensional model of the liver using warping and mutual information" Med. Phys. **30** 1128-1133 (2003)……..…..*(73)*.

Brock K.K., Sharpe M.B., Dawon L.A., Kim S.M. and D.A. Jaffray "Accuracy of finite element model-based multi-organ deformable image registration" Med. Phys. **32** 1647-1659 (2005)……...……..*(88)*.

Brock K., Moseley J. and D. Jaffray "A novel metric for automatic assessment of deformable image registration accuracy" Med. Phys. **32** 1942 (2005)…….…….*(90)*.

Brock K.K., Dawson L.A., Sharpe M.B., Moseley D.J. and D.A. Jaffray "Feasibility of a novel deformable image registration technique to facilitate classification, targeting and monitoring of tumor and normal tissue" Int. J. Radiat. Oncol. Biol. Phys. **64** 1245-1254 (2006)……..*(88)*.

Broit C. "Optimal registration of deformed images" PhD thesis, Department of computer and information science, University of Pennsylvania, Philadelphia (1981)……..….*(83)*.

Burden R.L. and J.D. Faires "Numerical Analysis" pp.465-480 (2001)…….*(76,85)*.

Cachier P., Pennec X. and N. Ayache "Fast non rigid matching by gradient descent: study and improvements of the "Demons" algorithm" INRIA report #3706, Institut National de Recherche en Informatique et en Automatique (1999)……..*(80)*.

Canadian Cancer Society/National Cancer Institute of Canada "Canadian Cancer Statistics 2007" Toronto, Canada (2007)……..*(1)*.

Chan T.C.Y., Bortfeld T. and J.N. Tsitsiklis "A robust approach to IMRT optimization" Phys. Med. Biol. **51** 2567-2583 (2006)……...…...….*(26)*.

Chen G.T.Y., Kung J.H. and K.P. Beaudette "Artifacts in computed tomography scanning of moving objects" Seminars in Radiation Oncology **14** 19-26 (2004)……..*(16)*.

Chetty I.J., Rosu M., Tyagi N., Marsh L.H., McShan D.L., Balter J.M., Fraass B.A. and R. Ten Haken "A fluence convolution method to account for respiratory motion in three-

dimensional dose calculations of the liver: a Monte Carlo study" Med. Phys. 30 1776-1780 (2003)…….*(56)*.

Chetty I.J., Rosu M., McShan D.L., Fraass B.A., Balter J.M. and R.K. Ten Haken "Accounting for center-of-mass target motion using convolution methods in Monte Carlo-based dose calculations of the lung" Med. Phys. **31** 925-932 (2004)……..*(18,56)*.

Cheung P.C.F., Sixel K.E., Tirona R. and Y.C. Ung "Reproducibility of lung tumor position and reduction of lung mass within the planning target volume using active breathing control (ABC)" Int. J. Radiat. Oncol. Biol. Phys. **57** 1437-1442 (2003)……....*(27)*.

Chi P-C M., Balter P., Luo D., Mohan R. and T. Pan "Relation of external surface to internal tumor motion studied with cine CT" Med. Phys. **33** 3116-3123 (2006)……..…*(28)*.

Chi Y., Liang J. and D. Yan "A material sensitivity study on the accuracy of deformable organ registration using linear biomechanical models" Med. Phys. **33** 421-433 (2006)……..……*(88)*.

Christensen G.E., Rabbitt R.D. and M.I. Miller "3D brain mapping using a deformable neuroanatomy" Phys. Med. Biol. **39** 609-618 (1994)…….……*(84)*.

Christensen G.E., R.D. Rabbitt and M.I. Miller "Deformable templates using large deformation kinematics" IEEE Transactions on Image Processing **5** 1435-1447 (1996)……...*(84,125)*.

Christensen G.E., Joshi S.C. and M.I. Miller "Volumetric transformation of brain anatomy" IEEE Transactions on Medical Imaging **16** 864-877 (1997)……..…*(84)*.

Christensen G.E., Carlson B., Chao K.S.C., Yin P., Grigsby P.W., Nguyen K., Dempsey J.F., Lerma F.A., Bae K.T., Vannier M.W. and J.F. Williamson "Image-based dose planning of intracavitary brachytherapy: registration of serial-imaging studies using deformable anatomic templates" Int. J. Radiat. Oncol. Biol. Phys. **51** 227-243 (2001)…...…*(84,85)*.

Christensen G.E. and H.J. Johnson "Consistent image registration" IEE Transactions on Medical Imaging **20** 568-582 (2001)…….…….*(83)*.

Collignon A., Vandermeulen D., Suetens P. and Marchal G. "3D multi-modality medical image registration using feature space clustering" Proceedings of the 1st International Conference on Computer Vision, Virtual Reality and Robotics in Medicine, Nice, France Springer, Berlin, pp. 195-204 (1995)…….….*(71)*.

Collignon A., Maes F., Delaere D., Vandermeulen D., Suetens P. and Marchal G. ”Automated multimodality medical image registration using information theory” Proceedings of the 14th International Conference on Information Processing in Medical Imaging” Computational Imaging and Vision **3** 263-274 (1995)……..…..*(72)*.

Collins D.L. “3D Model-based segmentation of individual brain structures from magnetic resonance imaging data” Ph.D. dissertation, Department of Biomedical Engineering, McGill University (1994)……...*(119,120)*.

Collins D.L., Holmes C.J., Peters T.M. and A.C. Evans “Automatic 3-D model-based neuroanatomical segmentation” Human Brain Mapping **3** 190-208 (1995)……..…*(119)*.

Collins D.L. and A.C. Evans “ANIMAL: validation and applications of nonlinear registration-based segmentation” Int. J. Pattern Recognition and Artificial Intelligence **11** 1271-1294 (1997)……...……..….*(119)*.

Coolens C., Evans P.M., Seco J., Webb S., Blackall J., Rietzel E. and G.T.Y. Chen “The susceptibility of IMRT dose distributions to intrafraction organ motion: An investigation into smoothing filters derived from four dimensional computed tomography data” Med. Phys. **33** 2809-2818 (2006)…….*(26,60)*.

Court L.E. and Dong L. “Automatic registration of the prostate for computed-tomography-guided radiotherapy” Med. Phys. **30** 2750-2757 (2003)…….……*(71)*.

Coselman M.M., Balter J.M., McShan D.L. and Kessler M.L. “Mutual information based CT registration of the lung at exhale and inhale breathing states using thin-plate splines” Med. Phys. **31** 2942-2948 (2004)……....*(74)*.

Craig T., Battista J., Moiseenko V. and J. Van Dyk “Considerations for the implementations of target volume protocols in radiation therapy” Int J Radiat. Oncol. Biol. Phys. **49** 241-250 (2001)……...*(22)*.

Craig T., Battista J. and J. Van Dyk “Limitations of a convolution method for modeling geometric uncertainties in radiation therapy. I. The effect of shift invariance.” Med. Phys. **30** 2001-2011(2003)……..*(56)*.

Craig T., Battista J. and J. Van Dyk “Limitations of a convolution method for modeling geometric uncertainties in radiation therapy. II. The effect of a finite number of fractions.” Med. Phys. **30** 2012-2020 (2003)……..……*(56)*.

Crum W.R., Griffin L.D., Hill D.L.G. and Hawkes D.J., "Zen and the art of medical image registration: correspondence, homology and quality" NeuroImage **20** 1425-1437 (2003)……..*(69)*.

Crum W.R., Hartkens T. and Hill D.L.G, "Non-rigid image registration: theory and practice", The British Journal of Radiology **77** S140-153 (2004)……....*(66,70,79)*.

Cui Y., Dy J.G., Sharp G.C., Alexander B. and S.B. Jiang "Robust fluoroscopic respiratory gating for lung cancer radiotherapy without implanted fiducial markers" Phys. Med. Biol. **52** 741-755 (2007)…….….*(28)*.

Curry T.S., Dowdey J.E. and Murry R.C. "Christensen's Physics of Diagnostic Radiology 4th Ed." pp. 303-307 Lippincott Williams & Wilkins, PA (1990)…….*(1)*.

DeMarco J.J., Solberg T.D. and J.B. Smathers "A CT-based Monte Carlo simulation tool for dosimetry planning and analysis" Med. Phys. **25** 1-11 (1998)……...……..*(8)*.

De Neve W. and C. De Wagter "Lethal pneumonitis in a phase I study of chemotherapy and IMRT for NSCLC: the need to investigate the accuracy of dose calculation" Radiotherapy and Oncology **75** 246-247 (2005)……...……*(8)*.

D'Souza W.D., Naqvi S.A. and C.X. Yu "Real-time intra-fraction-motion tracking using the treatment couch: a feasibility study" Phys. Med. Biol. **50** 4021-4033 (2005)……*(31)*.

Duan J., Shen S., Fiveash J.B., Popple R.A. and I.A. Brezovich "Dosimetric and radiobiological impact of dose fractionation on respiratory motion induced IMRT delivery errors: A volumetric dose measurement study" Med. Phys. **33** 1380-1387 (2006)……..*(21)*.

Ehler E.D., Nelms B.E. and W.A. Tome "On the dose to a moving target while employing different IMRT delivery mechanisms" Radiotherapy and Oncology **83** 9-56 (2007)……...…*(21)*.

Ehrardt J., Werner R., Saring D., Frenzel D., Lu W., Low D. and H. Handels "An optical flow based method for improved reconstruction of 4D CT data sets acquired during free breathing" Med. Phys. **34** 711-721 (2007)……...….*(166)*.

El Naqa I., Low D.A., Nystrom M., Parikh P., Lu W., Deasy J.O., Amini A., Hubenschmidt J. and S. Wahab "An optical flow approach for automated breathing motion tracking in 4D computed tomography" Proceedings of the 14th Conf. on the use of Computers in Radiation Therapy, Seoul pp.74-77 (2004)…….*(79)*.

Emami B., Lyman J., Brown A., Coia L., Goitein M., Munzenrider J.E., Shank B., Solin J.L. and M. Wesson "Tolerance of normal tissue to therapeutic irradiation" Int. J. Radiat. Oncol. Biol. Phys. **21** 109-122 (1991)……..……*(6)*.

Engelsman M., Damen E.M.F., De Jaeger K., van Ingen K.M. and B.J. Mijnheer "The effect of breathing and set-up errors on the cumulative dose to a lung tumor" Radiotherapy and Oncology **60** 95-105 (2001)…….*(18)*.

Engelsman M., Sharp G.C., Bortfeld T., Onimaru R. and H. Shirato "How much margin reduction is possible through gating or breath hold" Phys. Med. Biol. **50** 477-490 (2005)……..*(28)*.

Evans P.M., Coolens C. and E. Nioutsikou "Effects of averaging over motion and the resulting systematic errors in radiotherapy" Phys. Med. Biol. **51** N1-7 (2006)……..*(17)*.

Fano U., "Note on the Bragg-Gray cavity principle for measuring energy dissipation," Radiat. Res. **1** 237 (1954)…….…….*(110)*.

Fippel M. "Fast Monte Carlo dose calculation for photon beams based on the VMC electron algorithm" Med. Phys. **26** 1466-1475 (1999)……...……*(8)*.

Fitzpatrick M.J., Starkschall G., Antolak J.A., Fu J., Shukla H., Keall P.J., Klahr P. and R. Mohan "Displacement-based binning of time-dependent computed tomography image data sets" Med. Phys. **33** 235-246 (2006)……....*(24,155)*.

Flampouri S., Jiang S.B., Sharp G.C., Wolfgang J., Patel A.A. and N.C. Choi "Estimation of the delivered patient dose in lung IMRT treatment based on deformable registration of 4D-CT data and Monte Carlo simulations" Phys. Med. Biol. **51** 2763-2779 (2006)……...*(19,60,169,171)*.

Florack L.M.J., Romeny B.M.H., Koenderink J.J. and M.A. Viergever "Scale and differential structure of images" Image Vision and Computing **10** 376-388 (1992)…….....*(69)*.

Ford E.C., Mageras G.S., Yorke E. and C.C. Ling "Respiration-correlated spiral CT: a method of measuring respiratory-induced anatomic motion for radiation treatment planning" Med. Phys. **30** 88-97 (2003)……...…*(23)*.

Forsey D.R. and R.H. Bartels "Hierarchical b-spline refinement" Computer Graphics **22** 205-212 (1988)……...……*(76)*.

Foskey M., Davis B., Goyal L., Changs S., Chaney E., Strehl N., Tomei S., Rosenman J. and S. Joshi "Large deformation three-dimensional image registration in image-guided radiation therapy" Phys. Med. Biol. **50** 5869-5892 (2005)……..……*(85)*.

Gagne I.M. and D.M. Robinson "The impact of tumor motion upon CT image integrity and target delineation" Med. Phys. **31** 3378-3392 (2004)……..…*(16)*.

Gagne I.M., Robinson D.M., Halperin R. and W. Roa "The use of phase sequence image sets to reconstruct the total volume occupied by a mobile lung tumor" Med. Phys. **32** 2211-2221 (2005)…….*(25)*.

Gao S., Zhang L., Wang H., de Crevoisier R., Kuban D.D., Mohan R. and L. Dong "A deformable image registration method to handle distended rectums in prostate cancer radiotherapy" Med. Phys. **33** 3304-3312 (2006)…….……*(82)*.

Gee J.C. and R.K. Bajcsy "Elastic matching: continuum mechanical and probabilistic analysis" Brain Warping A.W. Toga Ed. Academic Press, San Diego (1999)…..….*(83)*.

George R., Ramakrishnan V., Siebers J.V., Chung T.D. and P.J. Keall "Investigation of patient, tumour and treatment variables affecting residual motion for respiratory-gated radiotherapy" Phys. Med. Biol. **51** 5305-5319 (2006)……*(28)*.

George R., Chung T.D., Vedam S.S., Ramakrishnan V., Mohan R., Weiss E. and P.J. Keall "Audio-visual biofeedback for respiratory-gated radiotherapy: impact of audio instruction and audio-visual biofeedback on respiratory-gated radiotherapy" Int. J. Radiat. Oncol. Biol. Phys. **65** 924-944 (2006)……*(25)*.

Giraud P., Elles S., Helfre S., De Rycke Y., Servois V., Carette M-F., Alsieu C., Bondiau P-Y., Dubray B., Touboul E., Housset M., Rosenwald J-C. and J-M. Cosset "Conformal radiotherapy for lung cancer: different delineation of the gross tumor volume (GTV) by radiologists and radiation oncologists" Radiotherapy and Oncology **62** 27-36 (2002)…….……...*(8)*.

Goitein M. "Calculation of the uncertainty in the dose delivered during radiation therapy" Med. Phys. **12** 608-612 (1985)……..….*(48)*.

Guckenberger M., Wilbert J., Meyer J., Baier K., Richter A. and M. Flentje "Is a single respiratory correlated 4D-CT study sufficient for evaluation of breathing motion?" Int. J. Radiat. Oncol. Biol. Phys. **67** 352-1359 (2007)……..……*(25)*.

Guerrero T., Zhang G., Huang T-C. and Lin K-P. "Intrathoracic tumour motion estimation from CT imaging using 3D optical flow method" Phys. Med. Biol. **49** 4147-4161 (2004)……..*(79)*.

Guerrero T., Zhang G., Segars W., Huang T-C., Bilton S., Ibbott G., Dong L., Forster K. and K.P. Lin "Elastic image mapping for 4-D dose estimation in thoracic radiotherapy" Radiation Protection Dosimetry **115** 497-502 (2005)……...…*(60,92)*.

Guerrero T., Sanders K., Castillo E., Zhang Y., Bidaut L., Pan T. and R. Komaki "Dynamic ventilation imaging from four-dimensional computed tomography" Phys. Med. Biol. **51** 777-791 (2006)……*(79)*.

Hanley J., Debois M.M., Mah D., Mageras G.S., Raben A., Rosenzweig K., Mychalczak B., Schwartz L.H., Gloeggler P.J., Lutz W., Ling C.C., Leibel S.A., Fuks Z. and G.J. Kutcher "Deep inspiration breath-hold technique for lung tumors: the potential value of target immobilization and reduced lung density in dose escalation" Int. J. Radiat. Oncol. Biol. Phys. **45** 603-611 (1999)……....*(27)*.

Hartkens T. "Measuring, analyzing, and visualizing brain deformation using non-rigid registration" Ph.D. thesis dissertation, University of London (2003)…….*(77)*.

Henkelman R.M. and K. Mah "How important is breathing in radiation therapy of the thorax?" Int. J. Radiat. Oncol. Biol. Phys. **8** 2005-2010 (1982)……..…*(17)*.

Hill D.L.G., Batchelor P.G., Holden M. and Hawkes D.J. "Medical image registration", Phys. Med. Biol. **36** R1-R45 (2001)…….……...*(70,72)*.

Horn B.K.P and Schunck B.G. "Determining optical flow" Artificial Intelligence **17** 185-204 (1981)……..……*(77)*.

International Commission on Radiation Units and Measurements (ICRU), ICRU Report 50 "Prescribing, Recording, and Reporting Photon Beam Therapy" ICRU, Bethesda MD (1993)……..…*(2,187)*.

International Commission on Radiation Units and Measurements (ICRU), ICRU Report 60 "Prescribing, Recording, and Reporting Photon Beam Therapy (Supplement to ICRU Report 50)" ICRU, Bethesda MD (1999)…….*(4,22)*.

Isaksson M., Jalden J. and M.J. Murphy "On using an adaptive neural network to predict lung tumor motion during respiration for radiotherapy applications" Med. Phys. **32** 3801-3809 (2005)……..…*(32)*.

Fippel M. “Fast Monte Carlo dose calculation for photon beams based on the VMC electron algorithm” Med. Phys. **26** 1466-1475 (1999)……...…*(7)*.

Jassem J. “The role of radiotherapy in lung cancer: where is the evidence?” Radiotherapy and Oncology **83** 203-213 (2007)……*(8)*.

Jiang S.B., Pope C., Al Jarrah K.M., Kung J.H., Bortfeld T. and G.T.Y. Chen “An experimental investigation on intra-fractional organ motion effects in lung IMRT treatments” Phys. Med. Biol. **48** 1773-1794 (2003)……...…*(21)*.

Jin J-Y., Ajlouni M., Ryu S., Chen Q., Li S. and B. Movsas “A technique of quantitatively monitoring both respiratory and nonrespiratory motion in patients using external body markers” Med. Phys. **34** 2875-2881 (2007)……*(28)*.

Joshi S.C. and M.I. Miller “Landmark matching via large deformation diffeomorphisms” IEEE Transactions on Image Processing **9** 1357-1370 (2000)……..…*(87)*.

Kakar M., Nystrom H., Aarup L.R., Nottrup T.J. and D.R. Olsen “Respiratory motion prediction by using the adaptive neuro fuzzy inference system (ANFIS)” Phys. Med. Biol. **50** 4721-4728 (2005)……..……*(32)*.

Kashani R., Lam K., Litzenberg D. And J. Balter ”Technical note: a deformable phantom for dynamic modeling in radiation therapy” Med. Phys. **34** 199-201 (2007)……..*(92)*.

Kawrakow I. “Accurate condensed history Monte Carlo simulation of electron transport. I EGSnrc, the new EGS4 version,” Med Phys **27**, 485 – 498 (2000)……..……*(105)*.

Kawrakow I. and D.W.O. Rogers, “The EGSnrc Code System: Monte Carlo Simulation of Electron and Photon Transport,” NRCC Reports PIRS-701, NRC Canada (2001)…….*(105,106)*.

Keall P.J., Beckham W.A., Booth J.T., Zavgorodni S.F. and M. Oppelaar “A method to predict the effect of organ motion and set-up variations on treatment plans” Australasian Physical and Engineering Sciences in Medicine **22** 48-52 (1999)…..…*(55)*.

Keall P.J., Kini V.R., Vedam S.S. and R. Mohan “Motion adaptive x-ray therapy: a feasibility study” Phys. Med. Biol. **46** 1-10 (2001)……*(31)*.

Keall P.J., Chen G.T.Y and S. Joshi “Time – the fourth dimension in radiotherapy (ASTRO panel discussion)” Int. J. Radiat. Oncol. Biol. Phys. **57** S8-9 (2003)…….……..*(9)*.

Keall P.J., Starkschall G., Shukla H., Forster K.M., Ortiz V., Stevens C.W., Vedam S.S., George R., Guerrero T. and R. Mohan "Acquiring 4D thoracic CT scans using a multislice helical method" Phys. Med. Biol. **49** 2053-2067 (2004)…….*(23,103)*.

Keall P.J., Siebers J.V., Joshi S. and R. Mohan "Monte Carlo as a four-dimensional radiotherapy treatment-planning tool to account for respiratory motion" Phys. Med. Biol. **49** 3639-3648 (2004)……...…*(60,103)*.

Keall P.J., Joshi S., Vedam S.S., Siebers J.V., Kini V.R. and R. Mohan "Four-dimensional radiotherapy planning for DMLC-based respiratory motion tracking" Med. Phys. **32** 942-951 (2005)……..…*(31,85)*.

Keall P.J., Mageras G.S., Balter J.M., Emery J.S., Forster K.M., Jiang S.B., Kapatoes J.M., Low D.A., Murphy M.J., Murray B.R., Ramsey C.R., Van Herk M.B., Vedam S.S., Wong J.W. and E. Yorke "The management of respiratory motion in radiation oncology report of AAPM Task Group 76" AAPM Report 91, Med. Phys. 33(10) pp.3874-3900 (2006)……...*(8,14)*.

Keall P.J., Cattell H., Pokhrel D., Dieterich S., Wong K.H., Murphy M.J., Vedam S.S., Wijesooriya K. and R. Mohan "Geometric accuracy of a real-time target tracking system with dynamic mutlileaf collimator tracking system" Int. J. Radiat. Oncol. Biol. Phys. **65** 1579-1584 (2006)…….*(31)*.

Kerdok A.E., Cotin S.M., Ottensmeyer M.P., Galea A., Howe R.D. and S.L. Dawson "TruthCube: establishing physical standards for real time soft tissue simulation" Int. Workshop on deformable modeling and soft tissue simulation, Bonn, Germany (2001)……..*(91)*.

Killoran J.H., Kooy H.M., Gladstone D.J., Welte F.J. and C.J. Beard "A numerical simulation of organ motion and daily setup uncertainties: implications for radiation therapy" Int. J. Radiat. Oncol. Biol. Phys. **37** 213-221 (1997)……...*(49)*.

Kim D.J.W., Murray B.R., Halperin R. and W.H.Y. Roa "Held-breath self-gating technique for radiotherapy of non-small-cell lung cancer: a feasibility study" Int. J. Radiat. Oncol. Biol. Phys. **49** 43-49 (2001)……*(27)*.

Kim J. and Fessler J.A. "Intensity-based image registration using robust correlation coefficients" IEEE Transactions on Medical Imaging **23** 1430-1444 (2004)…….*(71)*.

Kim S., Jaffray D.A. and K.K. Brock "The effect of heterogeneous and nonlinear material properties on organ deformation" Med. Phys. 3**2** 2143 (2005)……...*(88)*.

Kini V.R., Vedam S.S., Keall P.J., Patil S., Chen C. and R. Mohan "Patient training in respiratory-gated radiotherapy" Medical Dosimetry **28** 7-11 (2003)……..*(28)*.

Kleshneva T., Muzik K. and M. Alber "An algorithm for automatic determination of the respiratory phases in four-dimensional computed tomography" Phys. Med. Biol. **51** N269-276 (2006)…….*(25)*.

Knoos T., Ahnesjo A., Nilsson P. and L. Weber "Limitations of a pencil beam approach to photon dose calculations in lung tissue" Phys. Med. Biol. 40 pp.1411-1420 (1995)……*(8)*.

Koch N., Liu H.H., Starkschall G., Jacobson M., Forster K., Liao Z., Komaki R. and C.W. Stevens "Evaluation of internal lung motion for respiratory-gated radiotherapy using MRI: Part 1- correlating internal lung motion with skin fiducial motion" Int. J. Radiat. Oncol. Biol. Phys. **60** 1459-1472 (2004)……....*(28)*.

Kong F-M., Ten Haken R.K., Schipper M.J., Sullivan M.A., Chen M., Lopez C., Kalemkerian G.P. and J.A. Hayman "High-dose radiation improved local tumor control and overall survival in patients with inoperable/unresectable non-small-cell lung cancer: long-term results of a radiation dose escalation study" Int. J. Radiat. Oncol. Biol. Phys. **63** 324-333 (2005)…….……*(8)*.

Kontrisova K., Stock M., Dieckmann K., Bogner J., Poetter R. And D. Georg "Dosimetric comparison of stereotactic body radiotherapy in different respiration conditions: a modeling study" Radiotherapy and Oncology **81** 97-104 (2006)……...……*(27)*.

Kostelec P.J., Weaver J.B. and D.M. Healy "Multiresolution elastic image registration" Med. Phys. **25** 1593-1604 (1998)…….……*(75)*.

Kubo H.D. and B.C. Hill "Respiration gated radiotherapy treatment: a technical study" Phys. Med. Biol. **41** 83-91 (1996)……..…*(28)*.

Kubo H.D. and L. Wang "Compatibility of Varian 2100C gated operations with enhanced dynamic wedge and IMRT dose delivery" Med Phys **27** 1732-1738 (2000)……..*(29)*.

Kung J.H., Zygmanski P., Choi N. and G.T.Y. Chen "A method of calculating a lung clinical target volume DVH for IMRT with intrafractional motion" Med. Phys. **30** 1103-1109 (2006)…….*(18,57)*.

Lagerwaard F.J., van Sornsen de Koste J.R., Nijssen-Visser M.R., Schuchhard-Schipper R.H., Oei S.S., Munne A. and S. Senan "Multiple "slow" CT scans for incorporating lung tumor mobility in radiotherapy planning" Int. J. Radiat. Oncol. Biol. Phys. **51** 932-937 (2001)……...…*(22)*.

Lagerwaard F.J., Senan S., van Meerbeeck J.P. and Graveland W.J. "Has 3-D conformal radiotherapy (3D CRT) improved the local tumour control for stage I non-small cell lung cancer?" Radiotherapy and Oncology **63** 151-157 (2002)……..……..*(8)*.

Lax I., Blomgren H., Naslund I. and R. Svanstrom "Stereotactic radiotherapy of malignancies in the abdomen. Methodological aspects" Acta. Oncol. **33** 577-683 (1994)……..…*(26)*.

Lax I., Blomgren H., Larson D. and I. Naslund "Extracranial stereotactic radiosurgery of localized targets" Journal of Radiosurgery **1**135-148 (1998)…….*(26)*.

Leong J. "Implementation of random positioning error in computerized radiation treatment planning systems as a result of fractionation" Phys. Med. Biol. **32** 327-334 (1987)……..*(55)*.

Li J.G. and L. Xing "Inverse planning incorporating organ motion" Med. Phys. **27** 1573-1578 (2000)…….…*(26)*.

Li T., Schreibmann E., Thorndyke B., Tillman G., Boyer A., Koong A., Goodman K. and L. Xing "Radiation dose reduction in four-dimensional computed tomography" Med. Phys. **32** 3650-3660 (2005)…….……*(24)*.

Li T., Thorndyke B., Schreibmann E., Yang Y. and L. Xing "Model-based image reconstruction for four-dimensional PET" Med. Phys. **33** 288-1298 (2006)…….…*(76)*.

Li X.A., Stepaniak C. and E. Gore "Technical and dosimetric aspects of respiratory gating using a pressure-sensor motion monitoring system" Med. Phys. **33** 145-154 (2006)…….…….*(28)*.

Liang J. and D. Yan "Reducing uncertainties in volumetric image based deformable organ registration" Med. Phys. **30** 2116-2122 (2003)……...*(88)*.

Ling C.C., Yorke E., Amols H., Mchalakos J., Erdi Y., Leibel S., Rosenzweig K. and A. Jackson "High-tech will improve radiotherapy of NSCLC: a hypothesis waiting to be validated" Int. J. Radiat. Oncol. Biol. Phys. **60** 3-7 (2004)……...……*(8)*.

Litzenberg D.W., Hadley S.W., Tyagi N., Balter J.M., Ten Haken R.K. and I.J. Chetty "Synchronized dynamic dose reconstruction" Med. Phys. **34** 91-102 (2007)……....*(54)*.

Liu H.H., Wang X., Dong L., Wu Q., Liao Z., Stevens C.W., Guerrero T.M., Komaki R., Cox J.D. and R. Mohan "Feasibility of sparing lung and other thoracic structures with intensity-modulated radiotherapy for non-small-cell lung cancer" Int. J. Radiat. Oncol. Biol. Phys. **58** 1268-1279 (2004)…….....……*(4)*.

Lockman D.M., Yan D. and J. Wong "Estimating the dose variation in a volume of interest with explicit consideration of patient geometric variation" Med. Phys. **27** 2100-2108 (2000)……..…...*(50,51)*.

Low D.A., Harms W.B., Mutic S. and J.A. Purdy "A technique for the quantitative evaluation of dose distributions" Med. Phys. **25** 656-661 (1998)…….....…..*(90)*.

Lohr F., Debus J., Frank C., Herfarth K., Pastyr O., Rhein B., Bahner M.L., Schlegel W. and M. Wannenmacher "Noninvasive patient fixation for extracranial stereotactic radiotherapy" Int. J. Radiat. Oncol. Biol. Phys. **45** 521-527 (1999)……...…*(26)*.

Low D.A., Nystrom M., Kalini E., Parikh P., Dempsey J.F., Bradley J.D., Mutic S., Wahab S.H., Islam T., Christensen G., Politte D.G. and B.R. Whiting "A method for the reconstruction of four-dimensional synchronized CT scans acquired during free breathing" Med. Phys. **30** 1254-1263 (2003)…….*(23,25)*.

Lu W. "Motion detection and correction for image guided radiation therapy" PhD Thesis University of Wisconsin-Madison (2001)……..……*(91)*.

Lu W., Chen M-L., Olivera G.H., Ruchala K.J. and T.R. Mackie "Fast free-form deformable registration via calculus of variations" Phys. Med. Biol. **49** 3067-3087 (2004)…….*(82)*.

Lu W., Parikh P.J., El Naqa I.M., Nystrom M.M., Hubenschmidt J.P., Wahab S.H., Mutic S., Singh A.K., Christensen G.E., Bradley J.D. and D.A. Low "Quantitation of the reconstruction quality of a four-dimensional computed tomography process for lung cancer patients" Med. Phys. **32** 890-901 (2005)…….*(25)*.

Lu W., Parikh P.J., Hubenschmidt J.P., Politte D.G., Whiting B.R., Bradley J.D., Mutic S. and D.A. Low "Reduction of motion blurring artifacts using respiratory gated CT in sinogram space: a quantitative evaluation" Med. Phys. **32** 3295-3304 (2005)……...*(29)*.

Lu W., Parikh P.J., Hubenschmidt J.P., Bradley J.D. and D.A. Low "A comparison between amplitude sorting and phase-angle sorting using external respiratory measurement for 4D CT" Med. Phys. **33** 2964-2974 (2006)……...…*(24,155)*.

Lu W., Nystrom M.M., Parikh P.J., Fooshee D.R., Hubenschmidt J.P., Bradley J.D. and D.A. Low "A semi-automatic method for peak and valley detection in free-breathing respiratory waveforms" Med. Phys. **33** 3634-3636 (2006)……..……*(155)*.

Lu W., Olivera G.H., Chen Q., Chen M-L. and K.J. Ruchala "Automatic re-contouring in 4D radiotherapy" Phys. Med. Biol. **51** 1077-1099 (2006)……..…….*(82)*.

Lu W., Olivera G.H., Chen Q., Ruchala K.J., Haimerl J., Meeks S.L., Langen K.M. and P.A. Kupelian "Deformable registration of the planning image (kVCT) and the daily images (MVCT) for adaptive radiation therapy" Phys. Med. Biol. **51** 4357-4374 (2006)….*(82)*.

Lujan A.E., Larsen E.W., Balter J.M. and R.K. Ten Haken "A method for incorporating organ motion due to breathing into 3D dose calculations" Med. Phys. **26** 715-720 (1999)……..….*(55,109)*.

Lujan A.E., Ten Haken R.K., Larsen E.W. and J.M. Balter "Quantization of setup uncertainties in 3-D dose calculations" Med. Phys. **26** 2397 –2402 (1999)……...…*(55)*.

Lujan A.E., Balter J.M. and R.K. Ten Haken, "A method for incorporating organ motion due to breathing into 3D dose calculations in the liver: sensitivity to variations in motion," Med. Phys. 30(10), pp.2643-2649 (2003).

Ma C-M., Li J.S., Pawlicki T., Jiang S.B., Deng J., Lee M.C., Koumrian T., Luxton M. and Brain S. "A Monte Carlo dose calculation tool for radiotherapy treatment planning" Phys. Med. Biol. **47** 1671-1689 (2002)…….……*(8)*.

MacKay R I, Graham P.A., Moore C.J., Logue J.P., and P.J. Sharrock "Animation and radiobiological analysis of 3D motion in conformal radiotherapy" Radiotherapy and Oncology **52** 43-49 (1999)……..*(49)*.

Mackie T.R., Reckwedt P., McNutt T., Gehring M., Saunders C. "Photon beam dose computations. Teletherapy: present and future" pp.104-135 (1996)……*(5)*.

Mageras G.S., Kutcher G.J., Leibel S.A., Zelefsky M.J., Melian E., Mohan R. and Z. Fuks "A method of incorporating organ motion uncertainties into three-dimensional conformal treatment plans" Int. J. Radiat. Oncol. Biol. Phys. **35** 333-342 (1996)….*(49)*.

Mah D., Hanley J., Rosenzweig K.E., Yorke E., Braban L., Ling C.C. and S.A. Leibel "Technical aspects of the deep inspiration breath-hold technique in the treatment of thoracic cancer" Int. J. Radiat. Oncol. Biol. Phys. **48** 1175-1185 (2000)……...…*(27)*.

Maintz, J.B. and Viergever, M.A., "A survey of medical image registration", Medical Image Analysis **2** 1-36 (1998)……..……..*(67)*.

Maleike D., Unkelbach J. and U. Oelfke "Simulation and visualization of dose uncertainties due to interfractional organ motion" Phys. Med. Biol. **51** 223-2252 (2006)……..*(53)*.

Malsch U., Thieke C., Huber P.E. and R. Bendl "An enhance block matching algorithm for fast elastic registration in adaptive radiotherapy" Phys. Med. Biol **51** 4789-4806 (2006)…….……*(75)*.

Marquardt D.W. "An algorithm for least-squares estimation of nonlinear parameters" Journal of the Society for Industrial and Applied Mathematics **11** 431-441 (1963)……...…*(84)*.

Mattes D., Haynor D.R., Vesselle H., Lewellen T.K. and Eubank W. "PET-CT image registration in the chest using free-form deformations" IEEE Transactions on Medical Imaging **22** 120-128 (2003)…….……*(76)*.

McCarter S.D. and W.A. Beckham "Evaluation of the validity of a convolution method for incorporating tumour movement and set-up variations into the radiotherapy treatment planning system" Phys. Med. Biol. **45** 923-931 (2000)……..…*(55)*.

McClelland J., Blackall J.M., Tarte S., Chandler A.C., Hughes S., Ahmad S., Landau D.B. and D.J. Hawkes "A continuous 4D motion model from multiple respiratory cycles for use in lung radiotherapy" Med. Phys. **33** 3348-3358 (2006)……...…*(77,109)*.

McCollough C.H., Bruesewitz M.R., Daly T.R. and F.E. Zink "Motion artifacts in subsequent conventional CT and electron-beam CT: pictorial demonstration of temporal resolution" Radiographics **20** 1675-1681 (2000)…….…*(16)*.

McGarry R.C., Papiez L., Williams M. and R.D. Timmerman "Stereotactic body radiation therapy of early-stage non-small-cell lung carcinoma: Phase 1 study" Int. J. Radiat. Oncol. Biol. Phys. **63** 1010-1015 (2005)……....*(26)*.

Mechalakos J., Yorke E., Mageras G.S., Hertanto A., Jackson A., Obcemea C., Rosenzweig K. and C.C. Ling "Dosimetric effect of respiratory motion in external beam radiotherapy of the lung" Radiotherapy and Oncology **71** 191-200 (2004)……...*(18)*.

Meyer C.R., Boes J.L., Kim B., Bland P.H., Zasadny K.R., Kison P.V., Koral K., Frey K.A. and R.L. Wahl "Demonstration of accuracy and clinical versatility of mutual information for automatic multimodality image fusion using affine and thin-plate spline warped geometric deformations" Medical Image Analysis **1** 195-206 (1996)…….*(73)*.

Murphy M.J., Martin D., Whyte R., Hai J., Ozhasoglu C. and Q-T Le "The effectiveness of breath-holding to stabilize lung and pancreas tumors during radiosurgery" Int. J. Radiat. Oncol. Biol. Phys. **53** 475-482 (2002)……*(27)*.

Murphy M.J. "Tracking moving organs in real time" Seminars in Radiation Oncology **14** 91-100 (2004)……...*(30)*.

Murphy M.J. and S. Dieterich "Comparative performance of linear and nonlinear neural networks to predict irregular breathing" Phys. Med. Biol. **51** 5903-5914 (2006)..…*(32)*.

Murshed H. "Clinical fundamentals for radiation oncology residents" Medical Physics Publishing, Madison WI (2006)……..……..…*(1)*.

Mutaf Y.D., Antolak J.A. and D.H. Brinkmann "The impact of temporal inaccuracies on 4DCT image quality" Med. Phys. **34** 1615-1622 (2007)……..*(155)*.

Nakamura K., Shioyama Y., Nomoto S., Ohga S., Toba T., Yoshitake T., Anai S., Terashima H. and H. Honda "Reproducibility of the abdominal and chest wall position by voluntary breath-hold technique using a laser-based monitoring and visual feedback system" Int. J. Radiat. Oncol. Biol. Phys. **68** 267-272 (2007)……*(27)*.

Naqvi S.A. and W.D. D'Souza "A stochastic convolution/superposition method with isocenter sampling to evaluate intrafraction motion effects in IMRT" Med. Phys. **32** 1156-1163 (2005)……*(54)*.

Negoro Y., Nagata Y., Aoki T., Mizowaki T., Araki N., Takayama K., Kokubo M., Yano S., Koga S., Sasai K., Shibamoto Y. and M. Hiraoka "The effectiveness of an immobilization device in conformal radiotherapy for lung tumor: reduction of respiratory tumor movement and evaluation of the daily setup accuracy" Int. J. Radiat. Oncol. Biol. Phys. **50** 889-898 (2001)……....*(26)*.

Neicu T., Shirato H., Seppenwoolde Y. and S.B. Jiang "Synchronized moving aperture radiation therapy (SMART): average tumor trajectory for lung patients" Phys. Med. Biol. **48** 87-598 (2003)……...….*(31)*.

Neicu T., Berbeco R., Wolfgang J. and S.B. Jiang "Synchronized moving aperture radiation therapy (SMART): improvement of breathing pattern reproducibility using respiratory coaching" Phys. Med. Biol. **51** 617-636 (2006)…….….*(31)*.

Nelder J.A. and Mead R. "A simplex method for function minimization" Computer Journal **7** 308-313 (1965)……...…….*(74)*.

Nelson W.R., Hirayama J. and D.W.O Rogers, "The EGS4 code system," Stanford Linear Accelerator Report SLAC-265 (1985)……..*(105)*.

Nelson C., Starkschall G., Balter P., Fitzpatrick M.J., Antolak J.A., Tolani N. and K. Prado "Respiration-correlated treatment delivery using feedback-guided breath hold: a technical study" Med. Phys. **32** 175-181 (2005)…….*(27)*.

Niemierko A. "Reporting and analyzing dose distributions: a concept of equivalent uniform dose" Med. Phys. **24** 103-110…….……..…*(6)*.

Nioutsikou E., Webb S., Panakis N., Bortfeld T. and U. Oelfke "Reconsidering the definition of a dose-volume histogram" Phys. Med. Biol. **50** L17-9 (2005)…….……*(114)*.

Nioutsikou E., Symonds-Taylor J.R.N., Bedford J.L. and S. Webb "Quantifying the effect of respiratory motion on lung tumour dosimetry with the aid of a breathing phantom with deforming lungs" Phys. Med. Biol. **51** 3359-3374 (2006)……..*(18)*.

Noblet V., Heinrich C., Heitz F., and J-P. Armspach "3-D deformable image registration: a topology preservation scheme based on hierarchical deformation models and interval analysis optimization" IEEE Transactions on Image Processing **14** 553-566 (2005)……....*(150)*.

Ohara K., Okumura T. and M. Akisada "Irradiation synchronized with respiration gate" Int. J. Radiat. Oncol. Biol. Phys **17** 853-857 (1989)…….……*(27)*.

Onishi H., Kuriyama K., Komiyama T., Tanaka S., Sano N., Aikawa Y., Tateda Y., Araki T., Ikenaga S. and M. Uematsu "A new irradiation system for lung cancer combining linear accelerator, computed tomography, patient self-breath-holding, and patient-directed beam-control without respiratory monitoring devices" Int. J. Radiat. Oncol. Biol. Phys. **56** 14-20 (2003)……...……*(27)*.

Ozhasoglu C. and M.J. Murphy "Issues in respiratory motion compensation during external-beam radiotherapy" Int. J. Radiat. Oncol. Biol. Phys. **52** 1389-1399 (2002)…….*(32)*.

Paganetti H., Jiang H., Adams J.A., Chen G.T. and E.Rietzel "Monte Carlo simulations with time-dependent geometries to investigate effects of organ motion with high temporal resolution" Int. J. Radiat. Oncol. Biol. Phys. **60** 942-950 (2004)……..…*(60,103,217)*.

Pan T., Lee T-Y., Rietzel E. and G.T.Y. Chen "4D-CT imaging of a volume influenced by respiratory motion on multi-slice CT" Med. Phys. **31** 333-340 (2004)……..*(23,25,125)*.

Pan T. “Comparison of helical and cine acquisitions for 4D-CT imaging with mutlislice CT” Med. Phys. **32** 627-634 (2005)……*(23)*.

Papiez L., “DMLC leaf-pair optimal control of IMRT delivery for a moving rigid target” Med. Phys. **31** 2742-2754 (2004)……....*(31)*.

Parikh P., Hubenschmidt J., Dimmer S., Vertatschitsch E., Eidens R., Wright J.N. and D.A. Low ”4D verification of real-time accuracy of the Calypso system with lung cancer patient trajectory data” Int. J. Radiat. Oncol. Biol. Phys. **63** S26-27 (2005)……..*(31)*.

Pennec X., Cachier P. and N. Ayache “Understanding the ‘demon’s algorithm’: 3D non-rigid registration by gradient descent” Proceedings of MICCAI 1999, LNCS 1679 pp.697-606 Springer-Verlag (1999)…….....*(72,80)*.

Pekar V., McNutt T.R. and M.R. Kauss “Automated model-based organ delineation for radiotherapy planning in prostatic region” Int. J. Radiat. Oncol. Biol. Phys. **60** 973-980 (2004)……...….*(130)*.

Pekar V., Gladilin E. and K. Rohr “An adaptive irregular grid approach for 3D deformable image registration” Phys. Med. Biol. **51** 361-377 (2006)……...*(84)*.

Pevsner A., Davis B., Joshi S., Hertanto A., Mechalakos J., Yorke E., Rosenzweig K., Nehmeh S., Erdi Y.E. Erdi, Humm J.L., Larson S., Ling C.C. and G.S. Mageras “Evaluation of an automated deformable image matching method for quantifying lung motion in respiration-correlated CT images” Med. Phys. **33** 369-376 (2006)……..*(86,91,130)*.

Raeside D.E. “Monte Carlo principles and applications” Phys. Med. Biol. 21(2) pp.181-197 (1976)……*(7)*.

Ragan D., Starkschall G., McNutt T. and M. Kauss “Semiautomated four-dimensional computed tomography segmentation using deformable models“ Med. Phys. **32** 2254-2261 (2007)…….*(25)*.

Remeijer P., Rasch C., Lebesque J.V. and M. van Herk “A general methodology for three-dimensional analysis of variation in target volume delineation” Med. Phys. **26** 931-940 (1999)…….….*(91)*.

Rey D., Subsol G., Delingette H. and N. Ayache “Automatic detection and segmentation of evolving processes in 3D medical images: Application to multiple sclerosis” Medical Image Analysis **6** 163-179 (2002)…….……*(125)*.

Rietzel E., Chen G.T.Y., Choi N.C. and C.G. Willet "Four-dimensional image-based treatment planning: target volume segmentation and dose calculation in the presence of respiratory motion" Int. J. Radiat. Oncol. Biol. Phys. **61** 1535-1550 (2005)……..*(60)*.

Rietzel E., Pan T. and G.T.Y. Chen "Four-dimensional computed tomography: Image formation and clinical protocol" Med. Phys. **32** 874-889 (2005)……..*(23,25)*.

Rietzel E. and G.T.Y. Chen "Improving retrospective sorting of 4D computed tomography data" Med. Phys. **33** 377-379 (2006)……...*(24,155)*.

Rietzel E. and G.T. Chen "Deformable registration of 4D computed tomography data" Med. Phys. **33** 4423-4430 (2006)……...…*(77,131,149)*.

Ritchie C.J., Godwin J.D., Crawford C.R., Stanford W., Anno H. and Y. Kim "Minimum scan speeds for suppression of motion artifacts in CT" Radiology **185** 37-42 (1992)……..*(16)*.

Robbins, S., Evans A.C., Collins D.L. and S. Whiteside "Tuning and comparing spatial normalization methods" Proceedings of MICCAI 2003 pp. 910-917 (2003)……...*(134)*.

Rogers D.W.O. and A.F. Bielajew "Monte Carlo techniques of electron and photon transport for radiation dosimetry" The Dosimetry of Ionizing Radiation Chapt. 5 Vol III (1990)…….……*(7,115)*.

Rogers D.W.O., Faddegon B.A., Ding G.X., Ma C-M. and J. We "BEAM: a Monte Carlo code to simulate radiotherapy treatment units" Med. Phys **22** 503-524 (1995)……..*(8,105,106)*.

Rohlfing T., Maurer C.R., O'Dell W.G. and J. Zhong "Modeling liver motion and deformation during the respiratory cycle using intensity-based nonrigid registration of gated MR images" Med. Phys. **31** 427-432 (2004)…….*(77)*.

Rosenman J.G., Miller E.P., Tracton G. and T.J. Cullip "Image registration: an essential part of radiation therapy treatment planning" Int. J. Radiat. Oncol. Biol. Phys. **40** 197-205 (1998)……..*(66)*.

Rosenzweig K.E., Hanley J., Mah D., Mageras G., Hung M., Toner S., Burman C., Ling C.C., Mychalzak B., Fukz Z. and S.A. Leibel "The deep inspiration breath-hold technique in the treatment of inoperable non-small-cell lung cancer" Int. J. Radiat. Oncol. Biol. Phys. **48** 81-87 (2000)……....*(27)*.

Ross C.S., Hussey D.H., Pennington E.C., Stanford W. and J.F. Doornbos "Analysis of movement of intrathoracic neoplasms using ultrafast computerized tomography" Int. J. Radiat. Oncol. Biol. Phys. **18** 671-677 (1990)……....*(18)*.

Rosu M., Chetty I.J., Balter J.M., Kessler M.L., McShan D.L. and R.K. Ten Haken "Dose reconstruction in deforming lung anatomy: Dose grid size effects and clinical implications" Med. Phys. **32** 2487-2495 (2005)……...…*(19,59,103,132,167,169)*.

Rosu M., Balter J.M., Chetty I.J., Kessler M.L., McShan D.L., Balter P. and R.K. Ten Haken "How extensive of a 4D dataset is needed to estimate cumulative dose distribution plan evaluation metrics in conformal lung therapy?" Med. Phys. **34** 233-245 (2006)…...*(59)*.

Rosu M., Chetty I.J., Kessler M.L. and R.K. Ten Haken "Monte Carlo non-adaptive 4D treatment planning in conformal radiation therapy: why, how and what to look for", Integrating new technologies into the clinic: Monte Carlo and image-guided radiation therapy, Proceedings of theAAPM summer school, Windsor, Canada pp. 293-310 (2006)……...…….*(148)*.

Rosu M., Chetty I.J., Tatro D.S. and R.K. Ten Haken "The impact of breathing motion versus heterogeneity effects in lung cancer treatment planning" Med. Phys. **34** 1462-1473 (2007)……..…*(19)*.

Ruan D., Fessler J., Roberson M., Balter J. and M. Kessler "Deformable registration using regularization that accommodates local tissue rigidity" Med. Phys. **33** 2186 (2006)……...…….……*(77,132,150)*.

Ruan D., Fessler J.A., Balter J.M. and J-J. Sonke "Exploring breathing pattern irregularity with projection-based method" Med. Phys. **33** 491-2499 (2006)……...…*(32)*.

Rueckert D., Sonoda L.I., Hayes C., Hill D.L.G., Leach M.O. and Hawkes D.J. "Nonrigid registration using free-form deformations: application to breast MR images" IEEE Transactions on Medical Imaging **18** 712-721 (1999)……....*(76)*.

Sarrut D., Boldea V., Ayadi M., Badel J-N., Ginestet C., Clippe S. and C. Carrie "Nonrigid registration method to assess reproducibility of breath-holding with ABC in lung cancer" Int. J. Radiat. Oncol. Biol. Phys. **61** 594-607 (2005)……*(27,80)*.

Sarrut D., Boldea V., Miguet S. and C. Ginestat "Simulation of four-dimensional CT images from deformable registration between inhale and exhale breathe-hold CT scans" Med. Phys. **33** 605-617 (2006)……..*(81,145)*.

Sawada A., Yoda K., Kobubo M., Kunieda T., Nagata Y. and M. Hiraoko "A technique for noninvasive respiratory gated radiation treatment system based on a real time 3D ultrasound image correlation: A phantom study" Med. Phys. **31** 245-250 (2004)….*(28)*.

Schaefer M. Munter M.W., Thilmann C., Sterzing F., Haering P., Combs S.E. and J. Debus "Influence of intra-fractional breathing movement in step-and-shoot IMRT" Phys. Med. Biol. **49** N175-179 (2004)……...*(21)*.

Schaly B., Kempe J.A., Bauman G.S., Battista J.J. and J Van Dyk "Tracking the dose distribution in radiation therapy by accounting for variable anatomy" Phys. Med. Biol. **49** 791-805 (2004)……...*(58,103,75)*.

Schaly B., Baumann G.S., Battista J.J. and J. Van Dyk "Validation of contour-driven thin-plate splines for tracking fraction-to-fraction changes in anatomy and radiation therapy dose mapping" Phys. Med. Biol. **50** 459-475 (2005)……..……*(75)*.

Scherzer O. and J. Weickert "Relations between regularization and diffusion filtering" J. Math. Imaging Vision **12** 43-63 (2000)……..*(82)*.

Schnabel J.A., Rueckert D., Quist M, Blackall J.M., Castellano-Smith A.D., Hartkens T., Penney G.P., Hall W.A., Liu H.L., Truwitt C.L., Gerritsen F.A., Hill D.G. and Hawkes D.J. "A generic framework for non-rigid registration based on non-uniform multi-level free-form deformations" Proceedings of MICCAI 2001, LNCS 2208 Springer-Verlag, Berlin (2001)……....*(76,126)*.

Schreibmann E., Chen G.T.Y. and L. Xing "Image interpolation in 4D CT using a Bspline deformable registration model" Int. J. Radiat. Oncol. Biol. Phys. **64** 1537-1550 (2006)…….*(77,91)*.

Schweikard A., Glosser G., Bodduluri M., Murphy M.J. and J.R. Adler "Robotic motion compensation for respiratory movement during radiosurgery" Computer Aided Surgery **5** 263-277 (2000)…….*(30)*.

Seco J., Sharp G.C., Turcotte J., Gierga D., Bortfeld T. and H. Paganetti "Effects of organ motion on IMRT treatments with segments of few monitor units" Med. Phys. **34** 923-934 (2007)……...*(21)*.

Seco J., Sharp G.C., Wu Z., Gierga D., Buettner and H. Paganetti "Dosimetric impact of motion in free-breathing and gated lung radiotherapy: a 4D Monte Carlo study of intra/inter fraction effects" Med. Phys. **35** 356-366 (2008) …….*(176)*.

Segars W.P. "Development and application of the new dynamic nurbs-based cardiac-torso (NCAT) phantom," PhD. dissertation, University of North Carolina (2001)….....…*(92,158,172)*.

Segars W.P., D.S. Lalush and B.M.W. Tsui, "Modeling respiratory mechanics in the MCAT and spline-based MCAT phantoms," IEEE Trans. Nucl. Sci. **48** 89-97 (2001)….....*(92,158,172)*.

Seppenwoolde Y., Shirato H., Kitamura K., Shimizu S., van Herk M., Lebesque J.V. and K. Miyasaka "Precise and real-time measurement of 3D tumor motion in lung due to breathing and heartbeat, measured during radiotherapy" Int. J. Radiat. Oncol. Biol. Phys. **53** 822-834 (2002)……..……...*(14)*.

Seppenwoolde Y, Lebesque J.V., de Jaeger K., Belderbos J.S.A., Boersma L.J., Schilstra C., Henning G.T., Hayman J.A., Martel M.K. and R.K. Ten Haken "Comparing different NTCP models that predict the incidence of radiation pneumonitis" Int. J. Radiat. Oncol. Biol. Phys. **55** 724-735 (2003)……..……*(8)*.

Seppenwoolde Y., Berbeco R.I., Nishioka S., Shirato H. and Heijman B. "Accuracy of tumor motion compensation algorithm from a robotic respiratory tracking system: a simulation study" Med Phys **34** 2774-2784 (2007)……*(30)*.

Shannon C.E. "The mathematical theory of communication" Bell System Technical Journal **27** 379-423, 623-656 (1948)……...*(71)*.

Sharp G.C., Jiang S.B., Shimizu S. and H. Shirato "Prediction of respiratory tumour motion for real-time image-guided radiotherapy" Phys. Med. Biol. **49** 425-440 (2004)……*(28)*.

Shen S., Duan J., Fiveash J.B., Brezovich I.A., Plant B.A., Spencer S.A., Popple R.A., Pareek P.N. and J.A. Bonner "Validation of target volume and position in respiratory gated CT planning and treatment" Med. Phys. **30** 3196-3205 (2003)……..……..*(29)*.

Shimizu S., Shirato H., Kagei K., Nishioka T., Bo X., Dosaka-Akita H., Hashimoto S., Aoyama H., Tsuchiya K. and K. Miyasaka "Impact of respiratory movement on the computed tomographic images of small lung tumors in three-dimensional (3D) radiotherapy" Int. J. Radiat. Oncol. Biol. Phys. **46** 1127-1133 (2000)……...*(17)*.

Shih H.A., Jiang S.B., Aljarrah K.M., Doppke K.P. and N.C. Choi "Internal target volume determined with expansion margins beyond composite gross tumor volume in three-

dimensional conformal radiotherapy for lung cancer" Int. J. Radiat. Oncol. Biol. Phys. **60** 613-622 (2004)……..….*(22)*.

Shirato H., Shimizu S., Kunieda T., Kitamura K., van Herk M., Kagei K., Nishioka T., Hashimoto S., Fujita K., Aoyama H., Tsuchiya K., Kudo K. and K. Miyasaka "Physical aspects of a real-time tumor-tracking system for gated radiotherapy" Int. J. Radiat. Oncol. Biol. Phys. **48** 1187-1195 (2000)……*(28)*.

Shirato H., Seppenwoolde Y., Kitamura K., Onimura R. and S. Shimizu "Intrafractional tumor motion:lung and liver" Seminars in Radiation Oncology **14** 10-18 (2004)…….……*(14)*.

Siebers J.V., P.J. Keall, J.O. Kim and R. Mohan "A method for photon beam Monte Carlo multileaf collimator particle transport" Phys. Med. Biol. **47** 3225-3249 (2002)…..*(176)*.

Sillanpaa J., Chang J., Mageras G., Riem H., Ford H., Todor D., Ling C.C. and H. Amols "Developments in megavoltage cone beam CT with an amorphous silicon EPID: reduction of exposure and synchronization with respiratory gating" Med. Phys. **32** 819-829 (2005)……...*(29)*.

Sonke J-J., Zijp L., Remeijer P. and M. van Herk "Respiratory correlated cone beam CT" Med. Phys. **32** 1176-1186 (2005)……....*(24)*.

Stancanello J., Berna E., Cavedon C., Francescon P., Loeckx D., Cerveri P., Ferrigno G. and G. Baselli "Preliminary study on the use of nonrigid registration for thoraco-abdominal radiosurgery" Med. Phys. **32** 3777-3785 (2005)……..…*(77)*.

Starkschall G., Forster K.M., Kitamura K., Cardenas A., Tucker S.L. and C.W. Stevens "Correlation of gross tumor volume excursion with potential benefits of respiratory gating" Int. J. Radiat. Oncol. Biol. Phys. **60** 1291-1297 (2004)…….*(28)*.

Stock M., Kontrisova K., Dieckmann K., Bogner J., Poetter R. And D. Georg "Development and application of a real-time monitoring and feedback system for deep inspiration breath hold based on external marker tracking" Med. Phys. **33** 2868-2877 (2006)……..*(27)*.

Stromberg J.S., Sharpe M.B., Kim L.H., Kini V.R., Jaffray D.A., Martinez A.A. and J.W. Wong "Active breathing control (ABC) for Hodgkin's disease: reduction in normal tissue irradiation with deep inspiration and implications for treatment" Int. J. Radiat. Oncol. Biol. Phys. **48** 797-806 (2000)……....*(27)*.

Stroom J.C., de Boer H.C.J., Huizenga H. and A.G. Visser "Inclusion of geometrical uncertainties in radiotherapy treatment planning by means of coverage probability" Int. J. Radiat. Oncol. Biol. Phys. **43** 905-919 (1999)……*(22)*.

Studholme C., Hill D.G. and Hawkes D.J., "An overlap invariant entropy measure of 3D medical image alignment" Pattern Recognition **32** 71-86 (1999)……...*(72)*.

Tada T., Minakuchi K., Fujioka T., Sakurai M., Koda M., Kawase I., Nakajima T., Nishioka M., Tonai T. and T. Kozuka "Lung cancer: intermittent irradiation synchronized with respiratory motion – results of a pilot study" Radiology **207** 779-783 (1998)……...*(28)*.

Tai P., Yu E., Battista J. and J. Van Dyk "Radiation treatment of lung cancer – patterns of practice in Canada" Radiotherapy and Oncology **71** 167-174 (2004)……..……*(8)*.

Tanner C.,Schnabel J.A., Hill D.L.G., Hawkes D.J., Leach M.O. and D.R. Hose "Factors affecting the accuracy of biomechnical breast models" Med. Phys. **33** 1758-1769 (2006)……..*(89)*.

Tewatia D., Zhang T., Tome W., Paliwal B. and M. Metha "Clinical implementation of target tracking by breathing synchronized delivery" Med. Phys. **33** 4330-4336 (2006)..…*(31)*.

Thirion J.P. "Image matching as a diffusion process: an analogy with Maxwell's demons" Medical Image Analysis **2** 243-260 (1998)…….*(80)*.

Trofimov A., Rietzel E., Lu H-M., Martin B., Jiang S., Chen G.T.Y. and T. Bortfeld "Temporo-spatial IMRT optimization: concepts, implementation and initial results" Phys. Med. Biol. **50** 2779-2798 (2005)……...*(26)*.

Tyldesley S., Boyd C. Schulze K., Walker H. and W. J. Mackillop "Estimating the need for radiotherapy for lung cancer: an evidence-based, epidemiological approach" Int. J. Radiat. Oncol. Biol. Phys. **49** 973-985……..……*(1)*.

Underberg R.W.M., Lagerwaard F.J., Slotman B.J., Cuijpers J.P. and S. Senan "Benefit of respiration-gated stereotactic radiotherapy for stage 1 lung cancer: an analysis of 4DCT datasets" Int. J. Radiat. Oncol. Biol. Phys. **62** 554-560 (2005)……..…*(25,28)*.

Unkelbach J. and U. Oelfke "Inclusion of organ movements in IMRT treatment planning via inverse planning based on probability distributions" Phys. Med. Biol. **49** 4005-4029 (2004)……..…*(26)*.

van den Elsen, P. Pol E.D. and Viergever, M.A. "Medical image matching – a review with classification", IEEE Engineering in Medicine and Biology 26- 39 (1993)……...*(67)*.

Van Dyk J. "The modern technology of radiation oncology" Medical Physics Publishing, Madison WI (1999)……...*(2)*.

van Herk M., Remeijer P., Rasch C. and J.V. Lebesque "The probability of correct target dosage: dose-population histograms for deriving treatment margins in radiotherapy" Int. J. Radiati. Oncol. Biol. Phys. **47** 121-1135 (2000)……...*(22)*.

van Herk M., Remeijer P. and J.V. Lebesque "Inclusion of geometric uncertainties in treatment plan evaluation" Int. J. Radiat. Oncol. Biol. Phys. 52 1407-1422 (2002)……..…*(57)*.

van Herk M. "Errors and margins in radiotherapy" Seminars in Radiation Oncology **14** 52-64 (2004)……..…*(22)*.

Vandermeer A.D., Alasti H., Cho Y-B. and B. Norrlinger "Investigation of the dosimetric effect of respiratory motion using four-dimensional weighted radiotherapy" Phys. Med. Biol. **52** 4427-4448 (2007)……..…*(31)*.

Vedam S.S., Keall P.J., Kini V.R. and R.Mohan "Determining parameters for respiration-gated radiotherapy" Med. Phys. **28** 2139-2146 (2001)……..….*(28)*.

Vedam S.S., Kini V.R., Keall P.J., Ramakrishnan V., Mostafavi H. and R. Mohan "Quantifying the predictability of diaphragm motion during respiration with a noninvasive external marker" Med. Phys. 30 505-513 (2003)……...*(28)*.

Vedam S.S., Keall P.J., Kini V.R., Mostafavi H., Shukla H.P. and R. Mohan "Acquiring a four-dimensional computed tomography dataset using an external respiratory signal" Phys. Med. Biol. **48** 45-62 (2003)……..*(23)*.

Vedam S.S., Keall P.J., Docef A., Todor D.A., Kini V.R. and R. Mohan "Predicting respiratory motion for four-dimensional radiotherapy" Med. Phys. **31** 2274-2283 (2004)……..*(32)*.

Vedam S., Docef A., Fix M., Murphy M. and P. Keall "Dosimetric impact of geometric errors due to respiratory motion prediction on dynamic multileaf collimator-based four-dimensional radiation delivery" Med. Phys. **32** 1607-1620 (2005)……*(32)*.

Verhaegen F. and J. Seuntjens "Monte Carlo modeling of external radiotherapy photon beams" Phys. Med. Biol. **48** R107-164 (2003)…….,……*(8)*.

Viola P. and Wells W.M. "Alignment by maximization of mutual information" Proceedings of the 5th International Conference on Computer Vision, Cambridge MA pp.16-23 (1995)……..……*(72)*.

Vujaskovic Z., Marks L.B. and M.S. Anscher "The physical parameters and molecular events associated with radiation-induced lung toxicity" Seminars in Radiation Oncology **10** 296-307 (2000)…….……*(8)*.

Walters B., Kawrakow I., and D.W.O. Rogers, "DOSXYZ Users Manual," NRCC Report PIRS-794revB (2005)…….*(104,106)*.

Walters B.R.B. and I. Kawrakow "Technical note: Overprediction of dose with default PRESTA-I boundary crossing in DOSXYZnrc and BEAMnrc" Med. Phys. **34** 647-650 (2007)……..……..*(178)*.

Wang H., Dong L., O'Daniel J., Mohan R., Garden A.S., Ang K.K., Kuban D.A., Bonnen M., Chang J.Y. and R. Cheung "Validation of an accelerated "demons" algorithm for deformable image registration in radiation therapy" Phys. Med. Biol. **50** 2887-2905 (2005)……..*(81)*.

Wang H., Dong L., Lii M.F., Lee A., Crevoisier d R., Mohan R., Cox J.D., Kuban D. and R. Cheung "Implementation and validation of a 3-dimensional deformable registration algorithm for targeted prostate cancer radiotherapy" Int. J. Radiat. Oncol. Biol. Phys. **61** 725-735 (2005)……..….*(81)*.

Webb S. "Does elastic tissue intrafraction motion with density changes forbid motion-compensated radiotherapy?" Phys. Med. Biol. **51** 1449-1462 (2006)……*(53)*.

Willoughby T.R., Forbes A.R., Buchholz D., Langen K.M., Wagner T.H., Zeidan O.A., Kupelian P.A. and S.L. Meeks "Evaluation of an infrared camera and X-ray system using implanted fiducials in patients with lung tumor for gated radiation therapy" Int. J. Radiat. Oncol. Biol. Phys. **66** 568-575 (2006)……*(28)*.

Wolthaus J.W.H., Schneider C., Sonke J-J., van Herk M., Belderbos J.S.A., Rossie M.M.G., Lebesque J.V. and E.M.F. Damen "Mid-ventilation CT scan construction from four-dimensional respiration-correlated CT scans for radiotherapy planning of lung cancer patients" Int. J. Radiat. Oncol. Biol. Phys. **65** 1560-1571 (2006)……..……*(25)*.

Wong J.W., Sharpe M.B., Jaffray D.A., Kini V.R., Robertson J.M., Stromberg J.S. and A.A. Martinez "The use of active breathing control (ABC) to reduce margin for breathing motion" Int. J. Radiat. Oncol. Biol. Phys. **44** 911-919 (1999)……....*(27)*.

Wu Z., E. Rietzel, V. Boldea, D. Sarrut and G.C. Sharp "Evaluation of deformable registration of patient lung 4DCT with sub-anatomical region segmentations" Med. Phys in review (2007)……..…….*(172)*.

Wulf J., Hadinger U., Oppitz U., Olshausen B. and M. Flentje "Stereotactic radiotherapy of extracranial targets: CT-simulation and accuracy of treatments in the stereotactic body frame" Radiotherapy and Oncology **57** 225-236 (2000)…….*(26)*.

Wurstbauer K., Deutschmann H., Kopp P. and F. Sedlmayer "Radiotherapy planning for lung cancer: Slow CTs allow the drawing of tighter margins" Radiotherapy and Oncology **75** 65-170 (2005)……..*(22)*.

Yan D., Jaffray D.A. and J.W. Wong "A model to accumulate fractionated dose in a deforming organ" int. J. Radiat. Oncol. Biol. Phys. **44** 665-675 (1999)……...*(50,87)*.

Yan D. and D.M. Lockman "Organ/patient geometric variation in external beam radiotherapy and its effects" Med. Phys. **28** 593-602 (2001)……...*(52)*.

Yan H., Yin F-F., Zhu G-P., Ajlouni M. And J.H. Kim "The correlation evaluation of a tumor tracking system using multiple external markers" Med. Phys. **33** 4073-4084 (2006)……..……*(31)*.

Yan H, Yin F-F., Zhu G-P., Ajlouni M. and J.H. Kim "Adaptive prediction of internal target motion using external marker motion: a technical study" Phys. Med. Biol. **51** 31-44 (2006)..……*(32)*.

Yin F.F., Kim J.G., Haughton C., Brown S., Ajlouni M., Stronati M., Pamukov N. and J.H. Kim "Extracranial radiosurgery: immobilizing liver motion using high-frequency jet ventilation and total intravenous anesthesia" Int. J. Radiat. Oncol. Biol. Phys. **48** S361-362 (2000)……..…….*(27)*.

Yorke E. "Biologcial indices for evaluation and optimization of IMRT" Intensity Modulated Radiation Therapy, AAPM pp. 77-114 (2003)…….……*(6)*.

Yorke E.D., Jackson A., Rosenzweig K.E., Braban L., Leibel S.A. and C.C. Ling "Correlation of dosimetric factors and radiation pneumonitis incidence for non-small-

cell lung cancer (NSCLC) patients in a recently completed dose escalation study" Int. J. Radiat. Oncol. Biol. Phys. 60 S240 (2004)…….……..*(8)*.

Yu C.X., Jaffray D.A. and J.W. Wong "The effects of intra-fraction organ motion on the delivery of dynamic intensity modulation" Phys. Med. Biol. **43** 91-104 (1998)……*(20)*.

Xu Q. and R.J. Hamilton "A novel respiratory detection method based on automated analysis of ultrasound diaphragm video" Med. Phys. 33 916-921 (2006)……....*(28)*.

Zhang G., Guerrero T., Huang T-Z., Fitzpatrick M.J., Ibbott G., Lin K-P. and G. Starkschall "3D optical flow method implementation for mapping of 3D anatomical structure contours across 4D CT data" Proceedings of the 14th Conf. on the use of Computers in Radiation Therapy, Seoul pp.356-360 (2004)……...…..*(79)*.

Zhang T., Keller H., O'Brian M.J., Mackie T.R. and B. Paliwal "Application of the spirometer in respiratory gated radiotherapy" Med. Phys. **30** 3165-3171 (2003)…...*(28)*.

Zhang T., Jeraj R., Keller H., Lu W., Olivera G.H., McNutt T.R., Mackie T.R. and B. Paliwal "Treatment plan optimization incorporating respiratory motion" Med. Phys. **31** 1576-1586 (2004)……..…*(26)*.

Zhang T., Orton N.P. and W.A. Tome "On the automated definition of mobile target volumes from 4D-CT images for stereotactic body radiotherapy" Med. Phys. **32** 3493-3502 (2005)…….*(26,82)*.

**American Association of Physicists in Medicine**
One Physics Ellipse
College Park, MD 20740-3846
(301) 209-3350
Fax (301) 209-0862
http://www.aapm.org

*Office of the Executive Director*
Angela R. Keyser
Phone: 301-209-3385 Fax: 301-209-0862
E-mail: akeyser@aapm.org

**VIA EMAIL**

December 3, 2007

Emily Heath
Medical Physics Unit, McGill University
Montreal General Hospital RM L5-112
1650 Cedar Avenue
Montreal, QC H3G 1A4
CANADA

Dear Ms. Heath:

The American Association of Physicists in Medicine hereby grants permission to Emily Heath to use the material outlined below in your doctoral thesis:

> Heath, E., et al. "Quantification of accuracy of the automated nonlinear image matching and anatomical labeling (ANIMAL) non linear registration algorithm for 4D CT images of lung." Medical Physics 31 (11), 2007;4409-4421.

Sincerely,

Angela R. Keyser

MONTREAL INSTITUT ET McCONNELL BRAIN IMAGING CENTRE NEUROLOGICAL HOPITAL 3801, rue University
INSTITUTE NEUROLOGIQUES DE
AND HOSPITAL MONTREAL
Montreal, Quebec
Canada H3A 2B4
Telephone: (514) 398 8554 McGill University Telecopieur/Fax: (514) 398 2975
Universite McGill

December 13, 2007

To whom it may concern,

Dear sir,

With this note I explicitly grant permission to Emily Heath to use the materials from herpaper "Quantification of the accuracy of the automated nonlinear image matching and anatomical labeling (ANIMAL) nonlinear registration algorithm for 4D CT images of lung Med.Phys. 34(11) 4409 (2007)" authored by Heath *et al.* in her Doctoral thesis provided appropriate reference is used.

D. Louis Collins, Ph.D.Associate Professor Dept. Neurology & NeurosurgeryDept. Biomedical Engineering

STANFORD
UNIVERSITY
MEDICAL CENTER
*Hospital & Clinics · School of Medicine*

DEPARTMENT OF RADIATION ONCOLOGY
http://radonc.stanford.edu

Richard T. Hoppe, M.D., FA.C. R.
*Henry S. Kaplan-Harry Lebeson*
*Professor of Cancer Biology & Chairman*

Stanford Cancer Center
875 Blake Wilbur Drive
Stanford CA 94305-5847
T. 650.723.6171
F: 650.725.8231

*Radiation Therapy*
Malcolm A. Bagshaw, M.D.
*Emeritus*

Sarah S. Donaldson, M.D., FA.C.R.
*Catharine and Howard Avery Professor & Associate Chair*

Iris C. Gibbs, M.D.
Don R. Goffinet, M.D.
Karyn A. Goodman, M.D.
Steven L. Hancock, M.D., FA.C.R.
Kathleen C. Horst, M.D.
Daniel S. Kapp, M,D., Ph.D.
Christopher R. King, Ph.D., M.D.
Susan J. Knox, Ph.D., M.D.
Albert C. Koong, M.D., Ph.D.
Quynh-Thu Le, M.D,
Steve A. Leibel, M.D., F.A.C.R.
Melanie C. Smitt, M,D.

*Division of Radiation Physics*
Paul J. Keall, Ph.D.
*Director*

Peter Fessenden, Ph.D.
*Emeritus*

Edward Graves, Ph.D.
Dimitre Hristov, Ph.D.
Gary Luxton, Ph.D.
Peter Maxim, Ph.D.
Lei Xing, Ph.D.

*Division of Radiation & Cancer Biology*
CCSR - South
269 Campus Drive, Room 1255
Stanford, CA 94305-5152

Amato J. Glaccia, Ph.D.
*Director*

Laura D. Attardi, Ph. D.
Martin Brown, D. Phill
Nicholas C. Denko, Ph.D., M.D.

To whom it may concern,

Dear Sir,

With this note I explicitly grant permission to E. Heath to use the materials from her paper “Quantification of the accuracy of the automated nonlinear image matching and anatomical labeling (ANIMAL) nonlinear registration algorithm for 4D CT images of lung Med. Phys. 34(11) 4409 (2007)” authored by Heath et. al. in her Doctoral thesis provided appropriate reference is used.

Sincerely yours

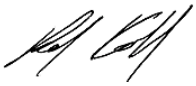

Paul Keall, Ph.D.
Associate Professor
and Director

McGill

*Medical Physics Unit* *Unité de physique médicale*

Montreal General Hospital
1650 avenue Cedar
Montréal, Québec H3G 1A4

Tel. (514) 934-8052
Fax (514) 934-8229

January 24, 2008

To whom it may concern

Dear sir,

With this note I explicitly grant permission to E. Heath to use the materials from her paper: "Quantification of the accuracy of the automated nonlinear image matching and anatomical labeling (ANIMAL) nonlinear registration algorithm for 4D CT images of lung Med. Phys. 34(11) 4409 (2007)" authored by Heath et al in her Doctoral thesis provided appropriate referencing is used.

Sincerely yours,

Jan Seuntjens, Ph.D., FAAPM Associate Professor & Research Scientist
National Cancer Inst. Canada McGill University, Medical Physics 1650 Cedar Ave, Montreal, H3G 1A4 Canada Tel: 514 934 8052 Fax: 514 934 8229 www: http://www.medphys.mcgill.ca

THE UNIVERSITY OF TEXAS
MD ANDERSON
CANCER CENTER

Department of Radiation Physics – 94

Date: December 11, 2007

(713) 745-4502 FAX – (713) 745-4505

To: McGill University

From: Lei Dong, Ph.D.
Department of Radiation Physics
The Univ. of Texas M.D. Anderson Cancer Center

Subject: Granting rights

To Whom It May Concern: This is to grant Emily Health in the Medical Physics Unit, Montreal General Hospital, McGill University, the permission to use the materials published in the paper "Quantification of accuracy of the automated nonlinear image matching and anatomical labeling (ANIMAL) nonlinear registration algorithm for 4D CT images of lung" in her Ph.D. thesis. If you have question, please feel free to contact me.

Yours truly,

Lei Dong, Ph.D. Associate Professor Deputy Director of Research Department of Radiation Physics - 94 Univ. of Texas M.D. Anderson Cancer Center 1515 Holcombe Boulevard Houston, Texas 77030

Tel: (713) 563-2544 Fax: (713) 563-2479 Internet: ldong@mdanderson.org

McGill

*Medical Physics Unit* *Unité de physique médicale*

Montreal General Hospital
1650 avenue Cedar
Montréal, Québec H3G 1A4

Tel. (514) 934-8052
Fax (514) 934-8229

September 19, 2007

To whom it may concern

Dear sir,

With this note I explicitly grant permission to E. Heath to use the materials from her paper: "A direct voxel tracking method for four-dimensional Monte Carlo dose calculations in deforming anatomy" Med. Phys.33, 434 (2006)" authored by Heath and Seuntjens in her Doctoral thesis provided appropriate referencing is used.

Jan Seuntjens, Ph.D., FAAPM Associate Professor & Research Scientist
National Cancer Inst. Canada McGill University, Medical Physics 1650 Cedar Ave, Montreal, H3G 1A4 Canada Tel: 514 934 8052 Fax: 514 934 8229 www: http://www.medphys.mcgill.ca

**American Association of Physicists in Medicine**
One Physics Ellipse
**College Park,** MÜ 20740-3846
**(301) 209^50**
Fax (301) 209-0862
301-^3385 Fax: 301-209-0862 E-roall: akcyscr@aapm.org

OJIyice oftHe Executlv€ S>^^r
ABgcla R_ Keyser http://www.aapm.org phone:

Via Fax: (514) 934-8229

September 20. 2007

Ms. Emily Heath
Medical Physics Ünit. McGill University
Montreal General Hospital Room L5-112
1650 Cedar Avenue
Montreal, QC H3G 1A6

DearMs. Heath:

The American Association of Physicists in Medicine hereby grants you permission to use the material outlined below for your dissertation.

> Heath, E., et al. "A direct voxel tracking method for four-dimensional Monte G dose caiculations in deforming anatomy/' *Medical Physics* 33, 2006; 434

Sincerely,

Angela R. Keyser

arlo